

**ELECTROMAGNETIC MODELING OF  
ACTIVE ANTENNAS WITH APPLICATION  
TO SPATIAL POWER COMBINING**

by

**MOSTAFA NAGUIB ABDULLA**

A dissertation submitted to the Graduate Faculty of  
North Carolina State University  
in partial fulfillment of the  
requirements for the Degree of  
Doctor of Philosophy

**ELECTRICAL ENGINEERING**

Raleigh

1999

**APPROVED BY:**

---

---

---

---

Chair of Advisory Committee

## Abstract

ABDULLA, MOSTAFA NAGUIB. Electromagnetic Modeling of Active Antennas with Application to Spatial Power Combining. (Under the direction of Michael B. Steer.)

A full-wave electromagnetic method of moments (MoM) simulator is developed for the analysis of active antenna elements and arrays. This electromagnetic simulator employs an efficient MoM technique with a unique way of extracting the parameters of passive networks. A strategy for solving active antenna is presented with emphasis on spatial power combining systems. What makes this MoM analysis unique is that it is formulated using a combination of spatial and spectral domains taking full advantage of the strengths of each method to ensure accurate and efficient evaluation of the MoM matrix elements. The method presented here is for analysis of two different structures: a CPW-based slot antenna structure and a slot-stripline-slot antenna structure. The analysis involves passive structure modeling and extraction of its circuit parameters. These circuit parameters can be used in any circuit simulator to calculate the exact terminal parameters. From the exact terminal parameters, other field parameters such as radiated near and far field profiles, gain and, antenna effective isotropic power gain (EIPG) are calculated. This modeling can handle either a unit cell or finite arrays. All other spatial power combining models developed previously have only considered the unit cell of the array or an infinitely periodic array, and hence does not include the actual mutual coupling from other unit cells. Results are presented here showing the effect of mutual coupling from finite arrays. Other results presented here include the driving point impedance of several antenna elements and arrays. The moment method simulator is also used to find the multiport parameters of an array for use in integrated circuit and field simulation. All simulations agree favorably with measurements.

## **Dedication**

This work is dedicated to my wife Shereen, my parents Naguib and Kawther, my sister Doaa, my grandma spirit, and my uncle Salah whose persisted patience, encouragement, understanding and support helped me and gave me the motivation and the power to complete my Ph.D.

I also wish to dedicate this work to my new coming baby....!

# Biographical Summary

MOSTAFA NAGUIB ABDULLA

He was born in Cairo, in 1970 and received his B.Sc. and M.Sc. in Electrical Engineering from Ain Shams University, Cairo, Egypt in 1992 and 1996 respectively.

From 1992 to 1996, he worked as an Assistant Lecturer and Research Assistant in the Electronics and Communication Engineering Department, Ain Shams University, Cairo, Egypt.

Up to August 1999 He was a Research Assistant and Ph.D student in the Department of Electrical and Computer Engineering at North Carolina State University, Raleigh, North Carolina. His research involved modeling and design of microwave circuits and antennas.

He is a student member of the Institute of Electrical and Electronic Engineers (IEEE), the Microwave Theory and Techniques (MTT) Society and, the Antennas and Propagation (AP) society. He is member of Phi Kappa Phi honor society.

## Acknowledgments

I would like to express my gratitude to my advisor Dr. Michael Steer for his support and guidance during my graduate studies. It was a privilege to be part of his research group.

I would also like to express my sincere appreciation to Dr. James Mink, Dr. Frank Kauffman, and Dr. Pierre Gremaud for showing an interest in my research and serving on my Ph.D. committee.

A special appreciation to Mr. Ahmed Khalil and a very big thanks go to my past and present graduate student colleagues and group members for their help especially to Dr. Todd Nuteson, Mr. Waled Mamdouh , and Mr. Rawy Iskander.

Also to thank all my previous professors and teachers.

I wish to thank my wife Shereen, my parents, and my sister, for their continuous support and encouragement.

# Table of Contents

|  |           |
|--|-----------|
| <b>List of Figures</b>                                     | <b>xv</b> |
| <b>1 Introduction</b>                                      | <b>1</b>  |
| 1.1 Motivation and Objective . . . . .                     | 1         |
| 1.2 Dissertation Overview . . . . .                        | 4         |
| 1.3 Original Contributions . . . . .                       | 6         |
| 1.4 Publications . . . . .                                 | 8         |
| <b>2 Literature Review</b>                                 | <b>13</b> |
| 2.1 Introduction . . . . .                                 | 13        |
| 2.2 Active Antennas . . . . .                              | 13        |
| 2.2.1 Diode Integrated Active Antennas . . . . .           | 14        |
| 2.2.2 Transistor Integrated Active Antennas . . . . .      | 15        |
| 2.3 Spatial Power Combining . . . . .                      | 18        |
| 2.3.1 Oscillators Arrays . . . . .                         | 20        |
| 2.3.2 Amplifier Arrays . . . . .                           | 22        |
| 2.4 Modeling of Spatial Power Combining Systems . . . . .  | 24        |
| 2.4.1 Method of Moments . . . . .                          | 29        |
| 2.4.2 Network Parameter Extraction Using MoM . . . . .     | 33        |
| 2.5 Summary . . . . .                                      | 35        |
| <b>3 MPIE and Green's Functions for CPW-Slot Structure</b> | <b>37</b> |
| 3.1 Introduction . . . . .                                 | 37        |
| 3.2 Integral Equation Formulation . . . . .                | 38        |
| 3.2.1 Model Geometry . . . . .                             | 38        |
| 3.2.2 Integral Equation . . . . .                          | 41        |

|          |   |           |
|----------|---|-----------|
| 3.2.3    | Potentials of Diffracted Fields . . . . .                   | 42        |
| 3.2.4    | Dyadic Green's Functions . . . . .                          | 43        |
| 3.3      | Mixed Potential Integral Equation . . . . .                 | 47        |
| 3.4      | Green's Function Formulation for Slot Antenna . . . . .     | 48        |
| 3.4.1    | Solution of Wave Equation . . . . .                         | 49        |
| 3.4.2    | Boundary Conditions . . . . .                               | 50        |
| 3.4.3    | Radiation Condition . . . . .                               | 52        |
| 3.4.4    | Green's Functions for Magnetic Current Potentials . . . . . | 53        |
| 3.4.5    | Surface Waves . . . . .                                     | 54        |
| 3.5      | Near and Far Field Approximations . . . . .                 | 56        |
| 3.6      | Numerical Evaluation of Sommerfeld Integral . . . . .       | 57        |
| 3.6.1    | Numerical Problems . . . . .                                | 58        |
| 3.6.2    | Implementing Numerical Integration on Real Axis . . . . .   | 59        |
| 3.6.3    | Numerical Results . . . . .                                 | 62        |
| 3.7      | Spectral Domain Green's Functions . . . . .                 | 62        |
| 3.7.1    | "a" Region (Half Space) . . . . .                           | 69        |
| 3.7.2    | "b" Region (Substrate-half space) . . . . .                 | 71        |
| 3.7.3    | Total Spectral Domain Magnetic Green's Functions . . . . .  | 74        |
| 3.8      | Summary . . . . .   | 75        |
| <b>4</b> | <b>MPIE Solution using MoM for CPW-Slot Structures</b>      | <b>77</b> |
| 4.1      | Introduction . . . . .                                      | 77        |
| 4.2      | Mixed Potential Integral Equation . . . . .                 | 79        |
| 4.3      | Method of Moments . . . . .                                 | 79        |
| 4.3.1    | Charge and Current Cells . . . . .                          | 80        |
| 4.3.2    | Basis Functions . . . . .                                   | 81        |

|          |   |            |
|----------|---|------------|
| 4.3.3    | Test Functions and Integral Equation Formulation . . . . .          | 84         |
| 4.4      | Matrix Equation . . . . .   | 85         |
| 4.5      | Spectral Domain Matrix Elements . . . . .                           | 87         |
| 4.6      | Excitation . . . . .  | 89         |
| 4.6.1    | Incident Wave Excitation . . . . .                                  | 91         |
| 4.6.2    | Coaxial Probe Excitation . . . . .                                  | 91         |
| 4.7      | Network Characterization and Port Definition . . . . .              | 92         |
| 4.8      | Computational Details and Numerical Considerations . . . . .        | 93         |
| 4.8.1    | Self and Overlapped Cell MoM Matrix Elements . . . . .              | 93         |
| 4.8.2    | Solution of Linear Systems . . . . .                                | 95         |
| 4.8.3    | Condition Number . . . . .  | 95         |
| 4.8.4    | Convergence Issues . . . . .  | 99         |
| 4.8.5    | Valid Frequency Ranges . . . . .                                    | 99         |
| 4.9      | Radiation Pattern . . . . .   | 103        |
| 4.9.1    | Near Field . . . . .  | 103        |
| 4.9.2    | Far Field . . . . .   | 104        |
| 4.10     | Summary . . . . .   | 105        |
| <b>5</b> | <b>MPIE and Green's Functions for Slot-Stripline-Slot Structure</b> | <b>107</b> |
| 5.1      | Introduction . . . . .  | 107        |
| 5.2      | Structure Geometry and Modeling . . . . .                           | 108        |
| 5.2.1    | Integral Equations . . . . .  | 111        |
| 5.2.2    | Potentials of the Diffracted Fields . . . . .                       | 112        |
| 5.3      | Green's Functions . . . . .   | 113        |
| 5.4      | Mixed Potential Integral Equations . . . . .                        | 114        |
| 5.5      | Spatial Domain Potential Green's Functions . . . . .                | 115        |

|          |  |            |
|----------|--|------------|
| 5.5.1    | Internal Region . . . . .  | 115        |
| 5.5.2    | External Region . . . . .  | 120        |
| 5.6      | Spectral Domain Green's Functions . . . . .                                    | 125        |
| 5.6.1    | Internal Region . . . . .  | 125        |
| 5.6.2    | External Region and Total Green's Functions . . . . .                          | 129        |
| 5.7      | Summary . . . . .  | 130        |
| <b>6</b> | <b>Slot-Stripline-Slot Structure MoM Solution and Network Characterization</b> | <b>131</b> |
| 6.1      | Introduction . . . . .   | 131        |
| 6.2      | MPIE for SSS structure . . . . .   | 134        |
| 6.3      | Method of Moments . . . . .  | 135        |
| 6.3.1    | Basis Functions . . . . .  | 136        |
| 6.3.2    | Testing Functions . . . . .  | 137        |
| 6.3.3    | Matrix Equation . . . . .  | 139        |
| 6.3.4    | Cascadable Representation . . . . .  | 141        |
| 6.3.5    | Spectral Domain Matrix Elements . . . . .                                      | 143        |
| 6.4      | Network Characterization for the SSS Array . . . . .                           | 144        |
| 6.4.1    | Introduction . . . . .   | 144        |
| 6.4.2    | Standing Wave Characterization . . . . .                                       | 146        |
| 6.4.3    | Stub De-embedding . . . . .  | 149        |
| 6.4.4    | Quarter-Wavelength Stub . . . . .  | 150        |
| 6.4.5    | Vertical Stub . . . . .  | 150        |
| 6.5      | Results . . . . .  | 155        |
| 6.6      | Summary . . . . .  | 157        |
| <b>7</b> | <b>CPW-Slot Antennas for Spatial Power Combining Applications</b>              | <b>161</b> |

|  |   |            |
|--|---|------------|
| 7.1  | Introduction . . . . .                          | 161        |
| 7.2  | Effective Isotropic Power Gain . . . . .        | 162        |
| 7.3  | Folded-Slot Array . . . . .                     | 163        |
| 7.3.1  | Single Element . . . . .                        | 163        |
| 7.3.2  | Unit Cell . . . . .                             | 164        |
| 7.3.3  | 1×2 Array . . . . .                             | 172        |
| 7.3.4  | 2×2 Array . . . . .                             | 172        |
| 7.3.5  | 4×4 Array . . . . .                             | 174        |
| 7.4  | Designing Slot Arrays . . . . .                 | 184        |
| 7.5  | Five-Slot Array . . . . .                       | 184        |
| 7.5.1  | Impedance Control with Multiple Slots . . . . . | 187        |
| 7.5.2  | Transmission Line Discontinuity . . . . .       | 189        |
| 7.5.3  | Radiation Pattern . . . . .                     | 193        |
| 7.5.4  | 4×4 five-Slot Array . . . . .                   | 193        |
| 7.6  | Summary . . . . .                               | 198        |
| <b>8 Slot-Stripline-Slot Antennas For Spatial Power Combining Applications</b> |   | <b>199</b> |
| 8.1  | Introduction . . . . .                          | 199        |
| 8.2  | SSS Structure . . . . .                         | 199        |
| 8.2.1  | Unit Cell . . . . .                             | 200        |
| 8.3  | 3×3 SSS Array . . . . .                         | 203        |
| 8.3.1  | Coupling Effect . . . . .                       | 206        |
| 8.4  | Power Combining Mechanism . . . . .             | 206        |
| 8.5  | Tolerance of The Amplifiers . . . . .           | 208        |
| 8.6  | Summary . . . . .                               | 214        |

|          |  |            |
|----------|--|------------|
| <b>9</b> | <b>Conclusions and Future Research</b>     | <b>215</b> |
| 9.1      | Conclusions . . . . .                      | 215        |
| 9.2      | Future Research . . . . .                  | 218        |
|          | <b>References</b>                          | <b>221</b> |
| <b>A</b> | <b>Evaluation of The Radiation Pattern</b> | <b>237</b> |
| A.1      | Far Field . . . . .                        | 237        |
| A.1.1    | Input Format . . . . .                     | 239        |
| A.1.2    | Output Format . . . . .                    | 239        |
| A.1.3    | Source Code of Farfield.f . . . . .        | 239        |
| A.2      | Near fields . . . . .                      | 245        |
| A.2.1    | Input Format . . . . .                     | 245        |
| A.2.2    | Output Files . . . . .                     | 245        |
| A.2.3    | Matlab File . . . . .                      | 245        |
| A.2.4    | Source Code of Nearfield.f . . . . .       | 246        |
| <b>B</b> | <b>ArraySim</b>                            | <b>251</b> |
| B.1      | Making ArraySim . . . . .                  | 251        |
| B.1.1    | Makefile . . . . .                         | 251        |
| B.2      | Running ArraySim . . . . .                 | 253        |
| B.3      | Input Files . . . . .                      | 253        |
| B.4      | Output Files . . . . .                     | 254        |
| B.5      | Sample Run . . . . .                       | 254        |

## List of Figures

|     |   |    |
|-----|---|----|
| 1.1 | Power capacities of microwave and millimeter-wave devices: solid line, tube devices; dashed line, solid state devices. After Sleger <i>et al.</i> [1] | 3  |
| 1.2 | Spatial power combiner.   | 3  |
| 1.3 | Top level <i>ArraySim</i> simulation environment for passive and active analysis of array structures.   | 4  |
| 1.4 | Extraction of passive structure parameters; (a) real active antenna ; (b) circuit model.  | 9  |
| 2.1 | A quasi-optical power combiner configuration for an open resonator.   | 19 |
| 2.2 | A grid amplifier/oscillator on a dielectric slab.   | 19 |
| 2.3 | A grid amplifier/oscillator on a dielectric slab with X and Y polarizers.   | 20 |
| 2.4 | Unit cell configuration for a grid oscillator.  | 27 |
| 3.1 | A general aperture structure on metallic conductor on the substrate.  | 39 |
| 3.2 | Transverse cross section of an aperture: (a) original problem; (b) equivalent problem.  | 40 |
| 3.3 | An arbitrary oriented magnetic dipole of momentum $Md\mathbf{l}$ .  | 43 |
| 3.4 | Region “a”.   | 45 |
| 3.5 | Region “b”.   | 45 |
| 3.6 | The complex plane, showing the integration path C for the Sommerfeld integrals and possible choice of branch cuts.                                    | 51 |
| 3.7 | A real axis integration path for the Sommerfeld integral.   | 58 |
| 3.8 | The integrand of the normalized electric vector potential for $NG_{F_{xx}}$ : (a) before singularity extraction ; (b) after singularity extraction.   | 60 |
| 3.9 | Calculated $NG_{F_{xx}}$ and $NG_{\psi}$ as function of normalized source-observation: (a) magnitude; (b) phase. distance.                            | 63 |

|      |   |     |
|------|---|-----|
| 3.10 | Effect of substrate relative permittivity on $NG_{F_{xx}}$ : (a) magnitude ; (b) phase. . . . .   | 64  |
| 3.11 | Effect of substrate thickness on $NG_{F_{xx}}$ : (a) magnitude ; (b) phase. . . . .   | 65  |
| 3.12 | Effect of substrate relative permittivity on $NG_{F_{\psi}}$ : (a) magnitude ; (b) phase. . . . .   | 66  |
| 3.13 | Effect of substrate thickness on $NG_{\psi}$ : (a) magnitude ; (b) phase. . . . .   | 67  |
| 3.14 | Equivalent transmission lines for the immittance approach. . . . .  | 69  |
| 3.15 | Equivalent transmission line model for the immittance approach for the half space dipole. . . . .   | 70  |
| 3.16 | Equivalent transmission lines for the immittance approach. . . . .  | 72  |
| 4.1  | Segmentation of the aperture. . . . .   | 80  |
| 4.2  | Discretization of aperture surface. . . . .   | 82  |
| 4.3  | $x$ -directed current cell centered at $r = 0$ and its associate surface current density $T_x(\mathbf{r})$ , and surface charge density $\Pi_x(\mathbf{r})$ . . . . . | 84  |
| 4.4  | Excitation mechanism:(a) transmitting mode ; (a) receiving mode . . . . .   | 90  |
| 4.5  | Extraction of passive structure parameters; (a) real active antenna ; (b) circuit model. . . . .  | 94  |
| 4.6  | The MoM admittance matrix elements for $31 \times 31$ matrix: (a) magnitude; (b) phase. . . . .   | 96  |
| 4.7  | MoM impedance matrix elements for $31 \times 31$ matrix: (a) magnitude; (b) phase. . . . .  | 97  |
| 4.8  | Condition number of the moment matrix. . . . .  | 98  |
| 4.9  | Driving point impedance of a slot dipole antenna divided into N cells: (a) resistance; (b) reactance. . . . .   | 100 |

|      |   |     |
|------|---|-----|
| 4.10 | Driving point reflection coefficient of a slot dipole antenna divided into<br>N cells: (a) magnitude; (b) phase. . . . .              | 101 |
| 4.11 | Convergence rate of the driving point reflection coefficient of a slot dipole<br>at 5 GHz: (a) magnitude; (b) phase. . . . .          | 102 |
| 5.1  | A SSS spatial power combining system, showing a simplified $3 \times 3$ array.  | 108 |
| 5.2  | Passive SSS unit cell. . . . .  | 109 |
| 5.3  | SSS unit cell: (a) original structure; and (b) structure after application<br>of the equivalence principle. . . . .                   | 110 |
| 5.4  | The convergence rate of $G_d$ using three representations for $r = 0.1\lambda$ : (a)<br>real; (b) imaginary. . . . .                  | 121 |
| 5.5  | The convergence rate of $G_d$ using three representations for $r = 0.001\lambda$ :<br>(a) real; (b) imaginary. . . . .                | 122 |
| 5.6  | The effect of $c$ on the convergence rate of the accelerated $G_d$ series for<br>$r = 0.1\lambda$ : (a) real; (b) imaginary. . . . .  | 123 |
| 5.7  | The effect of $c$ on the convergence rate of the accelerated $G_d$ series for<br>$r = 0.01\lambda$ : (a) real; (b) imaginary. . . . . | 124 |
| 5.8  | Equivalent transmission lines for the immittance approach of the internal<br>region for the SSS structure. . . . .                    | 126 |
| 5.9  | Equivalent transmission lines for the $\tilde{G}_{EJ}$ . . . . .  | 126 |
| 5.10 | Equivalent transmission lines for the $\tilde{G}_{HM}$ . . . . .  | 128 |
| 6.1  | A slot-stripline-slot spatial power combining system, showing a simplified<br>$3 \times 3$ array. . . . .                             | 132 |
| 6.2  | Passive slot-stripline-slot unit cell. . . . .  | 132 |
| 6.3  | Network model of large partitioned electromagnetic system. . . . .  | 133 |
| 6.4  | Discretization of the upper slot, lower slot, and stripline surfaces. . . . .   | 136 |

|      |  |     |
|------|--|-----|
| 6.5  | $x$ -directed current cell centered at $x = 0$ and its associate surface current density $T^x(x)$ , and surface charge density $\Pi^x(x)$ . . . . .  | 138 |
| 6.6  | Segmentation of the slot array system. . . . .   | 143 |
| 6.7  | Slot-stripline-slot: (a) amplifier unit cell; (b) equivalent network. . . . .  | 145 |
| 6.8  | Four techniques for establishing a circuit ports in MoM analysis: (a) standing wave characterization, (b) stub-de-embedding; (c) quarter wavelength stub; and (d) Vertical stub. . . . .   | 147 |
| 6.9  | Single port. . . . .   | 148 |
| 6.10 | Port definition for differential port and the differential bases cells. . . . .  | 149 |
| 6.11 | Port definition for a unit cell using vertical current cell and half cell. . . . .   | 152 |
| 6.12 | Configuration of $x$ -directed rooftop basis functions with the source basis in the left column and the test basis in the right column. . . . .  | 154 |
| 6.13 | Return loss for single slot antenna using: (a) port impedance $Z_{PORT}$ (solid line); and (b) differential impedance $Z_{DIFF}$ (dotted line). Referring to Fig. 6.9 $l_L = 50$ mm, $W_L = 2.5$ mm, $l_S = 30$ mm, $W_S = 2$ mm, $l_{OFF} = 10$ mm, $h = 1.57$ mm, and $\epsilon_r = 2.2$ . . . . . | 156 |
| 6.14 | Return loss for single port slot antenna: (a) using $\lambda/4$ stub (solid line); and (b) reflection coefficient method after [209] (dotted line). . . . .  | 157 |
| 6.15 | Resistance of single slot circuit in Fig. 6.9. . . . .   | 158 |
| 6.16 | Reactance of single slot circuit in Fig. 6.9. . . . .  | 158 |
| 7.1  | Measurement setup for computing EIPG (a) measurement (b) calibration   | 163 |
| 7.2  | The layout of the folded-slot antenna. . . . .   | 164 |
| 7.3  | Comparison between measurement (dotted line) and MoM simulation (solid line) of the folded-slot antenna in Fig. 7.2. . . . .   | 165 |

|      |  |     |
|------|--|-----|
| 7.4  | The calculated and measured input impedance of the folded slot. MoM simulation (solid line), FDTD (short dashed line), and measurement (long dashed line): (a) real; and (b) imaginary. . . . .        | 166 |
| 7.5  | The amplifier unit cell . . . . .  | 167 |
| 7.6  | Effect of the separation distance $S$ on the S-parameters of the unit cell in Fig. 7.5: (a) magnitude of $S_{11}$ ; and (b) magnitude of $S_{12}$ . . . . .  | 168 |
| 7.7  | $E_y$ near-field plots at 0.8 mm for a unit folded-slot cell with plane $E_y$ of 1V/m at 2 GHz. . . . .  | 169 |
| 7.8  | $E_x$ near-field plots at 0.8 mm for a unit cpw cell with incident plane $E_y$ of 1V/m at 2 GHz. . . . .   | 170 |
| 7.9  | Radiation pattern of the unit cell at 2 GHz: (a) in $\phi = 0$ plane ; (b) in $\phi = 90$ plane ( $E_\theta$ dotted line and $E_\phi$ solid line). . . . .   | 171 |
| 7.10 | $1 \times 2$ array: (a) layout ; (b) S-parameters. . . . .   | 173 |
| 7.11 | CPW $2 \times 2$ Array . . . . .   | 174 |
| 7.12 | Passive simulation of folded-slot $2 \times 2$ array (unit cells separated by 6mm): (a) $S_{11}$ of single antenna, unit cell, and $2 \times 2$ array (b) S parameters of $2 \times 2$ array . . . . . | 175 |
| 7.13 | Near field plots of folded-slot $2 \times 2$ array at 0.8mm: (a) $E_y$ (b) $E_x$ . . . . .   | 176 |
| 7.14 | CPW $4 \times 4$ Array . . . . .   | 177 |
| 7.15 | Input impedance of folded-slot array compared with unit cell. (a) real (b) imaginary . . . . .   | 178 |
| 7.16 | Coplanar waveguide (CPW) geometry . . . . .  | 179 |
| 7.17 | Simulation of the EIPG of a unit cell: (a) setup and; (b) open circuit voltages. . . . .   | 180 |
| 7.18 | Circuit analysis of the spatial amplifier given a Z port based matrix: (a) circuit model; and (b) MESFET model. . . . .  | 181 |

|      |  |     |
|------|--|-----|
| 7.19 | The calculated and measured EIPG. MoM simulation(solid line), and measurement (dashed line):(a) unit cell; and (b) array. . . . .  | 183 |
| 7.20 | Three designs for 2×2 folded-slot arrays with vertical slots as transmitting slots and horizontal slots as receiving slots . . . . .   | 185 |
| 7.21 | Near field plots for 2×2 array at 9 GHz . . . . .  | 186 |
| 7.22 | Layout of slot antenna element with CPW feeding line for antennas with varying number of slots: (a) a single slot; (b) a double slot; (c) a triple slot; (d) a four-slot; and (e) a five-slot CPW antenna. . . . . | 188 |
| 7.23 | Variation of multi-slots antenna input impedance with number of slots. . . . .   | 188 |
| 7.24 | Input impedance with number of slots: (a) resistance; (b) reactance . . . . .  | 190 |
| 7.25 | S11 for the slot antenna . . . . .   | 191 |
| 7.26 | Return loss of the five-slot antenna. . . . .  | 192 |
| 7.27 | The layout of the five-slot antenna. . . . .   | 192 |
| 7.28 | Effect of transmission line gap on S parameters of the five folded slot antenna: (a) magnitude; and (b) phase. . . . .   | 194 |
| 7.29 | The calculated far field of the five-slot antenna:(a)H-plane; and (b) E-plane ( $E_\theta$ dotted line and $E_\phi$ solid line). . . . .   | 195 |
| 7.30 | The layout of five-slot spatial amplifier: (a) 4×4 array; (b) unit cell. . . . .   | 196 |
| 7.31 | The EIPG of the 4×4 five-slot array. . . . .   | 197 |
| 7.32 | The calculated E-plane far field of the five-slot array. . . . .   | 197 |
| 8.1  | Three Layer SSS Unit Cell: (a) passive (b) active . . . . .  | 201 |
| 8.2  | Slot-Stripline antenna: (a) Structure layout; and (b) return loss ( <i>ArraySim</i> ; solid line, [213]; dotted line). . . . .   | 202 |
| 8.3  | Measurement showing minimum insertion loss around 10.3 GHz as expected by simulation results. . . . .  | 203 |

|      |  |     |
|------|--|-----|
| 8.4  | A 3×3 SSS array is excited with a hard horn and near field plots are made at various distances, $d$ , from array . . . . .   | 204 |
| 8.5  | 3x3 SSS Array . . . . .  | 205 |
| 8.6  | Simulation of a 3x3 SSS array shows minimum reflection of input power around 10 GHz . . . . .  | 205 |
| 8.7  | Near field plots for 3×3 array at 10GHz . . . . .  | 207 |
| 8.8  | 3×3 array radiation pattern of the H-plane at 10 GHz. . . . .  | 208 |
| 8.9  | The magnitude of the horizontally polarized electric field at a distance $z$ from the slot array surface: (b) $z = \lambda/4$ . (c) $z = \lambda/2$ . (d) $z = 3\lambda$ . . . . .                               | 209 |
| 8.10 | The magnitude of the horizontally polarized electric field at a distance $z$ from the slot array surface with one of the amplifier off: (b) $z = \lambda/4$ . (c) $z = \lambda/2$ . (d) $z = 3\lambda$ . . . . . | 210 |
| 8.11 | Near field plots for 3×3 array at 38 GHz: left side; identical amplifiers, right side; random tolerance . . . . .  | 211 |
| 8.12 | 3×3 array radiation pattern for identical amplifier case at 38 GHz ( $E_\theta$ ; solid line; $E_\phi$ ; dotted line) (a) H-plane ( $\phi = 0$ ) ;(b) E-plane ( $\phi = 90$ ). . . . .                           | 212 |
| 8.13 | 3×3 array radiation pattern for random variation in amplifier parameters at 38 GHz ( $E_\theta$ ; solid line; $E_\phi$ ; dotted line) (a) H-plane ( $\phi = 0$ ) ;(b) E-plane ( $\phi = 90$ ). . . . .           | 213 |
| 9.1  | More MoM based routines can be interfaced to handle more structures . . . . .  | 220 |
| A.1  | Actual and equivalent problem models. . . . .  | 238 |
| A.2  | The coordinate system. . . . .   | 238 |



# Chapter 1

## Introduction

### 1.1 Motivation and Objective

The quest for high-powered, light-weight, millimeter-wave sources is becoming more demanding. Tubes are used for producing high power at millimeter-wave frequencies but are becoming less desirable because of their short life span, bulky size and the need for high voltage DC power supplies. Fig. 1.1 shows a comparison of the power levels for various tube devices and solid state devices [1]. On the other hand solid state devices are generally more desirable in terms of small size, light weight, high reliability and excellent manufacturability but the power that can be generated at millimeter-wave frequencies is limited. Transmission lines suitable for integrated circuits become very lossy at higher frequencies due to radiation losses, substrate losses, and increased skin-effect ohmic losses. By integrating active elements directly in the antenna element of a single antenna or an array, these losses can be significantly reduced.

As the frequency of operation increases for most semiconductor oscillator or amplifier devices, the size of the devices must decrease in order to reduce capacitive and transit time effects. Size reductions reduce the maximum output power of the device proportional to a factor between  $1/f$  and  $1/f^2$  with the result that for moderate or high-power applications in the millimeter-wave frequency range, vacuum tube circuits are required. In order to overcome the fundamental limitations on the output power of semiconductor circuits at higher frequencies, particularly frequencies

in the millimeter-wave range and higher, integrated active antenna elements and spatial power combining techniques have been developed. There are many commercial and industrial applications for these techniques. For example, automotive radar system, such as collision avoidance and intelligent highway communications, are applications with huge potential markets and consequently very active commercial development. Active antennas also offer potential advantages for personal communications systems, sensors, RFID systems, and space systems. Cost, reliability, and size constraints are absolutely critical to these applications, and active antenna and spatial power combining are very promising approaches. The potential for lower weight, smaller, less expensive, more reliable, and more efficient circuits for millimeter-wave applications is extremely important for military applications.

Electromagnetic modeling of these large systems along with linear and nonlinear circuit components is emerging as one of the great challenges in microwave and millimeter-wave computer aided engineering. The target problem in the current work is the spatial power combining amplifier shown in Fig. 1.2 [2]. Each dimension of this amplifier is at least two wavelengths. The amplifiers are MMIC chips arranged in a  $5 \times 5$  or perhaps larger array. Each amplifying unit cell of the amplifier is an amplifier with a stripline or CPW line coupled slot input antenna and a similar antenna at the output.

In this dissertation a computer aided engineering tool (CAE) based on an advanced method of moments (MoM) approach to model active antennas, arrays, and spatial power combining systems is developed. With this formulation the MoM field solver can be conveniently used in the development of circuit-level models of the passive linear elements in the spatial systems which can then be interfaced with transient analysis (SPICE) and steady state analysis (harmonic balance). The CAE tool developed here, called *ArraySim*, simulated two types of antenna structures: (1)

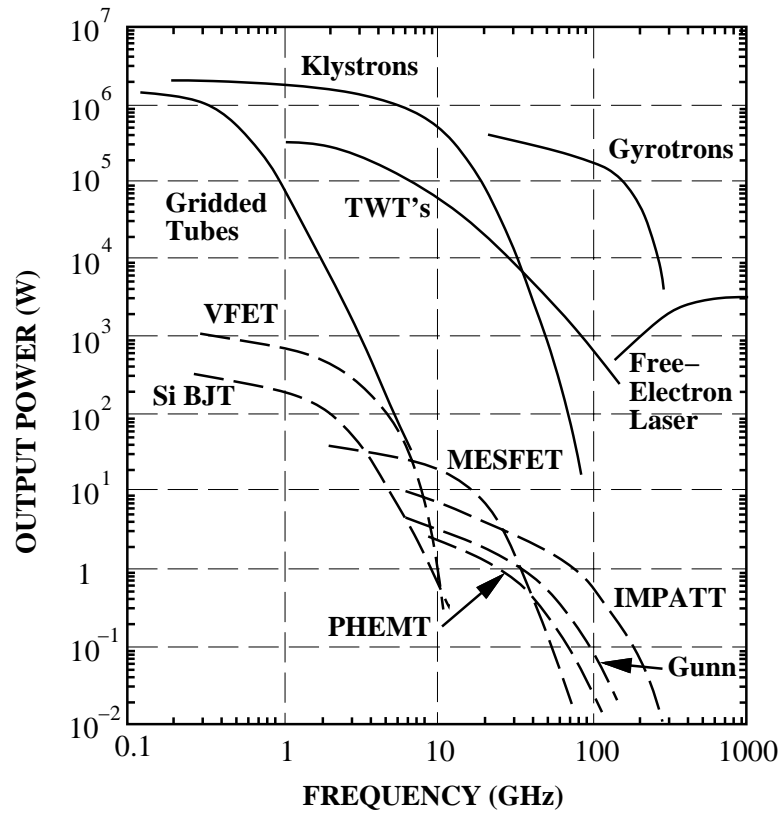


Figure 1.1: Power capacities of microwave and millimeter-wave devices: solid line, tube devices; dashed line, solid state devices. After Slegler *et al.* [1]

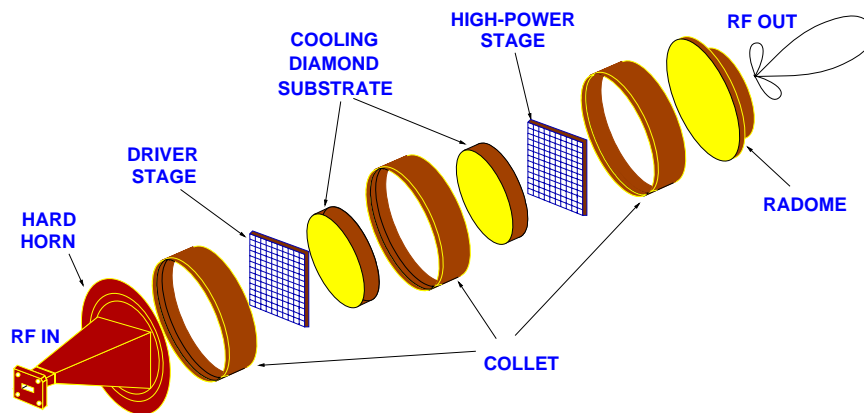


Figure 1.2: Spatial power combiner.

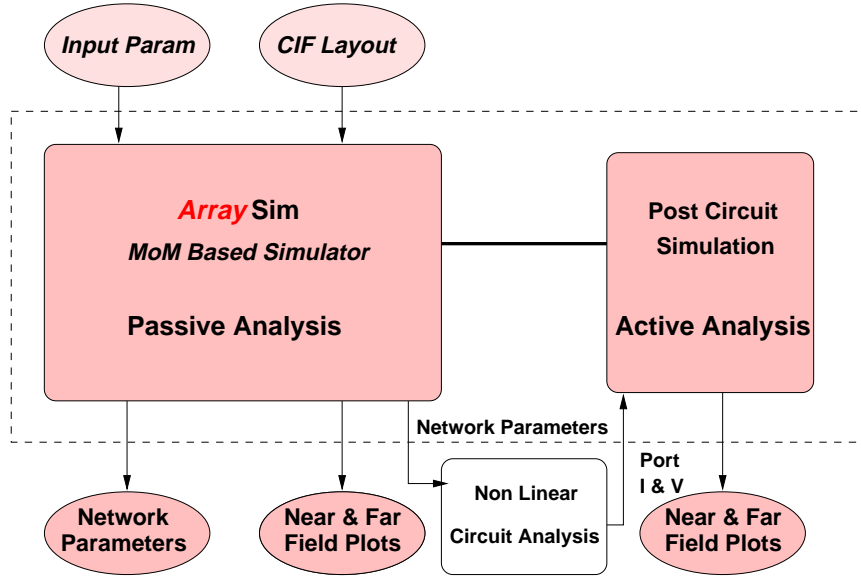


Figure 1.3: Top level *ArraySim* simulation environment for passive and active analysis of array structures.

a Coplanar Waveguide (CPW) slot antenna structure, and (2) a Slot Stripline Slot (SSS) structure. *ArraySim* allows users to study the behavior of a given structure. Fig. 1.3 shows a top level flow of *ArraySim*.

## 1.2 Dissertation Overview

Chapter 2 presents a review of the current literature in the field of active antennas, and spatial power combining focusing mainly on active antennas and arrays, spatial power combining systems, and electromagnetic modeling of these systems using MoM technique.

In Chapter 3 the derivation of the Mixed Potential Integral Equation (MPIE) for a slot over a dielectric slab structure is presented. Also included in this chapter is the formulation of the spatial domain dyadic Green's function using Sommerfeld

integral. Chapter 3 also includes the spectral domain dyadic Green's functions.

Chapter 4 focuses on solution of the MPIE derived in Chapter 3 using the MoM technique. The complete formulation including a unique MoM algorithm that combines both the spatial and spectral domain is given. Numerical considerations such as convergence and condition numbers of the moment matrix are discussed. Also the analysis for computing the network port parameters directly from the MoM matrix is presented.

In Chapter 5 the derivation of the MPIE for a slot-stripline-slot (SSS) structure is presented. Also included in this chapter is the formulation of the spatial domain dyadic Green's function. Chapter 3 also includes the spectral domain dyadic Green's functions.

Chapter 6 focuses on solution of the MPIEs derived in Chapter 5 using the MoM technique. The complete formulation including a unique moment method algorithm that combines both the spatial and spectral domain is given. Also a comprehensive study and analysis for computing the network port parameters directly from the MoM matrix for structures with ground plane is presented.

Chapter 7 investigates the CPW-slot antennas and arrays performance as a spatial power combining system. It also presents active analyses of two types of  $4 \times 4$  arrays and validates the MoM program by comparing simulations to measurements.

Chapter 8 presents and investigates the SSS structure as it is a candidate for spatial power combining arrays. Coupling effects are studied and validation of the simulator is presented by comparing code results with published measured data.

In Chapter 9 a summary of the dissertation is given along with conclusions and suggestions for future work in this topic.

### 1.3 Original Contributions

The original contributions presented in this dissertation are:

- The derivation of both spatial and spectral domain dyadic Green's functions for two different structure:
  1. An aperture over a dielectric slab structure (CPW-based slot antenna).
  2. A slot-stripline-slot structure.

In the first one, the spatial domain Green's functions are calculated using the Sommerfeld integral technique [3] which is more convenient for this type of structure. This derivation is given in Chapter 3. Otherwise in the slot-stripline-slot structure (SSS), which is a parallel plate-like structure, both modal and image representations are used following the approach in [4] and it is given in Chapter 5.

Also in Chapter 5, a numerical study of the convergence rate of the potential spatial domain Green's functions of the SSS structure is presented. This study yields the optimum value of the acceleration parameter for numerically efficient evaluation of the Green's function infinite series.

The derivations of the spectral domain dyadic Green's functions for the two structures are presented in Chapter 3 and 5. The immittance technique [5] is used in these derivations.

- Accurate and numerically efficient full-wave electromagnetic models are presented for both the CPW and SSS passive structures. These models are based on the MPIE and the MoM technique. In these models :

1. An advanced MoM implementation where both spatial and spectral domain techniques were used for accurate and efficient analysis.
2. An interpolation of the spatial domain Green's functions was used to reduce the CPU time required for MoM matrix elements calculations.
3. The symmetric and toeplitz properties of the MoM matrix are used to reduce the computational efforts.
4. The derivation of the near and far field equations are presented in Chapter 3. From these fields profile, the antenna (active or passive) parameters are calculated.

These MPIE-MoM models are presented in Chapter 4 for the CPW structure and in Chapter 6 for SSS structure.

- Based on the above models, a FORTRAN code was written to evaluate the MoM matrix and calculate the antenna parameters (gain, radiation patterns, etc.) and circuit parameters (S,Z,Y). Also, a Matlab code was developed to draw the near-field profile and antenna current distribution. These codes became the core engine of a CAE tool, called *ArraySim*, developed by U. Mughal [6].
- An active-passive analysis technique was developed to simulate the active and passive circuits simultaneously (Fig. 1.4(a)) which is similar to a spatial power combiner unit cell. In this technique, first, the extraction of the passive parameters is performed. This result in the excitation vectors  $V_1^e$  and  $V_2^e$  as shown in Fig. 1.4(b) and  $Z$  or  $Y$  passive network parameters. Using any circuit simulator, the exact currents and voltages at the device terminal are obtained. Again, the MoM field simulator is used to calculate the exact fields

and evaluate the EIPG or EIRP but in this case, the exact excitation vectors are used.

In Chapter 7, this technique is used to simulate an active unit cell and  $4 \times 4$  arrays of CPW-slot antenna. A good agreement has been shown between simulation and measurements.

- A comprehensive study of port definitions in the MoM technique is presented in Chapter 6. Using a vertical connection between the ground plane and the stripline, the exact port impedance was calculated. The port parameters are directly calculated from the MoM inverted matrix without the need for surface current calculations. Also the concepts of stub extraction and quarter wavelength extraction are developed to overcome the computational efforts needed in the vertical current method. Comparison of all these techniques and agreement with published results are given in Chapter 6.

## 1.4 Publications

The work described in this dissertation resulted in the following publications:

- M. N. Abdulla and M. B. Steer, "A Partitioning approach to large scale electromagnetic problem applied to an array of microstrip coupled slot antennas," *1999 IEEE MTT-S Int. Microwave Symp. Digest*, June 1998.
- M. N. Abdulla and M. B. Steer, "A finite double-layer slot array structure for spatial power combining amplifiers," *Proc. IEEE Antenna and Propagation Symp.*, June, 1998.
- M. B. Steer, M. N. Abdulla, C. E. Christoffersen, M. Summers, S. Nakazawa, A. Khalil and J. Harvey, "Integrated electromagnetic and circuit modeling of

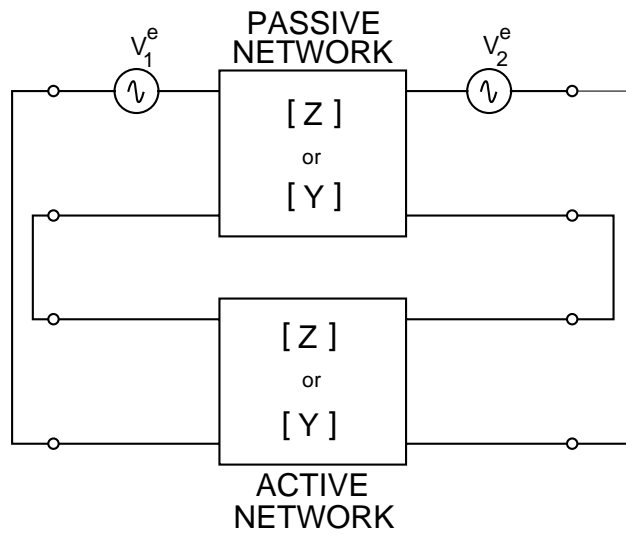
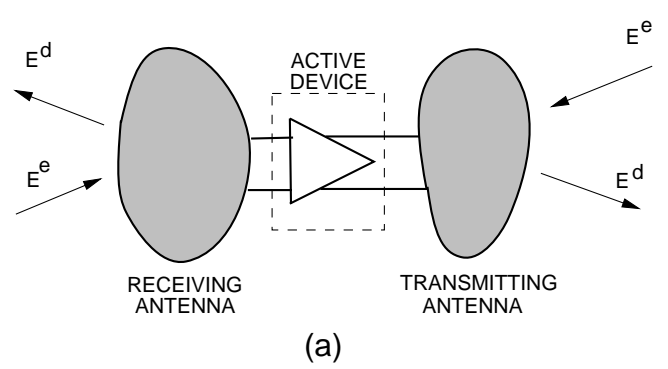


Figure 1.4: Extraction of passive structure parameters; (a) real active antenna ; (b) circuit model.

large microwave and millimeter-wave structures,” *Proc. IEEE Antenna and Propagation Symp.*, June, 1998.

- M. N. Abdulla, U. A. Mughal, H.-S. Tsai, M. B. Steer, and R. A. York, “A full-wave system simulation of a folded-slot spatial power combining amplifier array,” *1999 IEEE MTT-S Int. Microwave Symp. Digest*, June 1999.
- M. N. Abdulla, U. A. Mughal, and M. B. Steer, “Network characterization of a finite array of folded-slot antennas for spatial power combining application,” *Proc. IEEE Antenna and Propagation Symp.*, July, 1999.
- M. N. Abdulla and M. B. Steer, “Extraction of network parameters in the electromagnetic analysis of planar structure using the method of moments,” submitted to *IEEE Trans. Microwave Theory Tech.*
- U. A. Mughal, M. N. Abdulla, and M. B. Steer, “Coupling effects in a stripline-coupled-double-slot array,” submitted to *IEEE Microwave and Guided wave Letters*.
- M. B. Steer, J. F. Harvey, J. W. Mink, M. N. Abdulla, C. E. Christoffersen, H. M. Gutierrez, P. L. Heron, C. W. Hicks, A. I. Khalil, U. A. Mughal, S. Nakazawa, T. W. Nuteson, J. Patwardhan, S. G. Skaggs, M. A. Summers, S. Wang, and A. B. Yakovlev “Global modeling of spatially distributed millimeter-wave systems,” *IEEE Trans. Microwave Theory Tech.*, vol. 47, June 1999.
- M. B. Steer, C. E. Christoffersen, H. Gutierrez, S. Nakazawa, M. Abdulla, and T. W. Nuteson, “Modeling of Large Non-Linear Systems Integrating Thermal and Electromagnetic Models,” *European Gallium Arsenide and related III-V Compounds Application Symposium*, October 1998, pp. 169-174.

- U. A. Mughal, M. N. Abdulla, C. E. Christoffersen, J. Patwardhan, and M. B. Steer, “Hierarchical approach to modeling active antenna arrays,” submitted to *Int. J. of Microwave Millimeter-wave CAE*.



## Chapter 2

### Literature Review

#### 2.1 Introduction

In this chapter, a literature review of active antennas and spatial power combining techniques is presented. This literature review consists of three main sections. The first section reviews active antenna concepts and developments. The second reviews spatial power combining arrays including oscillator arrays and amplifier arrays. Here reviews are presented on experimental aspects of quasi-optical system development. The last section of this literature review is on modeling of spatial power combining systems. Reviews on what has been done with numerical modeling of spatial power combining systems is presented.

#### 2.2 Active Antennas

The concept of integration of the antenna with the active circuit was introduced by Hertz with the idea of using an end-loaded dipole transmitter and a resonant square-loop antenna receiver [7]. Neither the transmitter nor the receiver used any matching networks between the circuit and the antenna. Incorporating active devices directly into the antenna structure has been pursued at least since the mid-1940's. The concept of active antenna surfaced again in the 1960's. Active dipole and slot antennas employing parametric devices and tunnel diodes were developed by Frost and Pendinoff [8, 9]. In 1968 and 1969 Meinke and Landstorfer [10, 11] described the mating of a FET transistor to terminals of a dipole to serve as a

VHF amplifier for reception at 700 MHz. This early work uses matching networks near the antenna to optimize performance, but it shows remarkable foresight in its concept of integration. Ramsdale and Maclean [12] used BJTs and dipoles for transmitter applications in 1971. They demonstrated large length reductions in 1974 [13], and later in 1975 [14] by using active antenna concept. In the same year, a concept using injection-locked distributed oscillators demonstrated beam steering for active antenna [15]. In 1980, Armstrong *et al.* demonstrated the use of a single active antenna for Doppler sensing applications [16]. During the 1980s improvements in solid state devices and integrated circuit techniques made millimeter-wave operating frequencies more accessible. In the following sections, a review of both diode and transistor integrated active antennas from the 1980's till present is presented.

### 2.2.1 Diode Integrated Active Antennas

Early in the 1980's, investigators began to miniaturize circuits and bring them closer to the antenna. In 1982, the varactor-tunable passive microstrip patch antenna was introduced by Bhartia and Bahal [17]. The first modern active antenna was developed by Thomas *at al.* in 1985. It was a rectangular microstrip patch antenna with integrated Gunn effect device operating at X-band frequencies [18]. In the following year an IMPATT integrated circular patch was demonstrated by [19]. In 1986, the emphasis shifted from single active antennas to arrays of distributed sources for power combining. In 1988, a monolithic active antenna operates at 43.3 GHz with an output power of 27 mW was reported [20]. The IMPATT integrated monolithic configuration is ideally suited for coupling to rectangular waveguide or for large planar array. The configuration was used by Shillue *et al.* in a spatial array within a quasi-optical resonator in 1989 [21]. Gunn integrated microstrip patch

antennas [22] have demonstrated good power combining efficiency and fairly good radiation patterns. Early in 1988, Hummer and Chang investigated Gunn integrated microstrip antennas for spatial power combining [23]. An integrated Gunn active patch antenna was used by York, Compton and others to investigate synchronization of weakly coupled distributed oscillators [24, 25, 26]. York and Compton use a dual Gunn integrated antenna to provide more power and lower cross-polarization[26]. The use of an aperture-coupled patch for hybrid and monolithic circuit integration was proposed by Gao and Chang in 1988 [27]. The concept of an aperture-coupled antenna for power combiners has been demonstrated by Lin and Itoh in a  $4 \times 4$  array [28]. A V-band power combiner using 60 GHz pulsed IMPATT oscillators was demonstrated by Davidson et al. [29]. An active V-band antenna Gunn diode implementation along with bias-tuning characteristics and radiation patterns are shown in [30]. In 1994, Wu and Chang introduced another active antenna [31]. It uses one transistor and two circular, instead of rectangular, patches to load the transistor terminals. Superconductor T-Ba-Cu-O/GaAs hybrid oscillator coupled to a circular patch at 10 GHz was reported in 1993 [32].

### **2.2.2 Transistor Integrated Active Antennas**

Although diodes have shown higher operating frequencies and higher output power level, most investigators have used transistors in spatial power combining schemes. Transistors are low priced, monolithically compatible, and provide high dc-to-rf conversion efficiencies at low operating voltages. Furthermore transistors perform a variety of functions using a single technology, thereby allowing greater flexibility in a multi function design. The use of three terminal devices has brought on a wide range of integrated antenna for oscillators, amplifier, and other components.

The FET integrated microstrip patch antenna was first demonstrated by Chang *et al.* [33] in 1988 with a C-band radiating oscillator circuit operates at 7.5 GHz with power output of 17 mW. A similar configuration was analyzed by Fusco and Burns in 1990 [34]. Another transistor integrated antenna design was introduced by Birkeland and Itoh [35, 36]. Birkeland and Itoh introduced an approach to edge-coupled FETs to microstrip patches in 1990 [37]. The system operated at 6 GHz with typical effective isotropic radiated power (EIRP) of 19 dBm. Fusco also investigated an edge-fed transistor integrated active antenna as a more compact design over the feedback amplifier design in 1992 [38].

Another edge-fed dual FET integrated microstrip patch antenna oscillator was demonstrated by Hall and Haskins for beam-scanning applications in 1992 [39] and 1994 [40]. An operating frequency of 2.28 GHz and external injection-locking signal allows over  $40^\circ$  of beam steering for a four-element H-plane array. Another approach was shown by Birkeland and Itoh in 1991. It uses a directional microstrip coupler to develop two port FET oscillator [41]. with a 16-element array of these elements, a locking bandwidth of 453 MHz at 6 GHz was demonstrated for an injected power of 10.3 dBm [42]. A similar amplification concept was developed by Mader *et al.* [43]. Tasi and York developed a reflection amplifier module for quasi-optical arrays, which differs from the array shown earlier [44]. Another quasi-optical amplifier array with a gain of 5.5 dB at 10.9 GHz and 3 dB bandwidth of 1 GHz was shown by Sheth *et al.* [45]. In 1990 York *et al.* introduced a FET integrated active antenna [46]. A narrow slit splits the patch to provide dc isolation between the drain and gate during biasing. The active antenna requires vias to connect the FET source leads and quarter-wave stub on the gate side of the antenna to ground. The drain terminal is biased through a low-pass filter using a capacitor and an inductive line. The active antenna oscillates at 8.2 GHz with about 250 MHz of

bias-tuning range. A dual push-pull FET integrated patch was introduced by Wu *et al.* in 1992 [47]. The configuration allows separate loading of the drain and gate ports of the FET, which simplifies the design. The dual-FET split patch antenna generated 47 mW at 8.1 GHz. An active patch antenna with very good oscillating characteristics was demonstrated by Martines and Compton in 1994 [48]. This FET patch antenna oscillator operated at 9.84 GHz with 25 MHz tuning range and an EIRP of 360 mW with a dc-to rf conversion efficiency of 58%. In [49] a 10 GHz active antenna oscillator/modulator having a 3 dB modulation bandwidth of 1.4 GHz was introduced. The spectral oscillator jitter is below 50 kHz and the single-sideband noise is -65 dBc/Hz at 10 kHz from the carrier. The intermodulation distortion is less than -20 dBc for all modulation powers. A voltage controlled transistor oscillator using a varactor diode was introduced by Haskins, Hall, and Dahele in 1991 [50, 51]. It uses a BAR-28 diode to provide 100 MHz of tuning range at 2.2 GHz for the active antenna. Another VCO active antenna was shown by Liao and York and used in a  $1 \times 10$  elements [52]. In this configuration, the patch serves as a feedback from the drain to the gate through a coupled a coupled line section. The transistor requires vias to ground for the source leads and quarter-wave stub on the gate terminal. The varactor has a maximum to minimum capacitance ration of 3. The VCO operates at 8.45 GHz with 150 MHz of tuning bandwidth of 1.8%. The EIRP of the 10 elements array was 10.5 W at 8.43 GHz. An 8 and a 16 element MESFET array combiner with 5.54 and 17.38 W of EIRP at 10 GHz was demonstrated by Balasubramaniyan and Mortazawi [53]. The array exhibit excellent radiation patterns in both principal planes which agree well with the theoretical prediction. An amplifying active antenna array using conventional microstrip patches with an integrated amplifier at its terminals has shown excellent radiation patterns and very good efficiency [54]. Some of the most promising active

investigations deal with electro-optical applications. Transistors are ideal candidates for millimeter-wave power generation through optical interactions. A 60 GHz CW generator through optical mixing in FET integrated antennas has been shown by Plant *et al.* [55]. Three terminal devices such as HEMTs [56] and HBTs [57] can also be used. Optically driven solid state devices can generate microwaves by mixing two continuous-wave laser or by using a mode-locked laser [57]. Using fiber-optic lines throughout a complex circuit and later converting it to microwaves at an antenna appears to be an attractive alternative to current approaches.

Many other oscillators [58], amplifiers [59, 60], receivers [61, 62, 63, 64], and transponders [65] have been presented in the literature. Recent papers have started on full 3D field simulations of active antenna structures, including solid-state devices [66, 67]. Such an undertaking will allow accurate analysis to understand and correct many radiation problems often encountered with active antennas.

One of the main objectives of this dissertation is to develop a new strategy for simulating and integrating a passive antenna structure with nonlinear active devices.

### 2.3 Spatial Power Combining

It was not until an article by Mink [68] that the quest for quasi-optical power combining began in earnest. Mink describes the use of an array of current within a quasi-optical cavity as shown in Fig. 2.1. This was the first theoretical investigation of power combining using a source array in a quasi-optical resonator. Mink studied an array of filamentary current sources radiating into a plano-concave open resonator. The grid oscillator [69] and grid amplifier [70], shown in Fig. 2.2, are other methods of power combining where active devices or monolithic microwave integrated circuits (MMIC) are placed in a metal grid supported on a dielectric slab.

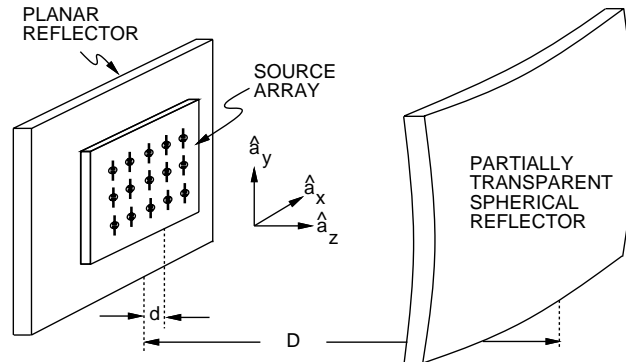


Figure 2.1: A quasi-optical power combiner configuration for an open resonator.

Polarizers are used to isolate the output from the input as shown in Fig. 2.3 along with a slab for tuning the system. The complex device-field interactions render it difficult to optimize efficiencies and ensure stable operation. However, computer aided analysis techniques are evolving to aid in design.

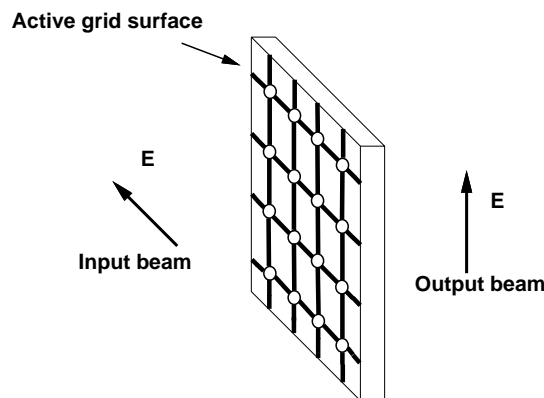


Figure 2.2: A grid amplifier/oscillator on a dielectric slab.

Several review papers have been written on the subject of quasi-optical systems. One of the first was by Goldsmith [71] which deals with quasi-optical techniques using Gaussian beams along with various quasi-optical components at millimeter and submillimeter wavelengths. Since then these quasi-optical techniques have been used with many power combining oscillator and amplifier arrays to combine power in

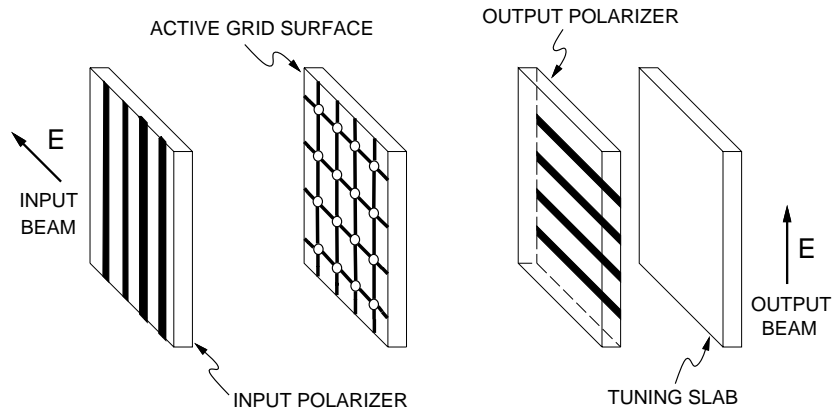


Figure 2.3: A grid amplifier/oscillator on a dielectric slab with X and Y polarizers.

free space. The *IEEE Transactions on Microwave Theory and Techniques* devoted an entire issue on quasi-optics in the 1993 October edition [72]. A recent review paper by York [73] provides some of the latest quasi-optical power combining techniques for oscillators and amplifiers. A proposal to set figures-of-merit for standard characterization of spatial and quasi-optical power combining arrays was presented in [74].

This section focuses on the experimental work that has been done for quasi-optical power combining including open cavity resonator oscillators, grid oscillators, and grid amplifiers.

### 2.3.1 Oscillators Arrays

The open cavity resonator shown in Fig. 2.1 has been used to produce several types of quasi-optical oscillators [75, 76, 77, 78, 79, 80, 81, 82]. In [75, 76, 77, 82] Gunn diode oscillators were demonstrated in an open cavity resonator. Other oscillator configurations include high electron mobility transistors (HEMT) [78, 79], impact avalanche transit time (IMPATT) diodes [80], and resonant tunneling diodes (RTD)

[81]. These experiments were done at X-band [75, 76, 77, 78, 80, 82], 40 GHz [79], U-band [77], W-band [77], and 75 GHz [81]. The work done on oscillators in an open cavity resonator has proven that locking is achievable through the resonator allowing for power combining. In [82] power combining was demonstrated with 24 oscillators with an efficiency of 90%. The most popular way of producing quasi-optical power combining oscillators has been using active arrays, see Figs. 2.2 and 2.3, to combine power in free space [69, 83, 84, 85, 86, 87, 88]. Popović *et al.* demonstrated a quasi-optical power combining oscillator at 9.7 GHz using a  $5 \times 5$  grid array with 25 metal semiconductor field effect transistors (MESFET) [69]. They reported an effective radiated power (ERP) of 37 W with a DC to RF conversion efficiency of 15%. Since then they have demonstrated a  $6 \times 6$  grid array with 36 MESFETs [83] and a  $10 \times 10$  grid array with 100 MESFETs [84] reporting an ERP of 3 W at 3 GHz and 21 W at 5 GHz with efficiencies of 22% and 20%, respectively. In [85] a MESFET grid oscillator with 16 transistors produced 335 mW of power at 11.6 GHz with an ERP of 15 W and an efficiency of 20%. Also reported in [85] was a 36 element MESFET grid oscillator which produced 235 mW of power at 17 GHz with an ERP of 3.3 W and an efficiency of 7%. The largest amount of power produced from a grid oscillator to date was reported in [87] with a 100 element MESFET grid producing a total radiated power of 10.3 W at 9.8 GHz with an ERP of 660 W and an efficiency of 23%. A grid oscillator using pseudomorphic high electron mobility transistors (pHEMT) was demonstrated in [88] with a 25 element grid producing 100 mW of power at 4.94 GHz and 4 cascaded 25 element grids producing 265 mW of power at 5.15 GHz with an ERP of 8 W. In [86] a voltage controlled oscillator (VCO) with a 10% tuning bandwidth with less than 2 dB power change was demonstrated for a MESFET grid containing a varactor diode tuning grid.

Other techniques for combining power in free space have used patch antennas

[25, 89, 90, 91] and slot antennas [92]. In [25] a  $4 \times 4$  array of microstrip patch antennas was reported. Using 16 Gunn diodes produced an equivalent isotropic radiated power (EIRP) of 22 W at 9.6 GHz with an efficiency of 1%. Also reported was a 16 element MESFET array with patch antennas producing an EIRP of 10 W at 8.2 GHz with an efficiency of 26 %. A 16 element quasi-optical FET oscillator power combining array using external injection locking with an ERP of 28.2 W at 6 GHz was demonstrated in [89]. In [90] a periodic second harmonic spatial power combining oscillator was demonstrated with a 4 element Gunn diode with microstrip patch antennas reporting an ERP of 25.7 dBm at 9.36 GHz with an efficiency of 10.2%. A MESFET array with a total radiated power of 7.92 W and an efficiency of 15% was reported in [91]. Slot antennas with 9 MESFETs were used in [92] producing an EIRP of 2.4 W at 10.11 GHz.

### 2.3.2 Amplifier Arrays

Several demonstrations of quasi-optical amplifier arrays have been reported over the past years. Power combining using grid arrays has been very popular. The first demonstration of a grid amplifier was reported by Kim *et al.* [70]. The grid consisted of 50 MESFETs and produced a gain of 11 dB at 3.3 GHz. Each unit cell of the grid had a MESFET pair resulting in a  $5 \times 5$  grid. In [93] a unit cell of a grid amplifier was reported with a gain of 10.5 dB at 5.92 GHz. Kim *et al.* [94] demonstrated a 100 heterojunction bipolar transistor (HBT) grid amplifier. The amplifier consisted of a  $10 \times 10$  grid with a chip in each unit cell made up of HBT differential-pairs. A peak gain of 10 dB at 10 GHz with a 3 dB bandwidth of 1 GHz was reported. Maximum output power was 450 mW and the minimum noise figure was 7 dB. Also demonstrated by Kim *et al.* [95] was a 6.5 GHz to 11.5 GHz

source using a grid amplifier with a twist reflector. The peak ERP was 6.3 W at 9.9 GHz. More recent quasi-optical grid amplifiers include a 36 element monolithic grid amplifier using HBTs [96]. This grid amplifier had a gain of 5 dB at 40 GHz with a 3 dB bandwidth of 1.8 GHz. The maximum saturated output power was 670 mW at 40 GHz with a peak power added efficiency (PAE) of 4%. This was the first reported power measurement for a monolithic quasi-optical amplifier. In [97] a 36 element monolithic grid amplifier using pHEMTs was demonstrated over a frequency range of 44 GHz to 60 GHz. A peak gain of 6.5 dB at 44 GHz and 2.5 dB at 60 GHz was reported.

Other types of quasi-optical power combining amplifiers include microstrip antenna arrays. In [98] a 9 MESFET array using microstrip patch antennas was demonstrated with an ERP of 6.06 W at 7.33 GHz. Quasi-optical microstrip amplifiers based on multilayer coupled structures were used in [99]. Here the amplifiers were placed back to back sharing a common ground plane in order to provide isolation for the input and output. A single stage had a gain of 7.54 dB at 10.04 GHz and a two-stage had a gain of 18.0 dB at 9.95 GHz. A two-level power combining pHEMT patch antenna lens amplifier with 8 dB of absolute power gain at 9.7 GHz was reported in [100]. The quasi-optical antenna array amplifier was used for beamforming and beam-switching. Also presented in [100] was a saturated class A polarization preserving 24 MESFET patch array producing 0.7 W at 10 GHz with a PAE of 21%.

The first demonstration of a quasi-optical millimeter-wave amplifier was reported in [101]. The unit cell consisted of a MMIC driver amplifier followed by a two-stage high powered amplifier chip. This circuit was used in a  $6 \times 6$  array producing a 6 dB gain at 29 GHz.

Slot antennas are also used for quasi-optical amplifiers. In [100] an X-band two-stage low noise coplanar waveguide (CPW) pHEMT amplifier cell using anti-

resonant slot antennas was demonstrated. An active gain of 21.7 dB with a 3.2 dB noise figure and a 6% 3 dB bandwidth was reported. Other slot antenna configurations included a quasi-optical amplifier array using a direct integration of MMICs with  $50 \Omega$  multi-slot antennas [102]. A  $4 \times 4$  array with a 10 dB gain at 11 GHz with a 4% bandwidth was reported. A CPW multiple slot antenna for active arrays and integrated antennas was demonstrated in [103] with a reported gain of 8 dB using an HBT gain block MMIC chip.

In [104] a combination of slot antennas and patch antennas were used. A monolithic plane wave pHEMT amplifier array was made up of a  $5 \times 7$  input slot antenna array and a  $4 \times 8$  output patch antenna array with a  $7 \times 8$  pHEMT amplifier array placed in between. The amplifier array was placed in an oversized waveguide with a reported gain of 3 dB at 43 GHz. A quasi-optical traveling wave amplifier (TWA) using Vivaldi-type slots and a hybrid microstrip MESFET TWA circuit was demonstrated in [105]. The amplifier had a 50% fractional bandwidth at 3.5 GHz.

## 2.4 Modeling of Spatial Power Combining Systems

Spatial power combining has been experimentally demonstrated but the power levels obtained so far are much smaller than what is needed for envisioned applications. It is not competitive with conventional power combiners. In order to obtain higher power we need to have computer aided engineering (CAE) tools available for spatial systems so optimization of the system can be done. Being able to optimize the system using CAE tools will greatly speed up the development of high powered spatial power combining systems by eliminating all unnecessary experimental work. This section will review the work that has been done on numerical modeling of spatial systems. Many of the approaches used today to model arrays are based on the

methods developed to model frequency selective surfaces (FSS) several years ago. In [106] periodic arrays of cross dipoles and Jerusalem crosses were analyzed. These structures were analyzed using the Galerkin's method in the spectral domain. A set of special entire-domain basis functions were developed to correctly account for the discontinuous nature of the induced current at the cross junctions. Computed results were presented for the reflection coefficient of the FSS structures for arbitrary incident fields. Infinite periodic arrays consisting of arbitrarily shaped patches were presented in [107]. Here the arrays were modeled using a fast Fourier transform (FFT) based iterative approach to compute the scattered fields of the infinite array. Sub-domain rooftop basis functions were employed. Techniques for realizing accurate and efficient FSS are discussed in [108].

An impedance model for a quasi-optical diode array was presented in [109]. This method models an infinite array of strips or slots loaded with two terminal semiconductor devices such as diodes. The problem was solved using a unit cell approach where the unit cell was modeled as a waveguide discontinuity problem and solved with the MoM. Computed results were presented for the inductance and capacitance of the diode array at 99 GHz.

In [110] a measurement technique was presented for determining the driving point impedance of active grid arrays. This technique assumes that all of the active elements in the array are locked and in phase. With this assumption the grid array problem was reduced using symmetry so that only the unit cell was considered. The driving point impedance measurement was done using the dielectric waveguide measurement (DWM) method where the unit cell was placed between two parallel metal plates emulating electric walls. The driving point impedance measurements were presented for a dipole array, a bow-tie array, a double-Vee array, and a slot array. Simple equivalent circuit models using only transmission lines were developed

for each array. Results show that the dipole array had the highest driving point impedance with the slot array having the smallest.

Modeling of quasi-optical arrays with thin rectangular patch and aperture elements were presented in [111]. The method of moments was employed with appropriate edge conditions incorporated into the basis functions to compute the scattering from periodic arrays with and without substrates and superstrates. For the aperture elements Floquet modes with the appropriate boundary conditions were used to express the fields. The patch elements followed in a similar manner setting up the integral equation for the unknown surface current density on the patch. Transmission and reflection characteristics of the arrays were presented for arbitrary incident fields.

Popović's group from the University of Colorado at Boulder has been doing numerical work on quasi-optical grids [112, 113, 114, 115, 116, 117]. A full-wave analysis using the MoM was developed by Bundy *et al.* [112, 115]. This method assumed that the grid array was an infinite periodic structure with all of the active devices locked and in phase. With this assumption the problem was modeled by only considering the unit cell with special boundary conditions along the unit cell edges as shown in Fig. 2.4. The moment method was formulated by relating the electric field to the surface current density on the metallic conductors on the grid and was represented by Fourier series. In [112, 115] the driving point impedance of several unit cell configurations including dipoles, cross dipoles, and bow-ties were given. The driving point impedance could be computed for unit cells having a dielectric with or without metal on both sides. The computed driving point impedances were validated by comparison to the EMF method [118]. In addition to the driving point impedance computations, the moment method simulator also computed the transmission coefficient of a passive periodic grid structure due to a normal incident

plane wave. In these computations the grid was analyzed in free space with a single metallic surface and the dielectric was added back with transmission line theory. In [113, 114, 115] results were presented for the transmission coefficient of cross dipoles and Jerusalem crosses and were validated with measurements. Further analysis of cascaded quasi-optical grids was presented in [116, 117]. Here each quasi-optical component was characterized by a multiport network allowing for cascading of all the components in the system. The components in the system included a grid oscillator, a planar reflector (mirror), and a FSS where the grid and FSS could be loaded with active and/or passive lumped devices.

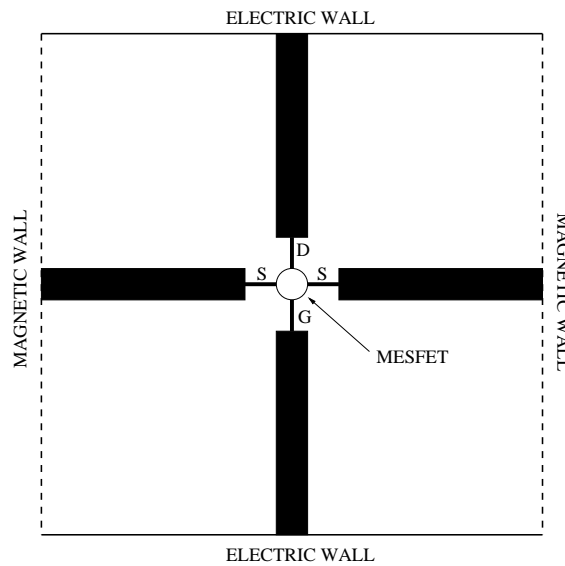


Figure 2.4: Unit cell configuration for a grid oscillator.

Here at North Carolina State University, Steer's group has been doing research on quasi-optical modeling [119, 120, 121, 122, 123, 124, 125, 126, 127, 128, 129]. In [119, 120, 121, 122, 123] Heron *et al.* developed an electric field dyadic Green's function for the open cavity resonator shown in Fig. 2.1. This Green's function was comprised of resonant and nonresonant terms corresponding to coupling from modal and nonmodal fields in the open cavity resonator. The Green's function was then

derived by considering the paraxial and nonparaxial components where the paraxial components described the quasi-optical modes. Losses due to diffraction from the finite spherical reflector and conductor losses of the reflectors were also considered. Results for 1 port and 2 port antennas were compared with measurements taken in an X-band open cavity resonator. The work presented in this dissertation is based on the open cavity Green's function where a full-wave moment method simulator was developed incorporating the open cavity Green's function [127, 128]. This Green's function analysis was further extended to the development of a dyadic Green's function for a quasi-optical grid system with lenses [129] and is also presented in [130]. Work is continuing on incorporating the full-wave analysis from this dissertation with transient analysis [124] and steady state (harmonic balance) analysis [125] in order to describe a complete quasi-optical system with active devices.

The finite-difference time-domain (FDTD) method was applied to quasi-optical arrays in [131]. The grid structure analyzed was assumed to be infinite and periodic so only the unit cell was modeled. The unit cell microstrip geometry consisted of two square metallic loops on the front side with a square aperture on the back side. Input and output polarizers were also included in the system. The unit cell was excited with a linearly polarized plane wave with a normal incidence on the unit cell surface. In the FDTD analysis Floquet boundary conditions were used along the unit cell transverse edges and Berenger's perfectly matched layer (PML) absorbing boundary conditions were used to terminate the fields along the longitudinal beam axis. The FDTD analysis was compared with measurements for transmitted and reflected powers through the system.

A generalized scattering matrix approach for analyzing quasi-optical grids consisting of grid amplifiers and grid oscillators was presented in [132]. The grid array was made up of cross dipoles with differential pair HEMTs embedded in the gaps.

Again the structure was assumed to be infinite and periodic so only the unit cell was considered. The gates of the HEMTs were connected to the horizontal dipole leads providing the input and the drains were connected to the vertical dipole terminals providing the output. The MoM was applied with spectral domain Green's functions including substrate and superstrate layers supporting the metallic layer. Instead of using electric and magnetic walls around the edges of the unit cell, Floquet harmonics were used to model the unit cell dimensions and the propagation constant of the incident field. Galerkin's method with sub-domain rooftop basis functions were used to find the currents allowing for the computation of the scattered fields in terms of Floquet harmonics reflected and transmitted by the grid. The scattering matrix representation of the periodic grid array was then combined with power wave representations at the device ports allowing for the scattering matrix of the grid array to be combined with the active device scattering matrix. Results for 1 port and 2 port devices were presented.

Analysis of an oscillator array embedded in a rectangular waveguide was presented in [133]. A 7 element oscillator was developed using planar dipole antennas with a pHEMT in the gap of each dipole. The MoM was used to determine the electric and magnetic fields of the passive waveguide system loaded with a dipole array. A time domain analysis was then used to predict the oscillation frequency, locked amplitudes, and output power from the circuit. The output power of the oscillator array was 220 mW at 12.4 GHz.

### 2.4.1 Method of Moments

The method of moments (MoM), first introduced by Harrington [134], is a numerical technique used to solve integral equations. In electromagnetics, many problems

are formulated as integral equations in which analytical solutions do not exist and therefore must be solved numerically. The MoM offers an accurate numerical solution for such problems where the integral equation is transformed into a set of linear equations which is then solved for with a computer.

Some of the first widely used applications of the MoM were in wire antenna simulation where the MoM was used to solve either Pocklington's integral equation or Hallen's integral equation. The MoM was used to solve for the current distribution on the wire antennas which then could be used to predict the input impedance of the antenna or the far-field radiation. In both cases the free space Green's function was used. Often the Galerkin's method was used with sub-domain sinusoidal expansion and weighting functions. In References [135, 136, 137], a complete formulation for wire antennas using the MoM is given. Other articles, such as [138, 139], give numerical aspects of the stability and convergence of the moment method solutions. The type of structures analyzed included Yagi-Uda array antennas [135], single and multiple log-periodic dipole antennas [136], and wire grid modeling of airplanes [135].

While the MoM was being used to model one-dimensional wire grid geometries, research was also conducted in modeling two-dimensional surfaces using MoM. References [140, 141, 142, 143, 144] present MoM techniques for modeling arbitrary surfaces in free space. The MoM programs were used to find the surface currents on the two-dimensional structure excited by an incident plane wave. Radar cross section (RCS) analysis of thin rectangular plates in free space are presented in [140]. Other popular studies of radiation and scattering from arbitrary surfaces are presented in [141, 142, 143, 144].

The biggest applications to date of moment method solutions have been in the modeling of microstrip geometries including multilayered dielectrics for open and closed structures. There are two main approaches for modeling microstrip

structures using the MoM, the first is the spectral domain approach [145, 5, 146, 147, 148, 149, 150, 151, 152, 153] and the second is the spatial domain approach [154, 161, 155, 156, 157, 158, 159, 160]. Applications of microstrip modeling include dispersion characteristics of printed transmission lines [145, 5, 149], input impedance and mutual coupling of microstrip antennas [146, 154, 155, 156, 157], phased array antennas [148, 151, 152], and microstrip discontinuities [147, 161, 150, 153].

There are several advantages and disadvantages for each moment method. For example in the spectral domain the microstrip dyadic Green's functions must be derived in closed form. A technique known as the immittance approach was developed by Itoh [5] where the Green's function is easily derived for multilayer geometries using a transverse equivalent transmission line for a spectral wave along with a coordinate transformation. This method is illustrated in Sections 3.7 and 5.6 of where several Green functions are derived using the immittance approach. In the spatial domain the microstrip Green's function is derived in terms of vector and scalar potentials expressed in terms of Sommerfeld integrals. Evaluation of the Sommerfeld integrals requires numerical analysis with special treatment for handling the complex poles due to surface waves in the dielectric and the oscillatory nature of the Sommerfeld integrals described by Bessel functions. Mosig has done several comprehensive studies on the numerical evaluation of Sommerfeld integrals [154, 162, 163]. In [164] Chow *et al.* developed a closed form approximation for the spatial domain scalar and vector potential microstrip Green's functions. Further development of the closed form Green's functions for multilayered microstrip geometries is given in [165, 166].

The main advantages of the spatial domain MoM approach is that it can model arbitrarily shaped structures by gridding the structure into unequal size cells and is also conceptually easier than the spectral domain MoM approach. The spectral

domain requires transformation from the spatial domain to the spectral domain through the use of Fourier transforms. The Fourier transforms are not a problem when the gridding is done with equal size cells but does pose a problem for unequal size cells. A disadvantage of a spatial domain implementation is that the self-terms contain a singularity which does not exist in the spectral domain. This singularity is handled in the spatial domain by doing singularity extraction. It is very important to evaluate the self-terms correctly because they dominate the moment matrix. The biggest disadvantage for a spectral domain analysis is that numerical integration is required over an infinite range due to taking the Fourier transforms. It then becomes very difficult to numerically evaluate elements separated by electrically large distances because of heavy oscillations. Techniques for efficient evaluation of spectral domain moment method elements are presented in [167, 168, 169]. In the spatial domain this is not a problem because everything is integrated over physical finite regions.

The main problems of both MoM approaches is the amount of CPU time and memory required for simulating electrically large structures. These problems occur when filling and inverting the moment matrix. Work on improving the matrix fill times has been done in [170] using frequency interpolation and in [171] using spatial interpolation of the moment matrix. The combination of these interpolation techniques result in very efficient matrix fills. Since the moment matrix is usually dense and often ill conditioned, the inversion of the moment matrix remains a problem for matrices of large order. An approach that is being researched today is the use of wavelets in the MoM [172, 173, 174, 175]. In this approach scaling functions and wavelets are used in place of the traditional orthogonal basis functions. When wavelets are used the moment matrix becomes sparse which allows for a fast solution of the inverted moment matrix.

In this dissertation both the spatial and spectral domain MoM approaches are used concurrently taking full advantage of the strengths of each method in order to accurately and efficiently solve quasi-optical systems.

### 2.4.2 Network Parameter Extraction Using MoM

The MoM is an efficient way of electromagnetically modeling structures as pre-analysis, embedded in the Green's function, is used to reduce the numerical computation that would otherwise be required in more general techniques such as the Finite Element Method (FEM) or the Finite Difference Method (FDM). This is especially true for antennas and open structures [176]. As sub-domain current basis functions and differential (or delta-gap) voltages are used in MoM formulation, the compatibility with general purpose microwave circuit simulators which use terminal current and voltage quantities, is near optimum. Several measurement-like electromagnetic (EM) techniques have been presented and shown to be well suited to extracting the scattering or circuit parameters of planar circuits [177]. These are classically deduced from the calculation of the surface current flowing on the structure [178]. This is analogous to slotted-line measurement of a standing-wave pattern and subsequent extraction of a one port reflection coefficient. Another approach implements a de-embedding procedure to compensate for the effect of opens or shorts[179], a procedure very similar to that used in actual measurements. This de-embedding becomes increasingly complex when parameters at more than two ports are to be extracted as multiple "measurements" are required [180, 181]. Accuracy is improved by implementing matched terminations in the EM analysis using an integral equation technique [182] and [183], but more computations of the MoM matrix elements involved. In MoM, basis functions of current are used and each,

typically a rooftop or half rooftop function, straddles two geometric cells so that the coefficient of a basis function is the “differential-port” current flowing from one cell into its neighbor. The MoM formulation also uses the voltages between cells as variables and these are just differential-port voltages if the cells are not electrically connected (i.e. shorted in which case the voltage is zero). In structures with single layer metalization, the network parameters so extracted are referenced to the differential ports where active devices are placed and so can be used directly in circuit simulation [184, 185]. The admittance parameter relationship between the currents and the voltage at the differential ports can be extracted from the inverted and reduced form of the MoM matrix [186, 187, 188].

The situation is more complicated when a ground plane is involved as inevitably a port is defined with respect to the ground plane. This is because the required ports here are not differential ports but are referred to the ground plane (i.e. the voltage is referred to the ground plane). Eleftheriades and Mosig [189] used a half basis function to define a port at the intersection of the walls of a shielded enclosure. This is an elegant procedure but not applicable in the absence of an enclosure (in open structures) or ports not at the walls of the enclosure but inside it. Building on the half basis function idea, Zhu *et al.* computed external port parameters for unbounded structures [190]. In [190], the authors use a segmentation approach to partition the feed lines from the rest of the circuit. In effect these feed lines are terminated in a virtual electrical wall and half basis functions are used. Then an images of the lines is used to compute the inner port parameters. However this approach alters the physical behavior of a circuit in general. Introducing a vertical current element (basis function) in the position of a circuit port is, conceivably, one way of defining the inner circuit port in the MoM formulation. In this dissertation, Chapter 6, port parameters extraction procedure directly from mom matrix is

presented.

## 2.5 Summary

Microwave and millimeter-wave technologies have advanced to the point where design of electrically large systems, a wavelength or even several wavelengths in the three dimensions, are being developed. Optimum design requires modeling and understanding of the inherent characteristics of these systems. Costly and tedious experiments to study these systems can be replaced by computer aided tools.

Electromagnetic modeling of these large systems along with linear and nonlinear circuit components is emerging as one of the great challenges in microwave and millimeter-wave computer aided engineering. Tight coupling between circuit and electromagnetic (EM) fields, integrated active array, circuit field interaction, global modeling, and compatibility of the circuit and EM simulators need to be investigated.

In conclusion, accurate and efficient modeling of circuit-field interaction for electrically large system is a hot point for circuit and EM research areas. More research and developing efforts are still needed to have a mature CAE for these complicated systems in the future.



## Chapter 3

# MPIE and Green's Functions for CPW-Slot Structure

### 3.1 Introduction

Models used to study planar structures range from greatly simplified ones, such as the transmission line model, planar circuit analysis, segmentation techniques, and up to quite sophisticated approaches based on an integral equation formulation. In the framework of the integral equation model, many different approaches exist, depending on the use of the spectral or space quantities and on the geometries to be included.

The most general and rigorous treatment of planar structures is given by the well-known electric-magnetic field integral equation technique, usually formulated in the spectral domain. A modified electric fields integral equation (EFIE) called mixed potential integral equation (MPIE) is used and solved in the space domain. MPIE is numerically stable and can be solved with efficient algorithms. Working in the space domain provides a good physical insight into the problem. MPIE formulation includes coupling, dispersion, radiation, and surface waves and therefore provides a powerful and flexible technique for the study of microstrip structures.

The MPIE was introduced by Harrington [134] and has been used for the analysis of wire antennas. Mosig [154, 155, 156, 157, 162] has applied MPIE to microstrip structures and showed that the MPIE model can be used at any frequency, from the DC case up to the determination of higher order modes in a resonant patch.

The MPIE model is able to handle structures of arbitrary shapes where no prior guess of the surface current distribution is possible. There is no limitation either on the operating frequency or on the substrate thickness. The model automatically takes into account mutual coupling between elements and can predict the performance of slots embedded in an array environment. Surface waves are included as well as dielectric and ohmic losses. The model thus allows accurate prediction of the input impedance, coupling factors, radiation patterns, gain and efficiency at any frequency. The model relies upon the identification of a slot antenna as a particular case of stratified media. The slot antenna is modeled by an integral equation where the main unknown is the electric field (or the equivalent magnetic current) on the slots. The Green's functions forming the kernel of this equation include the effect of the substrate, and are obtained in the form of inverse Hankel transforms. The integral equation is directly formulated in the space domain using both electric vector and scalar potentials. The resulting mixed potential integral equation (MPIE) similar to that obtained for wire antennas, is better suited for numerical analysis than the customary magnetic field integral equation (MFIE). This chapter is devoted to developing an efficient numerical model to investigate the performance of the slot array structure. The construction of the MPIE and its corresponding space domain Green's functions is demonstrated. Considerable attention is paid to the development of numerically efficient evaluation of the Green's functions.

## 3.2 Integral Equation Formulation

### 3.2.1 Model Geometry

The magnetic surface current model will be developed for an aperture on a ground plane over a dielectric layer of thickness  $h$  and relative permittivity  $\epsilon_r$  as shown in

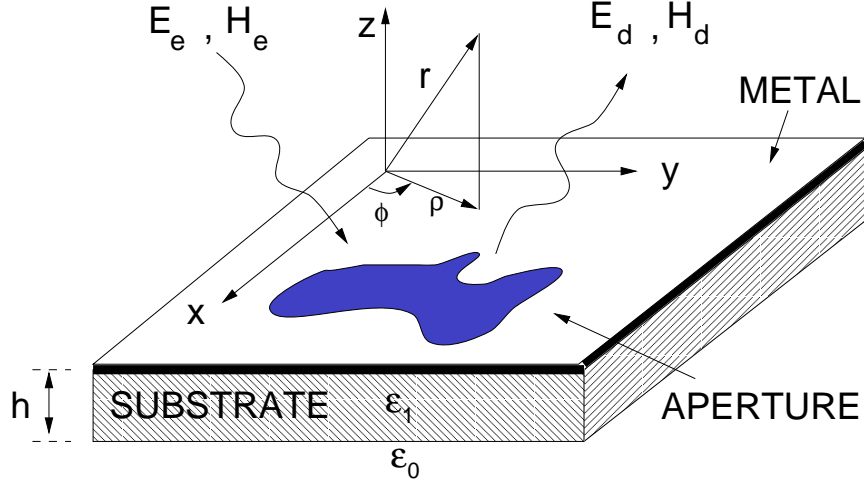


Figure 3.1: A general aperture structure on metallic conductor on the substrate.

Fig. 3.1. The substrate is assumed to extend to infinity in the transverse directions and is made of a nonmagnetic, isotropic, homogeneous material which could be lossy. The ground plane has also infinite dimension. The direction perpendicular to the ground plane is selected to be  $z$ -axis. The ground plane is located at  $z = 0$ . The interface between the air and the dielectric layer is located at  $z = -h$ . The electric field across the aperture has both  $x$  and  $y$  components. By using the equivalent principle [191] the aperture can be closed and replaced by an equivalent magnetic surface current density  $\mathbf{M}_s$  above the ground plane and  $-\mathbf{M}_s$  below the ground plane Fig. 3.2. The equation

$$\mathbf{M}_s = \hat{z} \times \mathbf{E}_s \quad (3.1)$$

relates the magnetic current  $\mathbf{M}_s$  to the unknown slot electric field  $\mathbf{E}_s$ . Therefore we can decompose the original problem into two isolated problem “a” and “b” Fig. 3.2:

1. Problem “a” is valid in the region  $z > 0$  with fields generated by the magnetic current  $\mathbf{M}_s$  in in half space.

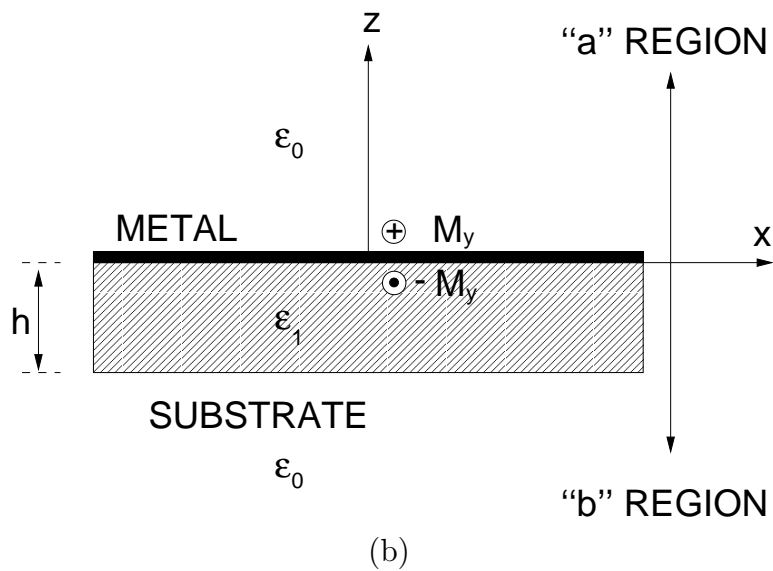
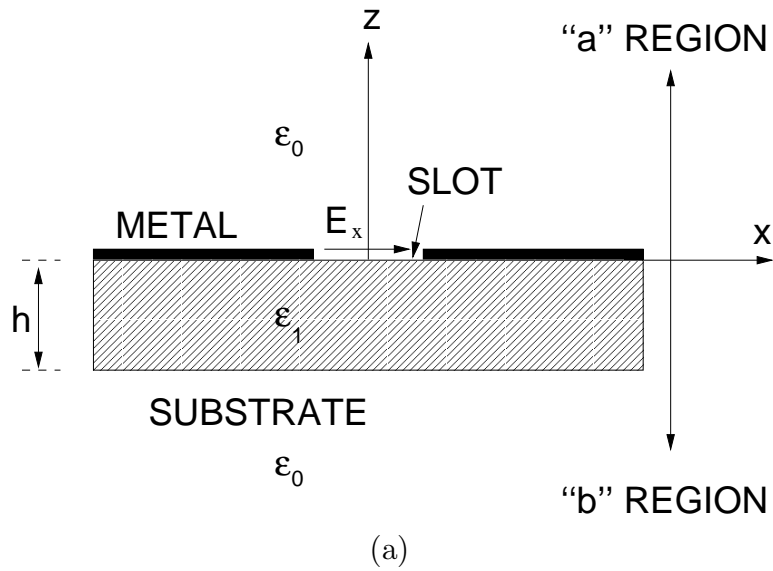


Figure 3.2: Transverse cross section of an aperture: (a) original problem; (b) equivalent problem.

2. Problem “b” is valid in region  $z < 0$  with fields generated by the magnetic current  $-\mathbf{M}_s$  in inhomogeneous medium.

The excitation electric and magnetic fields are denoted by  $\mathbf{E}_e$  and  $\mathbf{H}_e$ . They can be either fields of a plane wave coming from infinity (receiving antenna) or local fields created by finite source located within the slot (transmitting antenna). In either case, the excitation field induced a magnetic surface current on the aperture. The induced magnetic current in turn creates diffracted electromagnetic fields. These fields, denoted by  $\mathbf{E}_d$  and  $\mathbf{H}_d$ , are added to the excitation fields to yield the total fields  $\mathbf{E}$  and  $\mathbf{H}$  exist in the entire space.

### 3.2.2 Integral Equation

The integral equation can be obtained by enforcing the boundary conditions on the aperture. Here it should be noted that the continuity of the tangential electric field across the aperture has already been satisfied by using  $\mathbf{M}_s$  and  $-\mathbf{M}_s$  on different sides of the aperture. The other boundary condition, that the total tangential magnetic field is continuous across the aperture

$$\hat{z} \times \mathbf{H}^{(a)}|_{aperture} = \hat{z} \times \mathbf{H}^{(b)}|_{aperture} \quad (3.2)$$

where

$$\mathbf{H}^{(a)} = \mathbf{H}_d^{(a)} + \mathbf{H}_e^{(a)} \quad (3.3)$$

$$\mathbf{H}^{(b)} = \mathbf{H}_d^{(b)} + \mathbf{H}_e^{(b)} \quad (3.4)$$

### 3.2.3 Potentials of Diffracted Fields

Since no volume sources are considered in this model, the diffracted fields satisfy the homogeneous Maxwell's equations :

$$\nabla \times \mathbf{E}_d^{(a,b)} = -j\omega\mu_0 \mathbf{H}_d^{(a,b)} \quad (3.5)$$

$$\nabla \times \mathbf{H}_d^{(a,b)} = j\omega\epsilon_i \mathbf{E}_d^{(a,b)} \quad (3.6)$$

$$\nabla \cdot \mathbf{E}_d^{(a,b)} = 0 \quad (3.7)$$

$$\nabla \cdot \mathbf{H}_d^{(a,b)} = 0 \quad (3.8)$$

The solution of antenna problems can in many cases be simplified by introducing a scalar and electric vector potentials for the diffracted fields [192]

$$\mathbf{E}_d^{(a,b)} = -\frac{1}{\epsilon_i} \nabla \times \mathbf{F}^{(a,b)} \quad (3.9)$$

$$\mathbf{H}_d^{(a,b)} = -j\omega \mathbf{F}^{(a,b)} - \nabla \psi^{(a,b)} \quad (3.10)$$

subject to Lorentz's gauge:

$$\nabla \cdot \mathbf{F}^{(a,b)} = -j\omega\mu_0\epsilon_i \psi^{(a,b)} \quad (3.11)$$

Introducing the above expressions into Maxwell's equations, the two homogeneous Helmholtz's equations for the potentials are obtained

$$(\nabla^2 + k_i^2) \mathbf{F}^{(a,b)} = 0 \quad (3.12)$$

$$(\nabla^2 + k_i^2) \psi^{(a,b)} = 0 \quad (3.13)$$

where  $k_i$  is the wavenumber in medium  $i$  and in the substrate

$$k_i = \omega \sqrt{\mu_0 \epsilon_i} \quad (3.14)$$

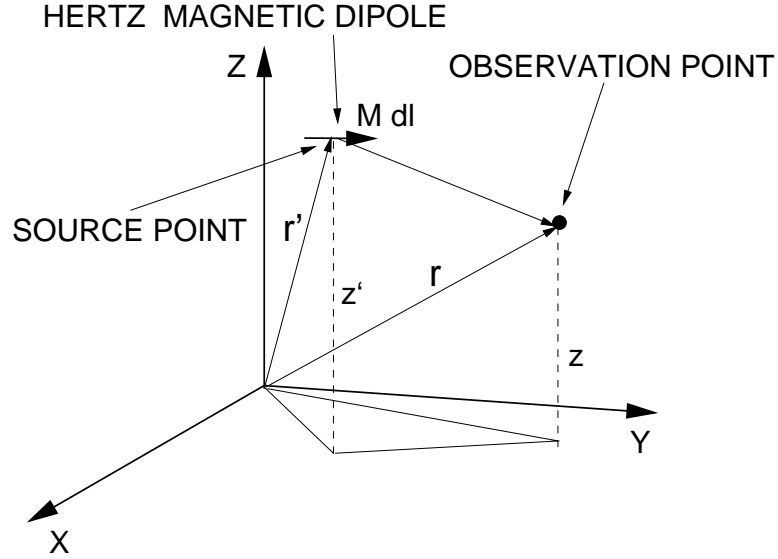


Figure 3.3: An arbitrary oriented magnetic dipole of momentum  $Md\mathbf{l}$ .

### 3.2.4 Dyadic Green's Functions

Let's consider an arbitrary oriented Hertz magnetic dipole of momentum  $Md\mathbf{l}$  located at the point  $\mathbf{r}'$  as Fig. 3.3. In general, the electrical vector potential at the point  $\mathbf{r}$  due to this dipole is given by the linear relation

$$\mathbf{F}(\mathbf{r}) = \overline{\overline{\mathbf{G}}}_F(\mathbf{r}, \mathbf{r}') \cdot Md\mathbf{l} \quad (3.15)$$

where  $\overline{\overline{\mathbf{G}}}_F$  is a three-dimensional dyadic Green's function given by

$$\overline{\overline{\mathbf{G}}}_F = \begin{bmatrix} G_{F_{xx}} & G_{F_{xy}} & G_{F_{xz}} \\ G_{F_{yx}} & G_{F_{yy}} & G_{F_{yz}} \\ G_{F_{zx}} & G_{F_{zy}} & G_{F_{zz}} \end{bmatrix} \quad (3.16)$$

where, for example,  $G_{F_{zz}}$  is the electric vector potential in the  $x$  direction created from  $z$  directed infinitesimal magnetic current source. If the source and the observation points are surrounded by an infinite homogeneous medium, the dyadic  $\overline{\overline{\mathbf{G}}}_F$  is diagonal and can be expressed as the product of scalar Green's function  $G_F(\mathbf{r}, \mathbf{r}')$

times the unit dyad  $\bar{\mathbf{I}}$ . In this case, the electric vector potential is always collinear with the source dipole. For a slot over substrate structure it is possible to use the scalar free space Green's function of the electric vector potential. However in this case it is necessary to use fictitious electric and magnetic surface currents on the aperture and air-dielectric interface in order to satisfy the boundary conditions. These currents are also unknowns in the integral equation formulation of the problem and add to the complexity of the numerical solution. The preferred solutions to include the effects of the dielectric substrate and the ground plane in the Green's functions. Therefore, the Green's functions must satisfy the following boundary conditions:

1—In the above region (“a” region):

- on the metallic surface

$$\hat{z} \times \mathbf{E}^{(a)}(\mathbf{r}_0) = \begin{cases} \mathbf{M}_s(\mathbf{r}_0), & \text{on the aperture} \\ 0, & \text{otherwise} \end{cases} \quad (3.17)$$

2—In the below region (“b” region):

- on the metallic surface

$$\hat{z} \times \mathbf{E}^{(b)}(\mathbf{r}_0) = \begin{cases} -\mathbf{M}_s(\mathbf{r}_0), & \text{on the aperture} \\ 0, & \text{otherwise} \end{cases} \quad (3.18)$$

- on the dielectric interface

$$\hat{z} \times (\mathbf{E}^{(a)}(\mathbf{r}_1) - \mathbf{E}^{(a)}(\mathbf{r}_2)) = 0 \quad (3.19)$$

$$\hat{z} \times (\mathbf{H}^{(a)}(\mathbf{r}_1) - \mathbf{H}^{(a)}(\mathbf{r}_2)) = 0 \quad (3.20)$$

where  $\mathbf{r}_0$ ,  $\mathbf{r}_1$ , and  $\mathbf{r}_2$  are defined as shown in Figs. 3.4 and 3.5.

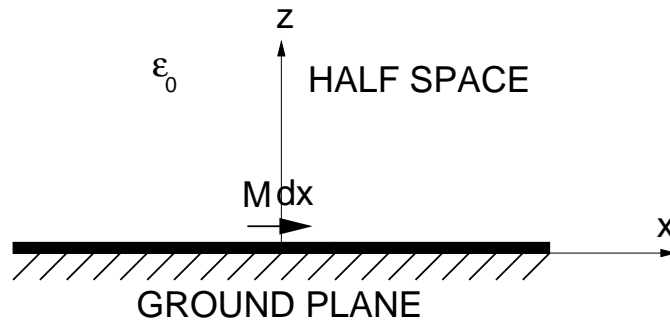


Figure 3.4: Region "a".

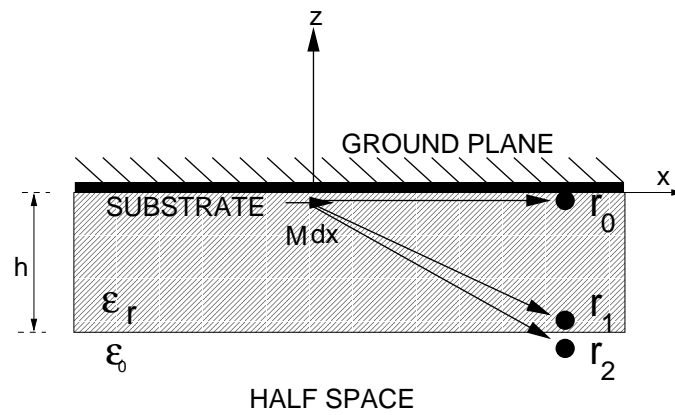


Figure 3.5: Region "b".

Because of the linearity of Maxwell's equations, the electric vector potential  $\mathbf{F}$  of a given magnetic current distribution can be written as a superposition integral involving the corresponding dyadic Green's function

$$\mathbf{F}(\mathbf{r}) = \int_{S'} \overline{\overline{\mathbf{G}}}_F(\mathbf{r}, \mathbf{r}') \cdot \mathbf{M}_s(\mathbf{r}') dS' \quad (3.21)$$

The magnetic charge scalar potential  $\psi$  is obtained by introducing the above expression in the Lorentz gauge with the

$$j\omega\mu_0\epsilon_i\psi(\mathbf{r}) = - \int_{S'} \nabla \cdot \overline{\overline{\mathbf{G}}}_F(\mathbf{r}, \mathbf{r}') \cdot \mathbf{M}_s(\mathbf{r}') dS' \quad (3.22)$$

The Green's function  $G_\psi$  associated with the scalar potential must be carefully defined. In fact, the uniqueness of  $G_\psi$  is guaranteed only if the divergence of  $\overline{\overline{\mathbf{G}}}_F$  is an irrotational vector [193]. Thus,

$$\nabla \cdot \overline{\overline{\mathbf{G}}}_F(\mathbf{r}, \mathbf{r}') = \mu_0\epsilon_i \nabla G_\psi(\mathbf{r}, \mathbf{r}') = -\mu_0\epsilon_i \nabla' G_\psi(\mathbf{r}, \mathbf{r}') \quad (3.23)$$

(3.22) can be written as

$$\psi(\mathbf{r}) = - \int_{S'} G_\psi(\mathbf{r}, \mathbf{r}') \frac{\nabla' \cdot \mathbf{M}_s(\mathbf{r}')}{j\omega} dS' + \int_{\partial l'} G_\psi(\mathbf{r}, \mathbf{r}') \mathbf{M}_s(\mathbf{r}') \cdot \hat{n} dl' \quad (3.24)$$

where  $\partial l'$  is the perimeter of the aperture and  $\hat{n}$  is the outward pointing normal unit vector. The edge condition guarantees that the normal component of the magnetic surface current vanishes on the perimeter of the aperture. Hence, the line integral in (3.24) can be eliminated. The associated magnetic surface charge density  $\rho_m$  is introduced via the continuity equation

$$\nabla \cdot \mathbf{M}_s + j\omega\rho_m = 0 \quad (3.25)$$

Finally, the magnetic charge scalar potential can be expressed as

$$\psi(\mathbf{r}) = \int_{S'} G_\psi(\mathbf{r}, \mathbf{r}') \rho_m(\mathbf{r}') dS' \quad (3.26)$$

The Green's function  $G_\psi$  can be viewed as a scalar potential created by a magnetic point charge, even if isolated time-varying magnetic point charge does not exist in the real world. Thus, owing to the lack of sound physical interpretation, it is better to consider  $G_\psi$  only as useful mathematical tool.

### 3.3 Mixed Potential Integral Equation

The diffracted field derived from the electrical vector and scalar potentials satisfy both Maxwell's equations and the boundary conditions (3.2). The next step is to relate these fields to the excitation fields (3.3) and (3.4), then

$$\hat{z} \times (\mathbf{H}_d^{(a)}(\mathbf{r}_0) - \mathbf{H}_d^{(b)}(\mathbf{r}_0)) = \hat{z} \times (\mathbf{H}_e^{(a)}(\mathbf{r}_0) - \mathbf{H}_e^{(b)}(\mathbf{r}_0))$$

$$\mathbf{r}_0 \in \text{on the aperture} \quad (3.27)$$

$$\hat{z} \times [-j\omega(\mathbf{F}_d^{(a)}(\mathbf{r}_0) - \mathbf{F}_d^{(b)}(\mathbf{r}_0)) - \nabla(\psi_d^{(a)}(\mathbf{r}_0) - \psi_d^{(b)}(\mathbf{r}_0))] = \hat{z} \times \Delta\mathbf{H}_e(\mathbf{r}_0)$$

$$\mathbf{r}_0 \in \text{on the aperture} \quad (3.28)$$

Finally, introducing the integral form of the potentials (3.21) and (3.26) in (3.28), the final expression for the MPIE can be written in the form

$$\hat{z} \times [-j\omega \int_{S'} [\overline{\mathbf{G}}_F^{(a)}(\mathbf{r}_0, \mathbf{r}') + \overline{\mathbf{G}}_F^{(b)}(\mathbf{r}_0, \mathbf{r}')] \cdot \mathbf{M}_s(\mathbf{r}') dS' -$$

$$\nabla \int_{S'} [G_\psi^{(a)}(\mathbf{r}_0, \mathbf{r}') + G_\psi^{(b)}(\mathbf{r}_0, \mathbf{r}')] \rho_m(\mathbf{r}') dS'] = \hat{z} \times \Delta\mathbf{H}_e(\mathbf{r}_0)$$

$$\mathbf{r}_0 \in \text{on the aperture} \quad (3.29)$$

Defining

$$\overline{\mathbf{G}}_F(\mathbf{r}_0, \mathbf{r}') = \overline{\mathbf{G}}_F^{(a)}(\mathbf{r}_0, \mathbf{r}') + \overline{\mathbf{G}}_F^{(b)}(\mathbf{r}_0, \mathbf{r}') \quad (3.30)$$

$$G_\psi(\mathbf{r}_0, \mathbf{r}') = G_\psi^{(a)}(\mathbf{r}_0, \mathbf{r}') + G_\psi^{(b)}(\mathbf{r}_0, \mathbf{r}') \quad (3.31)$$

(3.29) can be rewritten as

$$\hat{z} \times \left[ -j\omega \int_{S'} \overline{\overline{\mathbf{G}}}_F(\mathbf{r}_0, \mathbf{r}') \cdot \mathbf{M}_s(\mathbf{r}') dS' - \nabla \int_{S'} G_\psi(\mathbf{r}_0, \mathbf{r}') \rho_m(\mathbf{r}') dS' \right] = \hat{z} \times \Delta \mathbf{H}_e(\mathbf{r}_0)$$

$\mathbf{r}_0 \in \text{on the aperture}$

(3.32)

This is the desired MPIE applied on the surface of the aperture. The validity of this equation depends on the possibility of defining the magnetic charge scalar potential Green's function  $G_\psi$  by (3.26). The unknown in this integral equation is the magnetic surface current density  $\mathbf{M}_s$  and the magnetic surface charge density  $\rho_m$ . However, they are not independent, and are related through the continuity equation (3.25). The final form of the MPIE is

$$\hat{z} \times \left[ -j\omega \int_{S'} \overline{\overline{\mathbf{G}}}_F(\mathbf{r}_0, \mathbf{r}') \cdot \mathbf{M}_s(\mathbf{r}') dS' - j \frac{\nabla}{\omega} \int_{S'} G_\psi(\mathbf{r}_0, \mathbf{r}') [\nabla' \cdot \mathbf{M}(\mathbf{r}')] dS' \right] = \hat{z} \times \Delta \mathbf{H}_e(\mathbf{r}_0)$$

$\mathbf{r}_0 \in \text{on the aperture}$

(3.33)

### 3.4 Green's Function Formulation for Slot Antenna

In this section potentials created by a horizontal magnetic dipole (HMD) are formulated for two cases. The first case, region “b”, when the HMD is located on the metallic surface over a dielectric substrate (Fig. 3.5) and the second case, region “a”, is a half space magnetic dipole (Fig. 3.4). In the first case it necessary to use  $F_z$  component in addition to the parallel to source component  $F_x$  (for an  $x$ -directed horizontal dipole). Hence, the dyadic  $\overline{\overline{\mathbf{G}}}_F$  is given by

$$\overline{\overline{\mathbf{G}}}_F = \begin{bmatrix} G_{F_{xx}} & 0 & 0 \\ 0 & 0 & 0 \\ G_{F_{zx}} & 0 & 0 \end{bmatrix} \quad (3.34)$$

The components  $G_{F_{xx}}$  and  $G_{F_{zx}}$  are the components of the electric vector potential created by an  $x$ -directed horizontal magnetic dipole. Once these components are known, the other components  $G_{F_{yy}}$  and  $G_{F_{zy}}$  are deduced.

In the second case the dyadic  $\overline{\overline{\mathbf{G}}}_F$  is collinear. For example for an  $x$ -directed horizontal dipole, the  $G_{F_{xx}}$  is the only component.

### 3.4.1 Solution of Wave Equation

Assume that an  $x$ -directed HMD is located on the vertical  $z$ -axis. Outside the source, the scalars  $F_x$ ,  $F_z$ , and  $\psi$  satisfy the wave equation which are solved in cylindrical coordinates and satisfy the boundary conditions to provide the general solution inside each layer. The scalar wave equation in the cylindrical coordinates is written as

$$\frac{1}{\rho} \frac{\partial}{\partial \rho} \left( \rho \frac{\partial \Psi}{\partial \rho} \right) + \frac{1}{\rho^2} \frac{\partial^2 \Psi}{\partial \phi^2} + \frac{\partial^2 \Psi}{\partial z^2} + k^2 \Psi = 0 \quad (3.35)$$

Using separation of variables, the solution can be written in the form

$$\Psi(\rho, \phi, z) = R(\rho)\Phi(\phi)Z(z) \quad (3.36)$$

where  $R(\rho)$ ,  $\Phi(\phi)$ , and  $Z(z)$  are the solutions of the differential equations given by

$$\frac{1}{\rho} \frac{d}{d\rho} \left( \rho \frac{dR}{d\rho} \right) + [(k_\rho \rho)^2 - n^2] R = 0 \quad (3.37)$$

$$\frac{d^2 \Phi}{d\phi^2} + n^2 \Phi = 0 \quad (3.38)$$

$$\frac{d^2 Z}{dz^2} + k_z^2 Z = 0 \quad (3.39)$$

where  $k_\rho^2 + k_z^2 = k^2$  and  $n$  is an integer. The solution of the  $\Phi$  and  $Z$  equations can be written in the form

$$\Phi(\phi) = A e^{jn\phi} + B e^{-jn\phi} \quad (3.40)$$

$$Z(z) = C e^{jk_z z} + D e^{-jk_z z} \quad (3.41)$$

and the  $R$  equation is the Bessel differential equation of order  $n$  and its solution is given by

$$R(\rho) = E H_n^{(1)}(k_\rho \rho) + F H_n^{(2)}(k_\rho \rho) \quad (3.42)$$

where  $A, B, C, D, E$  and  $F$  are constants to be determined. In a stratified medium the general solution inside each layer is given by [194]

$$\Psi_i(\rho, \phi, z) = \sum_{n=-\infty}^{\infty} (A_i e^{jn\phi} + B_i e^{-jn\phi}) \int_C H_n^{(2)}(k_\rho \rho) [C_i(k_\rho) e^{-u_i z} + D_i(k_\rho) e^{u_i z}] k_\rho^{n+1} dk_\rho \quad (3.43)$$

since there is a symmetry in the  $\phi$  direction, the solution becomes

$$\Psi_i(\rho, z) = \int_C H_0^{(2)}(k_\rho \rho) [C_i(k_\rho) e^{-u_i z} + D_i(k_\rho) e^{u_i z}] k_\rho dk_\rho \quad (3.44)$$

where  $i = 0, 1$  denotes the layer,  $H_n^{(2)}$  is the Hankel function of  $n$ th order, and  $C$  is an infinite integration path in the complex plane of the spectral variable as shown in Fig. 3.6 where  $k_\rho = \lambda + j\nu$  and  $u_i^2 = k_\rho^2 - k_i^2$ . The unknowns parameters  $C_i$ , and  $D_i$  are obtained using both boundary conditions and Sommerfeld radiation conditions.

### 3.4.2 Boundary Conditions

The magnetic surface current density associated with the HMD is given by the Dirac's Delta distribution

$$\begin{aligned} \mathbf{M}_s &= \hat{x} \frac{\delta(\rho)}{2\pi\rho} M_s dx \\ &= \hat{x} \frac{M_s dx}{4\pi} \int_C H_0^{(2)}(k_\rho \rho) k_\rho dk_\rho, \quad z = 0 \end{aligned} \quad (3.45)$$

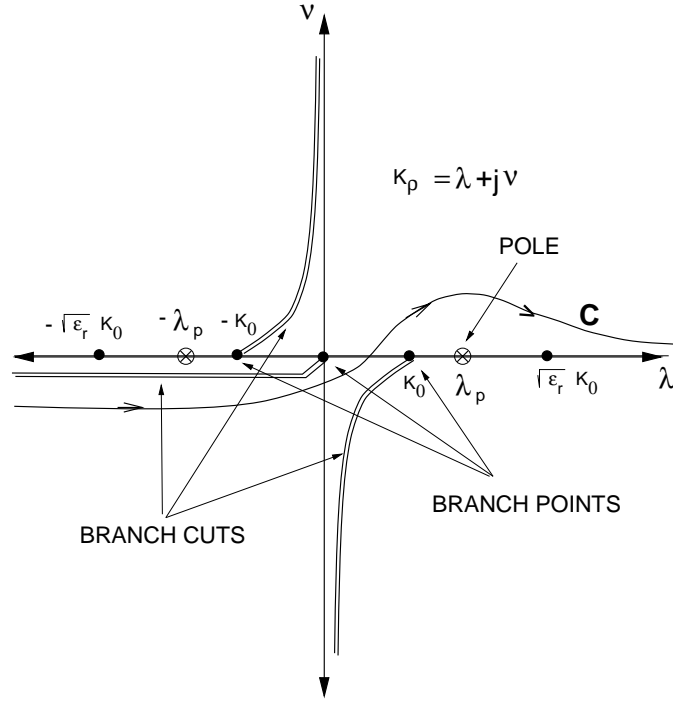


Figure 3.6: The complex plane, showing the integration path  $C$  for the Sommerfeld integrals and possible choice of branch cuts.

where the Hankel transform for  $\frac{\delta(\rho)}{\rho}$  has been utilized in (3.45).

The potential Green's functions must satisfy the following boundary conditions:

1—In the above region (“a” region):

- on the metallic surface

$$\hat{z} \times (\nabla \times \mathbf{F}^{(a)}(\mathbf{r}_0)) = \begin{cases} \mathbf{M}_s(\mathbf{r}_0), & \text{on the aperture} \\ 0, & \text{otherwise} \end{cases} \quad (3.46)$$

and

$$\frac{\partial \psi^{(a)}(\mathbf{r}_0)}{\partial z} = 0 \quad (3.47)$$

2—In the below region (“b” region):

- on the metallic surface

$$\hat{z} (\times \nabla \times \mathbf{F}^{(b)}(\mathbf{r}_0)) = \begin{cases} -\mathbf{M}_s(\mathbf{r}_0), & \text{on the aperture} \\ 0, & \text{otherwise} \end{cases} \quad (3.48)$$

$$\frac{\partial \psi^{(b)}(\mathbf{r}_0)}{\partial z} = 0 \quad (3.49)$$

- on the dielectric interface

$$\psi^{(b)}(\mathbf{r}_1) = \psi^{(b)}(\mathbf{r}_2) \quad (3.50)$$

$$\mathbf{F}^{(b)}(\mathbf{r}_1) = \mathbf{F}^{(b)}(\mathbf{r}_2) \quad (3.51)$$

$$\hat{z} \times \left[ \frac{1}{\epsilon_1} \nabla \times \mathbf{F}^{(b)}(\mathbf{r}_1) - \frac{1}{\epsilon_0} \nabla \times \mathbf{F}^{(a)}(\mathbf{r}_2) \right] = 0 \quad (3.52)$$

$$\hat{z} \times \left[ \nabla \psi^{(b)}(\mathbf{r}_1) - \nabla \psi^{(b)}(\mathbf{r}_2) \right] = 0 \quad (3.53)$$

where  $\mathbf{r}_0$ ,  $\mathbf{r}_1$ , and  $\mathbf{r}_2$  are defined as shown in Fig. 3.4 and 3.5.

### 3.4.3 Radiation Condition

For a distributed source of finite extent radiating in unbounded space, the boundary conditions must be imposed at infinity to obtain a unique solution of the radiation problem. Such a boundary condition is called the radiation condition and requires that solutions attenuate no slower than the inverse distance far away from the source and the wave must propagate outward to infinity. In mathematical terms, the radiation condition for the scalar wave equation  $\Psi$  that satisfies Helmholtz wave equation takes the form [3]

$$\lim_{r \rightarrow \infty} r \left( \frac{\partial \Psi}{\partial r} + jk\Psi \right) = 0 \quad (3.54)$$

### 3.4.4 Green's Functions for Magnetic Current Potentials

The Green's functions are expressed as Sommerfeld integrals in the complex plane of the radial component  $k_\rho$  of the wave vector. After solving the Helmholtz wave equation subjected to the boundary and radiation conditions, the Green's functions of the electric current potentials components are

#### “a” Region (Half Space)

- $z > 0$

$$G_{F_{xx}}^{(a)}(\rho, z) = \frac{\epsilon_0}{4\pi} \int_C \frac{e^{-u_0 z} H_0^{(2)}(k_\rho \rho) k_\rho dk_\rho}{u_0} \quad (3.55)$$

$$G_\psi^{(a)}(\rho, z) = \frac{1}{4\pi\mu_0} \int_C \frac{e^{-u_0 z} H_0^{(2)}(k_\rho \rho) k_\rho dk_\rho}{u_0} \quad (3.56)$$

#### “b” Region (substrate half space)

- $z < -h$

$$G_{F_{xx}}^{(b)}(\rho, z) = \frac{\epsilon_0}{4\pi} \int_C \frac{e^{u_0(z+h)} H_0^{(2)}(k_\rho \rho) k_\rho dk_\rho}{D_{TM} \cosh(uh)} \quad (3.57)$$

$$G_{F_{zx}}^{(b)}(\rho, z) = \frac{\epsilon_0(\epsilon_r - 1)}{4\pi} \frac{\partial}{\partial x} \int_C \frac{e^{u_0(z+h)} H_0^{(2)}(k_\rho \rho) k_\rho dk_\rho}{D_{TM} \cosh(uh)} \quad (3.58)$$

$$G_\psi^{(b)}(\rho, z) = \frac{1}{4\pi\mu_0} \int_C \frac{e^{u_0(z+h)} H_0^{(2)}(k_\rho \rho) k_\rho dk_\rho}{D_{TM} \cosh(uh)} \quad (3.59)$$

- $0 > z > -h$

$$G_{F_{xx}}^{(b)}(\rho, z) = \frac{\epsilon}{4\pi} \int_C \frac{\left(\frac{u_0 \epsilon_r}{u} \sinh(u(z+h)) + \cosh(u(z+h))\right) H_0^{(2)}(\rho k_\rho) k_\rho dk_\rho}{D_{TM} \cosh(uh)} \quad (3.60)$$

$$G_{F_{zx}}^{(b)}(\rho, z) = \frac{\epsilon(\epsilon_r - 1)}{4\pi} \frac{\partial}{\partial x} \int_C \frac{e^{u_0(z+h)} H_0^{(2)}(k_\rho \rho) k_\rho dk_\rho}{D_{TM} \cosh(uh)} \quad (3.61)$$

$$G_\psi^{(b)}(\rho, z) = \frac{\epsilon_r}{4\pi\mu_0} \int_C \frac{\left(\frac{u_0 \epsilon_r}{u} \sinh(u(z+h)) + \cosh(u(z+h))\right) H_0^{(2)}(\rho k_\rho) k_\rho dk_\rho}{D_{TM} \cosh(uh)} \quad (3.62)$$

where

$$u_0 = jk_{z0} = \sqrt{k_\rho^2 - k_0^2}, \quad (3.63)$$

$$u = jk_z = \sqrt{k_\rho^2 - \epsilon_r k_0^2}, \quad (3.64)$$

$$D_{TM} = \epsilon_r u_0 + u \tanh(uh). \quad (3.65)$$

### MPIE Green's Functions

Since the MPIE are solved on the aperture ( $z = 0$ ), we are only interested in  $G_{F_{xx}}$  and  $G_\psi$ . In MPIE we can write

$$G_{F_{xx}}(\rho, 0) = G_{F_{xx}}^{(a)}(\rho, 0) + G_{F_{xx}}^{(b)}(\rho, 0) \quad (3.66)$$

$$G_\psi(\rho, 0) = G_\psi^{(a)}(\rho, 0) + G_\psi^{(b)}(\rho, 0) \quad (3.67)$$

#### 3.4.5 Surface Waves

The equation  $D_{TM} = 0$  is the characteristics equations for the TM surface-wave modes propagation on a dielectric-coated conducting plane. Hence, the zeros of  $D_{TM}$

depend on the radial spectral variable  $k_\rho$ . In our case, the normalized potentials will be

$$NG_{F_{xx}} = \frac{2\pi}{\epsilon_0} G_{F_{xx}}(\rho, 0) = \int_C \left( \frac{1}{u_0} + \frac{\epsilon_r [\epsilon_r u_0 \tanh(uh) + u]}{uD_{TM}} \right) H_0^{(2)}(k_\rho \rho) k_\rho dk_\rho \quad (3.68)$$

$$NG_\psi = 2\pi\mu_0 G_\psi(\rho, 0) = \int_C \left( \frac{1}{u_0} + \frac{\epsilon_r u_0 \tanh(uh) + u}{uD_{TM}} \right) H_0^{(2)}(k_\rho \rho) k_\rho dk_\rho \quad (3.69)$$

The surface waves appears as poles of the integrand in the complex plane  $k_\rho = \lambda + j\nu$ . A knowledge of the location of these poles in the complex plane is essential to ensure the accuracy of the numerical evaluation procedure. Also, the coordinates of the poles have an essential role in the asymptotic expansions of the Green's functions in far fields. For a lossless dielectric layer, the poles lie on the real axis in the segment  $[k_0, \sqrt{\epsilon_r}k_0]$ . There is always at least one pole corresponding to the dominant  $TM_0$  surface wave mode. If the dielectric is lossy, the poles are shifted slightly below the real axis. The condition which guarantees the absence of higher order surface wave modes can be obtain by setting  $u_0 = 0$  in the TE expression resulting in the following condition

$$f[\text{GHz}] \leq \frac{75}{h[\text{mm}]\sqrt{\epsilon_r - 1}} \quad (3.70)$$

It will be assumed that no higher order modes are excited, and only one pole will be considered. This situation is normally met in practice for most applications. For substrates with moderate losses the pole  $\lambda_p + j\nu_p$  lies slightly below the real axis ( $\nu_p \leq 0$ ) and its real part is bounded by  $1 \leq \frac{\lambda_p}{k_0} \leq \sqrt{\epsilon_r}$  (Fig.3.6). A good approximation for electrically thin substrate [157] is

$$\frac{\lambda_p}{k_0} = 1 + (k_0 h)^2 \frac{(\epsilon_r - 1)^2}{2\epsilon_r^2} \quad (3.71)$$

which is useful as a starting point for a numerical pole search.

### 3.5 Near and Far Field Approximations

The integrals for the potentials have no analytical solution. However, it is possible to approximately perform the integration in particular cases of the near and far fields. These situations are characterized by the mathematical conditions  $k_0\rho \ll 1$  and  $k_0\rho \gg 1$ , and they will be calculated for the Green's functions  $G_\psi$  and  $G_{F_{xx}}$  from which the tangential magnetic field on the arbitrary aperture structure can be derived.

Near-field approximation are obtained by noting that the term  $u$  can be written as  $u^2 = u_0^2 - (\epsilon_r - 1)k_0^2$ . Thus, the obvious simplification is to make  $u = u_0$ . Moreover, in the Sommerfeld integral the term  $\tanh(uh) \rightarrow 1$  since  $\rho/\lambda_0 \rightarrow 0$ . With this substitution, analytical integration is possible and the following approximate expressions are obtained:

$$NG_{F_{xx}}(k_0\rho \ll 1) = \left[ \frac{\epsilon_r^2 + \epsilon_r + 2}{2\epsilon_r + 2} \right] \frac{e^{-jk\sqrt{\epsilon_r}\rho}}{\rho} \quad (3.72)$$

$$NG_\psi(k_0\rho \ll 1) = \frac{e^{-jk\sqrt{\epsilon_r}\rho}}{\rho} \quad (3.73)$$

It can be shown from the above expression that, in the near field, when  $\rho/\lambda_0 \rightarrow 0$ , the magnetic vector potential is related to the scalar potential by

$$\frac{NG_{F_{xx}}}{NG_\psi} = \frac{\epsilon_r^2 + \epsilon_r + 2}{2\epsilon_r + 2} \quad (3.74)$$

Far-field approximations can be obtained using standard asymptotic techniques, such as the steepest descent method [195]. The main contributions to the asymptotic expansion arise from the saddle point and from the poles on the real axis  $\lambda$ . They correspond, respectively, to the spatial wave (geometrical optics field) and to the surface wave terms.

On the aperture surface  $z = 0$  the saddle point contribution vanishes and the fields show the typical behavior of a surface wave, decreasing as  $\rho^{1/2}$ . As the dominant TM-mode in the metal coated dielectric slab has zero cutoff frequency, the term  $D_{TM}$  always has at least one zero and the potentials always include a surface wave term.

Under the condition given by (3.70), the leading terms in the asymptotical expansions of the Green's functions under consideration are:

$$NG_{F_{xx}}(k_0\rho \gg 1) = -j2\pi R_1 H_0^{(2)}(k_p\rho) \quad (3.75)$$

$$NG_\psi(k_0\rho \gg 1) = -j2\pi R_2 H_0^{(2)}(k_p\rho) \quad (3.76)$$

Where  $R_1$  and  $R_2$  are the residue of the integrand and the pole for both  $G_{F_{xx}}$  and  $G_\psi$  respectively.

The ratio between far field approximations of the normalized  $G_{F_{xx}}$  and  $G_\psi$  is given by

$$\frac{NG_{F_{xx}}}{NG_\psi} = \frac{2\epsilon_r + [\frac{u_p}{u_{0p}} + \epsilon_r^2 \frac{u_{0p}}{u_p}] \tanh(u_p h)}{(\epsilon_r + 1) + [\frac{u_p}{u_{0p}} + \epsilon_r \frac{u_{0p}}{u_p}] \tanh(u_p h)} \quad (3.77)$$

where

$$u_{0p} = \sqrt{k_p^2 - k_0^2}, \quad (3.78)$$

$$u_p = \sqrt{k_p^2 - \epsilon_r k_0^2} \quad (3.79)$$

and  $k_p$  is the integrand  $TM_0$  surface wave pole.

### 3.6 Numerical Evaluation of Sommerfeld Integral

When the MPIE is analyzed using the MoM, it is necessary to evaluate the interaction between points separated by distances ranging from zero to several wavelengths.

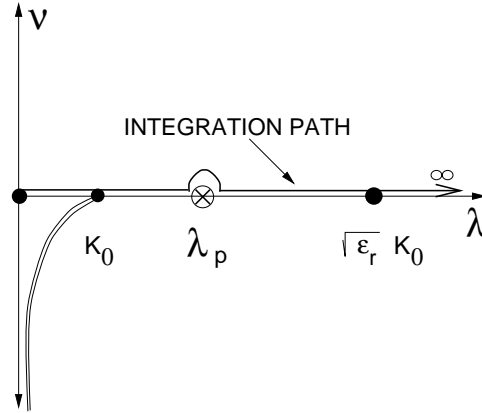


Figure 3.7: A real axis integration path for the Sommerfeld integral.

For most of these distances the accuracy of near field and far field approximation is not sufficient and the potentials must be numerically evaluated [196]. For an aperture on the ground plane over a dielectric substrate, the exponential function in the Sommerfeld integration disappear at the aperture surface. Numerically, this is the most difficult case and it will be concentrated on in this section. Even though many deformation of the original integration path  $C$  of Fig. 3.7 have been tried, the integration along the real positive axis of complex plane  $k_\rho$  provides the most efficient algorithm for evaluating the Sommerfeld integrals appearing in microstrip problems.

### 3.6.1 Numerical Problems

Numerical evaluation of the Sommerfeld integral is carried out by deforming the integration path over the real axis and using the relationship

$$\int_{-\infty}^{\infty} f(k_\rho) H_0^{(2)}(k_\rho \rho) k_\rho dk = 2 \int_0^{\infty} f(k_\rho) J_0(k_\rho \rho) k_\rho dk \quad (3.80)$$

where  $f(k_\rho)$  is an even function in  $k_\rho$

Since the integrand contains  $D_{TM}$  in the denominator (3.68) and (3.69), there is

a pole just below the real axis that produces very strong variation of the integrand, and if the theoretical case of lossless substrate is considered, then the pole is on the real axis. Since, by continuity, the integration path must remain above the pole, the integral from zero to infinity in the lossless case is interpreted as

$$\int_0^\infty = PV \int_0^\infty - j\pi R \quad (3.81)$$

where  $PV$  stands for Cauchy's principal value and  $R$  is the residue of the integral at the pole  $k_\rho = \lambda_p$ . In addition, the complex plane shows a branch point at  $k_\rho = \pm k_0$  due to the square root  $u_0 = \sqrt{\lambda^2 - k_0^2}$  which introduced a discontinuity in the derivative at  $\lambda = k_0$ . Finally, the semi-infinite integration of the oscillating integrand which has an envelope that converges very slowly should be evaluated efficiently. All these facts are illustrated in Fig. 3.8(a), which shows the integrand of the normalized electric vector potential  $NG_{F_{xx}}$  for  $k_0\rho = 2\pi$ ,  $k_0h = 0.419$ , and  $\epsilon_r = 10$ .

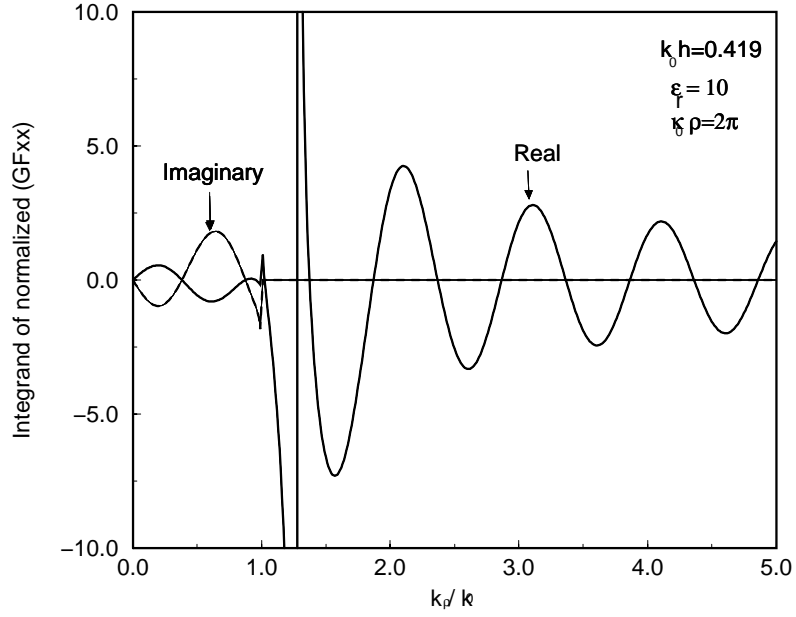
### 3.6.2 Implementing Numerical Integration on Real Axis

The integration interval is decomposed into three subintervals:  $[0, k_0]$ ,  $[k_0, \sqrt{\epsilon_r}k_0]$ , and  $[\sqrt{\epsilon_r}k_0, \infty]$ . In the interval  $[0, k_0]$  the infinite derivative in  $k_0$  is eliminated with change of variables  $\lambda = k_0 \cos(t)$ . The resulting smoother function is numerically integrated. In the interval  $[k_0, \sqrt{\epsilon_r}k_0]$ , the singularity is first extracted by writing the function under the integral sign in the form  $F(\lambda) = J_0(\lambda\rho) f(\lambda)$ , then

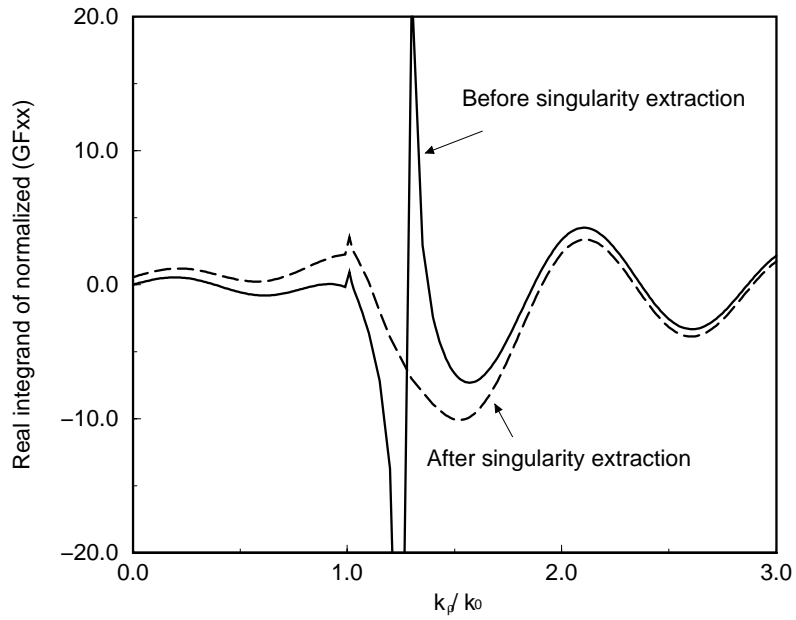
$$F(\lambda) = [J_0(\lambda\rho) f(\lambda) - F_{sing}(\lambda)] + F_{sing}(\lambda) \quad (3.82)$$

where

$$F_{sing}(\lambda) = \frac{R}{\lambda - \lambda_p} \quad (3.83)$$



(a)



(b)

Figure 3.8: The integrand of the normalized electric vector potential for  $NG_{F_{xx}}$ : (a) before singularity extraction ; (b) after singularity extraction.

here  $\lambda_p$  is the pole and  $R$  is the residue of  $F$  at the pole. Then the function  $F_{sing}$  is integrated analytically as :

$$I_{sing} = \int_{k_0}^{k_0\sqrt{\epsilon_r}} F_{sing} d\lambda = R \ln \frac{k_0\sqrt{\epsilon_r} - k_0}{\lambda_p - k_0} \quad (3.84)$$

Fig. 3.8(b) shows the real part of the original function  $F(\lambda)$  and the difference  $F(\lambda) - F_{sing}(\lambda)$  after the singularity has been extracted. There is still an infinite derivative in the curve at  $\lambda = k_0$ ; however, with change of variables,  $\lambda = k_0 \cosh(t)$ , one finally obtains a smooth integrand which is integrated numerically. Finally, in the region  $[\sqrt{\epsilon_r}k_0, \infty]$ , we have an integration in the type of

$$I(\rho) = \int_a^\infty g(\lambda\rho)f(\lambda)d\lambda \quad (3.85)$$

where

1— $g(\lambda\rho)$  is a real oscillating function with a strictly periodic behavior (sin, cos), or behaving asymptotically as the product of periodic function and a monotonic function (Bessel function).

2— $f(\lambda)$  is a non oscillating function which behaves asymptotically as  $\lambda^\alpha \exp(-\lambda z)$ . Therefore, for points at the interface ( $z = 0$ ),  $f(\lambda)$  decreases very slowly.

3—The lower integration bound  $a$  has been chosen that the interval  $[a, \infty]$  is far enough from any possible singularity of  $f(\lambda)$ , in our case  $a = k_0\sqrt{\epsilon_r}$ .

Using the method of averages [162], the integration in (3.85) is decomposed to

$$\int_a^\infty g(\lambda\rho) f(\lambda) d\lambda = \sum_{n=0}^\infty \int_{a+np/2}^{a+(n+1)p/2} g(\lambda\rho) f(\lambda) d\lambda \quad (3.86)$$

where  $p$  is the period of the function  $g$ . The integration over each cycle is performed prior to the series summation.

### 3.6.3 Numerical Results

The above numerical algorithms have been applied to the computation of Sommerfeld integrals giving the potentials. In this section, graphical results for normalized  $G_{F_{xx}}$  and  $G_{\psi}$  are presented.

Figs. 3.9(a) and 3.9(b) show both magnitude and phase for  $NG_{F_{xx}}$ ,  $NG_{\psi}$  and free space solution potential. The operating frequency is 10 GHz and the substrate parameters are  $\epsilon_r = 10$  and  $h = 2$  mm.

In Fig. 3.9(a), for small radial distance  $\rho$ , all the potentials vary as a  $1/\rho$  with difference between  $NG_{F_{xx}}$  and  $NG_{\psi}$  as a near field approximation in (3.72) and (3.73).

However, for radial distance greater than the substrate thickness  $h$ , the potential varies as  $1/\rho^2$  as a contribution from surface waves. In this case, we can see that the contribution of the surface wave propagation to the total fields. The difference between free space field and actual field make the use of free space approximation in the solution is impossible.

The effect of the substrate relative permittivity,  $\epsilon_r$ , on  $NG_{F_{xx}}$  and  $NG_{\psi}$  is examined in Figs. 3.10 and 3.12. Also the effect of the substrate thickness ( $h$ ) on  $NG_{F_{xx}}$  and  $NG_{\psi}$  is examined in Figs. 3.11 and 3.13.

## 3.7 Spectral Domain Green's Functions

In MoM matrix formulation, the matrix is diagonally dominant and the accuracy of diagonal elements describing the effect of a cell on itself is very important for accuracy of the solution. Because of the potential singularity when  $\rho \rightarrow 0$ , the accuracy of the self and overlapped elements is not guaranteed. In this dissertation both space and spectral domain Green's function were used to calculate the MoM matrix

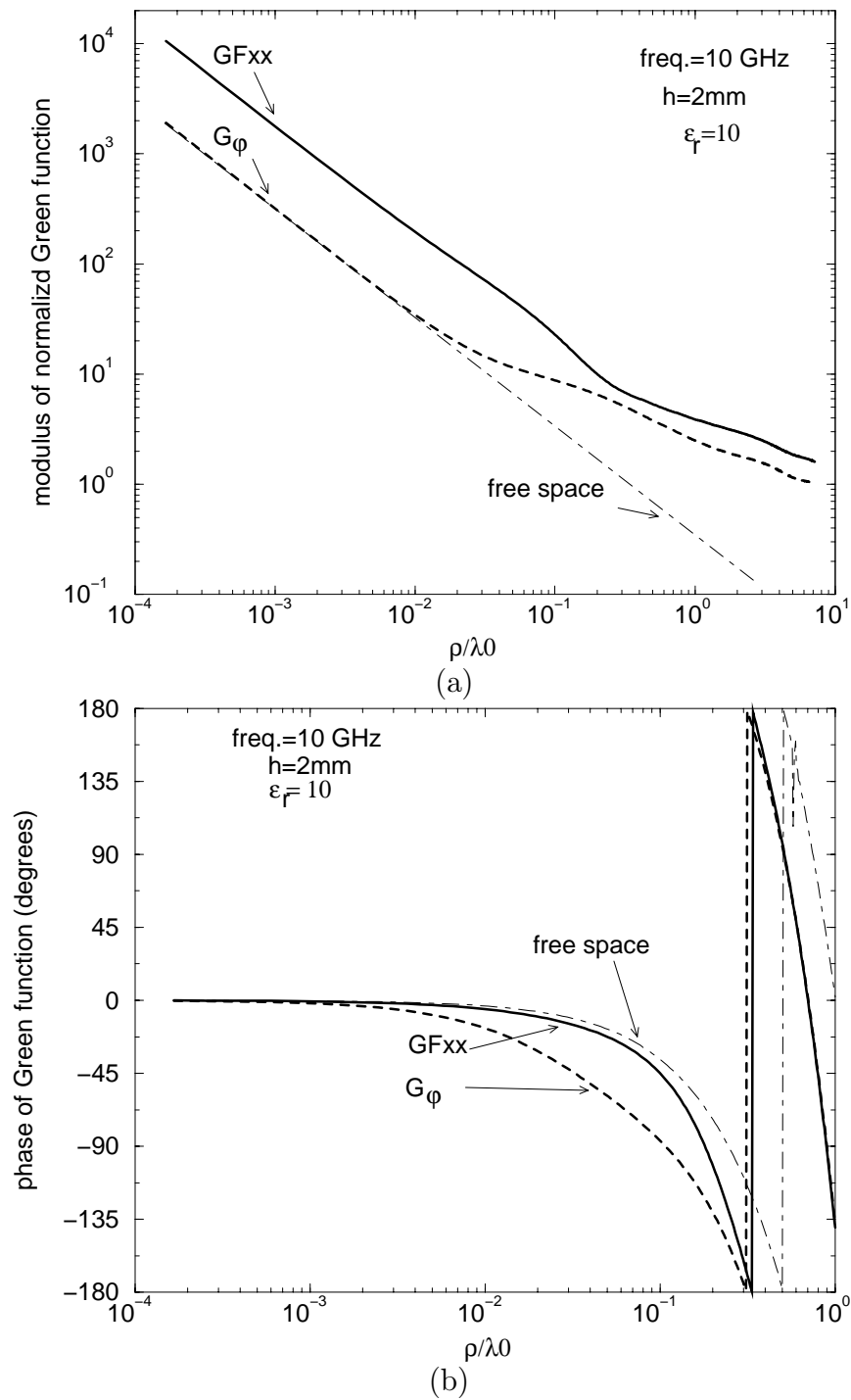


Figure 3.9: Calculated  $NG_{F_{xx}}$  and  $NG_{\psi}$  as function of normalized source-observation: (a) magnitude; (b) phase. distance.

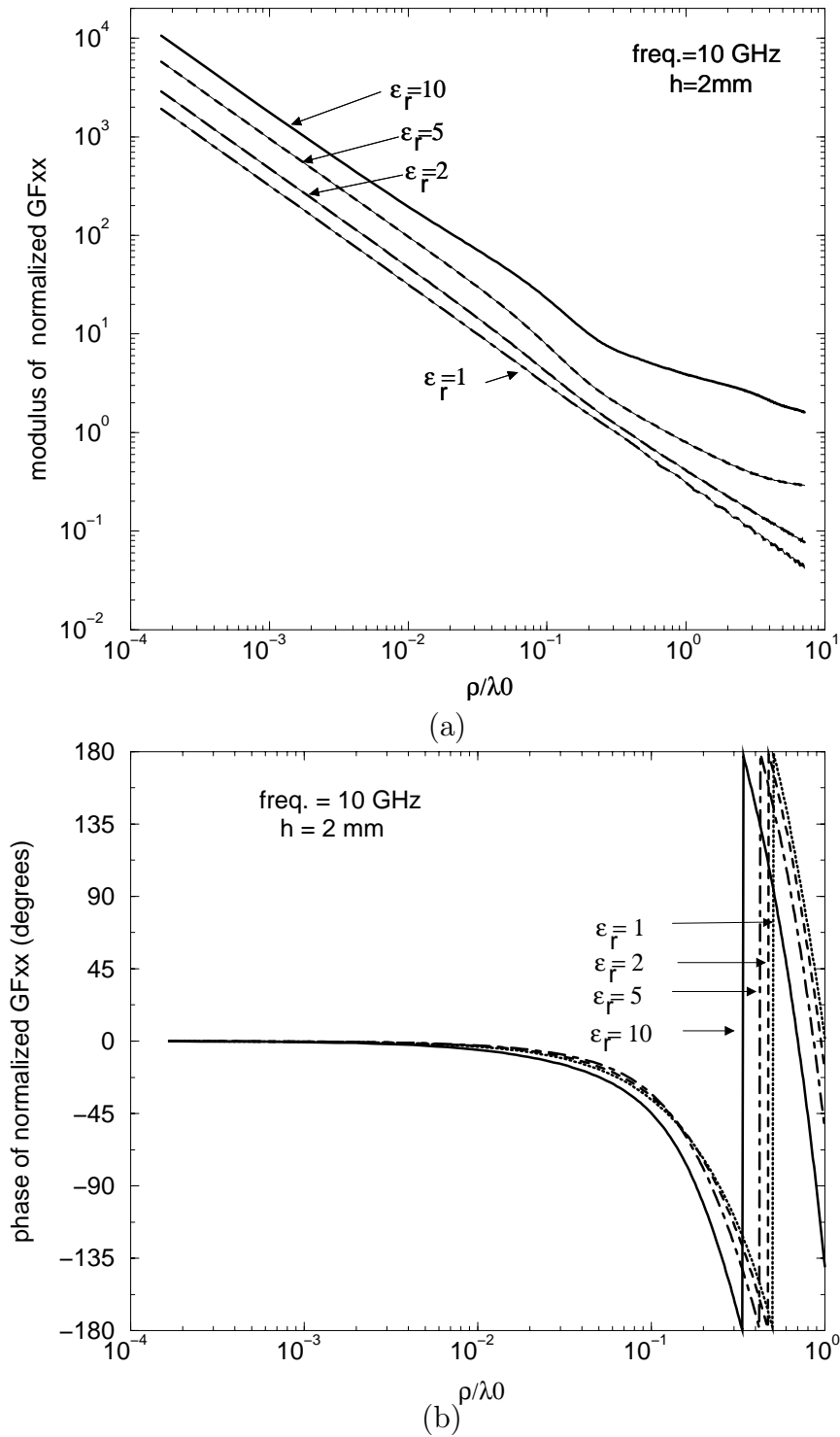


Figure 3.10: Effect of substrate relative permittivity on  $NG_{F_{xx}}$ : (a) magnitude ; (b) phase.

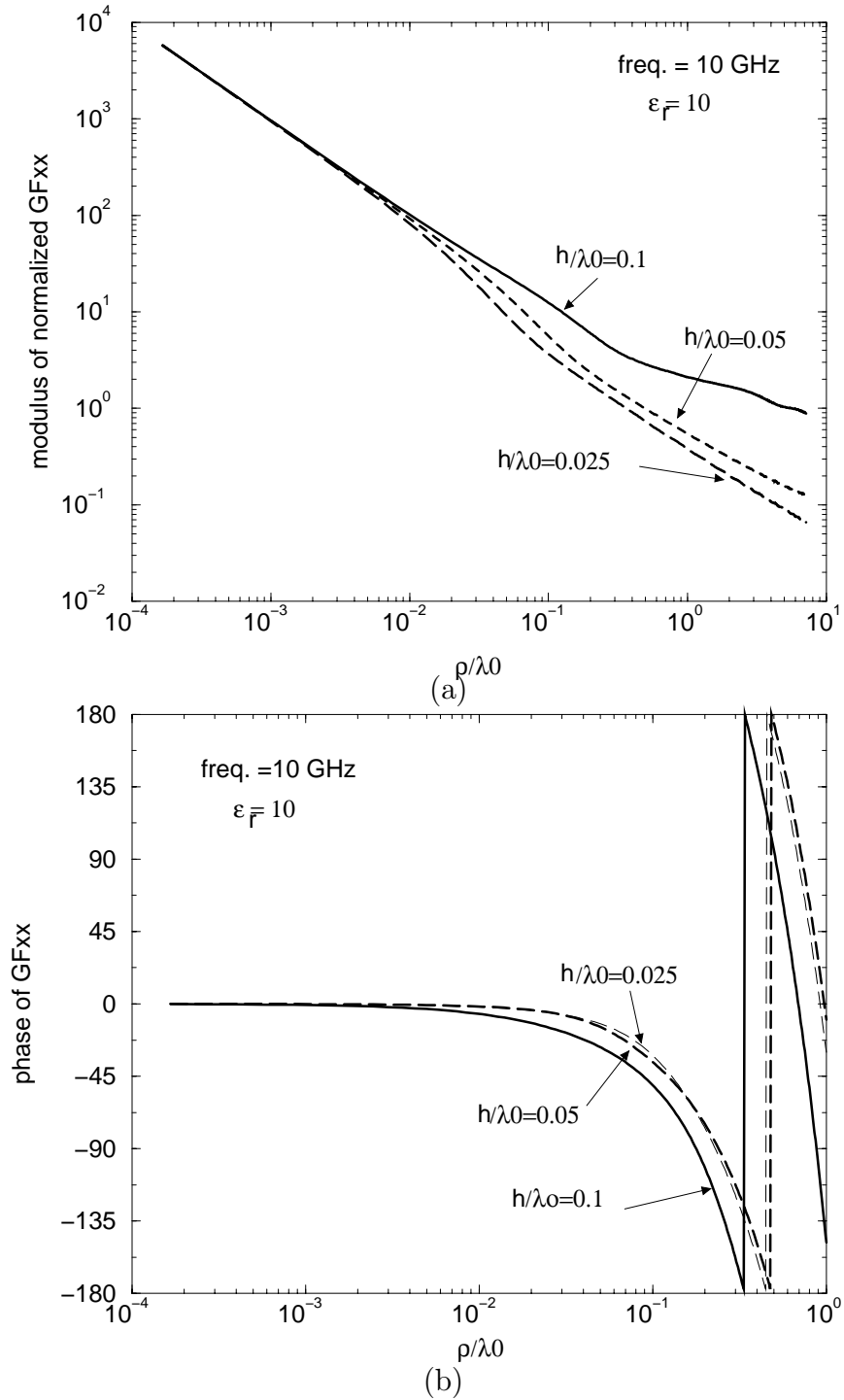


Figure 3.11: Effect of substrate thickness on  $NG_{F_{xx}}$ : (a) magnitude ; (b) phase.

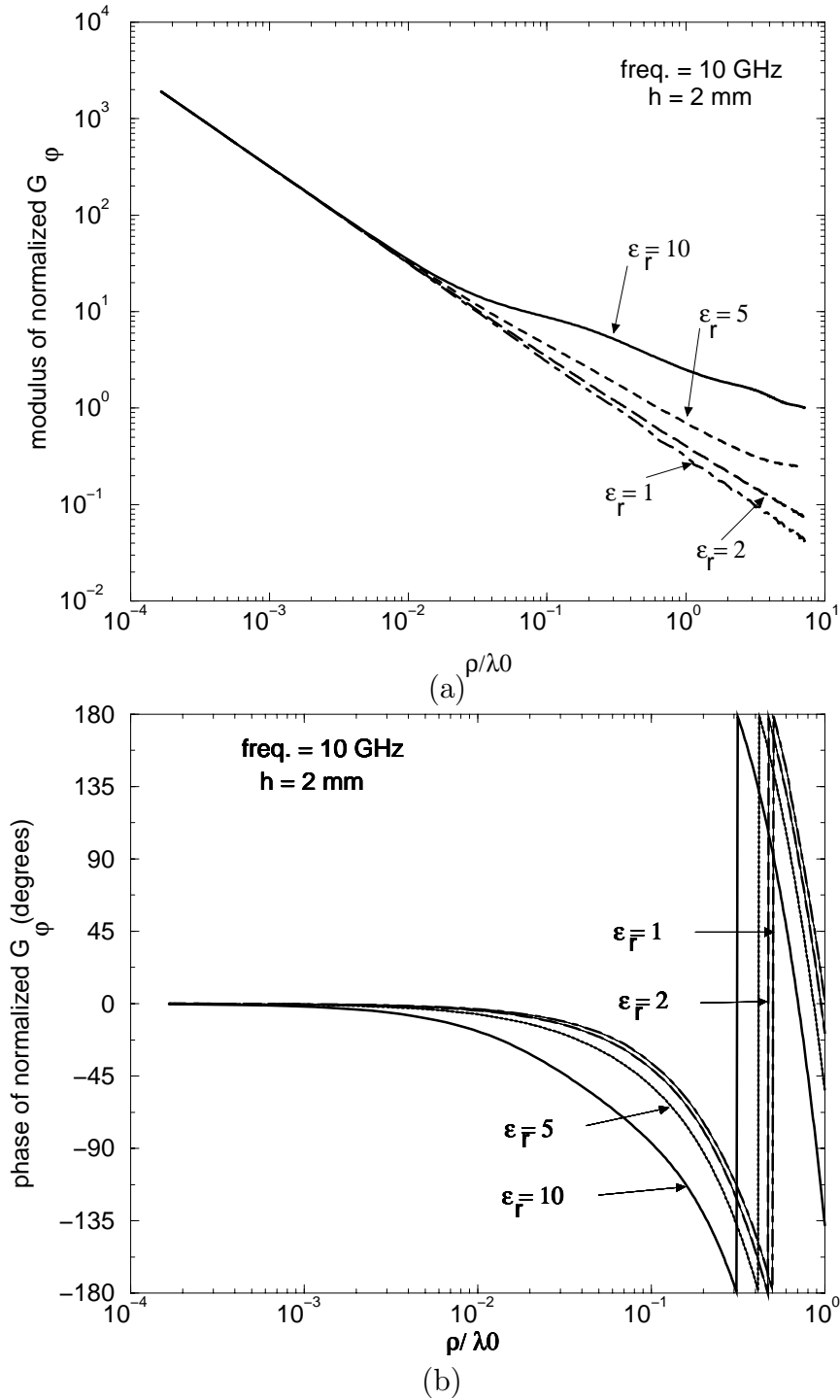


Figure 3.12: Effect of substrate relative permittivity on  $NG_{F_\psi}$ : (a) magnitude ; (b) phase.

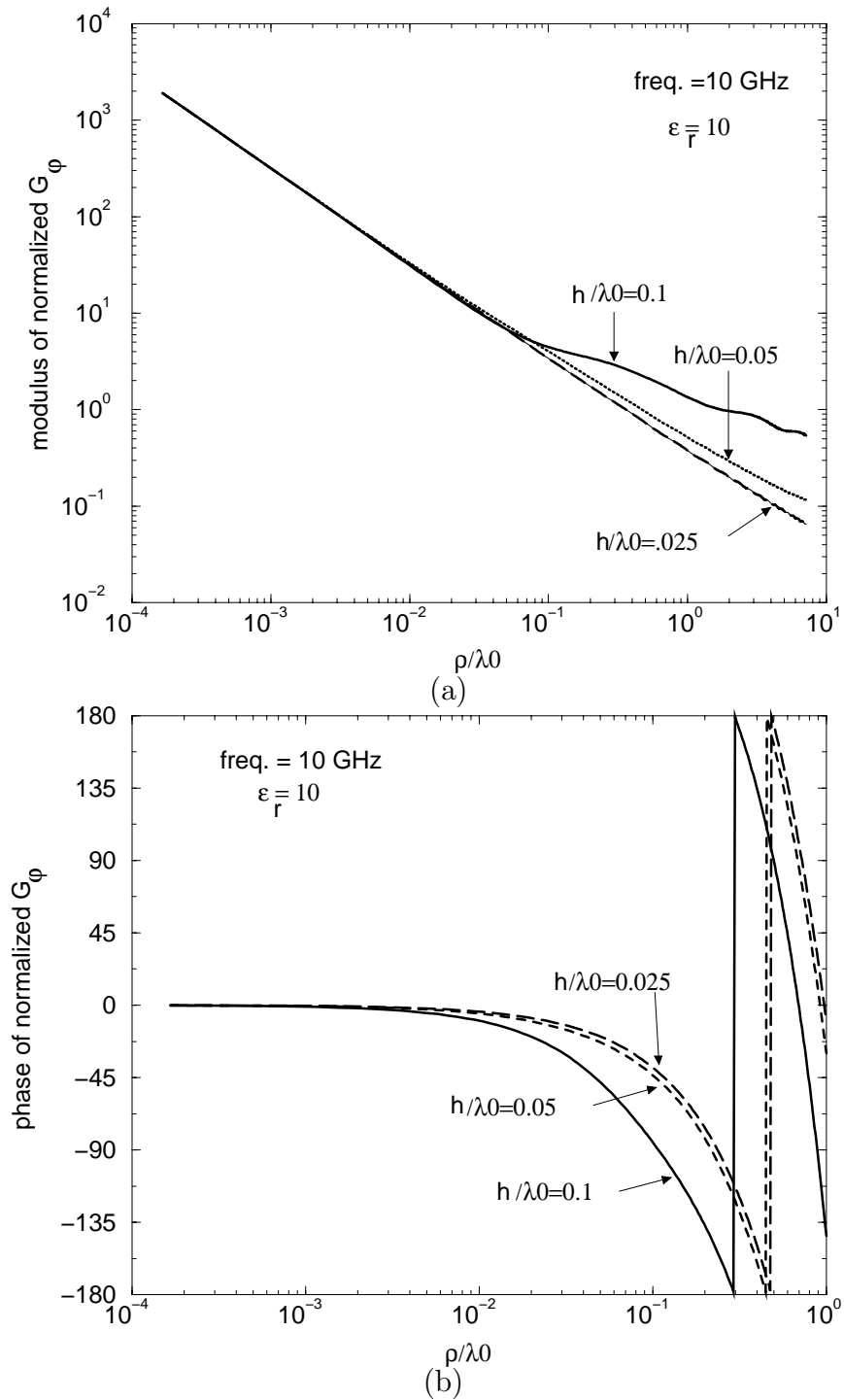


Figure 3.13: Effect of substrate thickness on  $NG_\psi$ : (a) magnitude ; (b) phase.

elements. The self and overlapped cell interaction elements are calculated using the spectral domain Green's functions which are more accurate and easy to calculate. However, for non-overlapped cell interaction elements space domain Green's functions are used since they are more accurate and numerically efficient in this case. Taking the advantage of both techniques, an efficient MoM technique was developed. In this section, the evaluation of the spectral domain magnetic field Green's functions are presented.

The space domain magnetic field Green's function  $\bar{\bar{\mathbf{G}}}_{HM}$  relates the magnetic current with the generated magnetic field by

$$\mathbf{H}(\mathbf{r}) = \int_{S'} \bar{\bar{\mathbf{G}}}_{HM}(\mathbf{r}, \mathbf{r}') \cdot \mathbf{M}_s(\mathbf{r}') dS' \quad (3.87)$$

It is difficult to obtain this spatial domain dyadic Green's function directly. Many techniques have been reported illustrating the ways of obtaining this function. The spectral domain using the immittance approach [5] is the direct way to calculate the spectral domain dyadic Green's functions and is used here.

The spectral domain dyadic Green's function is related to the spatial domain dyadic Green's function as the inverse Fourier transform

$$\bar{\bar{\mathbf{G}}}_{HM}(x|x'; y|y') = \frac{1}{4\pi^2} \int_{-\infty}^{\infty} \int_{-\infty}^{\infty} \tilde{\bar{\bar{\mathbf{G}}}}_{HM}(k_x, k_y) e^{jk_x(x-x')} e^{jk_y(y-y')} dk_x dk_y. \quad (3.88)$$

Using the immittance approach we write the geometry of the problem as equivalent transmission lines for the transverse electric (TE) and the transverse magnetic (TM) cases as shown in Fig. 3.14.

The components of the dyadic Green's functions in the spectral domain are then given as [176]

$$\tilde{G}_{HM_{xx}}(k_x, k_y) = \frac{-1}{\beta^2} (k_x^2 Y^{TE} + k_y^2 Y^{TM}) \quad (3.89)$$

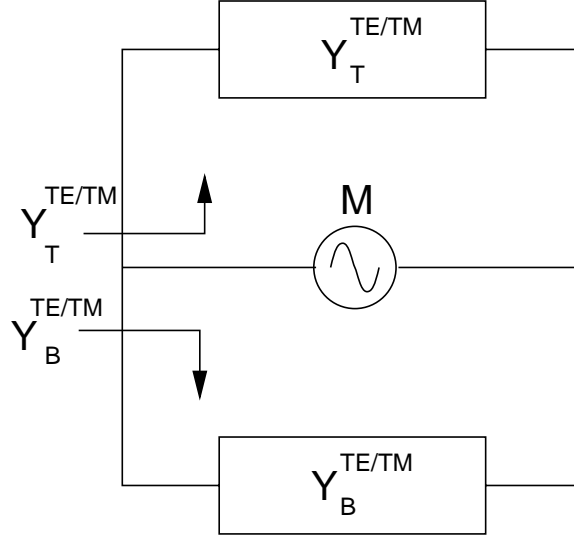


Figure 3.14: Equivalent transmission lines for the immittance approach.

$$\tilde{G}_{HM_{yy}}(k_x, k_y) = \frac{-1}{\beta^2} (k_x^2 Y^{TE} + k_y^2 Y^{TM}) \quad (3.90)$$

and

$$\tilde{G}_{HM_{xy}}(k_x, k_y) = \tilde{G}_{HM_{yx}}(k_x, k_y) = \frac{-k_x k_y}{\beta^2} (Y^{TE} - Y^{TM}) \quad (3.91)$$

where

$$Y^{TE} = Y_T^{TE} + Y_B^{TE} \quad (3.92)$$

$$Y^{TM} = Y_T^{TM} + Y_B^{TM}. \quad (3.93)$$

With everything defined for the equivalent transmission line model shown in Fig. 3.14, the dyadic Green's functions for half space and dielectric slab are derived in the next sections.

### 3.7.1 “a” Region (Half Space)

The half space geometry is shown in Fig. 3.4. In this configuration the source and observation point are located in the  $z = 0$  plane. The equivalent transmission line

model is shown in Fig. 3.15.

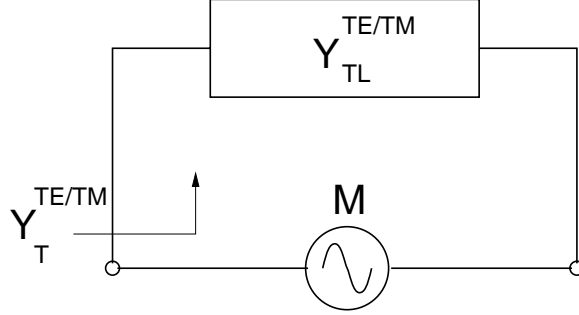


Figure 3.15: Equivalent transmission line model for the immittance approach for the half space dipole.

For the equivalent magnetic voltage source  $\mathbf{M}_s$  over a conductor the TE and TM loads at the bottom are open circuit, which means that

$$Y_{BL}^{TE} = 0 \quad (3.94)$$

$$Y_{BL}^{TM} = 0 \quad (3.95)$$

The equivalent admittance looking into the top for the TE and TM cases are half space and given by

$$Y_T^{TE} = Y_{TL}^{TE} = \frac{Y_0 k_{z0}}{k_0} \quad (3.96)$$

$$Y_T^{TM} = Y_{TL}^{TM} = \frac{Y_0 k_0}{k_{z0}} \quad (3.97)$$

where

$$k_{z0} = \sqrt{k_0^2 - \beta^2} \quad , \quad \text{Im}(k_{z0}) < 0 \quad (3.98)$$

and

$$\beta^2 = k_x^2 + k_y^2. \quad (3.99)$$

The total equivalent impedances of the top and bottom are

$$Y^{TE} = Y_T^{TE} \quad (3.100)$$

$$Y^{TM} = Y_T^{TM}. \quad (3.101)$$

Using (3.100) and (3.101) in expressions (3.89)–(3.91) yields the dyadic components of the half space Green's functions:

$$\tilde{G}_{HM_{xx}}^{(a)}(k_x, k_y) = \frac{Y_0}{k_0} \left( \frac{k_x^2 - k_0^2}{k_{z0}} \right) \quad (3.102)$$

$$\tilde{G}_{HM_{yy}}^{(a)}(k_x, k_y) = \frac{Y_0}{k_0} \left( \frac{k_y^2 - k_0^2}{k_{z0}} \right) \quad (3.103)$$

and

$$\tilde{G}_{HM_{xy}}^{(a)}(k_x, k_y) = \tilde{G}_{HM_{yx}}^{(a)}(k_x, k_y) = \frac{Y_0}{k_0} \left( \frac{k_x k_y}{k_{z0}} \right). \quad (3.104)$$

### 3.7.2 “b” Region (Substrate-half space)

The geometry configuration for a single layer slot antenna is shown in Fig. 3.5 and the its equivalent transmission line model is shown in Fig. 3.16. The ground plane is at ( $z = 0$ ) and above it is a conductor. Between the ground plane ( $z = 0$ ) and ( $z = -h$ ) is a dielectric slab and below the slab ( $z < -h$ ) is free space. In the Green's function derivation, the ground plane and dielectric slab are assumed to be infinite in the transverse directions.

For an equivalent magnetic voltage source  $\mathbf{M}_s$  the TE and TM loads at the top are open circuit

$$Y_{TL}^{TE} = 0 \quad (3.105)$$

$$Y_{TL}^{TM} = 0 \quad (3.106)$$

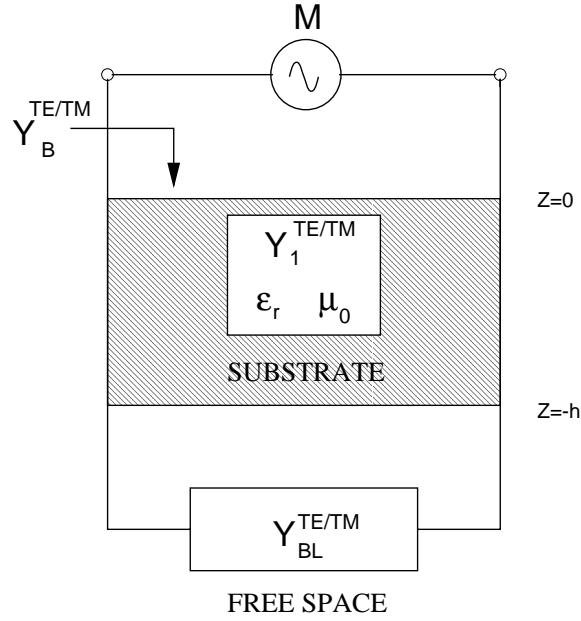


Figure 3.16: Equivalent transmission lines for the immittance approach.

due to the substrate plane located at the bottom. The equivalent impedances looking into the bottom for the TE and TM cases are

$$Y_B^{TE} = Y_1^{TE} \left[ \frac{Y_{BL}^{TE} \cos(k_{z1}d) + jY_1^{TE} \sin(k_{z1}d)}{Y_1^{TE} \cos(k_{z1}d) + jY_{BL}^{TE} \sin(k_{z1}d)} \right] \quad (3.107)$$

$$Y_B^{TM} = Y_1^{TM} \left[ \frac{Y_{BL}^{TM} \cos(k_{z1}d) + jY_1^{TM} \sin(k_{z1}d)}{Y_1^{TM} \cos(k_{z1}d) + jY_{BL}^{TM} \sin(k_{z1}d)} \right] \quad (3.108)$$

where

$$Y_1^{TE} = \frac{Y_1 k_{z1}}{k_1} \quad (3.109)$$

$$Y_1^{TM} = \frac{Y_1 k_1}{k_{z1}} \quad (3.110)$$

and

$$k_{z1} = \sqrt{k_1^2 - \beta^2} \quad , \quad \text{Im}(k_{z1}) < 0. \quad (3.111)$$

The wave number and impedance in the dielectric layer are given as

$$Y_1 = \sqrt{\epsilon_r} Y_0, \quad k_1 = \sqrt{\epsilon_r} k_0.$$

and the total equivalent impedances of the top and bottom are

$$Y^{TE} = Y_B^{TE} \quad (3.112)$$

$$Y^{TM} = Y_B^{TM} \quad (3.113)$$

Using (3.112) and (3.113) in expressions (3.89)–(3.91) yields the dyadic components of the slot Green's functions:

$$\begin{aligned} \tilde{G}_{HM_{xx}}^{(b)}(k_x, k_y) &= \frac{Y_0}{k_0} \\ &\cdot \left[ \frac{(k_x^2 - \epsilon_r k_0^2)(k_{z1} \cos(k_{z1}d) + jk_{z1} \sin(k_{z1}h))}{k_{z1} T_m} + \frac{(\epsilon_r - 1) k_x^2 k_{z1}}{T_e T_m} \right] \end{aligned} \quad (3.114)$$

$$\begin{aligned} \tilde{G}_{HM_{yy}}^{(b)}(k_x, k_y) &= \frac{Y_0}{k_0} \\ &\cdot \left[ \frac{(k_y^2 - \epsilon_r k_0^2)(k_{z1} \cos(k_{z1}d) + jk_{z1} \sin(k_{z1}h))}{k_{z1} T_m} + \frac{(\epsilon_r - 1) k_y^2 k_{z1}}{T_e T_m} \right] \end{aligned} \quad (3.115)$$

and

$$\tilde{G}_{HM_{yx}}^{(b)}(k_x, k_y) = \frac{Y_0}{k_0} k_x k_y \left[ \frac{k_{z1} \cos(k_{z1}h) + j\epsilon_r k_{z0} \sin(k_{z1}h)}{k_{z1} T_m} + \frac{(\epsilon_r - 1) k_{z1}}{T_e T_m} \right] \quad (3.116)$$

and

$$\tilde{G}_{HM_{xy}}^{(b)}(k_x, k_y) = \tilde{G}_{HM_{yx}}^{(b)}(k_x, k_y). \quad (3.117)$$

where

$$T_e = k_{z1} \cos(k_{z1}d) + jk_{z0} \sin(k_{z1}d) \quad (3.118)$$

and

$$T_m = \epsilon_r k_{z0} \cos(k_{z1}d) + jk_{z1} \sin(k_{z1}d). \quad (3.119)$$

The  $T_e$  and  $T_m$  terms represent the TE and TM surface wave poles, respectively. The TM surface wave has a zero cutoff frequency which means there is always at least one TM surface wave pole for  $\epsilon_r \neq 1$ . The surface wave poles are real for lossless dielectrics and complex for lossy dielectrics. Numerical evaluation of (3.114)–(3.116) needs special attention because of the surface wave poles in (3.118) and (3.119). Techniques for handling these surface wave poles are discussed in [146, 167].

As was the situation for the half space case, evaluation in the spatial domain is difficult due to singularities which are avoided in the spectral domain.

### 3.7.3 Total Spectral Domain Magnetic Green's Functions

As defined in Equations (3.66) and (3.67), the total spectral domain magnetic field dyadic Green's functions are given by

$$\tilde{G}_{HM_{xx}}(k_x, k_y) = \tilde{G}_{HM_{xx}}^{(a)}(k_x, k_y) + \tilde{G}_{HM_{xx}}^{(b)}(k_x, k_y) \quad (3.120)$$

$$\tilde{G}_{HM_{yy}}(k_x, k_y) = \tilde{G}_{HM_{yy}}^{(a)}(k_x, k_y) + \tilde{G}_{HM_{yy}}^{(b)}(k_x, k_y) \quad (3.121)$$

$$\tilde{G}_{HM_{xy}}(k_x, k_y) = \tilde{G}_{HM_{xy}}^{(a)}(k_x, k_y) + \tilde{G}_{HM_{xy}}^{(b)}(k_x, k_y) \quad (3.122)$$

and

$$\tilde{G}_{HM_{yx}}(k_x, k_y) = \tilde{G}_{HM_{yx}}^{(a)}(k_x, k_y) + \tilde{G}_{HM_{yx}}^{(b)}(k_x, k_y). \quad (3.123)$$

### 3.8 Summary

In this chapter, the MPIE of the CPW-slot structure and its kernel components of the Green's functions have been presented. The MPIE was derived based on the equivalent principle and the magnetic current model. The unknown of this MPIE is the magnetic current (the electric fields) on the slot surface.

The Green's functions were derived in both spectral and spatial domain. The spatial domain Green's functions were evaluated using the numerical integration of the Sommerfeld integral. The problems and implementation of the numerical evaluation were presented and discussed.

Analytical formulas for these Green's functions based on the near and far fields approximation were derived and compared with the numerical values. Also, the effect of the substrate thickness and material on the Green's functions was shown. This study showed how we can use these approximations to enhance the CPU computation time. The spectral domain Green's functions were derived for CPW-slot structure based on the immittance technique.

In the next chapter, the solution of the MPIE using both spectral and spatial domain MoM technique is presented.



# Chapter 4

## MPIE Solution using MoM for CPW-Slot Structures

### 4.1 Introduction

In this chapter, the MPIE solution using MoM is presented. In the beginning and as an introduction, a simple mathematical outline [197] is given to illustrate the MoM procedure. Consider the following inhomogeneous equation

$$Lu = f \quad (4.1)$$

or

$$Lu - f = 0 \quad (4.2)$$

where  $L$  is a linear operator,  $u$  is unknown, and  $f$  is known. In order to solve for  $u$  an approximate solution for (4.2) is found by the following procedure known as the MoM. Let  $u$  be approximated by a set of basis functions or expansion functions given by

$$u_n = \sum_{k=1}^n \alpha_k \phi_k, \quad n = 1, 2, \dots \quad (4.3)$$

where  $\phi_k$  is the expansion function,  $\alpha_k$  is its unknown amplitude, and  $n$  is the total number of expansion functions. Replacement of  $u$  by  $u_n$  in (4.2) and taking the inner product with a set of weighting functions or testing functions  $w_m$ , where the left side of (4.2) is orthogonal to the sequence  $\{w_m\}$ , results in

$$\langle Lu_n - f, w_m \rangle = 0, \quad m = 1, 2, \dots, n. \quad (4.4)$$

Substitution of (4.3) into (4.4) yields

$$\sum_{k=1}^n \alpha_k \langle L\phi_k, w_m \rangle = \langle f, w_m \rangle, \quad m = 1, 2, \dots, n \quad (4.5)$$

which is the final matrix equation of the MoM [134, 198]. In matrix form we can write

$$Ax = b \quad (4.6)$$

with each matrix and vector defined by

$$x = (\alpha_1 \ \alpha_2 \ \cdots \ \alpha_n)^T \quad (4.7)$$

$$b = (\langle f, w_1 \rangle \ \langle f, w_2 \rangle \ \cdots \ \langle f, w_n \rangle)^T \quad (4.8)$$

and

$$A = [a_{mk}] \quad (4.9)$$

where  $T$  denotes the transpose and  $a_{mk}$  are the individual matrix elements given by

$$a_{mk} = \langle L\phi_k, w_m \rangle. \quad (4.10)$$

The accuracy is highly dependent upon the choice and number of expansion and weighting functions used. The best accuracy is usually achieved when the same functions are used for both expansion and weighting which is known as the Galerkin's method [199]. Also it is important to note that the computation time and memory size increases significantly with the increase in the number of basis functions used.

For integral equations, the linear operator  $L$  will include a Green's function. The Green's function can best be described as the impulse response of the system. For example, an electric field Green's function would describe all of the electric fields at any location due to a current filament at a fixed position. In many applications dyadic Green's functions are used. Tai [200] gives a comprehensive and rigorous analysis of dyadic Green's functions.

## 4.2 Mixed Potential Integral Equation

As discussed in the previous chapter, the diffracted fields derived from the potentials satisfying Maxwell's equations and the boundary and radiation conditions are related to the excitation via the MPIE. This equation is simply the continuity condition of the total (sum of the excitation and scattered fields) tangential components of the magnetic fields over the aperture.

The diffracted fields are derived from the scalar and electric vector potentials, which in turn are expressed in terms of superposition integrals of the corresponding Green's functions, weighted by the unknown distribution of surface magnetic current. This desired MPIE is applied on the aperture and given by

$$\hat{z} \times \left[ -j\omega \int_{S'} \overline{\overline{\mathbf{G}}}_F(\mathbf{r}_0, \mathbf{r}') \cdot \mathbf{M}_s(\mathbf{r}') dS' - \frac{j\nabla}{\omega} \int_{S'} G_\psi(\mathbf{r}_0, \mathbf{r}') [\nabla' \cdot \mathbf{M}_s(\mathbf{r}')] dS' \right] = \hat{z} \times \Delta \mathbf{H}^{exc}(\mathbf{r}_0)$$

$\mathbf{r}_0 \in \text{on the aperture}$

(4.11)

## 4.3 Method of Moments

To obtain an exact solution of the surface magnetic current  $\mathbf{M}_s$ , one would have to satisfy the boundary condition at every point within the aperture. This is clearly not feasible, as it would require the solution of infinite set of equations. Some kind of truncation of the sets is an absolute requirement. the boundary conditions will then be satisfied over a limited number of points, carefully chosen over the aperture, using the MoM.

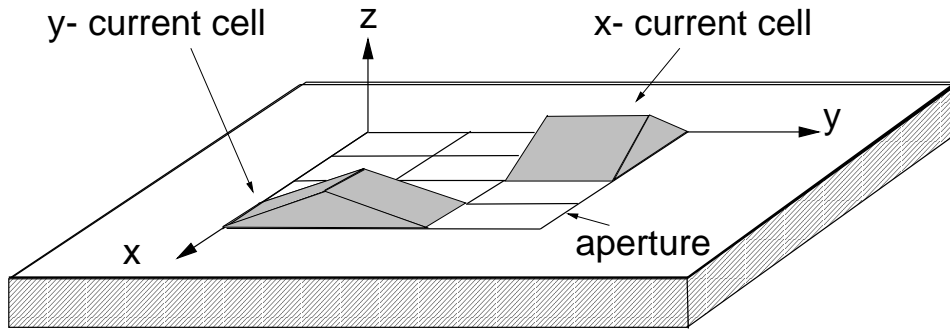


Figure 4.1: Segmentation of the aperture.

### 4.3.1 Charge and Current Cells

Using the MoM technique needs selection of the basis and test functions. These functions must be suitable for the study of arbitrarily shaped aperture at any frequency. Since, no prior assumption will be made for the magnetic current distribution on the aperture, this actually eliminates the use of basis functions defined over the entire domain. A comparison of available possibilities led to the selection of rooftop functions for the surface magnetic current, which has successfully been used in similar problems. To implement these functions, the aperture boundary is replaced by a mesh of rectangular cells (see Fig. 4.1).

The aperture surface is divided into rectangular cells, called charge cells with dimensions  $N_x \times N_y$ . The use of different cell sizes would considerably increase the length of the computation. Two adjacent charge cells, sharing a common border perpendicular to the  $x$ -direction ( $y$ -direction), will form  $x$ -directed ( $y$ -directed) current cell Fig. 4.1. An automatic overlapping of current cells is obtained in this manner, in which a charge cells may belong to up to four different current cells. The number of charge cells is thus related to the number of current cells, although the relationship is not a simple one, depending as it does on the shape of the aperture.

For single rectangular aperture with  $N_x \times N_y$  charge cells, the number of  $x$ -directed current cells is  $(N_x - 1) \times N_y$  and the  $y$ -directed current cells is  $N_x \times (N_y - 1)$  in Fig. 4.2

### 4.3.2 Basis Functions

The Cartesian components of the magnetic surface current are expanded over a set of basis functions  $T_x$  and  $T_y$

$$M_x(\mathbf{r}) = \sum_{k=1}^{N_y} \sum_{j=1}^{N_x-1} V_{kj}^x T_x(\mathbf{r} - \mathbf{r}_{kj}^x) \quad (4.12)$$

$$M_y(\mathbf{r}) = \sum_{k=1}^{N_y-1} \sum_{j=1}^{N_x} V_{kj}^y T_y(\mathbf{r} - \mathbf{r}_{kj}^y) \quad (4.13)$$

where the basis functions,  $T_x(\mathbf{r})$  and  $T_y(\mathbf{r})$ , are of rooftop type (Fig. 4.3) defined as

$$T_x(\mathbf{r}) = \begin{cases} \frac{1-|x|/a}{b}, & \text{at } |x| < a \text{ and } |y| < b/2 \\ 0, & \text{elsewhere} \end{cases} \quad (4.14)$$

$$T_y(\mathbf{r}) = \begin{cases} \frac{1-|y|/b}{a}, & \text{at } |y| < b \text{ and } |x| < a/2 \\ 0, & \text{elsewhere} \end{cases} \quad (4.15)$$

and

$$\mathbf{r}_{kj}^x = j a \hat{x} + (k + \frac{1}{2}) b \hat{y}, \quad (4.16)$$

$$\mathbf{r}_{kj}^y = (j + \frac{1}{2}) a \hat{x} + k b \hat{y}. \quad (4.17)$$

and  $V_{kj}^x$  and  $V_{kj}^y$  is the value of the voltage at the cell of coordinate  $j - k$  in the  $x$  or  $y$  direction.

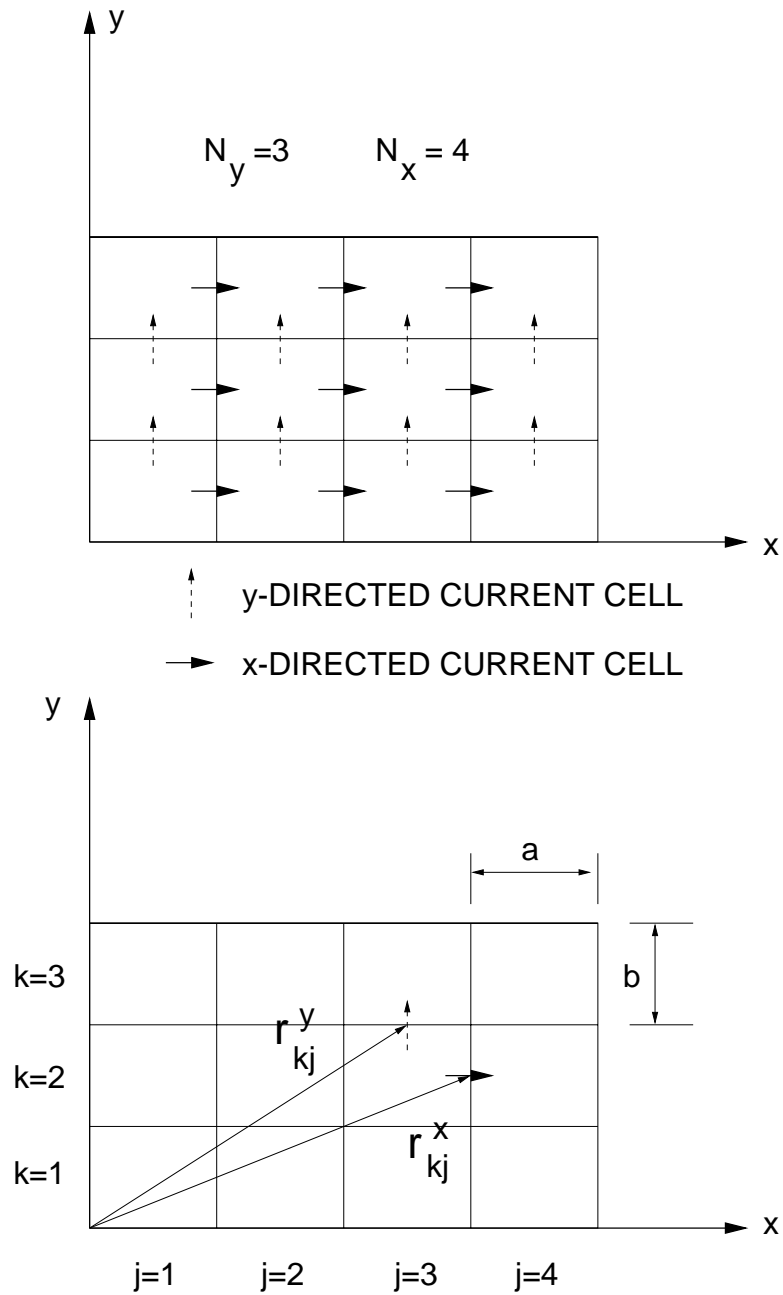


Figure 4.2: Discretization of aperture surface.

The introduction of the factors  $1/a$  and  $1/b$  in (4.14) and (4.15) yields unknown coefficients  $V_{kj}^x$  and  $V_{kj}^y$  having dimensions of voltage. Moreover, every coefficient gives the voltage across the common boundary of two charge cells.

The associated magnetic surface charge density is obtained from (4.12) and (4.13) by using the continuity equation, yielding

$$\rho_m(\mathbf{r}) = \frac{1}{j\omega} \left( \sum_{k=1}^{N_y} \sum_{j=1}^{N_x-1} V_{kj}^x \Pi_x(\mathbf{r} - \mathbf{r}_{kj}^x) + \sum_{k=1}^{N_y-1} \sum_{j=1}^{N_x} V_{kj}^y \Pi_y(\mathbf{r} - \mathbf{r}_{kj}^y) \right) \quad (4.18)$$

where  $\Pi(\mathbf{r})$  is two-dimensional unit pulse function defined over a rectangular of dimensions  $a \times b$  and centered at  $\mathbf{r} = 0$  (Fig. 4.3).

$$\Pi_x(\mathbf{r}) = \begin{cases} \frac{-1}{ab}, & \text{at } -a < x < 0 \text{ and } |y| < b/2 \\ \frac{1}{ab}, & \text{at } 0 < x < a \text{ and } |y| < b/2 \\ 0, & \text{elsewhere} \end{cases} \quad (4.19)$$

$$\Pi_y(\mathbf{r}) = \begin{cases} \frac{-1}{ab}, & \text{at } -b < y < 0 \text{ and } |x| < a/2 \\ \frac{1}{ab}, & \text{at } 0 < y < b \text{ and } |x| < a/2 \\ 0, & \text{elsewhere} \end{cases} \quad (4.20)$$

The charge density within every elementary cell remains constant. For the charge cell of Fig. 4.3, the magnetic surface charge density is simply given by

$$\rho_m(\mathbf{r}) = \frac{1}{j\omega} [V_{k,j+1}^x - V_{k,j}^x + V_{k+1,j}^y - V_{k,j}^y] \quad (4.21)$$

The magnetic charge density is discontinuous on the borders between charge cells. The electric scalar potential remains bounded, while the magnetic field becomes singular. this means that the test function must be selected carefully, avoiding the locations where the magnetic field is singular [155].

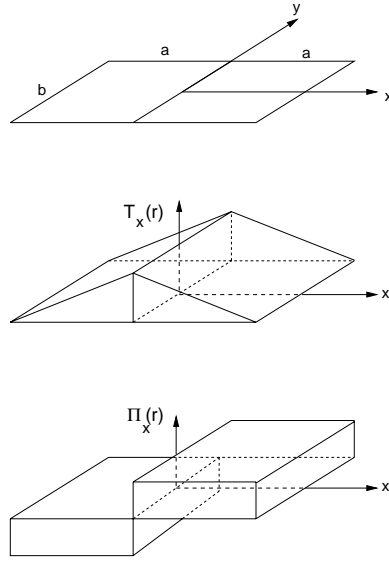


Figure 4.3:  $x$ -directed current cell centered at  $r = 0$  and its associate surface current density  $T_x(\mathbf{r})$ , and surface charge density  $\Pi_x(\mathbf{r})$ .

### 4.3.3 Test Functions and Integral Equation Formulation

The next step of the resolution with MoM is the selection of suitable test function. The most adequate choice, more accurate, and more compatible with the basis functions selected, is the use of the same basis function as a test functions. This is known as Galerkin's technique. Testing the boundary conditions on the aperture will be in two directions,  $x$ -direction using  $T_x(\mathbf{r} - \mathbf{r}_{nm}^x)$  and  $y$ -direction using  $T_y(\mathbf{r} - \mathbf{r}_{nm}^y)$ . Since we discretize the aperture to cells and we have the fields as

$$j\omega F_x + (\nabla\psi)_x = -\Delta H_x^e \quad (4.22)$$

$$j\omega F_y + (\nabla\psi)_y = -\Delta H_y^e \quad (4.23)$$

$$\mathbf{F}(\mathbf{r}) = \hat{x} \sum_{k=1}^{N_y} \sum_{j=1}^{N_x-1} V_{kj}^x \int_{S_{kj}} G_{F_{xx}}(\mathbf{r}, \mathbf{r}') T_x(\mathbf{r}' - \mathbf{r}_{kj}^x) dS'$$

$$+\hat{y} \sum_{k=1}^{N_y-1} \sum_{j=1}^{N_x} V_{kj}^y \int_{S_{kj}} G_{F_{xx}}(\mathbf{r}, \mathbf{r}') T_y(\mathbf{r}' - \mathbf{r}_{kj}^y) dS' \quad (4.24)$$

$$\begin{aligned} \psi(\mathbf{r}) = & \frac{1}{j\omega} \left[ \sum_{k=1}^{N_y} \sum_{j=1}^{N_x-1} V_{kj}^x \int_{S_{kj}} G_\psi(\mathbf{r}, \mathbf{r}') \Pi_x(\mathbf{r}' - \mathbf{r}_{kj}^x) dS' \right. \\ & \left. + \sum_{k=1}^{N_y-1} \sum_{j=1}^{N_x} V_{kj}^y \int_{S_{kj}} G_\psi(\mathbf{r}, \mathbf{r}') \Pi_y(\mathbf{r}' - \mathbf{r}_{kj}^y) dS' \right] \end{aligned} \quad (4.25)$$

$$j\omega \langle F_x, T_x^{nm} \rangle + \langle (\nabla\psi)_x, T_x^{nm} \rangle = \langle -H_x, T_x^{nm} \rangle \quad (4.26)$$

$$j\omega \langle F_y, T_y^{nm} \rangle + \langle (\nabla\psi)_y, T_y^{nm} \rangle = \langle -H_y, T_y^{nm} \rangle \quad (4.27)$$

Where  $\langle, \rangle$  denote the inner product and

$$T_x^{nm} = T_x(\mathbf{r} - \mathbf{r}_{nm}^x) \quad (4.28)$$

$$T_y^{nm} = T_y(\mathbf{r} - \mathbf{r}_{nm}^y) \quad (4.29)$$

## 4.4 Matrix Equation

Introducing the expansions (4.24) and (4.25) into (4.26) and (4.27) yields the following system of equations.

$$\begin{aligned} \sum_{k=1}^{N_y} \sum_{j=1}^{N_x-1} Y_{mn,kj}^{xx} V_{kj}^x + \sum_{k=1}^{N_x} \sum_{j=1}^{N_y-1} Y_{mn,kj}^{xy} V_{kj}^y = I_{mn}^{x-exc}; \\ m = 1, \dots, N_y \quad ; \quad n = 1, \dots, (N_x - 1) \end{aligned} \quad (4.30)$$

$$\begin{aligned} \sum_{k=1}^{N_y} \sum_{j=1}^{N_x-1} Y_{mn,kj}^{yx} V_{kj}^x + \sum_{k=1}^{N_x} \sum_{j=1}^{N_y-1} Y_{mn,kj}^{yy} V_{kj}^y = I_{mn}^{y-exc}; \\ m = 1, \dots, N_x \quad ; \quad n = 1, \dots, (N_y - 1) \end{aligned} \quad (4.31)$$

where

$$Y_{mn,kj}^{xx} = j\omega \int_{S_{mn}} T_x^{mn}(\mathbf{r}) \int_{S_{kj}} G_{F_{xx}}(\mathbf{r}; \mathbf{r}') T_x^{kj}(\mathbf{r}') dS' dS + \frac{1}{j\omega} \int_{S_{mn}} \Pi_x^{mn}(\mathbf{r}) \int_{S_{kj}} G_\psi(\mathbf{r}; \mathbf{r}') \Pi_x^{kj}(\mathbf{r}') dS' dS. \quad (4.32)$$

$$Y_{mn,kj}^{yy} = j\omega \int_{S_{mn}} T_y^{mn}(\mathbf{r}) \int_{S_{kj}} G_{F_{yy}}(\mathbf{r}; \mathbf{r}') T_y^{kj}(\mathbf{r}') dS' dS + \frac{1}{j\omega} \int_{S_{mn}} \Pi_y^{mn}(\mathbf{r}) \int_{S_{kj}} G_\psi(\mathbf{r}; \mathbf{r}') \Pi_y^{kj}(\mathbf{r}') dS' dS. \quad (4.33)$$

$$Y_{mn,kj}^{xy} = \frac{1}{j\omega} \int_{S_{mn}} \Pi_x^{mn}(\mathbf{r}) \int_{S_{kj}} G_\psi(\mathbf{r}; \mathbf{r}') \Pi_y^{kj}(\mathbf{r}') dS' dS. \quad (4.34)$$

$$Y_{mn,kj}^{yx} = \frac{1}{j\omega} \int_{S_{mn}} \Pi_y^{mn}(\mathbf{r}) \int_{S_{kj}} G_\psi(\mathbf{r}; \mathbf{r}') \Pi_x^{kj}(\mathbf{r}') dS' dS. \quad (4.35)$$

$$I_{mn}^{x-exc} = - \int_{S_{mn}} \Delta H_x^e(\mathbf{r}) T_x^{mn}(\mathbf{r}) dS. \quad (4.36)$$

$$I_{mn}^{y-exc} = - \int_{S_{mn}} \Delta H_y^e(\mathbf{r}) T_y^{mn}(\mathbf{r}) dS. \quad (4.37)$$

This system of linear equations, in which the magnetic currents (voltages) are the unknown, can be put it in matrix form which relates the vectors of the unknown magnetic currents on the aperture ( $\mathbf{V}^x$  and  $\mathbf{V}^y$ ) to the excitation vectors ( $\mathbf{I}^{x-exc}$  and  $\mathbf{I}^{y-exc}$ ) by the admittance matrix given by

$$\begin{bmatrix} \mathbf{Y}^{xx} & \mathbf{Y}^{xy} \\ \mathbf{Y}^{yx} & \mathbf{Y}^{yy} \end{bmatrix} \begin{bmatrix} \mathbf{V}^x \\ \mathbf{V}^y \end{bmatrix} = \begin{bmatrix} \mathbf{I}^{x-exc} \\ \mathbf{I}^{y-exc} \end{bmatrix} \quad (4.38)$$

In this form the sub-matrix the  $\mathbf{Y}^{uv}$  represents the coupling effect of the  $v$  directed cells on the  $u$  directed cells. Since the Green's functions are symmetric then the  $\mathbf{Y}^{yx}$  will be the transpose of the  $\mathbf{Y}^{xy}$  and

$$Y_{mn,kj}^{yx} = Y_{kj,mn}^{xy} \quad (4.39)$$

## 4.5 Spectral Domain Matrix Elements

By using the dyadic Green's functions in the spectral domain given in Sections 3.7.1–3.7.3, the moment matrix elements are found by inserting the spectral domain dyadic components as

$$Y_{nm,kj}^{xx} = \frac{-1}{4\pi^2} \int_{-\infty}^{\infty} \int_{-\infty}^{\infty} \tilde{G}_{HM_{xx}}(k_x, k_y) \tilde{T}_x^{mn}(k_x, k_y)^* \tilde{T}_x^{kj}(k_x, k_y) dk_x dk_y \quad (4.40)$$

$$Y_{nm,kj}^{xy} = \frac{-1}{4\pi^2} \int_{-\infty}^{\infty} \int_{-\infty}^{\infty} \tilde{G}_{HM_{xy}}(k_x, k_y) \tilde{T}_x^{nm}(k_x, k_y)^* \tilde{T}_y^{kj}(k_x, k_y) dk_x dk_y \quad (4.41)$$

$$Y_{nm,kj}^{yx} = \frac{-1}{4\pi^2} \int_{-\infty}^{\infty} \int_{-\infty}^{\infty} \tilde{G}_{HM_{yx}}(k_x, k_y) \tilde{T}_y^{nm}(k_x, k_y)^* \tilde{T}_x^{kj}(k_x, k_y) dk_x dk_y \quad (4.42)$$

$$Y_{nm,kj}^{yy} = \frac{-1}{4\pi^2} \int_{-\infty}^{\infty} \int_{-\infty}^{\infty} \tilde{G}_{HM_{yy}}(k_x, k_y) \tilde{T}_y^{nm}(k_x, k_y)^* \tilde{T}_y^{kj}(k_x, k_y) dk_x dk_y \quad (4.43)$$

where  $\tilde{T}_x$  and  $\tilde{T}_y$  are the Fourier transforms of the  $x$ - and  $y$ -directed rooftop basis functions, respectively, and the  $(*)$  denotes the complex conjugate. One of the advantages of using the spectral domain is that the Fourier transforms of the basis functions can be evaluated in closed form as follows:

$$\begin{aligned} \tilde{T}_x^{kj}(k_x, k_y) &= \int_{y_{kj}-\frac{b}{2}}^{y_{kj}+\frac{b}{2}} \int_{x_{kj}-a}^{x_{kj}+a} T_x^{kj}(\mathbf{r}) e^{-jk_x x} e^{-jk_y y} dx dy \\ &= a \left[ \frac{\sin(k_x a/2)}{(k_x a/2)} \right]^2 \left[ \frac{\sin(k_y b/2)}{(k_y b/2)} \right] e^{-jk_x x_{kj}} e^{-jk_y y_{kj}} \end{aligned} \quad (4.44)$$

$$\begin{aligned} \tilde{T}_y^{kj}(k_x, k_y) &= \int_{y_{kj}-b}^{y_{kj}+b} \int_{x_{kj}-\frac{a}{2}}^{x_{kj}+\frac{a}{2}} T_y^{kj}(\mathbf{r}) e^{-jk_x x} e^{-jk_y y} dx dy \\ &= b \left[ \frac{\sin(k_y b/2)}{(k_y b/2)} \right]^2 \left[ \frac{\sin(k_x a/2)}{(k_x a/2)} \right] e^{-jk_x x_{kj}} e^{-jk_y y_{kj}}. \end{aligned} \quad (4.45)$$

The moment matrix elements given in (4.40)–(4.43) now only involve two integrations but are of infinite limits. By using the even and odd properties of the integrand in (4.40)–(4.43), further simplifications can be made as follows [146, 167]:

$$Y_{nm,kj}^{xx} = \frac{-1}{\pi^2} \int_0^{\infty} \int_0^{\infty} \tilde{G}_{HM_{xx}}(k_x, k_y) F_{nm,kj}^{xx}(k_x, k_y) dk_x dk_y \quad (4.46)$$

$$Y_{nm,kj}^{yy} = \frac{-1}{\pi^2} \int_0^\infty \int_0^\infty \tilde{G}_{HM_{yy}}(k_x, k_y) F_{nm,kj}^{yy}(k_x, k_y) dk_x dk_y \quad (4.47)$$

$$Y_{nm,kj}^{xy} = \frac{-1}{\pi^2} \int_0^\infty \int_0^\infty \tilde{G}_{HM_{xy}}(k_x, k_y) F_{nm,kj}^{xy}(k_x, k_y) dk_x dk_y \quad (4.48)$$

$$Y_{nm,kj}^{yx} = Y_{kj,nm}^{xy} \quad (4.49)$$

where

$$\begin{aligned} F_{nm,kj}^{xx}(k_x, k_y) &= a^2 \left[ \frac{\sin(k_x a/2)}{(k_x a/2)} \right]^4 \left[ \frac{\sin(k_y b/2)}{(k_y b/2)} \right]^2 \\ &\cdot \cos[k_x(x_{nm} - x_{kj})] \cos[k_y(y_{nm} - y_{kj})] \end{aligned} \quad (4.50)$$

$$\begin{aligned} F_{nm,kj}^{yy}(k_x, k_y) &= b^2 \left[ \frac{\sin(k_x b/2)}{(k_x b/2)} \right]^4 \left[ \frac{\sin(k_y a/2)}{(k_y a/2)} \right]^2 \\ &\cdot \cos[k_x(x_{nm} - x_{kj})] \cos[k_y(y_{nm} - y_{kj})] \end{aligned} \quad (4.51)$$

$$\begin{aligned} F_{nm,kj}^{xy}(k_x, k_y) &= ab \left[ \frac{\sin(k_x a/2)}{(k_x a/2)} \right]^3 \left[ \frac{\sin(k_y b/2)}{(k_y b/2)} \right]^3 \\ &\cdot \sin[k_x(x_{nm} - x_{kj})] \sin[k_y(y_{nm} - y_{kj})]. \end{aligned} \quad (4.52)$$

The products of  $(\tilde{T}_x)(\tilde{T}_x)^*$ ,  $(\tilde{T}_y)(\tilde{T}_x)^*$ ,  $(\tilde{T}_x)(\tilde{T}_y)^*$ , and  $(\tilde{T}_y)(\tilde{T}_y)^*$  result in complex functions where the real parts are even functions and the imaginary parts are odd functions. Since  $\tilde{G}_{HM_{xx}}$  and  $\tilde{G}_{HM_{yy}}$  are even functions about the origin of the  $k_x, k_y$  space, only the real part of the products of  $(\tilde{T}_x)(\tilde{T}_x)^*$  and  $(\tilde{T}_y)(\tilde{T}_y)^*$  show up in  $F^{xx}$  and  $F^{yy}$ , respectively. The imaginary part of the products are odd functions which results in an odd integrand that integrates to zero over the  $k_x, k_y$  space. Similarly  $\tilde{G}_{HM_{xy}}$  is an odd function so only the imaginary part of the product of  $(\tilde{T}_x)(\tilde{T}_y)^*$  shows up in  $F^{xy}$ . Also the product of  $(\tilde{T}_y)(\tilde{T}_x)^*$  is equal to  $(\tilde{T}_x)(\tilde{T}_y)^*$ .

The integration is done only over the first quadrant of  $k_x, k_y$  space but still contains two upper limits that go to infinity. Changing the integration in (4.46)–(4.49) to polar coordinates will eliminate one of the infinite upper limits [146, 167].

The final moment matrix elements that will be numerically evaluated are given in polar coordinates as follows:

$$Y_{nm,kj}^{xx} = \frac{-1}{\pi^2} \int_0^{\pi/2} \int_0^\infty \tilde{G}_{HM_{xx}}(k_x, k_y) F_{nm,kj}^{xx}(k_x, k_y) \beta d\beta d\alpha \quad (4.53)$$

$$Y_{nm,kj}^{yy} = \frac{-1}{\pi^2} \int_0^{\pi/2} \int_0^\infty \tilde{G}_{HM_{yy}}(k_x, k_y) F_{nm,kj}^{yy}(k_x, k_y) \beta d\beta d\alpha \quad (4.54)$$

$$Y_{nm,kj}^{xy} = \frac{-1}{\pi^2} \int_0^{\pi/2} \int_0^\infty \tilde{G}_{HM_{xy}}(k_x, k_y) F_{nm,kj}^{xy}(k_x, k_y) \beta d\beta d\alpha \quad (4.55)$$

$$Y_{nm,kj}^{yx} = Y_{nm,kj}^{xy} \quad (4.56)$$

where

$$k_x = \beta \cos \alpha \quad (4.57)$$

$$k_y = \beta \sin \alpha. \quad (4.58)$$

## 4.6 Excitation

In general there are two types of excitation. The simplest kind of excitation of slot antenna is provided by a plane wave incident on the aperture. This excitation is suitable when the antenna is used as a receiver and utilized to calculate the radiation pattern. For transmitting antennas, more complex excitation model is necessary. Coaxial probe or delta source excitation can be used as an excitation model for the transmitting antenna. In this section we will discuss these different types of excitation and their mathematical models.

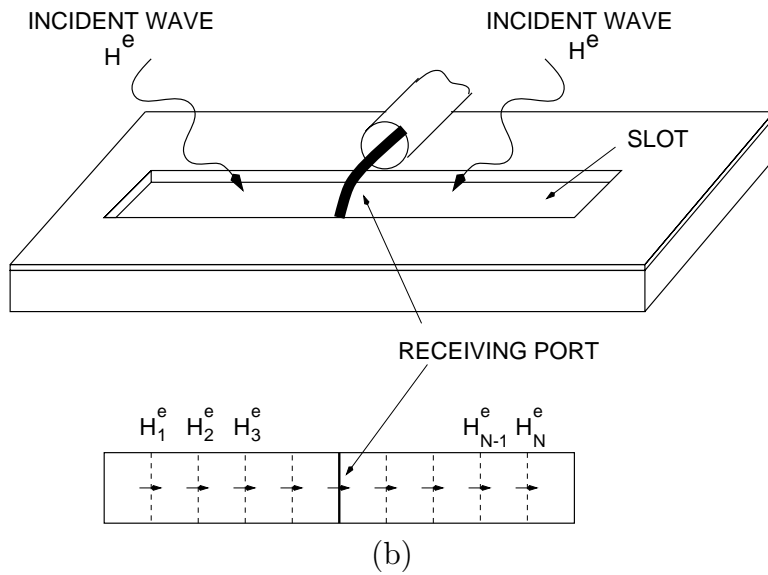
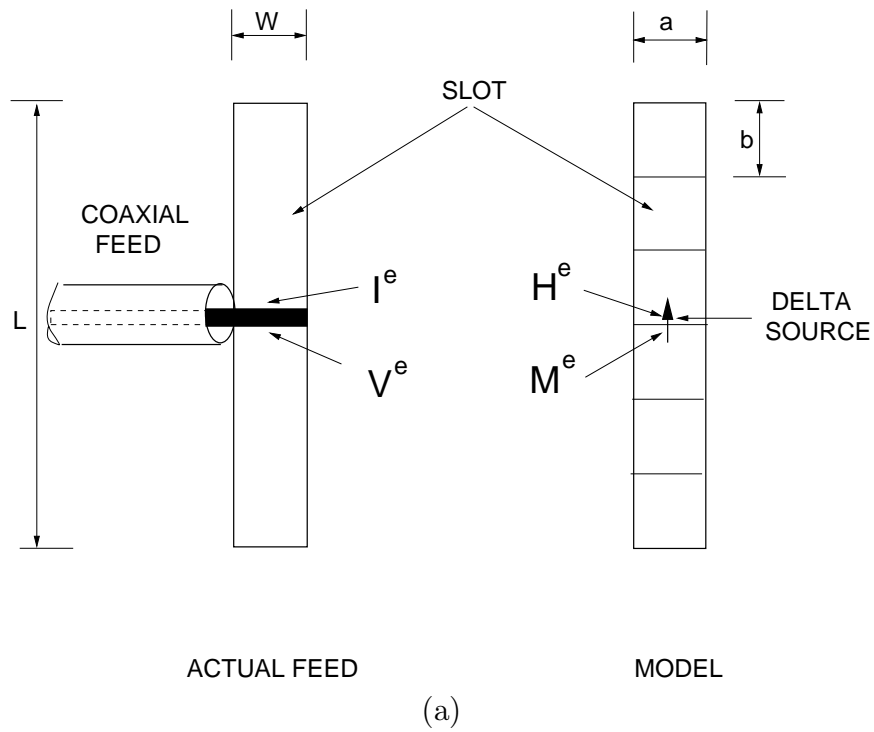


Figure 4.4: Excitation mechanism:(a) transmitting mode ; (a) receiving mode .

### 4.6.1 Incident Wave Excitation

In case of the incident wave excitation the excitation vector elements are derived as

$$I_{mn}^{x-exc} = - \int_{S_{mn}} \Delta H_x^e(\mathbf{r}) T_x^{mn}(\mathbf{r}) dS. \quad (4.59)$$

$$I_{mn}^{y-exc} = - \int_{S_{mn}} \Delta H_y^e(\mathbf{r}) T_y^{mn}(\mathbf{r}) dS. \quad (4.60)$$

where  $\Delta H_x^e$  and  $\Delta H_y^e$  are the excitation magnetic field at the slot surfaces.

### 4.6.2 Coaxial Probe Excitation

The coaxial current probe offers a more realistic method to excite electric fields on a slot antenna [146]. The coaxial probe is connected through the ground plane with the center conductor embedded horizontally and terminated on the other metal surface, where the outer conductor of the coax is connected to the ground plane. Fig. 4.4(a) shows the attachment of the coaxial probe to the slot antenna surface. The current flowing on the inner conductor of the coaxial probe is assumed to be constant with an amplitude of  $I_F$  Amp.

A delta-gap current generator is a simplistic source which is commonly used in MoM analysis of wire antennas [201]. Although such sources do not exist in practice, they do give good approximation to the probe feeding.

Fig. 4.4 (a) shows the implementation of a coaxial probe as a delta-gap voltage generator where a current source is placed between two cells, in a fictitious gap, giving rise to an impressed magnetic field  $\Delta H_x^{inc} = I_F/b$  confined entirely to the gap. Assume that  $I_F = 1$  Amp the excitation vector will be zeros except the value corresponding to the current cell where the coaxial probe is located. This excitation value is given by

$$I_{mn}^{x-e} = - \int_{S_{mn}} \Delta H_x^{inc}(\mathbf{r}) T_x^{mn}(\mathbf{r}) dS \quad (4.61)$$

## 4.7 Network Characterization and Port Definition

The MoM admittance matrix of the slot system, with electrical ports at the location of the active devices inserted in the slot, includes the interactions associated with the port and non-port magnetic current cells. we are interested in the reduced port impedance matrix and these ports are differential ports located on the slot at the interface of longitudinally adjacent MoM cells Fig. 4.5 (a). After rewriting the excitation vectors in terms of port currents and separate between the port cells and non port cells and then (4.38) can be expressed as

$$\begin{bmatrix} \mathbf{Y}^{cc} & \mathbf{Y}^{ct} \\ \mathbf{Y}^{tc} & \mathbf{Y}^{tt} \end{bmatrix} \begin{bmatrix} \mathbf{V}^c \\ \mathbf{V}^t \end{bmatrix} = \begin{bmatrix} \mathbf{0} \\ \mathbf{I}^t \end{bmatrix} \quad (4.62)$$

Here superscript  $t$  denotes terminal port quantities and superscript  $c$  denotes quantities pertinent to magnetic currents induced on the slot surface. The excitation vector  $\mathbf{I}^t$  is due to the delta-gap current generators at each port. (4.62) defines the complete moment matrix, which includes the interactions associated with the non-port magnetic currents. However, we are interested in the reduced port impedance matrix, from which one can infer the coupling coefficients between terminal ports. We will now find these network matrices for the ports. We obtain the voltages from (4.62) as

$$\begin{bmatrix} \mathbf{V}^c \\ \mathbf{V}^t \end{bmatrix} = \begin{bmatrix} \mathbf{Y}^{cc} & \mathbf{Y}^{ct} \\ \mathbf{Y}^{tc} & \mathbf{Y}^{tt} \end{bmatrix}^{-1} \begin{bmatrix} \mathbf{0} \\ \mathbf{I}^t \end{bmatrix} \quad (4.63)$$

$$= \begin{bmatrix} \mathbf{Z}^{cc} & \mathbf{Z}^{ct} \\ \mathbf{Z}^{tc} & \mathbf{Z}^{tt} \end{bmatrix} \begin{bmatrix} \mathbf{0} \\ \mathbf{I}^t \end{bmatrix}. \quad (4.64)$$

From (4.64), we identify the *reduced port impedance matrix*  $\mathbf{Z}^t = \mathbf{Z}^{tt}$ , since  $\mathbf{V}^t = \mathbf{Z}^t \mathbf{I}^t$  from circuit theory.  $\mathbf{Z}^t$  is used as an equivalent circuit for the passive antenna

structure Fig.4.5(b).

## 4.8 Computational Details and Numerical Considerations

The program developed in this dissertation uses a numerical Gaussian quadrature integration routine for the double and quadruple integrations required for computing the moment matrix elements. The MoM solution is computed using LU decomposition and double precision is used in all calculations. Techniques for computing the singular self elements using spectral domain moment matrix reactions and convergence issues are present next along with the moment matrix conditioning. The valid frequency ranges for the moment method simulator are also discussed.

### 4.8.1 Self and Overlapped Cell MoM Matrix Elements

When the observation point belongs to the source cell, the Green's function becomes singular as  $\rho \rightarrow 0$ . Some difficulties arise in the integration process. Using the spectral domain Green's function is an efficient way to calculate these singular elements. The self and overlapped cells MoM matrix elements are calculated using the spectral domain. The numerical integration of these MoM elements given in (4.53)–(4.56) are best handled by dividing the integral into two parts [146, 167, 153],

$$Y_f = \frac{-1}{\pi^2} \left[ \int_0^{\pi/2} \int_0^{k_0} \tilde{G}F \beta d\beta d\alpha + \int_0^{\pi/2} \int_{k_0}^{\infty} \tilde{G}F \beta d\beta d\alpha \right]. \quad (4.65)$$

At  $\beta = k_0$  the integrand of (4.53)–(4.56) has a zero in the denominator. This is not a singularity because it can easily be shown that the integrand has a limit at  $\beta = k_0$ . In the first integral in (4.65) the  $\beta$  variable ranges from 0 to  $k_0$  and in the second integral in (4.65) the  $\beta$  variable ranges from  $k_0$  to  $\infty$ . By keeping  $\beta = k_0$  as an endpoint in both integrals, this point is never computed when using a

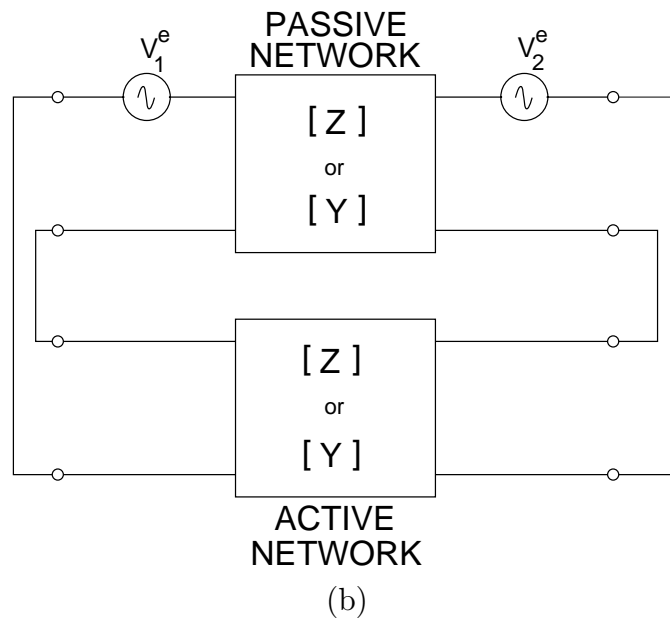
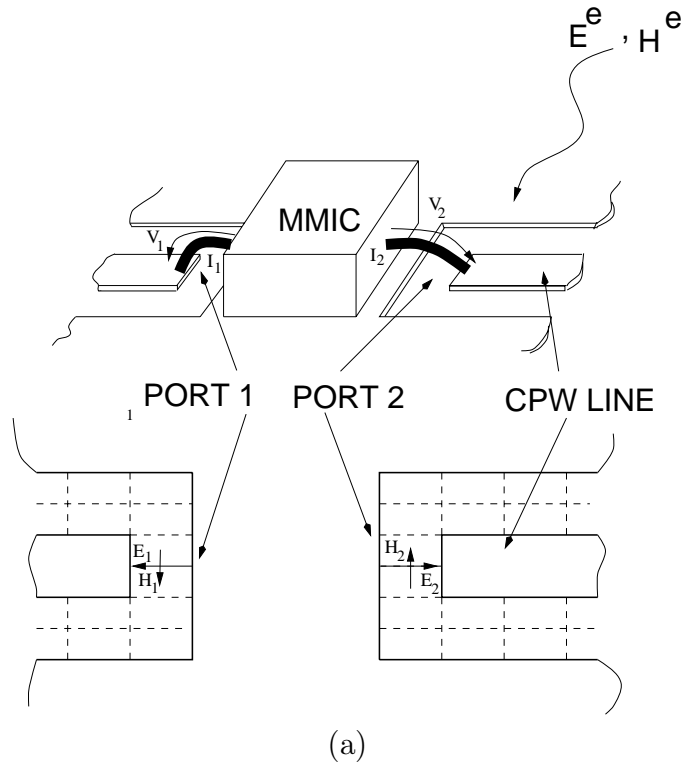


Figure 4.5: Extraction of passive structure parameters; (a) real active antenna ; (b) circuit model.

Gaussian quadrature numerical integration routine. Also in the range  $0 < \beta < k_0$ , the moment matrix elements have both real and imaginary terms whereas in the range  $k_0 < \beta < \infty$ , they only have imaginary terms. The infinite upper limit can be truncated at  $50k_0$  for the self-terms and  $100k_0$  for all the other terms [167].

### 4.8.2 Solution of Linear Systems

The system of linear equations (4.38) is solved by standard Gaussian elimination. The  $\mathbf{Y}$  matrix is ill-conditioned, so that careful evaluation of its elements is needed. This matrix is diagonal dominated, so the accuracy requirements may be relaxed for the off-diagonal elements. Fig.4.6 shows the  $\mathbf{Y}$  matrix for slot dipole antenna at  $31 \times 31$  elements whereas Fig.4.7 shows its inversion.

The root of the complex determinant of the MoM matrix yields the resonant frequencies, which are, in general, complex (they correspond to open radiating structure). On the real frequency axis, the determinant does not vanish, but goes through sharp minima at the points closest to the complex root. The condition number of the matrix is used to locate the resonances.

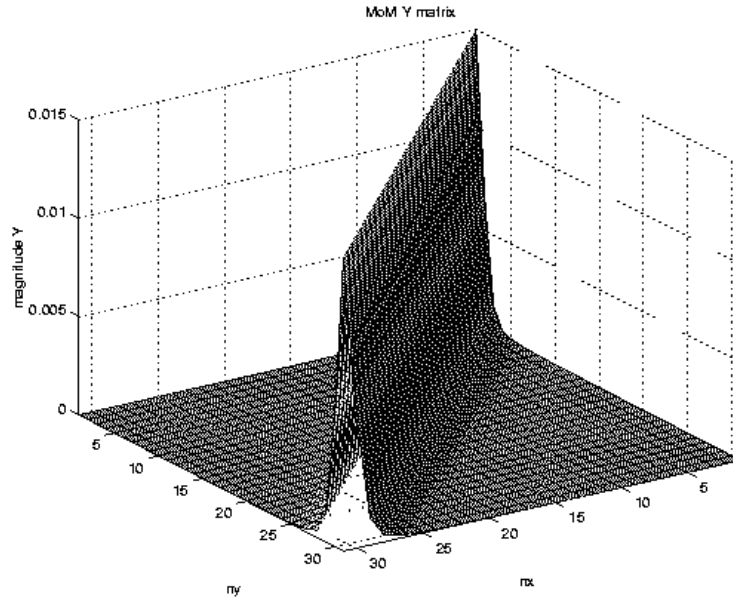
### 4.8.3 Condition Number

One other numerical concern is the condition number of the moment matrix. The condition number is computed as follows:

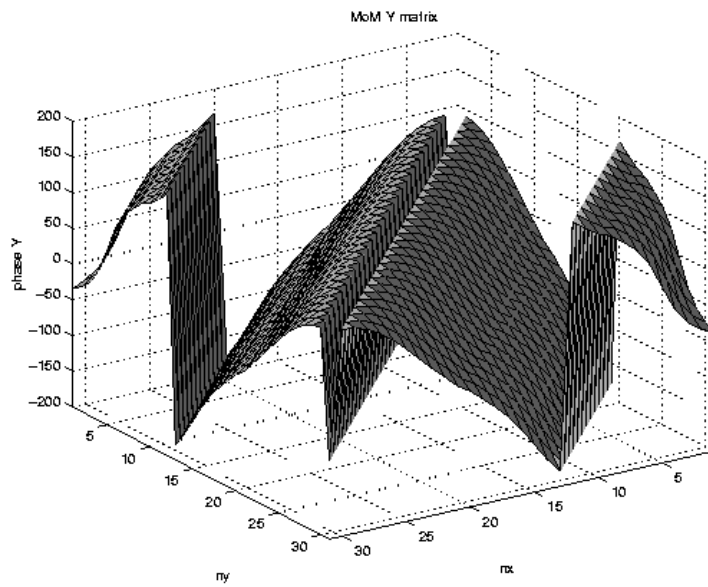
$$\text{COND}(\mathbf{Y}) = \|\mathbf{Y}\| \|\mathbf{Z}\| \quad (4.66)$$

where

$$\|\mathbf{Y}\| = \max_j \sum_i |y_{ij}| \quad (4.67)$$

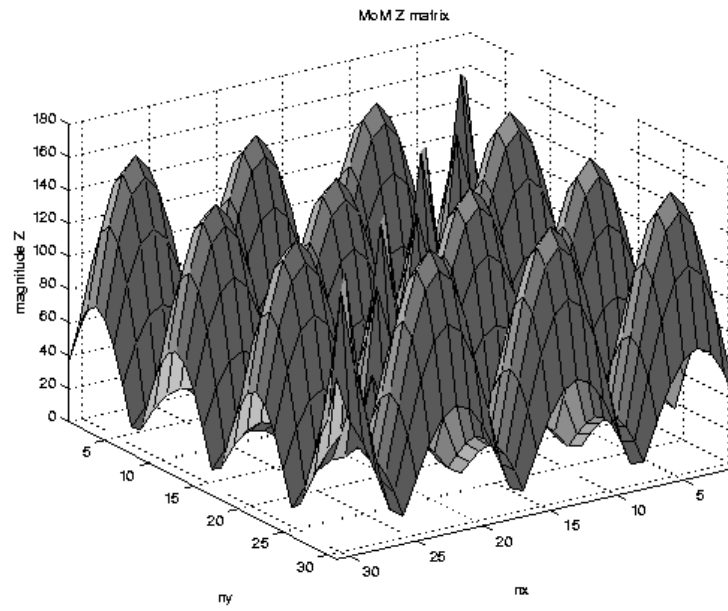


(a)

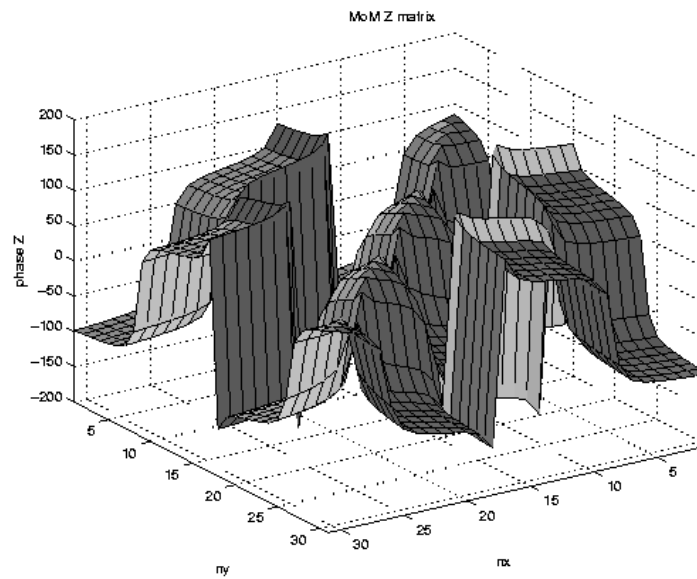


(b)

Figure 4.6: The MoM admittance matrix elements for  $31 \times 31$  matrix: (a) magnitude; (b) phase.



(a)



(b)

Figure 4.7: MoM impedance matrix elements for  $31 \times 31$  matrix: (a) magnitude; (b) phase.

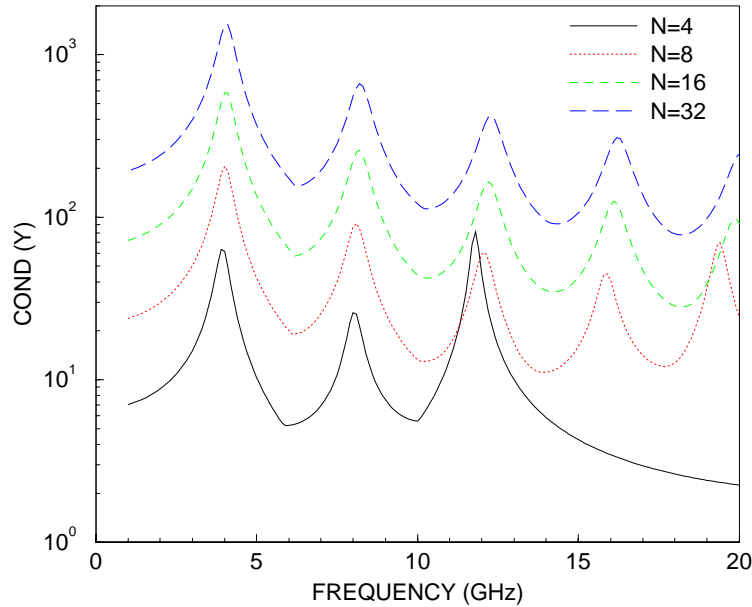


Figure 4.8: Condition number of the moment matrix.

and

$$\|\mathbf{Z}\| = \max_j \sum_i |z_{ij}| \quad (4.68)$$

with  $\mathbf{Y}$  being the moment matrix and  $\mathbf{Z}$  being the inverted moment matrix. For a well-conditioned matrix the condition number ranges from 1 to 1000 with 1 being the best. Above 1000 the matrix becomes ill-conditioned. Fig. 4.8 shows the condition number of the moment matrix for several cell subdivisions of the slot dipole antenna. In all cases the condition number is almost below 1000. The peaks in Fig. 4.8 correspond to half-wavelength multiples of the slot dipole antenna. If the moment matrix were to become ill-conditioned, it would occur at a resonant frequency where the matrix becomes singular. All of the moment matrices of the structures simulated

in this dissertation are well-conditioned when using LU decomposition.

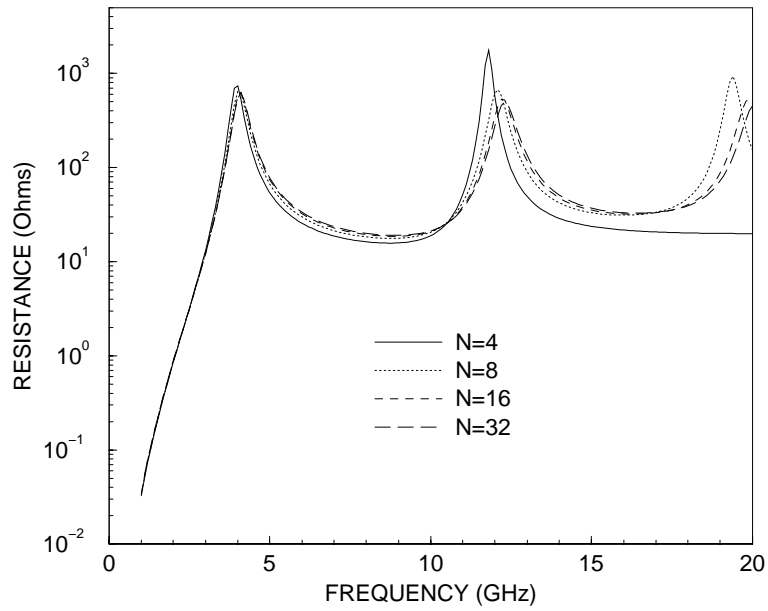
#### 4.8.4 Convergence Issues

Convergence is a big concern in MoM solutions. As a rule of thumb there should be at least 10 cell subdivisions per wavelength to obtain reliable solutions. Cell subdivisions consisting of 20 cells are often used for the most accurate solutions. Figs. 4.9 and 4.10 show the driving point impedance and reflection coefficient of a slot dipole antenna for different cell subdivisions. The slot dipole has a length of 30 mm and a width of 1 mm and the substrate thickness is 1.57 mm and relative permittivity  $\epsilon_r = 2.2$ .

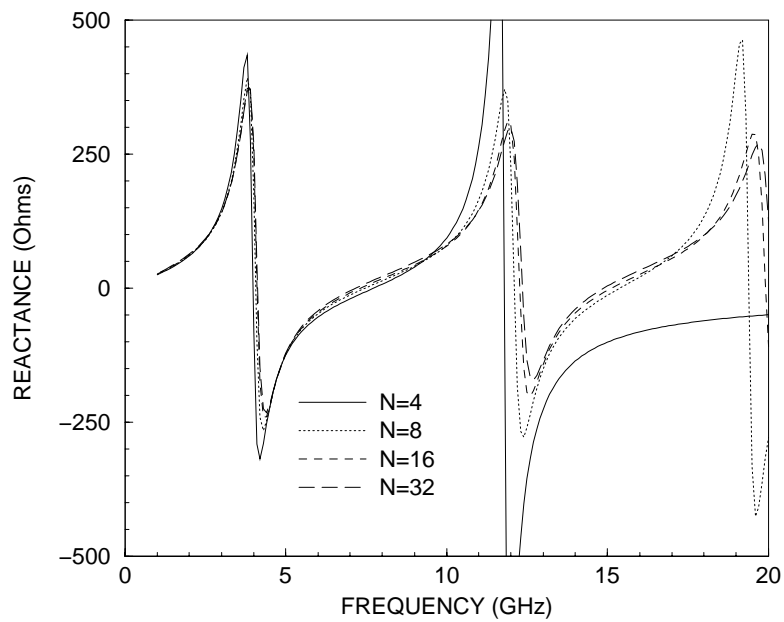
In Fig. 4.11 the convergence rate of the reflection coefficient at 5 GHz is presented. Convergence of the reflection coefficient magnitude occurs between 10 to 20 cells per wavelength and the convergence of the reflection coefficient phase occurs closer to 20 cells per wavelength. By keeping the number of cells about 20 cells per wavelength, convergence is obtained. This has been the case for all of the structures analyzed in this dissertation.

#### 4.8.5 Valid Frequency Ranges

One of the attractive features of this moment method simulator is that it can compute from DC to any frequency. It is very common for electromagnetic simulators not to work at low frequencies. The MoM cannot handle DC ( $f = 0$ ) directly but can handle any positive real number greater than zero. For example  $f = 10^{-2}$  Hz works in the MoM simulator and from Fig. 4.10 it is shown that the solution converges at DC. The upper frequency has no limit but the MoM cell subdivision is determined from the highest frequency and should obey the minimum 10 cells per

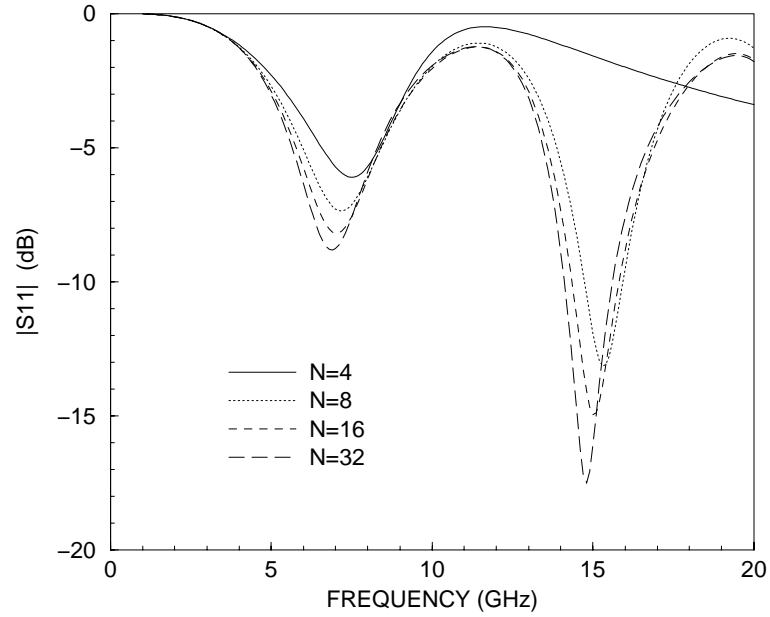


(a)

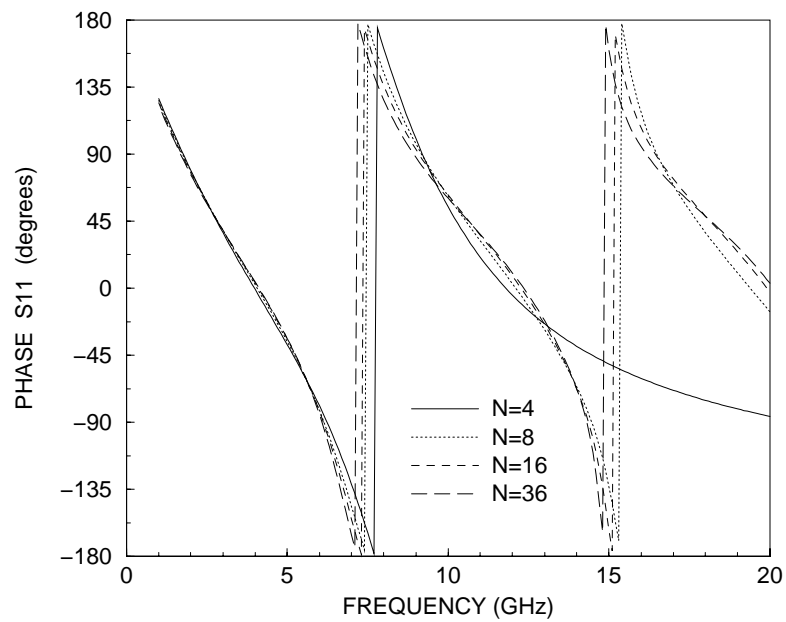


(b)

Figure 4.9: Driving point impedance of a slot dipole antenna divided into  $N$  cells: (a) resistance; (b) reactance.

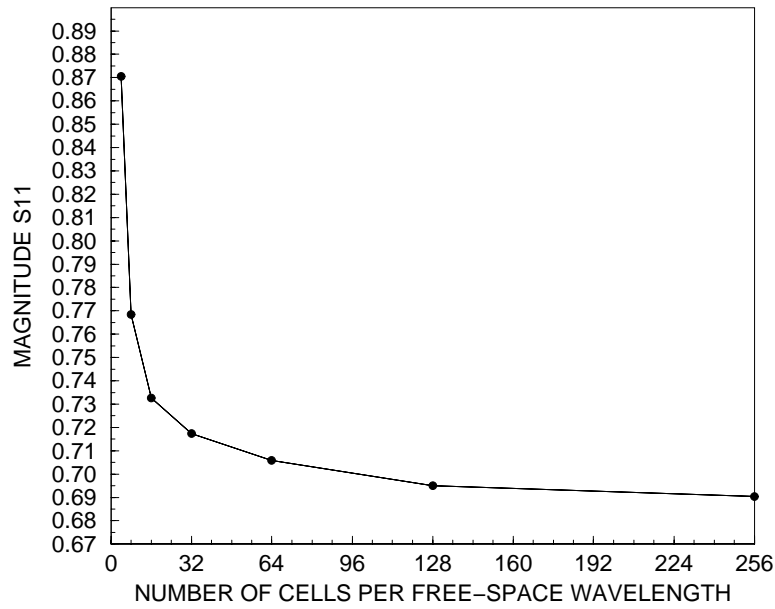


(a)

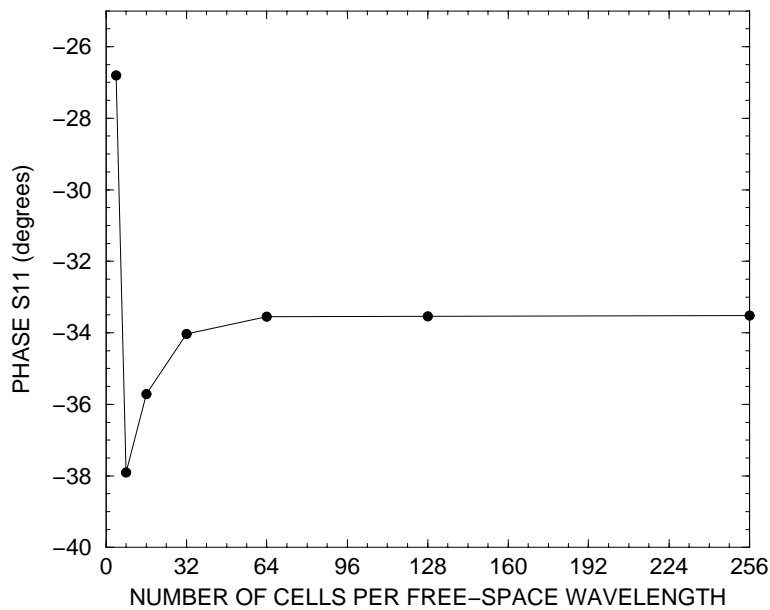


(b)

Figure 4.10: Driving point reflection coefficient of a slot dipole antenna divided into  $N$  cells: (a) magnitude; (b) phase.



(a)



(b)

Figure 4.11: Convergence rate of the driving point reflection coefficient of a slot dipole at 5 GHz: (a) magnitude; (b) phase.

wavelength requirement for convergence.

## 4.9 Radiation Pattern

Once the magnetic current on the aperture is known, the scattered field can be evaluated from

$$\mathbf{H}(\mathbf{r}) = \int_S \overline{\mathbf{G}}_H(\mathbf{r}, \mathbf{r}') \cdot \mathbf{M}_s(\mathbf{r}') dS' \quad (4.69)$$

where  $\overline{\mathbf{G}}_H$  is the magnetic field associated dyadic Green's functions. The dyadic Green's functions formulation derived in Chapter 3 can still be used to determine the far fields.

### 4.9.1 Near Field

The near-field radiated by the antenna can be obtained by assuming that we have an array of magnetic dipoles. Every current cell represents a magnetic dipole. By summing the field resulting from each dipole the total antenna near-field is obtained.

The magnetic dipole near fields are given as

$$G_{E_y M_x} = \frac{1}{2\pi} z \left[ \frac{1 + jkR}{R^2} \right] \frac{e^{-jkR}}{R} \quad (4.70)$$

$$G_{E_x M_y} = \frac{-1}{2\pi} z \left[ \frac{1 + jkR}{R^2} \right] \frac{e^{-jkR}}{R} \quad (4.71)$$

$$G_{E_z M_x} = \frac{-1}{2\pi} (y - y') \left[ \frac{1 + jkR}{R^2} \right] \frac{e^{-jkR}}{R} \quad (4.72)$$

$$G_{E_z M_y} = \frac{-1}{2\pi} (x - x') \left[ \frac{1 + jkR}{R^2} \right] \frac{e^{-jkR}}{R} \quad (4.73)$$

where

$$R = \sqrt{(x - x')^2 + (y - y')^2 + (z - z')^2} \quad (4.74)$$

### 4.9.2 Far Field

The radiated field can be obtained by evaluation of the Sommerfeld integrals. To calculate these integrations, where the condition  $k_0 r \gg 1$  is satisfied, they are evaluated asymptotically using a steepest descent technique.

The magnetic field radiated by an elementary  $x$ -directed Hertzian dipole, which corresponds to the Green's function  $\overline{\mathbf{G}}_H$ , is firstly calculated in the rectangular coordinate system. Then, using the transformation into spherical coordinate system and applying the asymptotical form of the Sommerfeld integrals, the magnetic Green's functions for the far field can be expressed as

$$G_{H_x}^r = O\left(\frac{1}{r^2}\right) \quad (4.75)$$

$$G_{H_x}^\theta = \frac{\epsilon_0 \omega}{2\pi} \cos(\theta) \cos(\phi) \left[ \cos(\theta) k_0 \frac{NX}{D_{TM}} + j \sin^2(\theta) \frac{k_0^2 NZ}{D_{TM} D_{TE}} \right] \frac{e^{(-jk_0 R)}}{R} \quad (4.76)$$

$$G_{H_x}^\phi = -\frac{\epsilon_0 \omega}{2\pi} \cos(\theta) \sin(\phi) \left[ k_0 \frac{NX}{D_{TM}} \right] \frac{e^{(-jk_0 R)}}{R} \quad (4.77)$$

where

$$NX = \begin{cases} \epsilon_r e^{(u_0 h)} / \cosh(u_1 h), & \text{for region "b"} \\ D_{TM} / u_0, & \text{for region "a"} \end{cases} \quad (4.78)$$

$$NZ = \begin{cases} (\epsilon_r - 1) e^{(u_0 h)} / \cosh(u_1 h), & \text{for region "b"} \\ 0, & \text{for region "a"} \end{cases} \quad (4.79)$$

and

$$D_{TM} = u_0 \epsilon_r + \tanh(u_1 h) \quad (4.80)$$

$$D_{TE} = u_0 + \frac{u_1}{\tanh(u_1 h)} \quad (4.81)$$

where

$$u_0 = \sqrt{\sin^2(\theta) - 1} \quad (4.82)$$

$$u_1 = \sqrt{\sin^2(\theta) - \epsilon_r}. \quad (4.83)$$

The expression of  $G_{H_y}^r$ ,  $G_{H_y}^\theta$ , and  $G_{H_y}^\phi$  can be obtained by changing  $\phi$  to  $\phi + \frac{\pi}{2}$  in (4.75), (4.76), and (4.77). The total magnetic field components radiated by the slot antenna and its feeding line for any couple of value  $(\theta, \phi)$  can be written as

$$\mathbf{H}^{dir}(\mathbf{r}) = \left[ G_{H_x}^{dir} \sum_{k=1}^{N_y} \sum_{j=1}^{N_x-1} k_0 V_{kj}^x + G_{H_y}^{dir} \sum_{k=1}^{N_y-1} \sum_{j=1}^{N_x} k_0 V_{kj}^y \right] \cdot \exp(jk_0(x \sin(\theta) \cos(\phi) + y \sin(\theta) \sin(\phi))) \quad (4.84)$$

where  $dir=\theta$  or  $\phi$  and  $k_0^2 = \omega^2 \mu_0 \epsilon_0$ .

## 4.10 Summary

This chapter was devoted to solve the MPIE for the CPW-slot structure introduced in Chapter 3. The MoM technique was used to solve the MPIE. The solution procedure and formulation was introduced and the numerical problems and difficulties have been addressed.

The self and overlapped MoM matrix elements were calculated using the spectral domain to ensure the accuracy and the calculation efficiency. The other MoM matrix elements were calculated using spatial domain. Using both spatial and spectral domains enhances the accuracy and efficiency of the MoM technique.

The condition of the MoM matrix and the convergence rate of the solution have been investigated. A cell size no longer than one tenth of a wavelength can guarantee good convergence behavior.

The technique for extracting the network parameters of the passive antenna structure was presented. This reduced matrix, the port network, is obtained from the MoM matrix. The network parameters is used in the circuit simulator for active-passive circuit simulation.

At the end of this chapter, the near- and far-field equations were presented to calculate the antenna radiation parameters such as the gain and beamwidth.

## Chapter 5

# MPIE and Green's Functions for Slot-Stripline-Slot Structure

### 5.1 Introduction

The quest for high power from solid state devices at millimeter-wave frequencies and above has created a focus on combining power from spatially distributed sources. Paralleling this is the desire to minimize metallic losses at near-terahertz frequencies by realizing circuit functions in a distributed electromagnetic environment [202]. Engineering of these systems for high volume production and reasonable cost requires a high degree of insight into their performance and consequently the ability to model circuit-field interactions.

The slot-stripline-slot (SSS) spatial power combining architecture [2] is shown in Fig. 5.1. Each dimension of this system is around two wavelengths. The amplifiers are MMIC chips arranged in an  $N \times N$  array ( a  $3 \times 3$  array is shown here for clarity) of MMIC's yielding the powers required. Each amplifying unit cell of the array amplifier is itself an amplifier with a stripline coupled slot input antenna and a similar antenna at the output. Experimental investigations of prototype systems of various implementations have shown that the interactions of cells significantly affects nonlinear stability and field patterns. These considerations require accurate electromagnetic modeling of the entire, finite-sized structure and treatment of the electromagnetic model as an integral part of the circuit [203],[204].

In this chapter, the development of the MPIE model for the SSS structure is

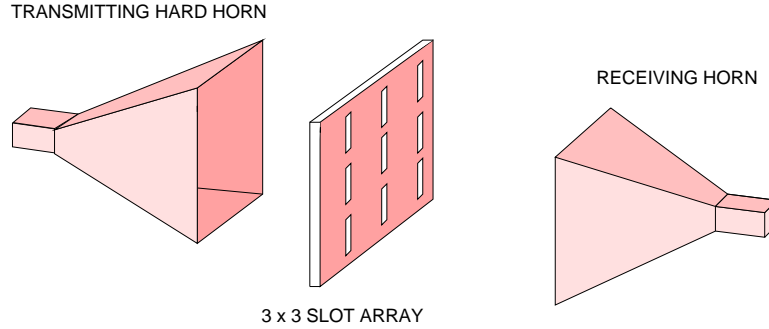


Figure 5.1: A SSS spatial power combining system, showing a simplified  $3 \times 3$  array.

presented. The electromagnetic modeling of the SSS unit cell of Fig. 5.2 begins with the development of the Green's functions. A numerically efficient technique for the potential Green's function evaluation is introduced. At the end of the chapter, the spectral domain dyadic Greens's functions required for MoM self and overlapped cells matrix elements are derived.

## 5.2 Structure Geometry and Modeling

A unit cell, shown in Fig.5.2, has a slot antenna coupled to a stripline which transmits an input signal to the input port of a MMIC inserted between referee planes 1 and 2. Using the equivalence principle [191] the center conductor at  $z = 0$  is removed and replaced by an equivalent electric surface current,  $J_s$ , see Fig. 5.3. The slots in the upper and lower planes ( $z = h$  and  $z = -h$  respectively) are removed and replaced by perfect electric conductors and the equivalent magnetic surface currents flowing at  $z = h^-$  for the upper slot and at  $z = -h^+$  for the lower slot are then

$$\mathbf{M}_u^{int} = \hat{z} \times \mathbf{E}_u \quad (5.1)$$

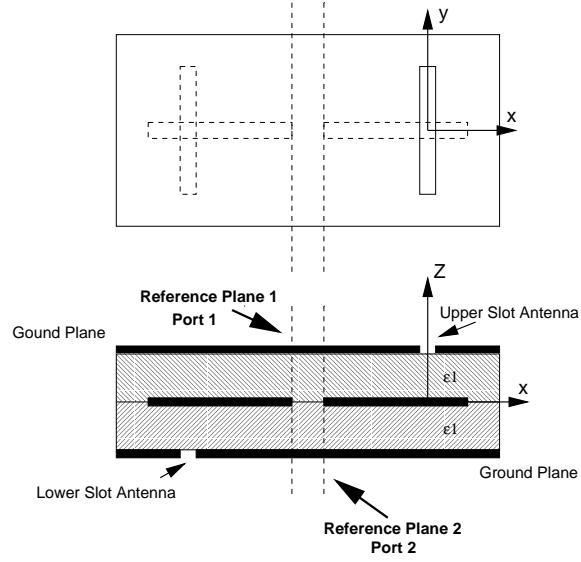


Figure 5.2: Passive SSS unit cell.

$$\mathbf{M}_l^{int} = -\hat{z} \times \mathbf{E}_l. \quad (5.2)$$

respectively. For the fields in the region  $z > h$  and  $z < -h$  the equivalent sources are magnetic surface currents flowing at  $z > h^+$  for the upper slot and in  $z < -h^-$  for the lower slot and they given by

$$\mathbf{M}_u^{ext} = -\mathbf{M}_u^{int}. \quad (5.3)$$

$$\mathbf{M}_l^{ext} = -\mathbf{M}_l^{int}. \quad (5.4)$$

respectively. The structure is decomposed into three regions as shown in Fig. 5.3 (b) and the analysis reduces to determining the induced electric and magnetic surface currents,  $\mathbf{J}_s$ ,  $\mathbf{M}_u^{int}$ , and  $\mathbf{M}_l^{int}$ . This is accomplished using a MoM formulation which solves the field integral equations whose kernels are the Green's functions.

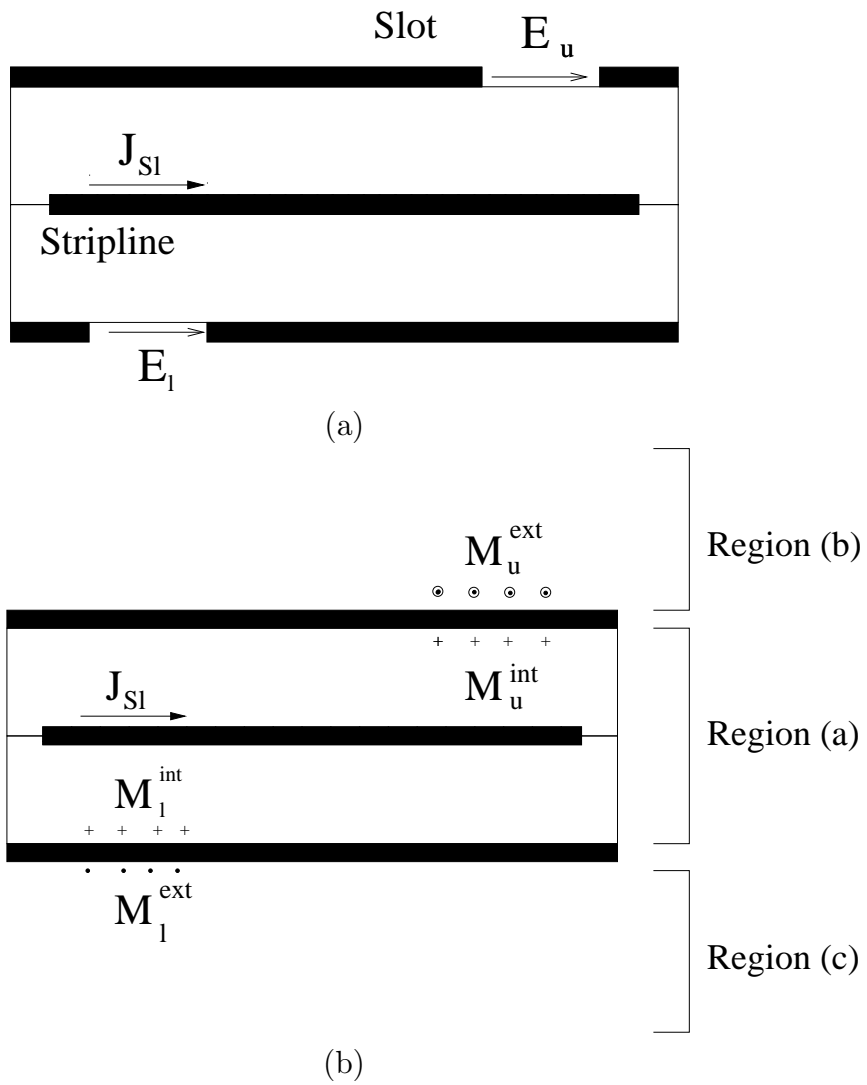


Figure 5.3: SSS unit cell: (a) original structure; and (b) structure after application of the equivalence principle.

### 5.2.1 Integral Equations

In the internal region, Region (a), see Fig.5.3 (b), the total electric and magnetic field distributions can be expressed as

$$\mathbf{E}^{int}(\mathbf{r}) = \mathbf{E}_{inc}^{int}(\mathbf{r}) + \mathbf{E}_{dif}^{int}(\mathbf{r}) \quad (5.5)$$

$$\mathbf{H}^{int}(\mathbf{r}) = \mathbf{H}_{inc}^{int}(\mathbf{r}) + \mathbf{H}_{dif}^{int}(\mathbf{r}) \quad (5.6)$$

where  $\mathbf{E}_{inc}^{int}$  and  $\mathbf{H}_{inc}^{int}$  are the electric and magnetic fields due to the external excitation respectively. Whereas the diffracted electric and magnetic fields are  $\mathbf{E}_{dif}^{int}$  and  $\mathbf{H}_{dif}^{int}$  respectively. The same equations will be for the external region, region (b), since there are no electric sources

$$\mathbf{E}^{ext}(\mathbf{r}) = \mathbf{E}_{inc}^{ext}(\mathbf{r}) + \mathbf{E}_{dif}^{ext}(\mathbf{r}) \quad (5.7)$$

$$\mathbf{H}^{ext}(\mathbf{r}) = \mathbf{H}_{inc}^{ext}(\mathbf{r}) + \mathbf{H}_{dif}^{ext}(\mathbf{r}) \quad (5.8)$$

here, the notation is the same as above, but for the external region (*ext*). Once the electric and magnetic field distributions are defined, the boundary conditions are enforced at the stripline and aperture. Since the tangential components of the electric fields are zero on the stripline, this boundary condition is formulated as

$$\hat{z} \times \mathbf{E}^{int}(\mathbf{r}) = 0|_{stripline}. \quad (5.9)$$

Also the tangential components of the magnetic fields are continuous across the aperture so that

$$\hat{z} \times [\mathbf{H}^{ext}(\mathbf{r}) - \mathbf{H}^{int}(\mathbf{r})] = 0|_{apertures}. \quad (5.10)$$

### 5.2.2 Potentials of the Diffracted Fields

The diffracted fields can be represented by using both magnetic and electric potentials and hence the total fields

- In the internal region:

$$\mathbf{E}^{int}(\mathbf{r}) = \mathbf{E}_{inc}^{int}(\mathbf{r}) - j\omega\mathbf{A}^{int}(\mathbf{r}) - \nabla\phi^{int}(\mathbf{r}) - \frac{1}{\epsilon}\nabla\times\mathbf{F}^{int}(\mathbf{r}) \quad (5.11)$$

$$\mathbf{H}^{int}(\mathbf{r}) = \mathbf{H}_{inc}^{int}(\mathbf{r}) - j\omega\mathbf{F}^{int}(\mathbf{r}) - \nabla\psi^{int}(\mathbf{r}) + \frac{1}{\mu_0}\nabla\times\mathbf{A}^{int}(\mathbf{r}) \quad (5.12)$$

- In the external region:

$$\mathbf{E}^{ext}(\mathbf{r}) = \mathbf{E}_{inc}^{ext}(\mathbf{r}) - \frac{1}{\epsilon_0}\nabla\times\mathbf{F}^{ext}(\mathbf{r}). \quad (5.13)$$

$$\mathbf{H}^{ext}(\mathbf{r}) = \mathbf{H}_{inc}^{ext}(\mathbf{r}) - j\omega\mathbf{F}^{ext}(\mathbf{r}) - \nabla\psi^{ext}(\mathbf{r}). \quad (5.14)$$

where  $\mathbf{A}$  is the magnetic vector potential,  $\phi$  is the scalar potential from electric charges,  $\mathbf{F}$  is the electric vector potential, and  $\psi$  is the scalar potential from magnetic charges, and the subscripts *int* and *ext* denotes for the internal and external regions respectively.

These potentials are taken to satisfy the Lorentz gauge, so

- In the internal region

$$(\nabla^2 + k^2)\mathbf{A}^{int} = -\mu_0\mathbf{J}_s^{int} \quad (5.15)$$

$$(\nabla^2 + k^2)\phi^{int} = -\frac{\rho^{int}}{\epsilon} \quad (5.16)$$

$$(\nabla^2 + k^2)\mathbf{F}^{int} = -\epsilon\mathbf{M}_s^{int} \quad (5.17)$$

$$(\nabla^2 + k^2)\psi^{int} = -\frac{\rho_m^{int}}{\mu_0} \quad (5.18)$$

- In the external region

$$(\nabla^2 + k_0^2)\mathbf{F}^{ext} = -\epsilon_0 \mathbf{M}_s^{ext} \quad (5.19)$$

$$(\nabla^2 + k_0^2)\psi^{ext} = -\frac{\rho_m^{ext}}{\mu_0} \quad (5.20)$$

where the quantities  $\rho_s$  and  $\rho_{m_s}$  are the electric and magnetic charges respectively and they are related to the electric and magnetic currents ( $\mathbf{J}_s(\mathbf{r}')$  and  $\mathbf{M}_s(\mathbf{r}')$ ) via the continuity equations:

$$\nabla \cdot \mathbf{J}_s = -j\omega\rho_s \quad (5.21)$$

$$\nabla \cdot \mathbf{M}_s = -j\omega\rho_{m_s}. \quad (5.22)$$

### 5.3 Green's Functions

These potentials can be represented as a superposition integration over the source regions

- In the internal region:

$$\mathbf{A}^{int}(\mathbf{r}) = \int_{S_1} \bar{\bar{\mathbf{G}}}_A^{int}(\mathbf{r}, \mathbf{r}') \cdot \mathbf{J}_s(\mathbf{r}') dS'_1 \quad (5.23)$$

$$\phi^{int}(\mathbf{r}) = \int_{S_1} G_\phi^{int}(\mathbf{r}, \mathbf{r}') \rho_s(\mathbf{r}') dS'_1 \quad (5.24)$$

$$\mathbf{F}^{int}(\mathbf{r}) = \int_{S_2} \bar{\bar{\mathbf{G}}}_F^{int}(\mathbf{r}, \mathbf{r}') \cdot \mathbf{M}_s(\mathbf{r}') dS'_2 \quad (5.25)$$

$$\psi^{int}(\mathbf{r}) = \int_{S_2} G_\psi^{int}(\mathbf{r}, \mathbf{r}') \rho_{m_s}(\mathbf{r}') dS'_2. \quad (5.26)$$

where  $\bar{\bar{\mathbf{G}}}_A^{int}(\mathbf{r}, \mathbf{r}')$  and  $\bar{\bar{\mathbf{G}}}_F^{int}(\mathbf{r}, \mathbf{r}')$ , are the spatial-domain dyadic Green's functions of magnetic and electric vector potentials, whereas  $G_\phi^{int}(\mathbf{r}, \mathbf{r}')$ , and  $G_\psi^{int}(\mathbf{r}, \mathbf{r}')$  are the spatial-domain scalar Green's functions of the electric and magnetic charge scalar potentials respectively.

- In the external region:

$$\mathbf{F}^{ext}(\mathbf{r}) = \int_{S_2} \bar{\bar{\mathbf{G}}}_F^{ext}(\mathbf{r}, \mathbf{r}') \cdot [-\mathbf{M}_s(\mathbf{r}')] dS'_2 \quad (5.27)$$

$$\psi^{ext}(\mathbf{r}) = \int_{S_2} G_\psi^{ext}(\mathbf{r}, \mathbf{r}') [-\rho_{m_s}(\mathbf{r}')] dS'_2. \quad (5.28)$$

where  $\bar{\bar{\mathbf{G}}}_F^{ext}(\mathbf{r}, \mathbf{r}')$ , is the spatial-domain dyadic Green's function of the electric vector potential and  $G_\psi^{ext}(\mathbf{r}, \mathbf{r}')$  is the spatial-domain scalar Green's function of the magnetic charge scalar potential.

## 5.4 Mixed Potential Integral Equations

The integral equations can be obtained by enforcing the boundary conditions on both the stripline and the aperture. Two integral equations are obtained, the first comes from the boundary condition on the stripline and is given as

$$\begin{aligned} \hat{\mathbf{z}} \times \mathbf{E}_{inc}^{int}(\mathbf{r}_0) &= \hat{\mathbf{z}} \times [j\omega \int_{S_1} \bar{\bar{\mathbf{G}}}_A^{int}(\mathbf{r}_1, \mathbf{r}') \cdot \mathbf{J}_s(\mathbf{r}') dS'_1 \\ &+ \frac{j\nabla}{\omega} \int_{S_1} G_\phi^{int}(\mathbf{r}_1, \mathbf{r}') [\nabla' \cdot \mathbf{J}_s(\mathbf{r}')] dS'_1] \\ &+ \hat{\mathbf{z}} \times \left[ \frac{1}{\epsilon} \nabla \times \int_{S_2} \bar{\bar{\mathbf{G}}}_F^{int}(\mathbf{r}_1, \mathbf{r}') \cdot \mathbf{M}_s(\mathbf{r}') dS'_2 \right], \end{aligned}$$

$\mathbf{r}_1 \in \text{stripline}$  (5.29)

The second integral equation comes from the boundary condition on the aperture and given as

$$\begin{aligned} \hat{\mathbf{z}} \times \Delta \mathbf{H}_{inc}(\mathbf{r}_1) &= \hat{\mathbf{z}} \times [j\omega \int_{S_2} \bar{\bar{\mathbf{G}}}_F(\mathbf{r}_2, \mathbf{r}') \cdot \mathbf{M}_s(\mathbf{r}') dS'_2 \\ &+ \frac{j\nabla}{\omega} \int_{S_2} G_\psi(\mathbf{r}_2, \mathbf{r}') [\nabla' \cdot \mathbf{M}_s(\mathbf{r}')] dS'_2] \\ &- \hat{\mathbf{z}} \times \left[ \frac{1}{\mu_0} \nabla \times \int_{S_1} \bar{\bar{\mathbf{G}}}_A^{int}(\mathbf{r}_2, \mathbf{r}') \cdot \mathbf{J}_s(\mathbf{r}') dS'_1 \right], \end{aligned}$$

$\mathbf{r}_2 \in \text{aperture}$  (5.30)

where  $\Delta\mathbf{H}_{inc}(\mathbf{r})$ ,  $\bar{\bar{\mathbf{G}}}_F(\mathbf{r}, \mathbf{r}')$  and  $G_\psi(\mathbf{r}, \mathbf{r}')$  are defined as

$$\Delta\mathbf{H}_{inc}(\mathbf{r}) = \mathbf{H}_{inc}^{int}(\mathbf{r}) - \mathbf{H}_{inc}^{ext}(\mathbf{r}) \quad (5.31)$$

$$\bar{\bar{\mathbf{G}}}_F(\mathbf{r}, \mathbf{r}') = \bar{\bar{\mathbf{G}}}_F^{int}(\mathbf{r}, \mathbf{r}') + \bar{\bar{\mathbf{G}}}_F^{ext}(\mathbf{r}, \mathbf{r}') \quad (5.32)$$

$$G_\psi(\mathbf{r}, \mathbf{r}') = G_\psi^{int}(\mathbf{r}, \mathbf{r}') + G_\psi^{ext}(\mathbf{r}, \mathbf{r}') \quad (5.33)$$

## 5.5 Spatial Domain Potential Green's Functions

In this section, the derivation of the spatial domain potential Green's function are presented. Partitioning the structure into two different regions helps us to calculate the structure Green's functions. The internal region, which is a parallel plate waveguide with perfect conductors inside it, is handled by two approaches. The first approach is the modal representation which is obtained by solving the Helmholtz equation using the spectral domain (eigenvectors). In the second approach, the image theory, we represent the Green's functions as a sum of the fields from infinite number of sources (images). The first representation, the modal representation, is numerically efficient when the source and observation points are well separated. Otherwise the image representation converges very well when the source and observation points are closed to each other. Using both representations, we can obtain an efficient numerical representation for the Green's Functions, which is valid for all source/observation distance range. In the external region, the solution is simply a magnetic dipole in a half space.

### 5.5.1 Internal Region

The potentials differential equations in (5.15-5.18) can be simplified as

$$(\nabla^2 + k^2) G(\mathbf{r}, \mathbf{r}') = -\delta(\mathbf{r}, \mathbf{r}') \quad (5.34)$$

where  $G$  is the scalar function which satisfy the inhomogenous Helmholtz equation with delta function. The required potentials Green's functions satisfy (5.34) and an appropriate boundary conditions on the parallel plate. We have here two types of boundary conditions, Dirichlet boundary conditions ( $G = 0$ ) and Neumann boundary conditions ( $\frac{\partial G}{\partial z} = 0$ ) on the parallel plates. Defining  $G_d$  as the Dirichlet Green's function which satisfies both (5.34) and the Dirichlet boundary conditions. Similarly  $G_n$  is defined for the Neumann Green's function.

The boundary conditions of the potentials on the perfect conductors are

$$\phi = 0 \quad (5.35)$$

$$\frac{\partial \psi}{\partial z} = 0 \quad (5.36)$$

$$\hat{z} \times \mathbf{A} = 0 \quad (5.37)$$

$$\nabla_z \cdot \mathbf{A} = 0 \quad (5.38)$$

$$\hat{z} \times (\nabla \times \mathbf{F}) = 0 \quad (5.39)$$

$$\hat{z} \cdot \mathbf{F} = 0 \quad (5.40)$$

From the above boundary conditions and (5.15-5.18) the potentials Green's function can be written as

$$G_\phi^{int} = \frac{1}{\epsilon} G_d \quad (5.41)$$

$$G_{A_{xx}}^{int} = G_{A_{yy}}^{int} = \mu_0 G_d \quad (5.42)$$

$$G_{A_{xy}}^{int} = G_{A_{yx}}^{int} = 0 \quad (5.43)$$

$$G_{A_{xz}}^{int} = G_{A_{yz}}^{int} = \mu_0 G_n \quad (5.44)$$

$$G_{\psi}^{int} = \frac{1}{\mu_0} G_n \quad (5.45)$$

$$G_{F_{xx}}^{int} = G_{F_{yy}}^{int} = \epsilon G_n \quad (5.46)$$

$$G_{F_{xy}}^{int} = G_{F_{yx}}^{int} = 0. \quad (5.47)$$

### Dirichlet Boundary Conditions

The modal series expansion of  $G_d$  is

$$G_d^{(m)}(\mathbf{r}, \mathbf{r}') = \frac{1}{2\pi h} \sum_{n=1}^{\infty} \sin\left(\frac{n\pi}{2h}(z+h)\right) \sin\left(\frac{n\pi}{2h}(z'+h)\right) K_0(\alpha_n \rho_0) \quad (5.48)$$

where

$$\rho_0 = \sqrt{(x-x')^2 + (y-y')^2} \quad (5.49)$$

$$\alpha_n = \sqrt{\left(\frac{n\pi}{2h}\right)^2 - k^2} \quad (5.50)$$

and  $K_0$  is the modified Bessel function of order zero. This modal representation is useful when  $\mathbf{r}$  and  $\mathbf{r}'$  are well separated. The convergence rate is slow when  $\rho_0 \rightarrow 0$ . An alternative series can be obtained by imaging the source through the parallel plate walls and summing the contributions of the images, which may now be considered to be radiating in a medium without boundaries. Using these images, the  $G_d$  can be expressed as

$$G_d^{(i)}(\mathbf{r}, \mathbf{r}') = \frac{1}{4\pi} \sum_{n=-\infty}^{\infty} \left( \frac{e^{-jkR_n^+}}{R_n^+} - \frac{e^{-jkR_n^-}}{R_n^-} \right) \quad (5.51)$$

where  $R_n^+$  and  $R_n^-$  are distances between the observation point and the  $n$ th order image point given by

$$R_n^+ = \sqrt{\rho_0^2 + (z - z' - 4nh)^2} \quad (5.52)$$

$$R_n^- = \sqrt{\rho_0^2 + (z - z' - (2n + 1)2h)^2} \quad (5.53)$$

Using the Simon technique [4], and the acceleration technique described in [205], by combining (5.48) and (5.51) to arrive at a single numerically efficient formula valid for all  $\mathbf{r}$  and  $\mathbf{r}'$ . For  $c \geq 0$ , define  $\rho_c$ ,  $P_n^+$ , and  $P_n^-$  as

$$\rho_c = \sqrt{\rho_0^2 + c^2} \quad (5.54)$$

$$P_n^+ = \sqrt{\rho_c^2 + (z - z' - 4nh)^2} \quad (5.55)$$

$$P_n^- = \sqrt{\rho_c^2 + (z - z' - (2n + 1)2h)^2} \quad (5.56)$$

now we can write

$$G_d(\mathbf{r}, \mathbf{r}') = g_d^{(m)} + \frac{1}{4\pi} \sum_{n=-\infty}^{\infty} \left( \frac{e^{-jkR_n^+}}{R_n^+} - \frac{e^{-jkP_n^+}}{P_n^+} - \frac{e^{-jkR_n^-}}{R_n^-} + \frac{e^{-jkP_n^-}}{P_n^-} \right) \quad (5.57)$$

where

$$g_d^{(m)}(\mathbf{r}, \mathbf{r}') = \frac{1}{2\pi h} \sum_{n=1}^{\infty} \sin\left(\frac{n\pi}{2h}(z+h)\right) \sin\left(\frac{n\pi}{2h}(z'+h)\right) K_0(\alpha_n \rho_c) \quad (5.58)$$

and

$$\begin{aligned} \frac{\partial G_d(\mathbf{r}, \mathbf{r}')}{\partial z} &= \frac{\partial g_d^{(m)}}{\partial z}(\mathbf{r}, \mathbf{r}') \\ &+ \frac{1}{4\pi} \sum_{n=-\infty}^{\infty} \left[ (z - z' - 4nh) \left[ e^{-jkP_n^+} \left( \frac{jk}{P_n^{+2}} + \frac{1}{P_n^{+3}} \right) - e^{-jkR_n^+} \left( \frac{jk}{R_n^{+2}} + \frac{1}{R_n^{+3}} \right) \right] \right. \\ &+ \left. (z - z' - (2n + 1)2h) \left[ e^{-jkR_n^-} \left( \frac{jk}{R_n^{-2}} + \frac{1}{R_n^{-3}} \right) - e^{-jkP_n^-} \left( \frac{jk}{P_n^{-2}} + \frac{1}{P_n^{-3}} \right) \right] \right] \end{aligned} \quad (5.59)$$

where

$$\frac{\partial g_d^{(m)}}{\partial z}(\mathbf{r}, \mathbf{r}') = \frac{1}{4h^2} \sum_{n=1}^{\infty} n \cos\left(\frac{n\pi}{2h}(z+h)\right) \sin\left(\frac{n\pi}{2h}(z'+h)\right) K_0(\alpha_n \rho_c) \quad (5.60)$$

we are only interested in  $G_d(\rho, z = 0, \rho', z' = 0)$  and  $\frac{\partial G_d}{\partial z}|_{(\rho, z=h, \rho', z'=0)}$

### Neumann Boundary Conditions

A similar procedure is followed for the Neumann Green's functions. The modal series expansion of  $G_n$  is

$$G_n^{(m)}(\mathbf{r}, \mathbf{r}') = -\frac{j}{8h} H_0^{(2)}(k\rho_0) + \frac{1}{2\pi h} \sum_{n=1}^{\infty} \cos\left(\frac{n\pi}{2h}(z+h)\right) \cos\left(\frac{n\pi}{2h}(z'+h)\right) K_0(\alpha_n \rho_0) \quad (5.61)$$

where  $H_0^{(2)}$  is the zero order Hankel function of the second kind. The multiple image expansion is

$$G_n^{(i)}(\mathbf{r}, \mathbf{r}') = \frac{1}{4\pi} \sum_{n=-\infty}^{\infty} \left( \frac{e^{-jkR_n^+}}{R_n^+} + \frac{e^{-jkR_n^-}}{R_n^-} \right) \quad (5.62)$$

after combining these expressions as before, the accelerated formula for the Neumann Green's function

$$G_n(\mathbf{r}, \mathbf{r}') = g_n^{(m)} + \frac{1}{4\pi} \sum_{n=-\infty}^{\infty} \left( \frac{e^{-jkR_n^+}}{R_n^+} - \frac{e^{-jkP_n^+}}{P_n^+} + \frac{e^{-jkR_n^-}}{R_n^-} - \frac{e^{-jkP_n^-}}{P_n^-} \right) \quad (5.63)$$

where

$$g_n^{(m)}(\mathbf{r}, \mathbf{r}') = -\frac{j}{8h} H_0^{(2)}(k\rho_c) + \frac{1}{2\pi h} \sum_{n=1}^{\infty} \cos\left(\frac{n\pi}{2h}(z+h)\right) \cos\left(\frac{n\pi}{2h}(z'+h)\right) K_0(\alpha_n \rho_c) \quad (5.64)$$

and

$$\begin{aligned} \frac{\partial G_n(\mathbf{r}, \mathbf{r}')}{\partial z} &= \frac{\partial g_n^{(m)}}{\partial z}(\mathbf{r}, \mathbf{r}') \\ &+ \frac{1}{4\pi} \sum_{n=-\infty}^{\infty} \left[ (z - z' - 4nh) \left[ e^{-jkP_n^+} \left( \frac{jk}{P_n^{+2}} + \frac{1}{P_n^{+3}} \right) - e^{-jkR_n^+} \left( \frac{jk}{R_n^{+2}} + \frac{1}{R_n^{+3}} \right) \right] \right. \\ &+ \left. (z - z' - (2n+1)2h) \left[ e^{-jkP_n^-} \left( \frac{jk}{P_n^{-2}} + \frac{1}{P_n^{-3}} \right) - e^{-jkR_n^-} \left( \frac{jk}{R_n^{-2}} + \frac{1}{R_n^{-3}} \right) \right] \right] \end{aligned} \quad (5.65)$$

where

$$\frac{\partial g_n^{(m)}}{\partial z}(\mathbf{r}, \mathbf{r}') = -\frac{1}{4h^2} \sum_{n=1}^{\infty} n \sin\left(\frac{n\pi}{2h}(z+h)\right) \cos\left(\frac{n\pi}{2h}(z'+h)\right) K_0(\alpha_n \rho_c) \quad (5.66)$$

again we are only interested in  $G_n(\rho, z = h, \rho', z' = h)$  and its derivative  $\left. \frac{\partial G_n}{\partial z} \right|_{(\rho, z=0, \rho', z'=h)}$

## Numerical Convergence

The constant  $c$  is carefully adjusted so that the series (5.57) and (5.63) converge rapidly. The optimum value of the constant  $c$  depend on the structure parameters.

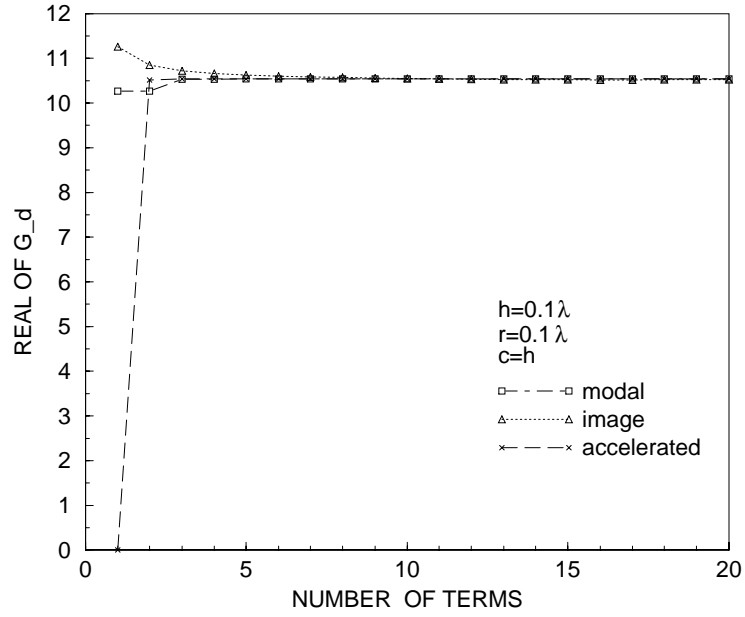
Figs. 5.4 shows the convergence rate of  $G_d$  using the three representations when the separation between the source and observation is  $0.1\lambda$ ,  $h = 0.1\lambda$  and  $c = h$ . Fig. 5.5 shows the convergence rate for the separation between the source and observation is  $0.001\lambda$ . It is obvious that the accelerated series converges better than the others in both cases.

The value of the acceleration parameter ( $c$ ) was chosen after numerical investigation of the accelerated series convergence rate. The series was computed with changing the acceleration parameters for several times. For example Figs. 5.6 and 5.7 show the convergence rate of the accelerated function with changing  $c$  for  $r = 0.1\lambda$  and  $r = 0.01\lambda$  respectively. After this numerical studies, we found that the optimum value of  $c$  is  $h$ .

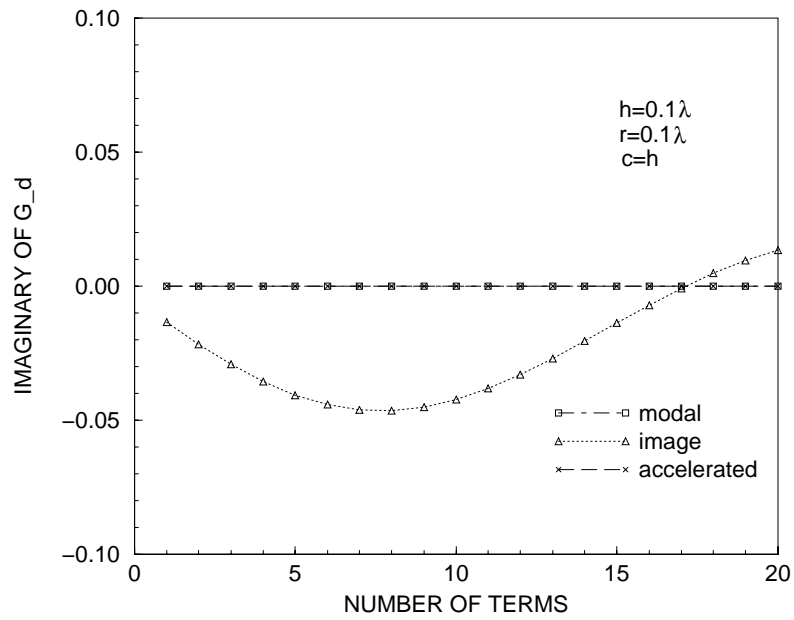
### 5.5.2 External Region

For the external region the Green's functions are the solutions for the half space boundary conditions as presented in [192]:

$$G_{\psi}^{ext} = \frac{1}{4\pi\mu_0} \frac{e^{-jk_0 R}}{R} \quad (5.67)$$

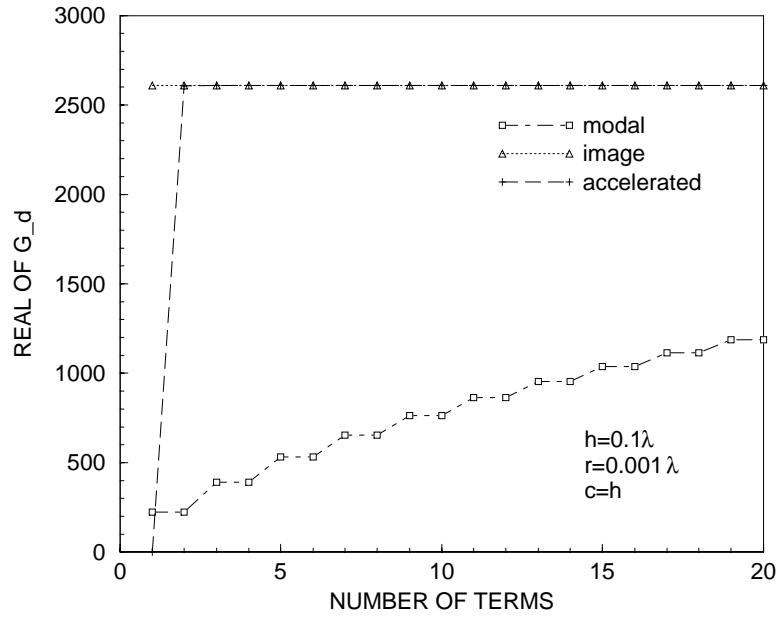


(a)

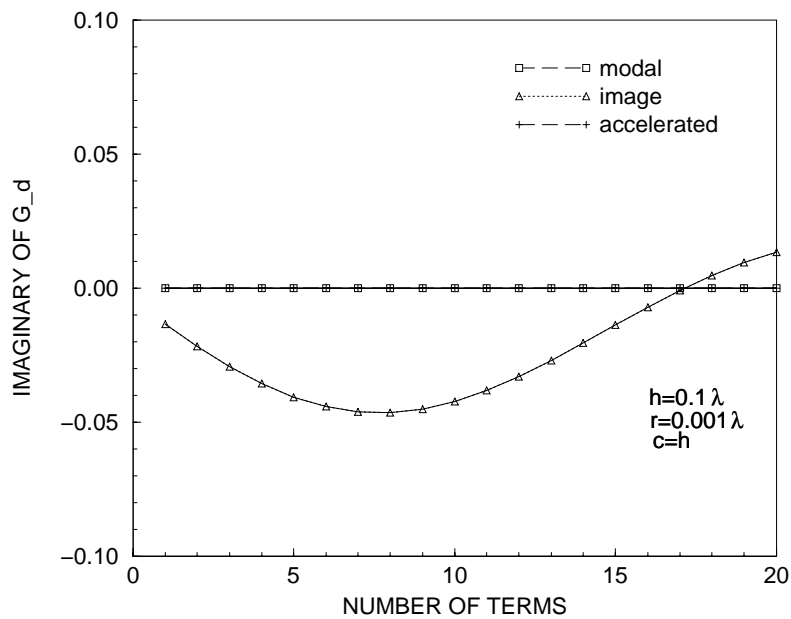


(b)

Figure 5.4: The convergence rate of  $G_d$  using three representations for  $r = 0.1\lambda$  : (a) real; (b) imaginary.

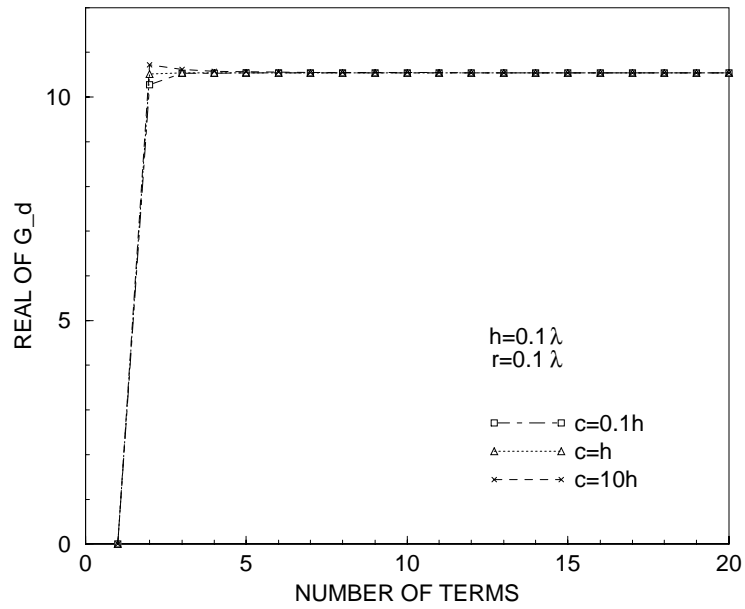


(a)

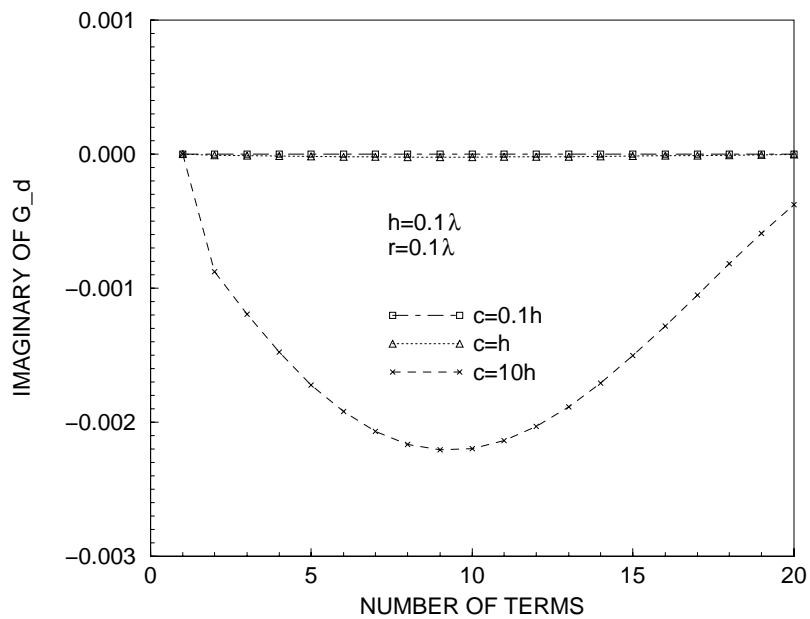


(b)

Figure 5.5: The convergence rate of  $G_d$  using three representations for  $r = 0.001\lambda$  : (a) real; (b) imaginary.

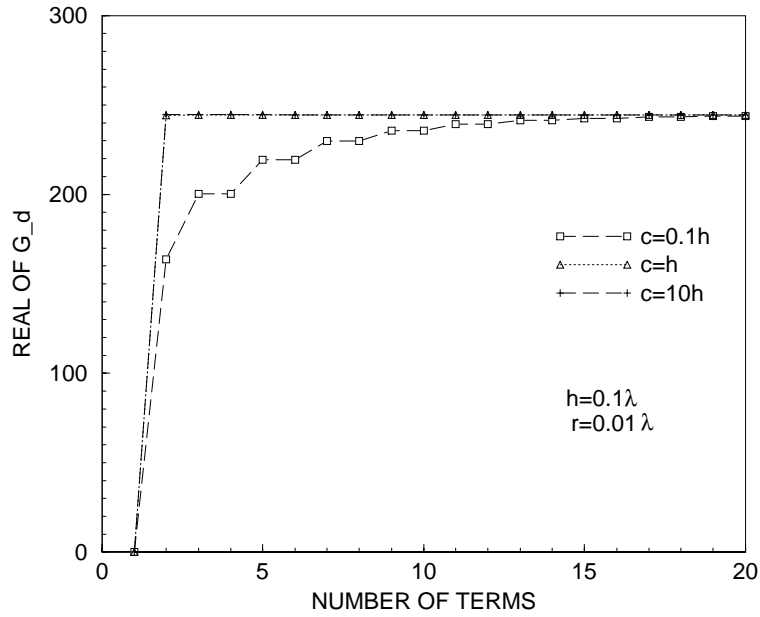


(a)

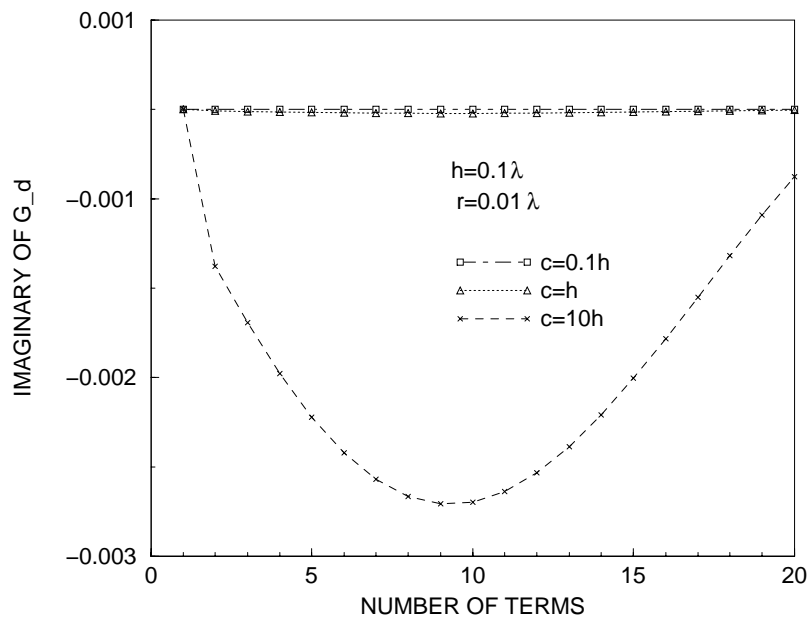


(b)

Figure 5.6: The effect of  $c$  on the convergence rate of the accelerated  $G_d$  series for  $r = 0.1\lambda$ : (a) real; (b) imaginary.



(a)



(b)

Figure 5.7: The effect of  $c$  on the convergence rate of the accelerated  $G_d$  series for  $r = 0.01\lambda$ : (a) real; (b) imaginary.

and

$$G_{F_{xx}}^{ext} = G_{F_{yy}}^{ext} = \frac{\epsilon_0}{4\pi} \frac{e^{-jk_0 R}}{R}. \quad (5.68)$$

where

$$R = \sqrt{(x - x')^2 + (y - y')^2 + (z - z')^2} \quad (5.69)$$

## 5.6 Spectral Domain Green's Functions

In this section the spectral domain dyadic Green's functions for both the internal and external regions are derived using the immittance approach.

### 5.6.1 Internal Region

Using the immittance approach shown in Section 3.7, we write the geometry of the problem as equivalent transmission lines for the transverse electric (TE) and the transverse magnetic (TM) cases. In this case we have both current and voltage sources. The voltage sources are due to the magnetic currents on the slots and the current source is due to the electric current on the strip (see Fig. 5.8).

Since we need the spectral domain dyadic Green's functions to calculate the singular MoM matrix elements (self and overlapped cells elements), we do not need to calculate all the dyadic Green's function components. For example, the coupling MoM matrix elements between the lower and upper slots are not singular ( since  $|\mathbf{r} - \mathbf{r}'| > 0$  ). The spectral domain dyadic Green's functions between the upper and lower slots are not needed.

From the equivalent transmission line circuit shown in Fig. 5.9 and following the immittance approach [5], The components of the electric field dyadic Green's

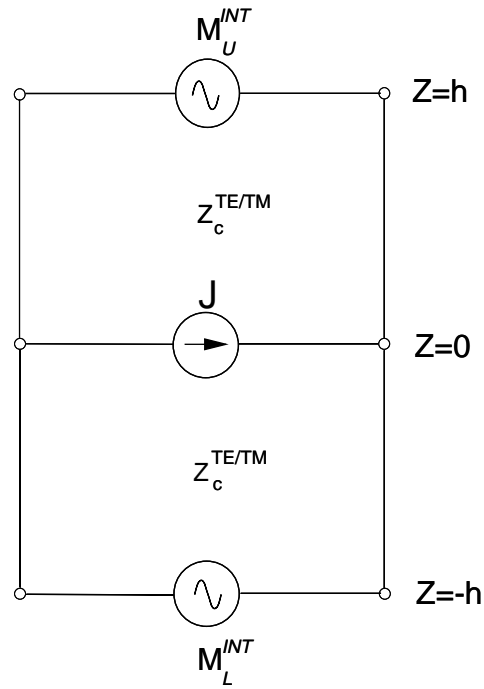


Figure 5.8: Equivalent transmission lines for the immittance approach of the internal region for the SSS structure.

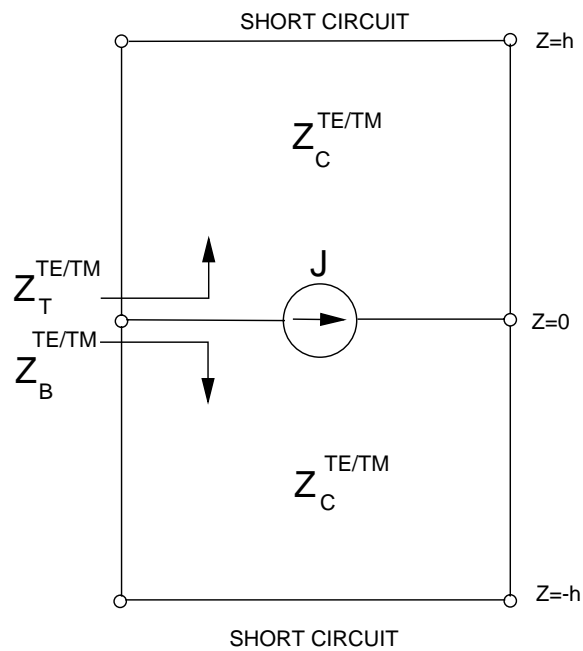


Figure 5.9: Equivalent transmission lines for the  $\tilde{G}_{EJ}$ .

functions in the spectral domain are then given as

$$\tilde{G}_{EJ_{xx}}^{int}(k_x, k_y) = \frac{-1}{\beta^2} (k_x^2 Z^{TM} + k_y^2 Z^{TE}) \quad (5.70)$$

$$\tilde{G}_{EJ_{yy}}^{int}(k_x, k_y) = \frac{-1}{\beta^2} (k_x^2 Z^{TE} + k_y^2 Z^{TM}) \quad (5.71)$$

$$\tilde{G}_{EJ_{xy}}^{int}(k_x, k_y) = \tilde{G}_{EJ_{yx}}^{int}(k_x, k_y) = \frac{-k_x k_y}{\beta^2} (Z^{TM} - Z^{TE}) \quad (5.72)$$

where

$$Z^{TE} = Z_T^{TE} \parallel Z_B^{TE} = j \frac{Z_C^{TE}}{2} \tan(k_{z0} h) \quad (5.73)$$

$$Z^{TM} = Z_T^{TM} \parallel Z_B^{TM} = j \frac{Z_C^{TM}}{2} \tan(k_{z0} h) \quad (5.74)$$

where

$$Z_C^{TE} = \frac{Z k_0}{k_{z0}} \quad (5.75)$$

$$Z_C^{TM} = \frac{Z k_{z0}}{k_0} \quad (5.76)$$

$$k_{z0} = \sqrt{k^2 - \beta^2} \quad , \quad \text{Im}(k_{z0}) < 0 \quad (5.77)$$

$$\beta^2 = k_x^2 + k_y^2 \quad (5.78)$$

and

$$Z = \frac{Z_0}{\sqrt{\epsilon_r}}. \quad (5.79)$$

Using (5.73) and (5.74) in expressions (5.70)–(5.72) yields the dyadic components of the electric field internal region Green's functions:

$$\tilde{G}_{EJ_{xx}}^{int}(k_x, k_y) = \frac{jZ}{2k} \left( \frac{k_x^2 - k^2}{k_{z0}} \right) \tan(k_{z0} h) \quad (5.80)$$

$$\tilde{G}_{EJ_{yy}}^{int}(k_x, k_y) = \frac{jZ}{2k} \left( \frac{k_y^2 - k^2}{k_{z0}} \right) \tan(k_{z0}h) \quad (5.81)$$

and

$$\tilde{G}_{EJ_{xy}}^{int}(k_x, k_y) = \tilde{G}_{EJ_{yx}}^{int}(k_x, k_y) = \frac{jZ}{2k} \left( \frac{k_x k_y}{k_{z0}} \right) \tan(k_{z0}h). \quad (5.82)$$

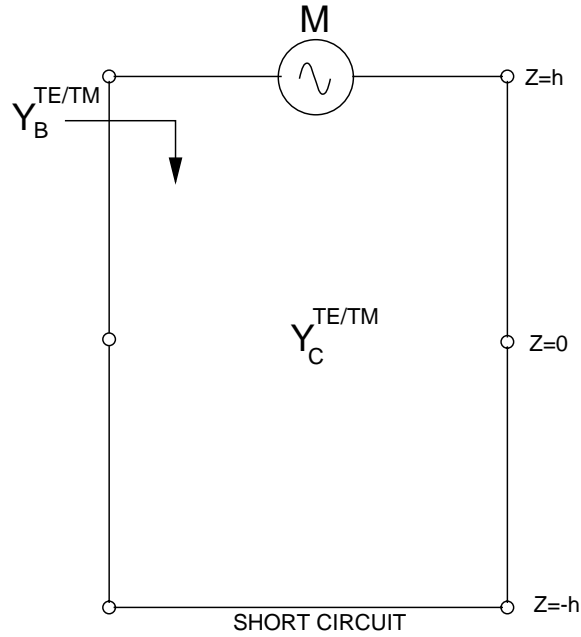


Figure 5.10: Equivalent transmission lines for the  $\tilde{G}_{HM}$ .

For the magnetic field dyadic Green's functions consider the equivalent transmission line circuit shown in Fig. 5.10 and following the immittance approach, then

$$\tilde{G}_{HM_{xx}}^{int}(k_x, k_y) = \frac{-1}{\beta^2} \left( k_x^2 Y^{TE} + k_y^2 Y^{TM} \right) \quad (5.83)$$

$$\tilde{G}_{HM_{yy}}^{int}(k_x, k_y) = \frac{-1}{\beta^2} \left( k_x^2 Y^{TE} + k_y^2 Y^{TM} \right) \quad (5.84)$$

$$\tilde{G}_{HM_{xy}}^{int}(k_x, k_y) = \tilde{G}_{HM_{yx}}^{int}(k_x, k_y) = \frac{-k_x k_y}{\beta^2} \left( Y^{TE} - Y^{TM} \right) \quad (5.85)$$

where

$$Y^{TE} = Y_B^{TE} = -jY_C^{TE} \cot(2k_{z0}h) \quad (5.86)$$

$$Y^{TM} = Y_B^{TM} = -jY_C^{TM} \cot(2k_{z0}h) \quad (5.87)$$

and

$$Y_C^{TE} = \frac{Yk_{z0}}{k_0} \quad (5.88)$$

$$Y_C^{TM} = \frac{Yk_0}{k_{z0}} \quad (5.89)$$

$$Y = \sqrt{\epsilon_r}Y_0 \quad (5.90)$$

Using (5.86) and (5.87) in expressions (5.83)–(5.85) yields the dyadic components of the magnetic field internal region Green's functions:

$$\tilde{G}_{HM_{xx}}^{int}(k_x, k_y) = \frac{jY}{k} \left( \frac{k_x^2 - k^2}{k_{z0}} \right) \cot(2k_{z0}h) \quad (5.91)$$

$$\tilde{G}_{HM_{yy}}^{int}(k_x, k_y) = \frac{jY}{k} \left( \frac{k_y^2 - k^2}{k_{z0}} \right) \cot(2k_{z0}h) \quad (5.92)$$

and

$$\tilde{G}_{HM_{xy}}^{int}(k_x, k_y) = \tilde{G}_{HM_{yx}}^{int}(k_x, k_y) = \frac{jY}{k} \left( \frac{k_x k_y}{k_{z0}} \right) \cot(2k_{z0}h) \quad (5.93)$$

### 5.6.2 External Region and Total Green's Functions

The external region magnetic dyadic Green's functions are the same as in Section 3.7.1 for the half space and given by

$$\tilde{G}_{HM_{xx}}^{ext}(k_x, k_y) = \frac{Y_0}{k_0} \left( \frac{k_x^2 - k_0^2}{k_{z0}} \right) \quad (5.94)$$

$$\tilde{G}_{HM_{yy}}^{ext}(k_x, k_y) = \frac{Y_0}{k_0} \left( \frac{k_y^2 - k_0^2}{k_{z0}} \right) \quad (5.95)$$

$$\tilde{G}_{HM_{xy}}^{ext}(k_x, k_y) = \tilde{G}_{HM_{yx}}^{ext}(k_x, k_y) = \frac{Y_0}{k_0} \left( \frac{k_x k_y}{k_{z0}} \right). \quad (5.96)$$

As defined in Section 3.7.3, the total spectral domain magnetic field dyadic Green's functions are given by

$$\tilde{G}_{HM_{xx}}(k_x, k_y) = \tilde{G}_{HM_{xx}}^{int}(k_x, k_y) + \tilde{G}_{HM_{xx}}^{ext}(k_x, k_y) \quad (5.97)$$

$$\tilde{G}_{HM_{yy}}(k_x, k_y) = \tilde{G}_{HM_{yy}}^{int}(k_x, k_y) + \tilde{G}_{HM_{yy}}^{ext}(k_x, k_y) \quad (5.98)$$

$$\tilde{G}_{HM_{xy}}(k_x, k_y) = \tilde{G}_{HM_{xy}}^{int}(k_x, k_y) + \tilde{G}_{HM_{xy}}^{ext}(k_x, k_y) \quad (5.99)$$

$$\tilde{G}_{HM_{yx}}(k_x, k_y) = \tilde{G}_{HM_{yx}}^{int}(k_x, k_y) + \tilde{G}_{HM_{yx}}^{ext}(k_x, k_y). \quad (5.100)$$

## 5.7 Summary

In this chapter the MPIE formulation for the SSS structure was presented. The kernel of these integral equations, the Green's functions, were derived in both spatial and spectral domains.

The spatial domain potential Green's functions were calculated using an accelerated series. An acceleration technique which combines both the modal and image series representations of the scalar Green's functions was used.

The convergence rate of this accelerated series was studied and the optimum value of the acceleration parameter was determined. Also the spectral domain dyadic Green's functions of the SSS structure were derived.

## Chapter 6

# Slot-Stripline-Slot Structure MoM Solution and Network Characterization

### 6.1 Introduction

Microwave technology has advanced to the point where electrically large systems, a wavelength or even several wavelengths in each of the three dimensions, are being developed. Electromagnetic modeling of these large systems, including modeling of the linear and nonlinear circuit components, is emerging as one of the great challenges in microwave and millimeter-wave computer aided engineering. The target problem in the current work is the spatial power combining amplifier [2]. Each dimension of this amplifier is at least two wavelengths and is a  $5 \times 5$  or perhaps larger array of unit cells. Each amplifying unit cell of the amplifier is an MMIC with a stripline coupled slot input antenna and a similar antenna at the output.

A simplified view of this system is shown in Fig. 6.1 and a unit cell in Fig. 6.2. The unit cell has an amplifier, typically a MMIC in the center of the stripline. In addition to the problem size, one characteristic of this system is the tight coupling of the nonlinear device to its electromagnetic environment.

There have been a few attempts to model systems with interacting fields and circuit elements. In transient analysis of distributed microwave structures lumped circuit elements can be embedded in the mesh of a time discretized electromagnetic field solver such as a finite difference time domain (FDTD) field modeler [206, 207]. There are also commercial products that allow the interfacing of electromagnetically

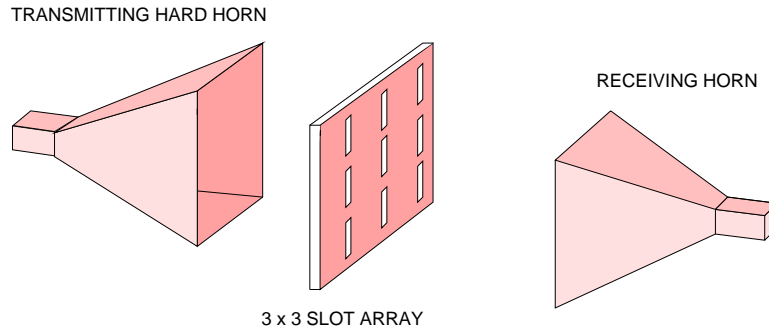


Figure 6.1: A slot-stripline-slot spatial power combining system, showing a simplified  $3 \times 3$  array.

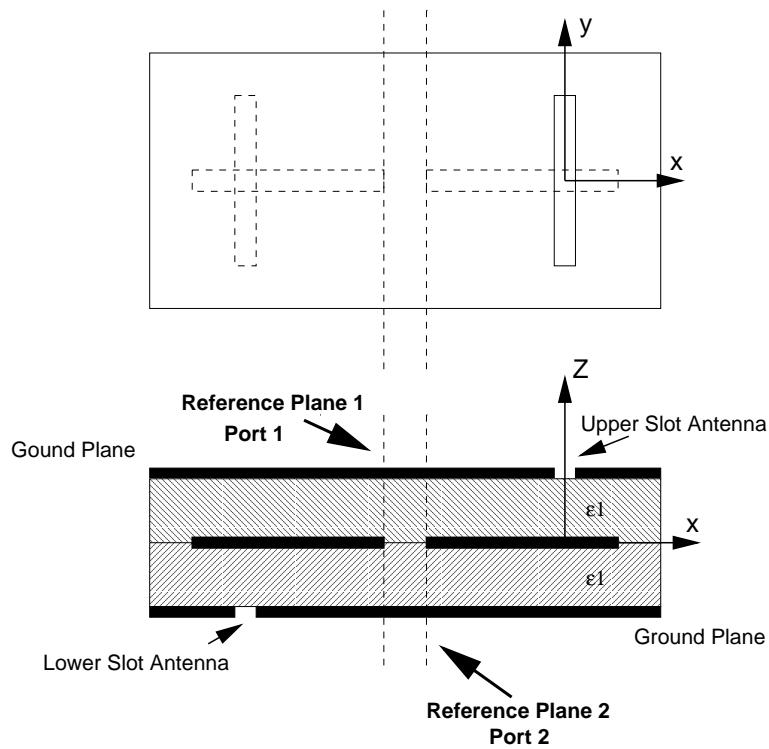


Figure 6.2: Passive slot-stripline-slot unit cell.

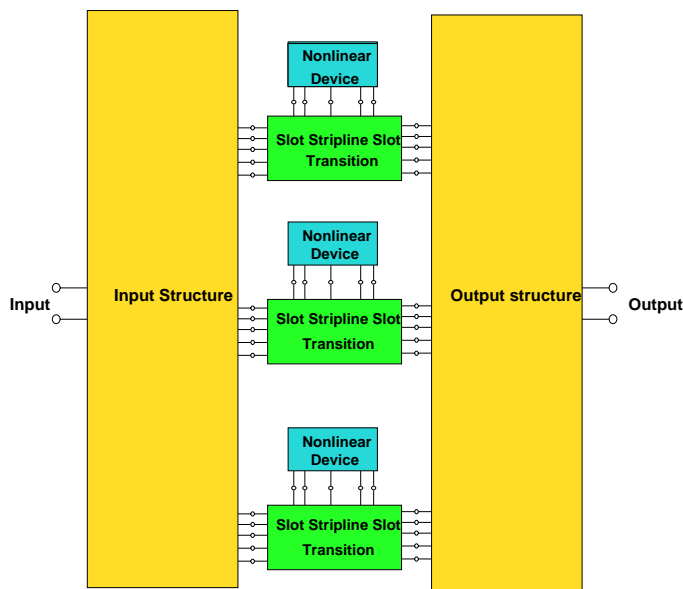


Figure 6.3: Network model of large partitioned electromagnetic system.

derived models with circuits but for now only fairly simple systems with a few ports can be handled.

In this chapter, a network based model of the electromagnetic environment is developed whereby sections of the large electromagnetic structure are interfaced to each other at “electromagnetic terminals” and to the conventional nodal-based circuit at the ports. The depiction shown in Fig. 6.3 represents three unit cells. Each of the SSS blocks is interfaced to a nonlinear network using normal current/voltage defined terminals. The exterior of the block is represented by multiport networks at the input and at the output. Each of the ports corresponds to one of the basis functions used in the discretization of the field at the slot. These input and output ports are denoted electromagnetic terminals to distinguish them from the current-voltage terminals of conventional circuit analysis. The electromagnetic terminals are defined in terms of incident and reflected waves.

The interfacing quantities at the “electromagnetic terminals” can be of any type as long as the same basis is used for the evaluation of the networks on either side of the interface. In this work a MoM simulator was used and the interfacing quantities were the weighted basis functions of the incident and scattered magnetic field of individual cells. This is then a generalization of the scattering matrix concept with forward and backward traveling waves. The aim of the overall analysis is to develop a single network representing the linear network with the minimum possible representation of the linear sub-networks.

## 6.2 MPIE for SSS structure

As discussed in Chapter 5, the diffracted fields derived from the potentials satisfying Maxwell’s equations and the boundary and radiation conditions are related to the excitation via the MPIEs. These equations simply state the continuity of the tangential components of the magnetic field over the lower and the upper aperture and also that the tangential electric field over the stripline is zero. we have here three equations, lower slot, upper slot and the stripline. The desired MPIEs are:

- On the upper slot :

$$\begin{aligned}
\hat{z} \times \Delta \mathbf{H}_{inc}^u(\mathbf{r}_2) &= \hat{z} \times [j\omega \int_{S_2} \bar{\bar{\mathbf{G}}}_F(\mathbf{r}_2, \mathbf{r}') \cdot \mathbf{M}_s^u(\mathbf{r}') dS'_2 \\
&+ \frac{\nabla}{j\omega} \int_{S_2} G_\psi(\mathbf{r}_2, \mathbf{r}') [\nabla' \mathbf{M}_s^u(\mathbf{r}')] dS'_2 \\
&- \frac{1}{\mu_0} \nabla \times \int_{S_1} \bar{\bar{\mathbf{G}}}_A^{int}(\mathbf{r}_2, \mathbf{r}') \cdot \mathbf{J}_s(\mathbf{r}') dS'_1 \\
&+ j\omega \int_{S_3} \bar{\bar{\mathbf{G}}}_F(\mathbf{r}_2, \mathbf{r}') \cdot \mathbf{M}_s^l(\mathbf{r}') dS'_3 \\
&+ \frac{\nabla}{j\omega} \int_{S_3} G_\psi(\mathbf{r}_1, \mathbf{r}') [\nabla' \mathbf{M}_s^l(\mathbf{r}')] dS'_3]
\end{aligned} \tag{6.1}$$

where  $\mathbf{r}_2 \in$  upper aperture.

- On the stripline :

$$\begin{aligned}
\hat{z} \times \mathbf{E}_{inc}^{int}(\mathbf{r}_1) &= \hat{z} \times \left[ \frac{\nabla}{\epsilon} \times \int_{S_2} \bar{\bar{\mathbf{G}}}_F^{int}(\mathbf{r}_1, \mathbf{r}') \cdot \mathbf{M}_s^u(\mathbf{r}') dS'_2 \right. \\
&+ j\omega \int_{S_1} \bar{\bar{\mathbf{G}}}_A^{int}(\mathbf{r}_1, \mathbf{r}') \cdot \mathbf{J}_s(\mathbf{r}') dS'_1 \\
&+ \frac{\nabla}{j\omega} \int_{S_1} G_\phi^{int}(\mathbf{r}_1, \mathbf{r}') [\nabla' \cdot \mathbf{J}_s(\mathbf{r}')] dS'_1 \\
&\left. + \frac{\nabla}{\epsilon} \times \int_{S_3} \bar{\bar{\mathbf{G}}}_F^{int}(\mathbf{r}_1, \mathbf{r}') \cdot \mathbf{M}_s^l(\mathbf{r}') dS'_3 \right]
\end{aligned} \tag{6.2}$$

where  $\mathbf{r}_1 \in$  stripline.

- On the lower slot :

$$\begin{aligned}
\hat{z} \times \Delta \mathbf{H}_{inc}^l(\mathbf{r}_3) &= \hat{z} \times \left[ j\omega \int_{S_2} \bar{\bar{\mathbf{G}}}_F(\mathbf{r}_3, \mathbf{r}') \cdot \mathbf{M}_s^u(\mathbf{r}') dS'_2 \right. \\
&+ \frac{\nabla}{j\omega} \int_{S_2} G_\psi(\mathbf{r}_3, \mathbf{r}') [\nabla' \cdot \mathbf{M}_s^u(\mathbf{r}')] dS'_2 \\
&- \frac{1}{\mu_0} \nabla \times \int_{S_1} \bar{\bar{\mathbf{G}}}_A^{int}(\mathbf{r}_3, \mathbf{r}') \cdot \mathbf{J}_s(\mathbf{r}') dS'_1 \\
&+ j\omega \int_{S_3} \bar{\bar{\mathbf{G}}}_F(\mathbf{r}_3, \mathbf{r}') \cdot \mathbf{M}_s^l(\mathbf{r}') dS'_3 \\
&\left. + \frac{\nabla}{j\omega} \int_{S_3} G_\psi(\mathbf{r}_3, \mathbf{r}') [\nabla' \cdot \mathbf{M}_s^l(\mathbf{r}')] dS'_3 \right]
\end{aligned} \tag{6.3}$$

where  $\mathbf{r}_3 \in$  lower aperture.

### 6.3 Method of Moments

The MoM is an efficient way of electromagnetically modeling structures as pre-analysis, embedded in the Green's functions, is used to reduce the numerical computation that would otherwise be required in more general techniques such as finite element method (FEM) or finite difference method (FDM). This is especially true

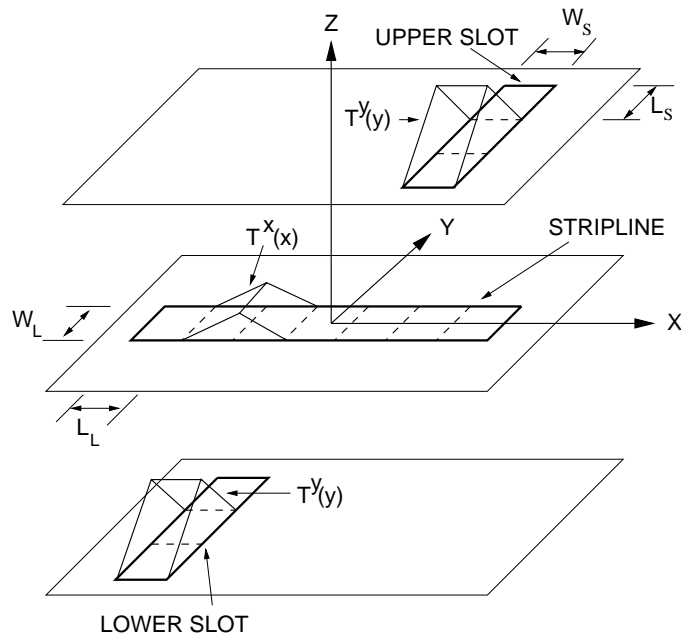


Figure 6.4: Discretization of the upper slot, lower slot, and stripline surfaces.

for antennas and open structures. As sub-domain current basis functions and differential (or delta-gap) voltages are used in MoM formulation, the compatibility with general purpose microwave circuit simulators which use terminal current and voltage quantities, is near optimum. In this section, the solution of the three MPIEs is presented using MoM.

### 6.3.1 Basis Functions

The formulation of the MoM is developed by expanding the magnetic and electric currents into basis functions. In the following analysis, the electric current is assumed to be in the  $x$ -direction and the magnetic current to be in the  $y$ -direction. The Cartesian components of the electric and magnetic surface currents are expanded

over a set of basis functions as shown in Fig. 6.4 and given by

$$M_s^u(y) = \sum_{i=1}^M V_i^u T_i^y(y) \quad (6.4)$$

$$J_s(x) = \sum_{i=1}^N I_i T_i^x(x) \quad (6.5)$$

$$M_s^l(y) = \sum_{i=1}^M V_i^l T_i^y(y) \quad (6.6)$$

where  $T_i^x(x)$  and  $T_i^y(y)$ , are the rooftop basis functions. Fig. 6.5 shows the  $T_i^x(x)$  and its associate surface charge density.  $T_i^x(x)$  and  $T_i^y(y)$  are defined by

$$T_i^s(s) = \begin{cases} [1 + (s - s_i)/L]/W, & s_i - l < s < s_i \\ [1 - (s - s_i)/L]/W, & s_i < s < s_i + l \\ 0, & \text{otherwise} \end{cases} \quad (6.7)$$

where  $s = x$  or  $y$ . The surface charge density is found using the continuity equation resulting in pulse doublet, see Fig. 6.5,

$$\Pi_i^s(s) = \begin{cases} -1/(LW), & s_i - L < s < s_i \\ 1/(LW), & s_i < s < s_i + l \\ 0, & \text{otherwise} \end{cases} \quad (6.8)$$

where again  $s = x$  or  $y$ .

### 6.3.2 Testing Functions

Upon introducing these distribution functions into the MPIE's and testing them, the following system of equations is obtained:

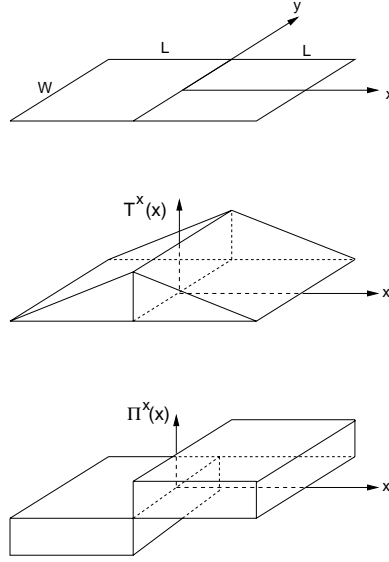


Figure 6.5:  $x$ -directed current cell centered at  $x = 0$  and its associate surface current density  $T^x(x)$ , and surface charge density  $\Pi^x(x)$ .

- On the upper slot :

$$\langle \Delta H_{y_{inc}}^u, T_j^y \rangle = j\omega \langle F_{y_{ji}}, T_j^y \rangle + \langle (\nabla \psi_{ji})_y, T_j^y \rangle - \frac{1}{\mu_0} \langle (\nabla \times \mathbf{A}_{ji})_y, T_j^y \rangle$$

$$j = 1 \cdots N \quad (6.9)$$

- On the stripline:

$$\langle E_{x_{inc}}, T_k^x \rangle = j\omega \langle A_{x_{ji}}, T_j^x \rangle + \langle (\nabla \phi_{ji})_x, T_j^x \rangle + \frac{1}{\epsilon} \langle (\nabla \times \mathbf{F}_{ji})_x, T_j^x \rangle$$

$$j = 1 \cdots M \quad (6.10)$$

- On the lower slot :

$$\langle \Delta H_{y_{inc}}^l, T_j^y \rangle = j\omega \langle F_{y_{ji}}, T_j^y \rangle + \langle (\nabla \psi_{ji})_y, T_j^y \rangle - \frac{1}{\mu_0} \langle (\nabla \times \mathbf{A}_{ji})_y, T_j^y \rangle$$

$$j = 1 \cdots N \quad (6.11)$$

where  $\langle, \rangle$  specifies the inner product operation.

### 6.3.3 Matrix Equation

After reformulating the equations above, the matrix equation becomes

$$\begin{bmatrix} \mathbf{I}_{inc}^u \\ \mathbf{V}_{inc} \\ \mathbf{I}_{inc}^l \end{bmatrix} = \begin{bmatrix} \mathbf{Y}^{uu} & \mathbf{U}^{us} & \mathbf{Y}^{ul} \\ \mathbf{W}^{su} & \mathbf{Z}^{ss} & \mathbf{W}^{sl} \\ \mathbf{Y}^{lu} & \mathbf{U}^{ls} & \mathbf{Y}^{ll} \end{bmatrix} \begin{bmatrix} \mathbf{V}^u \\ \mathbf{I} \\ \mathbf{V}^l \end{bmatrix} \quad (6.12)$$

where  $\mathbf{Y}^{uu}$  is an  $M \times M$  self-coupling submatrix of the upper slot,  $\mathbf{Y}^{ll}$  is an  $M \times M$  self-coupling submatrix of the lower slot,  $\mathbf{Z}^{ss}$  is an  $N \times N$  self-coupling submatrix of the stripline,  $\mathbf{U}^{us}$  is an  $M \times N$  coupling submatrix between the upper slot and the stripline,  $\mathbf{U}^{ls}$  is an  $M \times N$  coupling submatrix between the lower slot and the stripline,  $\mathbf{W}^{su}$  is an  $N \times M$  coupling submatrix between the stripline and the upper slot, and  $\mathbf{W}^{sl}$  is an  $N \times M$  coupling submatrix between the stripline and the lower slot. The element of these submatrices are given by:

$$\begin{aligned} Y_{ji}^{uu} &= j\omega \langle F_{y_{ji}}, T_j^y \rangle + \langle (\nabla \psi_{ji})_y, T_j^y \rangle \\ &= j\omega \int_{y_j-L_s}^{y_j+L_s} \int_{x_j-\frac{W_s}{2}}^{x_j+\frac{W_s}{2}} \int_{y_i-L_s}^{y_i+L_s} \int_{x_i-\frac{W_s}{2}}^{x_i+\frac{W_s}{2}} T_j^y(y) G_{F_{yy}}(\rho; h|h) T_i^y(y') dx' dy' dx dy \\ &\quad + \frac{1}{j\omega} \int_{y_j-L_s}^{y_j+L_s} \int_{x_j-\frac{W_s}{2}}^{x_j+\frac{W_s}{2}} \int_{y_i-L_s}^{y_i+L_s} \int_{x_i-\frac{W_s}{2}}^{x_i+\frac{W_s}{2}} \Pi_j^y(y) G_\psi(\rho; h|h) \Pi_i^y(y') dx' dy' dx dy \end{aligned} \quad (6.13)$$

$$\begin{aligned} Y_{ji}^{ll} &= j\omega \langle F_{y_{ji}}, T_j^y \rangle + \langle (\nabla \psi_{ji})_y, T_j^y \rangle \\ &= j\omega \int_{y_j-L_s}^{y_j+L_s} \int_{x_j-\frac{W_s}{2}}^{x_j+\frac{W_s}{2}} \int_{y_i-L_s}^{y_i+L_s} \int_{x_i-\frac{W_s}{2}}^{x_i+\frac{W_s}{2}} T_j^y(y) G_{F_{yy}}(\rho; -h|-h) T_i^y(y') dx' dy' dx dy \\ &\quad + \frac{1}{j\omega} \int_{y_j-L_s}^{y_j+L_s} \int_{x_j-\frac{W_s}{2}}^{x_j+\frac{W_s}{2}} \int_{y_i-L_s}^{y_i+L_s} \int_{x_i-\frac{W_s}{2}}^{x_i+\frac{W_s}{2}} \Pi_j^y(y) G_\psi(\rho; -h|-h) \Pi_i^y(y') dx' dy' dx dy \end{aligned} \quad (6.14)$$

$$Z_{ji}^{ss} = j\omega \langle A_{x_{ji}}^{int}, T_j \rangle + \langle (\nabla \phi_{ji}^{int})_x, T_j \rangle$$

$$\begin{aligned}
&= j\omega \int_{y_j - \frac{W_l}{2}}^{y_j + \frac{W_l}{2}} \int_{x_j - L_l}^{x_j + L_l} \int_{y_i - \frac{W_l}{2}}^{y_i + \frac{W_l}{2}} \int_{x_i - L_l}^{x_i + L_l} T_j^x(x) G_{A_{xx}}^{int}(\rho; 0|0) T_i^x(x') dx' dy' dx dy \\
&\quad + \frac{1}{j\omega} \int_{y_j - \frac{W_l}{2}}^{y_j + \frac{W_l}{2}} \int_{x_j - L_l}^{x_j + L_l} \int_{y_i - \frac{W_l}{2}}^{y_i + \frac{W_l}{2}} \int_{x_i - L_l}^{x_i + L_l} \Pi_j^x(x) G_{\phi}^{int}(\rho; 0|0) \Pi_i^x(x') dx' dy' dx dy
\end{aligned} \tag{6.15}$$

$$\begin{aligned}
Y_{ji}^{ul} &= j\omega \langle F_{yji}^{int}, T_j^y \rangle + \langle (\nabla \psi_{ji}^{int})_y, T_j^y \rangle \\
&= j\omega \int_{y_j - L_s}^{y_j + L_s} \int_{x_j - \frac{W_s}{2}}^{x_j + \frac{W_s}{2}} \int_{y_i - L_s}^{y_i + L_s} \int_{x_i - \frac{W_s}{2}}^{x_i + \frac{W_s}{2}} T_j^y(y) G_{F_{yy}}^{int}(\rho; h|h) T_i^y(y') dx' dy' dx dy \\
&\quad + \frac{1}{j\omega} \int_{y_j - L_s}^{y_j + L_s} \int_{x_j - \frac{W_s}{2}}^{x_j + \frac{W_s}{2}} \int_{y_i - L_s}^{y_i + L_s} \int_{x_i - \frac{W_s}{2}}^{x_i + \frac{W_s}{2}} \Pi_j^y(y) G_{\psi}^{int}(\rho; h|h) \Pi_i^y(y') dx' dy' dx dy
\end{aligned} \tag{6.16}$$

$$Y_{ji}^{lu} = Y_{ji}^{ul} \tag{6.17}$$

$$\begin{aligned}
W_{ji}^{su} &= -\frac{1}{\epsilon} \langle (\nabla \times \mathbf{F}_{ji}^{int})_x, T_j^x \rangle \\
&= -\frac{1}{\epsilon} \int_{y_j - \frac{W_l}{2}}^{y_j + \frac{W_l}{2}} \int_{x_j - L_l}^{x_j + L_l} \int_{y_i - L_s}^{y_i + L_s} \int_{x_i - \frac{W_s}{2}}^{x_i + \frac{W_s}{2}} T_j^x(x) \frac{\partial G_{F_{yy}}^{int}}{\partial z}(\rho; 0, h) T_i^y(y') dx' dy' dx dy
\end{aligned} \tag{6.18}$$

$$\begin{aligned}
W_{ji}^{sl} &= -\frac{1}{\epsilon} \langle (\nabla \times \mathbf{F}_{ji}^{int})_x, T_j^x \rangle \\
&= -\frac{1}{\epsilon} \int_{y_j - \frac{W_l}{2}}^{y_j + \frac{W_l}{2}} \int_{x_j - L_l}^{x_j + L_l} \int_{y_i - L_s}^{y_i + L_s} \int_{x_i - \frac{W_s}{2}}^{x_i + \frac{W_s}{2}} T_j^x(x) \frac{\partial G_{F_{yy}}^{int}}{\partial z}(\rho; 0, -h) T_i^y(y') dx' dy' dx dy
\end{aligned} \tag{6.19}$$

$$\begin{aligned}
U_{ji}^{us} &= \frac{1}{\mu_0} \langle (\nabla \times \mathbf{A}_{ji}^{int})_y, T_j^y \rangle \\
&= \frac{1}{\mu_0} \int_{y_j - L_s}^{y_j + L_s} \int_{x_j - \frac{W_s}{2}}^{x_j + \frac{W_s}{2}} \int_{y_i - \frac{W_l}{2}}^{y_i + \frac{W_l}{2}} \int_{x_i - L_l}^{x_i + L_l} T_j^y(y) \frac{\partial G_{A_{xx}}^{int}}{\partial z}(\rho; h, 0) T_i^x(x') dx' dy' dx dy
\end{aligned} \tag{6.20}$$

$$\begin{aligned}
U_{ji}^{ls} &= \frac{1}{\mu_0} \langle (\nabla \times \mathbf{A}_{ji}^{int})_y, T_j^y \rangle \\
&= \frac{1}{\mu_0} \int_{y_j-L_s}^{y_j+L_s} \int_{x_j-\frac{W_s}{2}}^{x_j+\frac{W_s}{2}} \int_{y_i-\frac{W_l}{2}}^{y_i+\frac{W_l}{2}} \int_{x_j-L_l}^{x_j+L_l} T_j^y(y) \frac{\partial G_{A_{xx}}^{int}}{\partial z}(\rho; -h, 0) T_i^x(x') dx' dy' dx dy
\end{aligned} \tag{6.21}$$

The vectors,  $\mathbf{V}^u$  of length  $M$ ,  $\mathbf{I}$  of length  $N$ , and  $\mathbf{V}^l$  of length  $M$ , are the unknown coefficients of the basis functions on the upper slot, stripline, and lower slot respectively. The  $\mathbf{I}_{inc}^u$ ,  $\mathbf{V}_{inc}$ ,  $\mathbf{I}_{inc}^l$  are the external excitation vectors from the external sources and their elements are

$$I_{inc_j}^u = \int_{y_j-L_s}^{y_j+L_s} \int_{x_j-\frac{W_s}{2}}^{x_j+\frac{W_s}{2}} T_j^y(y) \Delta H_u^{inc} dx dy \tag{6.22}$$

$$V_{inc_j} = \int_{y_j-\frac{W_l}{2}}^{y_j+\frac{W_l}{2}} \int_{x_j-L_s}^{x_j+L_s} T_j^x(x) E_y^{inc} dx dy \tag{6.23}$$

$$I_{inc_j}^l = \int_{y_j-L_s}^{y_j+L_s} \int_{x_j-\frac{W_s}{2}}^{x_j+\frac{W_s}{2}} T_j^y(y) \Delta H_l^{inc} dx dy \tag{6.24}$$

### 6.3.4 Cascadable Representation

The MoM matrix in (6.12) is further partitioned three ways: an array structure matrix; the left side matrix; and the right side matrix. The Green's functions of the array structure have been determined. The left and right side Green's functions are calculated separately and they depend on the cascading structures[208]. The MoM matrix in (6.12) is therefore calculated as

$$\begin{bmatrix} \mathbf{Y}^{uu} & \mathbf{U}^{us} & \mathbf{Y}^{ul} \\ \mathbf{W}^{su} & \mathbf{Z}^{ss} & \mathbf{W}^{sl} \\ \mathbf{Y}^{lu} & \mathbf{U}^{ls} & \mathbf{Y}^{ll} \end{bmatrix} = \begin{bmatrix} \mathbf{Y}_{ext}^{uu} & \mathbf{0} & \mathbf{0} \\ \mathbf{0} & \mathbf{0} & \mathbf{0} \\ \mathbf{0} & \mathbf{0} & \mathbf{0} \end{bmatrix} + \begin{bmatrix} \mathbf{Y}_{int}^{uu} & \mathbf{U}^{us} & \mathbf{Y}^{ul} \\ \mathbf{W}^{su} & \mathbf{Z}^{ss} & \mathbf{W}^{sl} \\ \mathbf{Y}^{lu} & \mathbf{U}^{ls} & \mathbf{Y}_{int}^{ll} \end{bmatrix} + \begin{bmatrix} \mathbf{0} & \mathbf{0} & \mathbf{0} \\ \mathbf{0} & \mathbf{0} & \mathbf{0} \\ \mathbf{0} & \mathbf{0} & \mathbf{Y}_{ext}^{ll} \end{bmatrix} \tag{6.25}$$

where  $\mathbf{Y}_{ext}^{uu}$  and  $\mathbf{Y}_{ext}^{ll}$  are the mutual coupling integrals for the external left and right sides respectively as shown in Fig. 6.6 whereas  $\mathbf{Y}_{int}^{uu}$  and  $\mathbf{Y}_{int}^{ll}$  are the mutual coupling integrals for the closed structure. These matrix elements are given by:

$$\begin{aligned}
Y_{extji}^{uu} &= j\omega \langle F_y^{ext}{}_{ji}, T_j^y \rangle + \langle (\nabla \psi_{ji})_y, T_j^y \rangle \\
&= j\omega \int_{y_j-L_s}^{y_j+L_s} \int_{x_j-\frac{W_s}{2}}^{x_j+\frac{W_s}{2}} \int_{y_i-L_s}^{y_i+L_s} \int_{x_i-\frac{W_s}{2}}^{x_i+\frac{W_s}{2}} T_j^y(y) G_{F_{yy}}^{ext}(\rho; h|h) T_i^y(y') dx' dy' dx dy \\
&\quad + \frac{1}{j\omega} \int_{y_j-L_s}^{y_j+L_s} \int_{x_j-\frac{W_s}{2}}^{x_j+\frac{W_s}{2}} \int_{y_i-L_s}^{y_i+L_s} \int_{x_i-\frac{W_s}{2}}^{x_i+\frac{W_s}{2}} \Pi_j^y(y) G_{\psi}^{ext}(\rho; h|h) \Pi_i^y(y') dx' dy' dx dy
\end{aligned} \tag{6.26}$$

$$\begin{aligned}
Y_{extji}^{ll} &= j\omega \langle F_y^{ext}{}_{ji}, T_j^y \rangle + \langle (\nabla \psi_{ji})_y, T_j^y \rangle \\
&= j\omega \int_{y_j-L_s}^{y_j+L_s} \int_{x_j-\frac{W_s}{2}}^{x_j+\frac{W_s}{2}} \int_{y_i-L_s}^{y_i+L_s} \int_{x_i-\frac{W_s}{2}}^{x_i+\frac{W_s}{2}} T_j^y(y) G_{F_{yy}}^{ext}(\rho; -h|-h) T_i^y(y') dx' dy' dx dy \\
&\quad + \frac{1}{j\omega} \int_{y_j-L_s}^{y_j+L_s} \int_{x_j-\frac{W_s}{2}}^{x_j+\frac{W_s}{2}} \int_{y_i-L_s}^{y_i+L_s} \int_{x_i-\frac{W_s}{2}}^{x_i+\frac{W_s}{2}} \Pi_j^y(y) G_{\psi}^{ext}(\rho; -h|-h) \Pi_i^y(y') dx' dy' dx dy
\end{aligned} \tag{6.27}$$

$$\begin{aligned}
Y_{intji}^{uu} &= j\omega \langle F_y^{int}{}_{ji}, T_j^y \rangle + \langle (\nabla \psi_{ji})_y, T_j^y \rangle \\
&= j\omega \int_{y_j-L_s}^{y_j+L_s} \int_{x_j-\frac{W_s}{2}}^{x_j+\frac{W_s}{2}} \int_{y_i-L_s}^{y_i+L_s} \int_{x_i-\frac{W_s}{2}}^{x_i+\frac{W_s}{2}} T_j^y(y) G_{F_{yy}}^{int}(\rho; h|h) T_i^y(y') dx' dy' dx dy \\
&\quad + \frac{1}{j\omega} \int_{y_j-L_s}^{y_j+L_s} \int_{x_j-\frac{W_s}{2}}^{x_j+\frac{W_s}{2}} \int_{y_i-L_s}^{y_i+L_s} \int_{x_i-\frac{W_s}{2}}^{x_i+\frac{W_s}{2}} \Pi_j^y(y) G_{\psi}^{int}(\rho; h|h) \Pi_i^y(y') dx' dy' dx dy
\end{aligned} \tag{6.28}$$

$$\begin{aligned}
Y_{intji}^{ll} &= j\omega \langle F_y^{int}{}_{ji}, T_j^y \rangle + \langle (\nabla \psi_{ji})_y, T_j^y \rangle \\
&= j\omega \int_{y_j-L_s}^{y_j+L_s} \int_{x_j-\frac{W_s}{2}}^{x_j+\frac{W_s}{2}} \int_{y_i-L_s}^{y_i+L_s} \int_{x_i-\frac{W_s}{2}}^{x_i+\frac{W_s}{2}} T_j^y(y) G_{F_{yy}}^{int}(\rho; -h|-h) T_i^y(y') dx' dy' dx dy \\
&\quad + \frac{1}{j\omega} \int_{y_j-L_s}^{y_j+L_s} \int_{x_j-\frac{W_s}{2}}^{x_j+\frac{W_s}{2}} \int_{y_i-L_s}^{y_i+L_s} \int_{x_i-\frac{W_s}{2}}^{x_i+\frac{W_s}{2}} \Pi_j^y(y) G_{\psi}^{int}(\rho; -h|-h) \Pi_i^y(y') dx' dy' dx dy
\end{aligned} \tag{6.29}$$

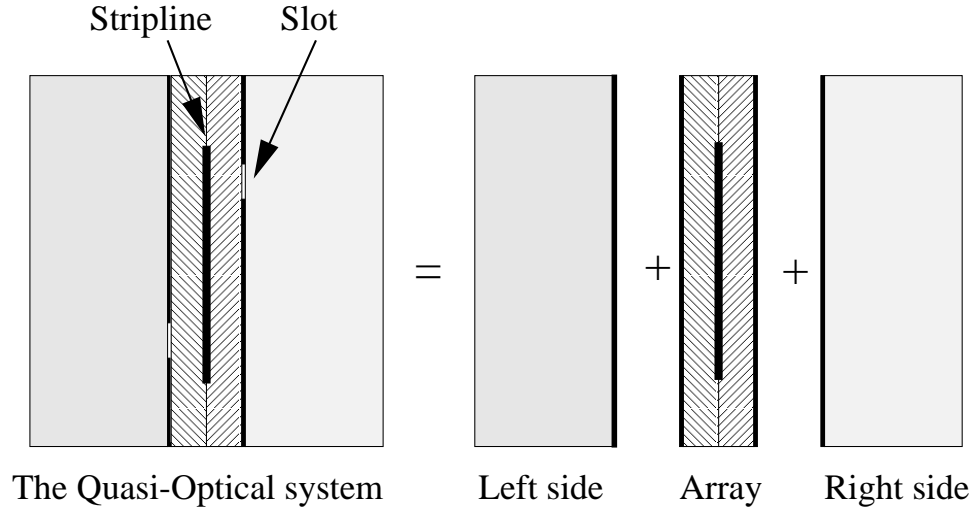


Figure 6.6: Segmentation of the slot array system.

This cascadable representation of the electromagnetic environment is important for efficient computation. It supports efficient implementation by maximizing reusability of previously calculated quantities (e.g. for equi-spaced cells) and representing different parts of the structure as circuit-like elements.

### 6.3.5 Spectral Domain Matrix Elements

By using the dyadic Green's functions in the spectral domain given in Sections 5.6, the self and overlapped cells MoM matrix elements are given by

$$Y_{ji}^{uu} = \frac{-1}{4\pi^2} \int_{-\infty}^{\infty} \int_{-\infty}^{\infty} \tilde{G}_{HM_{yy}}(k_x, k_y) \tilde{T}_j^y(k_x, k_y)^* \tilde{T}_i^y(k_x, k_y) dk_x dk_y \quad (6.30)$$

$$Y_{ji}^{ll} = \frac{-1}{4\pi^2} \int_{-\infty}^{\infty} \int_{-\infty}^{\infty} \tilde{G}_{HM_{yy}}(k_x, k_y) \tilde{T}_j^y(k_x, k_y)^* \tilde{T}_i^y(k_x, k_y) dk_x dk_y \quad (6.31)$$

$$Z_{ji}^{ss} = \frac{-1}{4\pi^2} \int_{-\infty}^{\infty} \int_{-\infty}^{\infty} \tilde{G}_{EJ_{xx}}(k_x, k_y) \tilde{T}_j^x(k_x, k_y)^* \tilde{T}_i^x(k_x, k_y) dk_x dk_y \quad (6.32)$$

where  $\tilde{T}^x$  and  $\tilde{T}^y$  are the Fourier transforms of the  $x$ - and  $y$ -directed rooftop basis functions, respectively, and the  $(*)$  denotes the complex conjugate.

## 6.4 Network Characterization for the SSS Array

The tight coupling of the antennas, circuit and electromagnetic (EM) environment requires global modeling of the entire, finite-sized structure and strategies for treating the EM model as an integral part of the circuit model [203, 204, 188].

The aim of this section is to develop a single network representation of the EM structure. The network is interfaced to circuit models at “electromagnetic terminals” defined to be consistent with nodal-based circuit descriptions. The depiction shown in Fig. 6.7 shows how the passive structure is reduced to an integrated model for a unit cell. In modeling an  $N \times N$  array the two port network is replaced by a network with  $2N^2$  ports. Input excitation is modeled using  $N$  equivalent sources at the input-side ports of the network. Each of the ports in Fig. 6.7 must be interfaced to the conventional circuit at normal current/voltage defined terminals referenced to the ground planes. The terminals so referenced are called circuit ports whereas the ports immediately available from MoM analysis are differential ports [184, 185, 188]. The main contribution of this work is the development and contrasting of a number of techniques for extracting the network parameters at circuit ports from EM-device characterization at differential ports. Earlier work by our group relates these to the nodal parameters required by circuit simulators [204].

### 6.4.1 Introduction

Incorporation of EM characterization in a circuit model requires extraction of immittance like parameters at ports compatible with circuit concepts. Without loss of generality consider the structure in Fig. 6.2, circuit compatibility requires that the parameters be referred to ports each of which has one terminal located on the stripline and the other located at the ground plane (assuming that the two ground

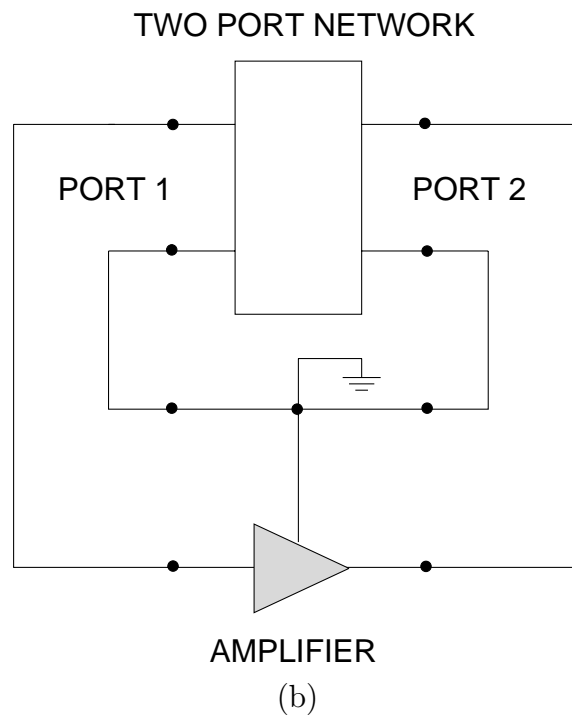
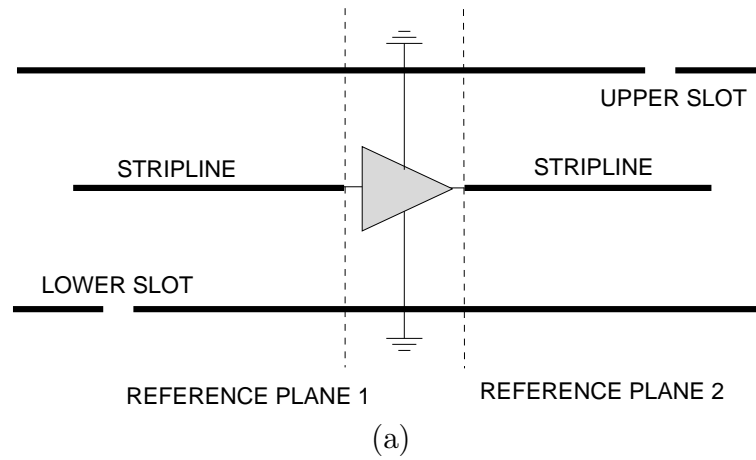


Figure 6.7: Slot-stripline-slot: (a) amplifier unit cell; (b) equivalent network.

planes are electrically identical). However only differential ports, with each port having two terminals located on either side of a break in the stripline is immediately available from EM analysis. In this section four techniques, illustrated in Fig. 6.8, are presented for translating the parameters extracted at the differential ports to parameters referred to the circuit ports. The first, Fig. 6.8 (a), uses standard *standing wave characterization* determined by detecting the standing wave pattern on the line. Practically this is used only for one-port structures as multiport characterization would require multiple EM analyses with various impedance terminations at ports not being driven. However only one MoM matrix fill operation is required. The *stub de-embedding* technique, Fig. 6.8 (b), is also used for one-port characterization, subsequently using removing the impedance of the open circuit stub from the differential impedance to obtain the circuit port impedance. The third approach, Fig. 6.8 (c), uses an open circuit *quarter wavelength stub* to present a short-circuit at one terminal of a differential port thus transforming the differential port into the desired circuit port. The final technique, Fig. 6.8 (d), a *vertical stub* effectively introduces a conductor from the ground plane to the stripline so that the differential port between the wire and the stripline because the desired circuit port in the MoM formulation. The techniques are described in greater detail below referring to the extraction of the input impedance,  $Z_{PORT}$ , of the simpler structure in Fig. 6.9.

### 6.4.2 Standing Wave Characterization

The *standing wave characterization* method mimics a laboratory measurement procedure as source is applied to a port and the standing wave pattern detected, see Fig. 6.8(a). Here a delta-gap source is introduced between two MoM cells at the differential port. From the standing wave pattern enables the input reflection coef-

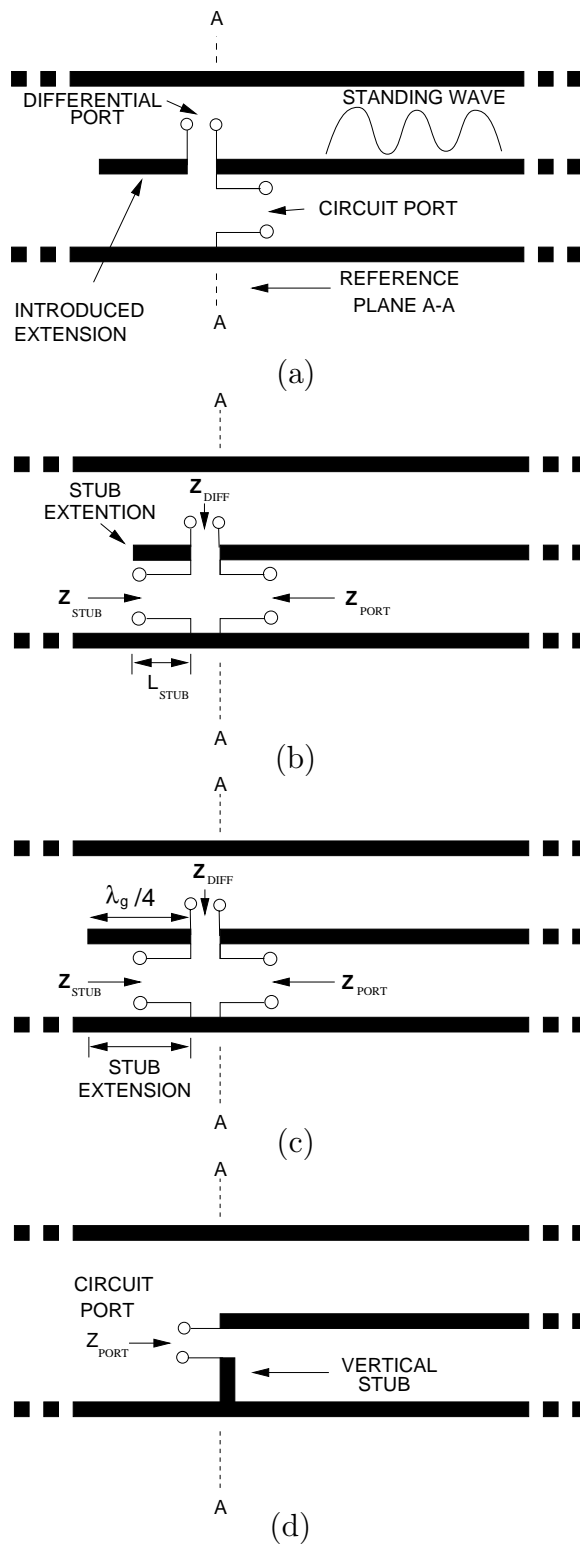


Figure 6.8: Four techniques for establishing a circuit ports in MoM analysis: (a) standing wave characterization, (b) stub-de-embedding; (c) quarter wavelength stub; and (d) Vertical stub.

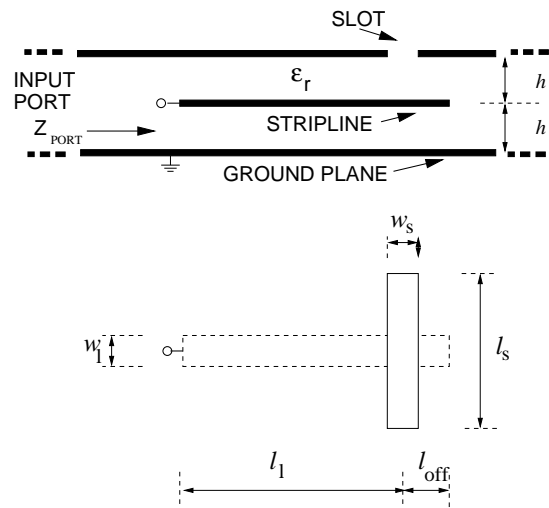


Figure 6.9: Single port.

ficient to be determined and referred to the desired reference plane. In this manner the discontinuity introduced by the source and the line extension does not affect the characterization. Multiport parameters are obtained by either exciting one port at a time and detecting the standing wave pattern at the other port or, by determining the input reflection coefficient at one port at a time with various loads at the other ports using a multiport extraction procedure [180, 181]. The number of additional calculations required increases combinatorially as the number of ports increases and so the method is practically unusable for the characterization of large multiport EM structures. Generally an additional length of the line, at least one wavelength, must be introduced between the excitation source and the reference plane to ensure TEM propagation where the standing wave pattern is detected. However, in some situation it may not be possible to insert such a long line. If the line can be inserted without interfering with the structure being model, coupling between the added line and the rest of the circuit can be excluded during matrix fill.

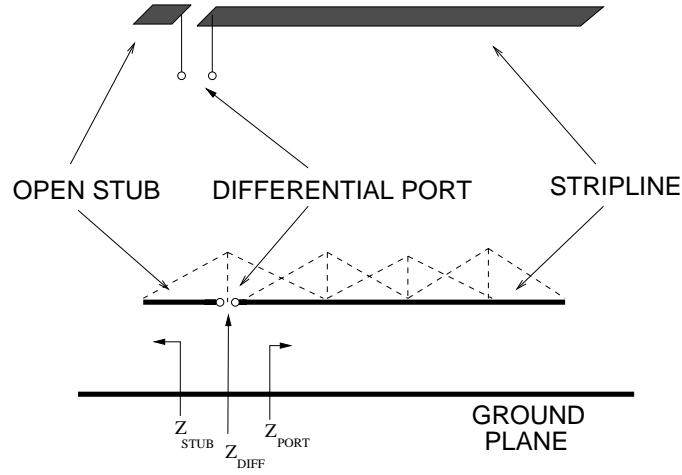


Figure 6.10: Port definition for differential port and the differential bases cells.

### 6.4.3 Stub De-embedding

The stub de-embedding procedure is illustrated in Fig. 6.8(b). The input impedance calculated directly from the MoM with and introduced stub of length  $L_{STUB}$  is the impedance  $Z_{DIFF}$  looking into the differential port which is the series combination of  $Z_{PORT}$  and the stub impedance  $Z_{STUB}$ , see Fig. 6.10 so that

$$Z_{PORT} = Z_{DIFF} - Z_{STUB} \quad (6.33)$$

$Z_{STUB} = Z_c \coth(\gamma L_{STUB})$  where the characteristic impedance  $Z_c$  and the propagation constant  $\gamma$  can be determined analytically or numerically. For an  $N$ -port structure an  $N \times N$  differential impedance matrix  $\mathbf{Z}_{DIFF}$  can be extracted from the inverted and then reduced form of the MoM impedance matrix (details are provided in [188]). Then the  $\mathbf{Z}_{PORT}$  matrix, also  $N \times N$  is

$$\mathbf{Z}_{PORT} = \mathbf{Z}_{DIFF} - \mathbf{Z}_{STUB} \quad (6.34)$$

and  $\mathbf{Z}_{STUB}$  is a diagonal matrix with elements  $Z_{STUB,i}$ ,  $i = 1, \dots, N$  at the  $i$ th port. This method is computationally efficient as there is only one MoM matrix fill and solve. However the method does not account for fringing effects at end of the stub, nor possible non-TEM mode excitation on the stub and increases the size of the MoM matrix. Also as in two port structure in Fig. 6.2, it is not always be physically possible to insert the stub, even if it is of the minimum half basis function length.

#### 6.4.4 Quarter-Wavelength Stub

If the stub of the previous technique is one quarter wavelength long,  $\mathbf{Z}_{PORT}$  can be calculated directly from the MoM as the  $\mathbf{Z}_{STUB} = \mathbf{0}$  and so  $\mathbf{Z}_{PORT} = \mathbf{Z}_{DIFF}$  see Fig. 6.8(c). The open circuit stub increases the MoM matrix size and has the same drawbacks of the previous method, but the advantage that the characteristic impedance of the stub is not require. Also, the physical length of the stub must be changed with frequency.

#### 6.4.5 Vertical Stub

The introduction of a vertical stub, see Fig. 6.8(d), brings the ground reference up to the strip and forms a differential port which approximates the circuit port:  $\mathbf{Z}_{PORT} \approx \mathbf{Z}_{DIFF}$ . An appropriate basis function selection for one port is shown in Fig. 6.11. With a half rooftop basis function on the strip side of the port and pulse basis function on the vertical stub both with current  $I^t$  at the port terminals. The differential constrain imposed by  $I^t$  being the coefficient of two basis functions

results in an expanded form of the MoM impedance matrix for an  $N$  port system:

$$\begin{bmatrix} \mathbf{Z}^{cc} & \mathbf{Z}^{ct} \\ \mathbf{Z}^{tc} & \mathbf{Z}^{tt} \end{bmatrix} \begin{bmatrix} \mathbf{I}^c \\ \mathbf{I}^t \end{bmatrix} = \begin{bmatrix} \mathbf{0} \\ \mathbf{V}^t \end{bmatrix} \quad (6.35)$$

where the superscript  $t$  denotes terminal quantities and the superscript  $c$  denotes quantities pertinent to currents induced on the conductor surface.  $\mathbf{I}^c$  and  $\mathbf{I}^t$  are the vectors of conductor and terminal current respectively, and  $\mathbf{Z}^{cc}$  in (6.35) is the MoM impedance matrix using the full rooftop basis functions.  $\mathbf{V}^t$  is the vector of delta-gap voltage generators at the circuit ports and  $\mathbf{I}^t$  is the vector of the port currents. The port admittance matrix  $\mathbf{Y}^t$ , defined by  $\mathbf{I}^t = \mathbf{Y}^t \mathbf{V}^t$ , is obtained as follows: from (6.35)

$$\begin{bmatrix} \mathbf{I}^c \\ \mathbf{I}^t \end{bmatrix} = \begin{bmatrix} \mathbf{Z}^{cc} & \mathbf{Z}^{ct} \\ \mathbf{Z}^{tc} & \mathbf{Z}^{tt} \end{bmatrix}^{-1} \begin{bmatrix} \mathbf{0} \\ \mathbf{V}^t \end{bmatrix} \quad (6.36)$$

or

$$\begin{bmatrix} \mathbf{I}^c \\ \mathbf{I}^t \end{bmatrix} = \begin{bmatrix} \mathbf{Y}^{cc} & \mathbf{Y}^{ct} \\ \mathbf{Y}^{tc} & \mathbf{Y}^{tt} \end{bmatrix} \begin{bmatrix} \mathbf{0} \\ \mathbf{V}^t \end{bmatrix}. \quad (6.37)$$

From (6.37),  $\mathbf{Y}^t = \mathbf{Y}^{tt}$  which is the  $N \times N$  submatrix in the lower right hand corner of the inverted impedance matrix in (6.36). This method introduces the smallest discontinuity and can be used with any multiport configuration in microstrip or stripline.

### Spatial Domain vertical Current basis Matrix Elements

A new vector must be added to the MoM matrix (6.36) to include the effect of the vertical connection to the ground. This vector represents the coupling between the transverse field ( $x$ -direction) generated by the vertical current ( $z$ -direction). This

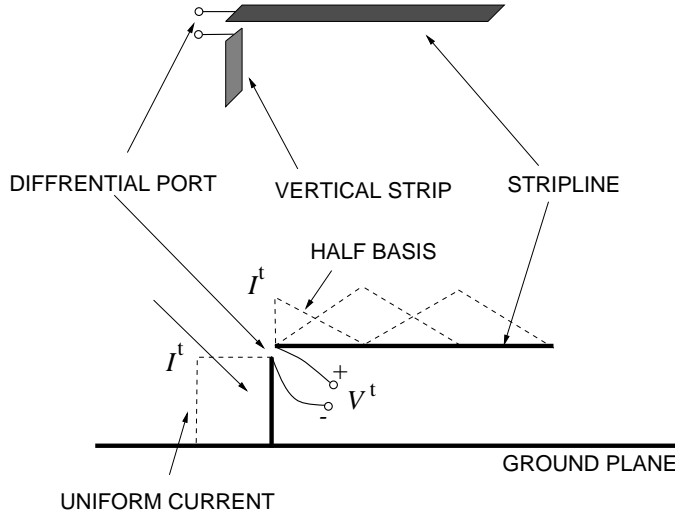


Figure 6.11: Port definition for a unit cell using vertical current cell and half cell.

vector is added to the the MoM matrix as

$$\begin{bmatrix} \mathbf{Z}_{new}^{cc} & \mathbf{Z}_{new}^{ct} \\ \mathbf{Z}_{new}^{tc} & \mathbf{Z}_{new}^{tt} \end{bmatrix} = \begin{bmatrix} \mathbf{Z}^{cc} & \mathbf{Z}^{ct} \\ \mathbf{Z}^{tc} & \mathbf{Z}^{tt} \end{bmatrix} + \begin{bmatrix} \mathbf{0} & \mathbf{Z}_{xzct} \\ \mathbf{0} & \mathbf{Z}_{xztt} \end{bmatrix} \quad (6.38)$$

where  $\mathbf{Z}_{xzct}$  is the coupling matrix between the vertical strip and the complete basis cells and  $\mathbf{Z}_{xztt}$  is the coupling matrix between the vertical strip and the half basis cells( port cells). Their elements are given by

$$\begin{aligned} Z_{ji}^{xzct} &= j\omega \int_{y_j - \frac{W_l}{2}}^{y_j + \frac{W_l}{2}} \int_{x_j - L_l}^{x_j + L_l} \int_{y_i - \frac{W_l}{2}}^{y_i + \frac{W_l}{2}} \int_{-h}^0 T_j^x(x) G_{A_{xz}}^{int}(x|x'; y|y'; 0|z') dz' dy' dx dy \\ &+ \frac{1}{j\omega} \int_{y_j - \frac{W_l}{2}}^{y_j + \frac{W_l}{2}} \int_{x_j - L_l}^{x_j + L_l} \int_{y_i - \frac{W_l}{2}}^{y_i + \frac{W_l}{2}} \int_{-h}^0 \Pi_j^x(x) G_{\phi}^{int}(x|x'; y|y'; 0|z') \delta(z') dz' dy' dx dy \end{aligned} \quad (6.39)$$

$$\begin{aligned} Z_{ji}^{xztt} &= j\omega \int_{y_j - \frac{W_l}{2}}^{y_j + \frac{W_l}{2}} \int_{x_p}^{x_p + L_l} \int_{y_i - \frac{W_l}{2}}^{y_i + \frac{W_l}{2}} \int_{-h}^0 T_j^x(x) G_{A_{xz}}^{int}(x|x_p; y|y'; 0|z') dz' dy' dx dy \\ &+ \frac{1}{j\omega} \int_{y_j - \frac{W_l}{2}}^{y_j + \frac{W_l}{2}} \int_{x_p}^{x_p + L_l} \int_{y_i - \frac{W_l}{2}}^{y_i + \frac{W_l}{2}} \int_{-h}^0 \Pi_j^x(x) G_{\phi}^{int}(x|x_p; y|y'; 0|z') \delta(z') dz' dy' dx dy. \end{aligned} \quad (6.40)$$

where the vertical connection at  $x_p$ .

### Spectral Domain Half Basis Matrix Elements

Filling the moment matrix in (6.38) now requires interactions containing a mixture of half and complete rooftop basis functions. In order to evaluate these new elements in the spectral domain, we need to consider the Fourier transforms of the half basis elements.

The Fourier transform of the rooftop basis function in Fig. 6.5 is rewritten here as

$$\tilde{T}_{iT}^x(k_x, k_y) = 2A_x B_y e^{-jk_x x_i} e^{-jk_y y_i} \quad (6.41)$$

where

$$A_x = \frac{L}{2} \left[ \frac{\sin(k_x L/2)}{k_x L/2} \right]^2 \quad (6.42)$$

$$B_y = \frac{\sin(k_y W/2)}{(k_y W/2)} \quad (6.43)$$

$$D_x = \frac{k_x L - \sin(k_x L)}{k_x^2 L}. \quad (6.44)$$

Dividing the rooftop basis function up into two halves yield the following Fourier transforms:

$$\tilde{T}_{iL}^x(k_x, k_y) = (A_x + jD_x) B_y e^{-jk_x x_i} e^{-jk_y y_i} \quad (6.45)$$

for the left half of the basis element and

$$\tilde{T}_{iR}^x(k_x, k_y) = (A_x - jD_x) B_y e^{-jk_x x_i} e^{-jk_y y_i} \quad (6.46)$$

for the right half side. The subscripts  $T$ ,  $L$ , and  $R$  in equations (6.41), (6.45) and (6.46) denote a total basis, left half basis and right half basis, respectively. Summing both halves in (6.45) and (6.46) yields the total basis in (6.41).

The different configurations for the  $xx$  moment matrix elements are shown in Fig.

6.12. The moment matrix elements are formulated using the even and odd properties

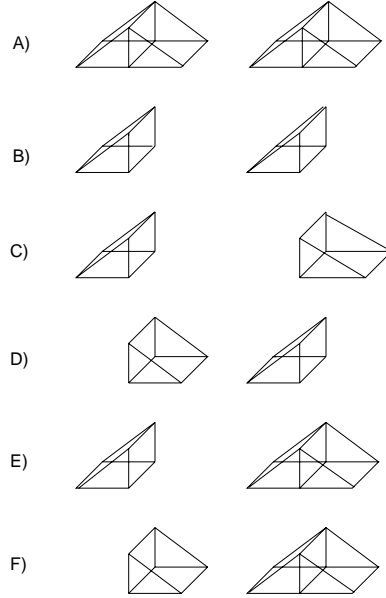


Figure 6.12: Configuration of  $x$ -directed rooftop basis functions with the source basis in the left column and the test basis in the right column.

of the integrand and converting to polar coordinates as was done in Section 4.5 and referring to Fig. 6.12, the  $xx$  moment matrix elements are given as follows:

case A ( $xx$  components of  $\mathbf{Z}^{cc}$ )

$$Z_{ji}^{cc} = \frac{-1}{\pi^2} \int_0^{\pi/2} \int_0^\infty 4\tilde{G}_{EJ_{xx}} A_x^2 B_y^2 C_x C_y \beta d\beta d\alpha \quad (6.47)$$

case B ( $xx$  components of  $\mathbf{Z}^{tt}$ )

$$Z_{ji}^{tt} = \frac{-1}{\pi^2} \int_0^{\pi/2} \int_0^\infty \tilde{G}_{EJ_{xx}} (A_x^2 + D_x^2) B_y^2 C_x C_y \beta d\beta d\alpha \quad (6.48)$$

case C ( $xx$  components of  $\mathbf{Z}^{tt}$ )

$$Z_{ji}^{tt} = \frac{-1}{\pi^2} \int_0^{\pi/2} \int_0^\infty \tilde{G}_{E_{xx}} [(A_x^2 - D_x^2) C_x - 2A_x D_x S_x] B_y^2 C_y \beta d\beta d\alpha \quad (6.49)$$

case D ( $xx$  components of  $\mathbf{Z}^{tt}$ )

$$Z_{ji}^{tt} = \frac{-1}{\pi^2} \int_0^{\pi/2} \int_0^\infty \tilde{G}_{EJ_{xx}} [(A_x^2 - D_x^2) C_x + 2A_x D_x S_x] B_y^2 C_y \beta d\beta d\alpha \quad (6.50)$$

case E ( $xx$  components of  $\mathbf{Z}^{ct}$  and  $\mathbf{Z}^{tc}$ )

$$Z_{ji}^{tc} = \frac{-1}{\pi^2} \int_0^{\pi/2} \int_0^\infty 2\tilde{G}_{EJ_{xx}} [A_x^2 C_x - A_x D_x S_x] B_y^2 C_y \beta d\beta d\alpha \quad (6.51)$$

case F ( $xx$  components of  $\mathbf{Z}^{ct}$  and  $\mathbf{Z}^{tc}$ )

$$Z_{ji}^{tc} = \frac{-1}{\pi^2} \int_0^{\pi/2} \int_0^\infty 2\tilde{G}_{EJ_{xx}} [A_x^2 C_x + A_x D_x S_x] B_y^2 C_y \beta d\beta d\alpha \quad (6.52)$$

where

$$C_x = \cos [k_x (x_j - x_i)] \quad (6.53)$$

$$S_x = \sin [k_x (x_j - x_i)] \quad (6.54)$$

$$C_y = \cos [k_y (y_j - y_i)]. \quad (6.55)$$

The same procedure is applied for finding the other elements.

## 6.5 Results

Fig. 6.13 compares the return loss of a single slot shown in Fig. 6.9 calculated using the differential impedance  $Z_{DIFF}$  and using port impedance  $Z_{PORT}$ . This slot antenna has a minimum return loss of 9 dB at 4.5 GHz. The return loss based on the differential impedance gives a return loss of about 1 dB at the same frequency (4.5 GHz) which is not the actual value. It is obvious from this comparison that the network characterization and extraction of the passive circuit parameters should be carefully handled otherwise an accurate result will not be guaranteed.

To illustrate and verify that the differential impedance may be used as a port impedance in case of the quarter-wavelength stub method. Fig. 6.14 shows the return loss when the differential input impedance is calculated for the same single

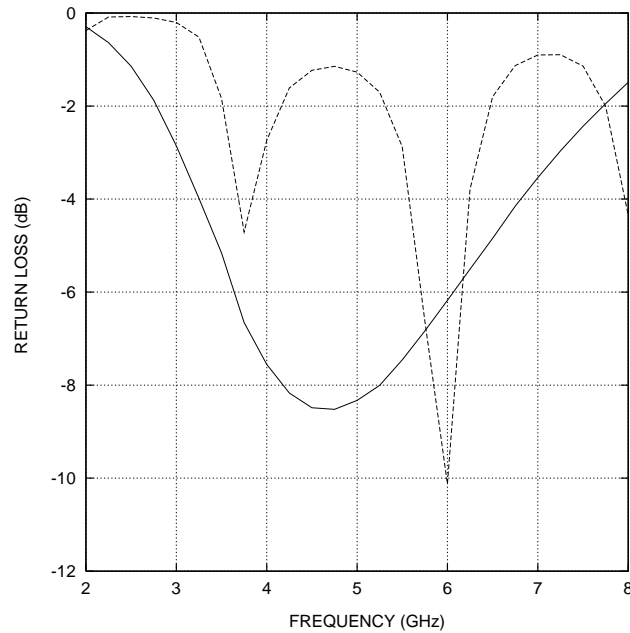


Figure 6.13: Return loss for single slot antenna using: (a) port impedance  $Z_{PORT}$  (solid line); and (b) differential impedance  $Z_{DIFF}$  (dotted line). Referring to Fig. 6.9  $l_L = 50$  mm,  $W_L = 2.5$  mm,  $l_S = 30$  mm,  $W_S = 2$  mm,  $l_{OFF} = 10$  mm,  $h = 1.57$  mm, and  $\epsilon_r = 2.2$ .

slot structure but with making the open circuit stub length equals to the quarter wavelengths and the other curve by [209] was calculated using the *standing wave method*. Good agreement has been shown.

As a comparison between the techniques presented in this work, Figs. 6.15 and 6.16 show the input impedance for the same structure using the three different method. Fig. 6.15 shows the input resistance. Since the resistive part of the impedance comes only from the antenna radiation, the difference between the three method is not noticeable because the resistive part does not affected by the stub modification which is mainly reactive part. Otherwise in Fig. 6.16 the imaginary part of the input impedance is changed from method to another. The difference between these values is due to the stub reactance which is added to the circuit when

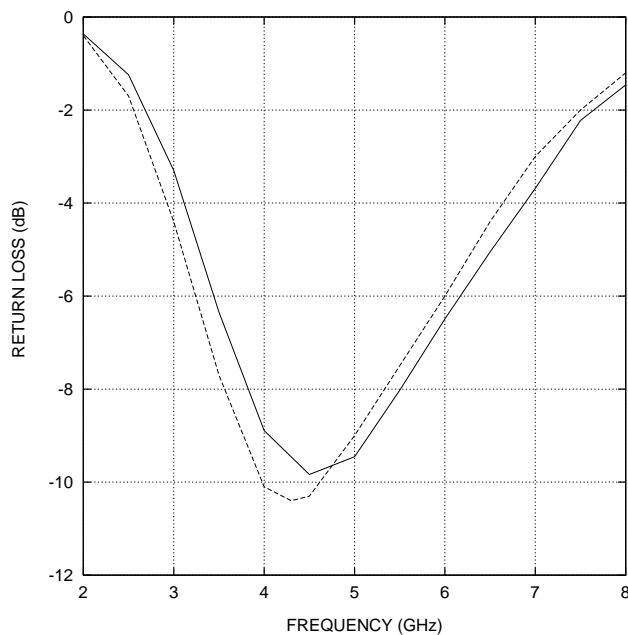


Figure 6.14: Return loss for single port slot antenna: (a) using  $\lambda/4$  stub (solid line); and (b) reflection coefficient method after [209] (dotted line).

the stub is used. For example, in the vertical stub method the vertical stub reactance is included in the input impedance of the circuit which could be inductive or capacitive. This added reactance is a function of the operating frequency. However the value of this reactance changes the value of the input impedance, this input impedance is the actual circuit impedance seen by the active device.

## 6.6 Summary

A straightforward and computationally efficient technique for extracting the multi-port impedance matrix of a system with ports referenced to ground was presented. This matrix is derived from differential port-based impedance matrix in the MoM analysis. The original differential port-base matrix is modified by inserting a stub

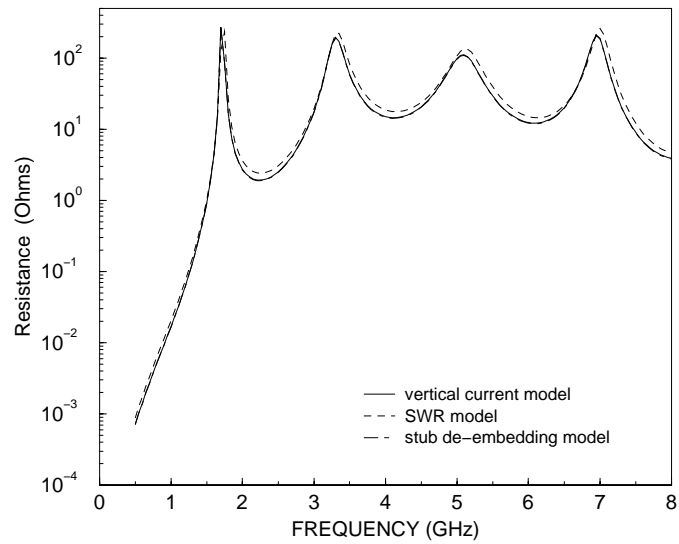


Figure 6.15: Resistance of single slot circuit in Fig. 6.9.

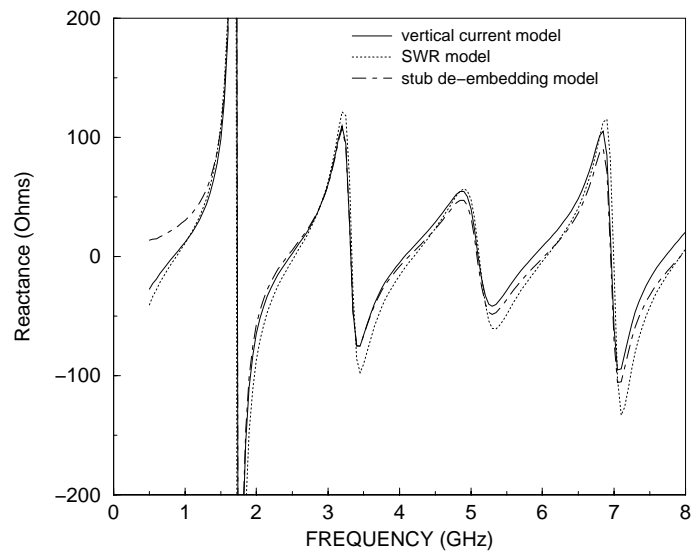


Figure 6.16: Reactance of single slot circuit in Fig. 6.9.

which in effect short one side of a differential port to ground.

As well, an MoM formulation for a SSS configurations was developed. This formulation is in a cascable form to permit maximum utilization of precomputed results. So that, if the cell-to-cell interactions in the central stripline region are negligible the characterization of the central stripline region of a single cell can be reused.



## Chapter 7

# CPW-Slot Antennas for Spatial Power Combining Applications

### 7.1 Introduction

In this chapter, the investigation and simulation of CPW based slot active antennas and arrays are presented. The simulation here is based on the MPIE-MoM model introduced in Chapter 3 and 4. We also show how *ArraySim*[6] is used to study the behavior of various CPW based slot antennas. Most of the analysis and simulations are oriented in the direction of spatial power combining applications, however these studies could be more general as an analysis and design of CPW based slot antennas.

In the beginning of this chapter, Section 7.2, the EIPG of spatial amplifier array is introduced to define the spatial amplifier overall gain. After this introductory section, the simulated arrays are presented in the two following sections. Section 7.3 presents the analysis and design of folded-slot antennas and an array. The simulated EIPG for a unit cell and a  $4 \times 4$  array are presented. The simulation results were verified with measurements that were taken at the University of California Santa Barbara (UCSB) [210]. In Section 7.4, a discussion of array configurations and their effects on the array performance has been presented. In the following section, Section 7.5, another type of slot array, five-slot antenna is analyzed and simulated. In this section, a study of a five-slot antenna element and a  $4 \times 4$  array has been shown. Also controlling the input impedance of the slot antenna to match the amplifier  $50 \Omega$  input impedance using parallel slots is illustrated in Section 7.5.1. The simulation

of the  $4 \times 4$  array agreed with the measurement. At the end of the chapter, Section 7.6 summarizes and draws conclusions on what are presented.

## 7.2 Effective Isotropic Power Gain

Effective Isotropic Power Gain, EIPG, refers to the actual measured gain of the quasi-optical system which includes a transmitting horn, antenna array with active devices and polarizers. A more precise definition of EIPG follows. The EIPG measurement setup is shown in Fig. 7.1 (a). The signal is transmitted by a standard gain horn with vertical polarization. The signal is then amplified by the active antenna array and then received by another standard gain horn with horizontal polarization. If  $P_{tran}$  and  $P_{meas}$  are the transmitted and received power respectively, then according to [210]

$$P_{meas} = P_{tran} \left( \frac{\lambda_0}{4\pi R} \right)^2 G_{horn}^2 G_{array}^2 G_{amp} \quad (7.1)$$

in the free space,  $G_{horn}$  and  $G_{array}$  are the gain of the horn and antenna array while  $G_{amp}$  is the gain of the amplifier connected in the array.

As discussed in [210], measurement apparatus dependence is eliminated by the calibration procedure shown in Fig. 7.1 (b). In this case the array has been removed and the receiving and the transmitting horn have the same vertical polarization. The power received in the this case,  $P_{cali}$ , is expressed as

$$P_{cali} = P_{trans} \left( \frac{\lambda_0}{8\pi R} \right)^2 G_{horn}^2 \quad (7.2)$$

Using (7.1) and (7.2), a term EIPG is defined as

$$EIPG = G_{array}^2 G_{amp} = \frac{P_{meas}}{4P_{cali}} \left( \frac{4\pi R}{\lambda_0} \right)^2 \quad (7.3)$$

*ArraySim* uses the definition on the left hand side of (7.3) to compute the EIPG.

Note, EIPG is not the amplifier gain,  $G_{amp}$ .

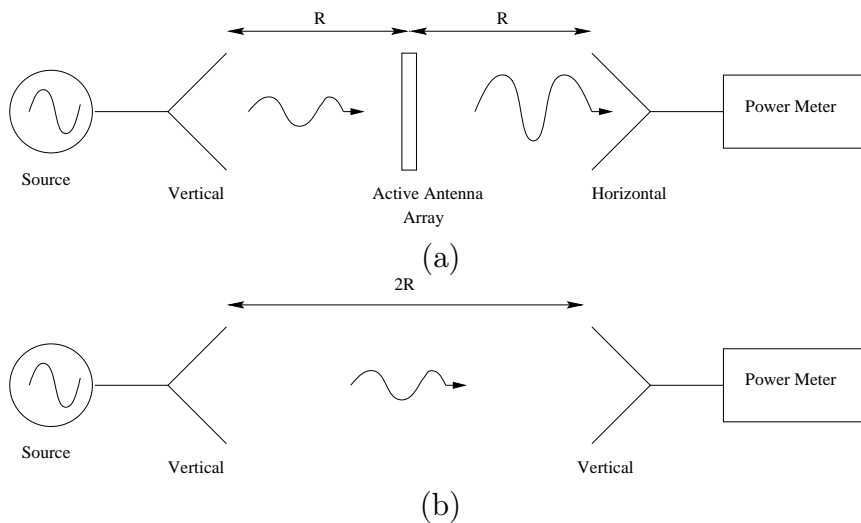


Figure 7.1: Measurement setup for computing EIPG (a) measurement (b) calibration

### 7.3 Folded-Slot Array

The folded-slot antennas are chosen as a radiating elements of the spatial power amplifier arrays because they are very simple to make (one mask step) and they can be integrated easily with three terminal devices (HTB's and HEMTs) in CPW configuration. The bandwidth of folded-slot antennas is expected to be larger than that of the regular slot antenna because the extra slot tends to cancel the off-resonance reactance of the single slot. In addition, the input impedance of folded-slot antenna is of the order of  $100 \Omega$ . This impedance is expected from the considerations of the complementary structure (the folded-dipole) [192].

#### 7.3.1 Single Element

To study the behavior of CPW based folded-slot arrays of various sizes, it is meaningful to simulate a single antenna as its behavior provides an insight into overall

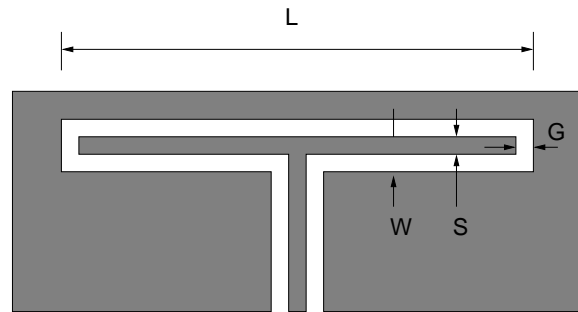


Figure 7.2: The layout of the folded-slot antenna.

array characteristics. In this section simulation results for a folded slot antenna are compared with measured results.

Fig. 7.2 shows a folded-slot antenna layout. This simple folded slot structure is simulated with dimensions  $L = 78$  mm,  $S=G=W= 2$  mm, slot width = 2 mm, metal width = 2 mm,  $\epsilon_r = 2.2$  and substrate thickness = 0.813 mm. Fig. 7.3 shows simulated and measured  $S_{11}$  [210] at the port. Good agreement is seen between simulation and measured results. These results indicate the correct working of the code and show that it can be used to study basic structures as well as complicated arrays. Also the input impedance of this folded-slot antenna is compared with the results obtained previously using FDTD simulation [102] and to measurements in Fig. 7.4.

### 7.3.2 Unit Cell

The folded-slot amplifier unit cell is the basic block of the amplifier array configuration. The amplifier unit cell consists of two orthogonal antennas as shown in Fig. 7.5. One of the antennas is used as a receiving antenna and the other as a transmitting antenna in the orthogonal polarization to minimize the coupling effect

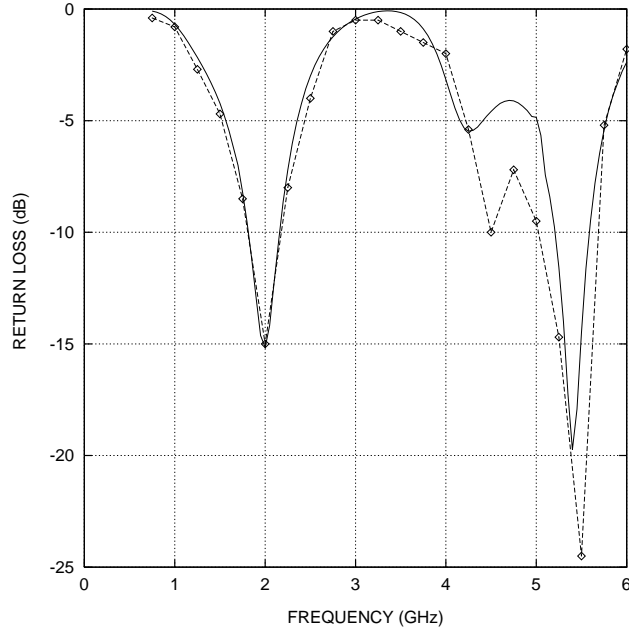


Figure 7.3: Comparison between measurement (dotted line) and MoM simulation (solid line) of the folded-slot antenna in Fig. 7.2.

between the two fields. The interaction of the two antennas is presented in Fig. 7.6 for various separations,  $S$ , of the two antennas.

From Fig. 7.6 (a), the resonance frequencies of the unit cell are almost the same as for the single antenna (see Fig. 7.3). However the insertion loss may change by a few dBs in magnitude. The coupling factor  $S_{12}$  changes with antenna separation. As expected, when  $S$  increases more isolation between the two antenna is obtained. At the antenna resonance frequencies, the coupling factor is in the range of -10 to -20 dB (see Fig. 7.6 (b)).

Other issues that affect the antenna performance are the near and far field profiles of the unit cell. To study these, near and far field analysis is performed on the folded-slot unit cell. For the near field calculation, cells are excited with a uniform electric field,  $E_y$ , with a magnitude of 1 V/m. The horizontal slots are receivers

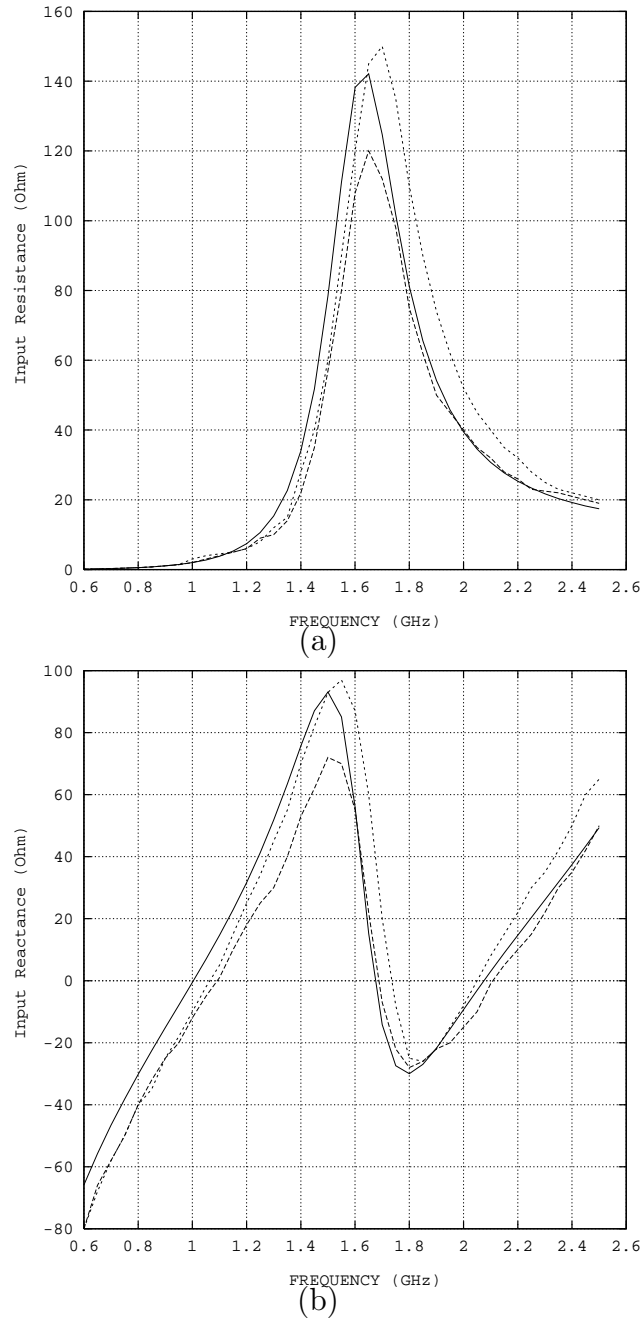


Figure 7.4: The calculated and measured input impedance of the folded slot. MoM simulation (solid line), FDTD (short dashed line), and measurement (long dashed line): (a) real; and (b) imaginary.

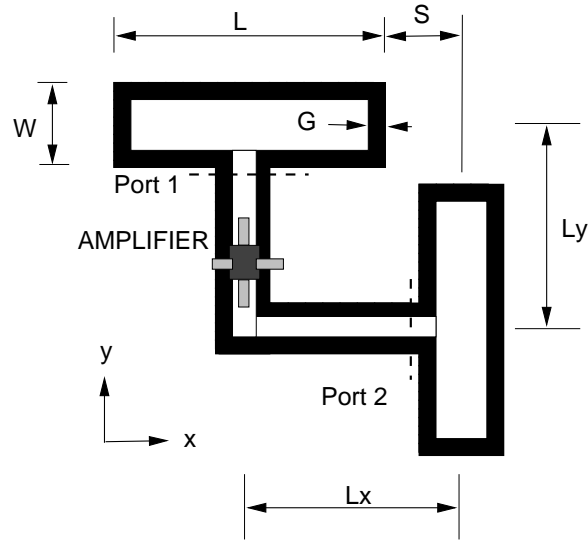
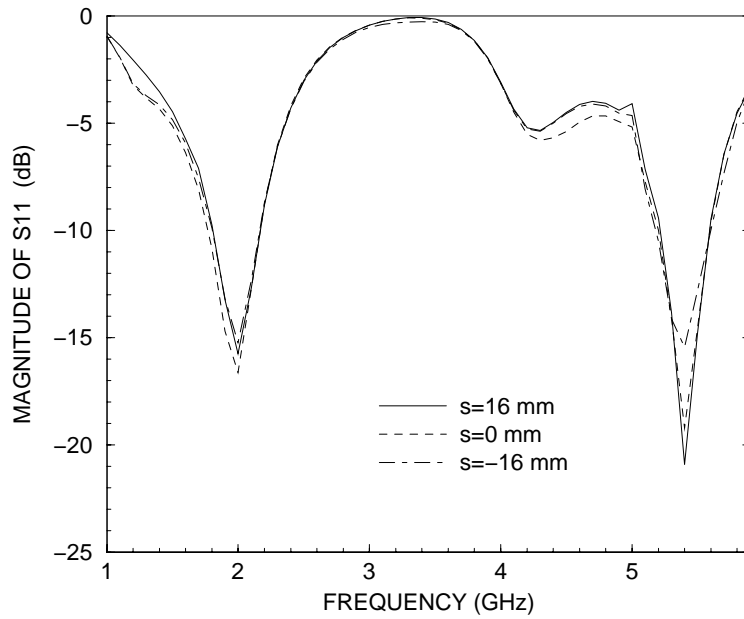


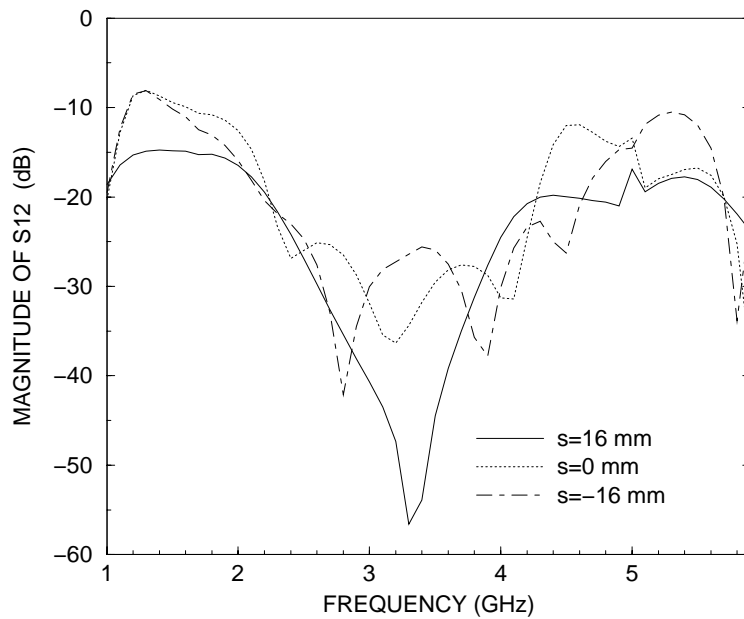
Figure 7.5: The amplifier unit cell .

while vertical slots are transmitters. Initially during passive analysis we vertical slots are expected to transmit less field than the scattered fields by the horizontal slots. This is because the horizontal and vertical slots are not connected to each other. However, during active analysis, vertical slots are excited with amplified currents and voltages that result in stronger transmitted field. The dimensions for this structure (Fig. 7.5) are  $L = 18$  mm,  $W = 7$  mm, metal and slot width = 1 mm, layout cell size =  $1 \times 1$  mm,  $\epsilon_r = 10.8$ , and substrate thickness = 0.635 mm. Near field analysis is performed at distance of 0.8 mm away from the slots as shown in Figs. 7.7 and 7.8. As expected, for passive analysis, the horizontal slots show higher field intensity than the vertical slots because there is no transmission line or active device involved to amplify transmitted fields.

Far field analysis has been performed on the same unit cell. Fig. 7.9 shows a far field plot. Fig. 7.9 (a) shows the radiation pattern in the  $H$ -plane ( $\phi = 0$ ) where Fig. 7.9 (b) shows  $E$ -plane ( $\phi = 90$ ).

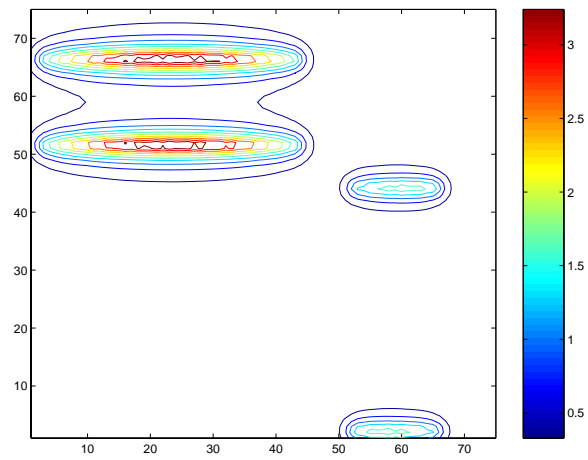


(a)

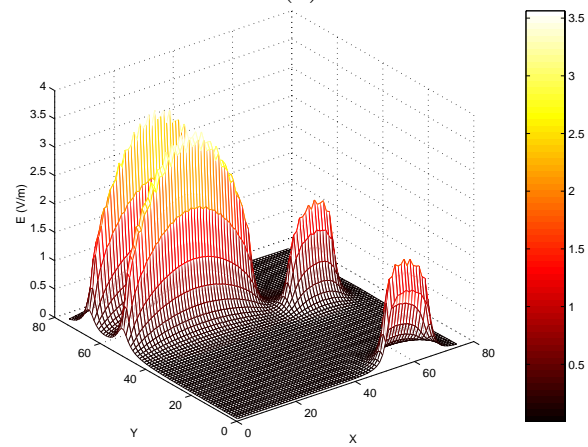


(b)

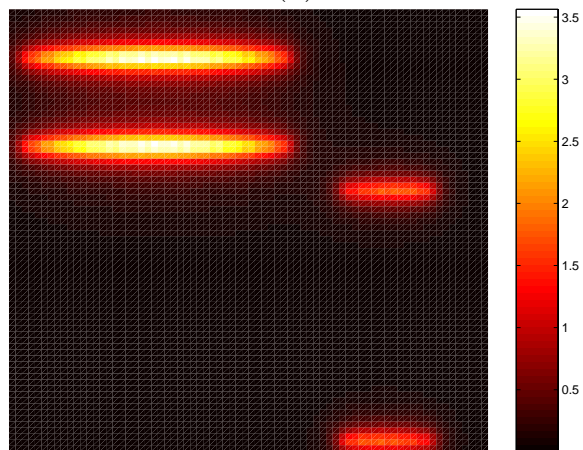
Figure 7.6: Effect of the separation distance  $S$  on the S-parameters of the unit cell in Fig. 7.5: (a) magnitude of  $S_{11}$ ; and (b) magnitude of  $S_{12}$ .



(a)

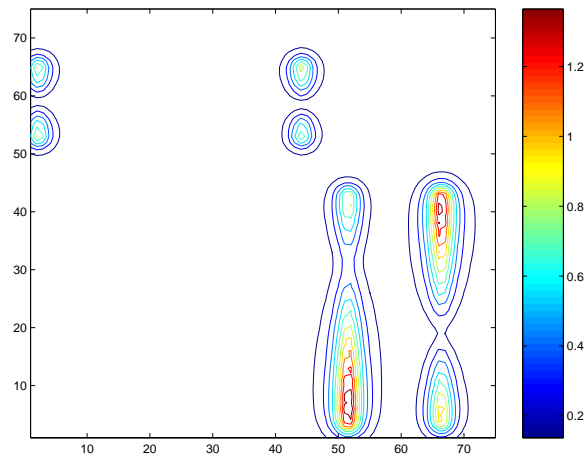


(b)

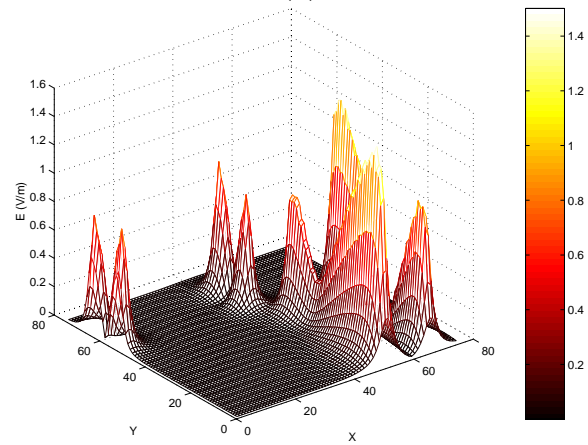


(c)

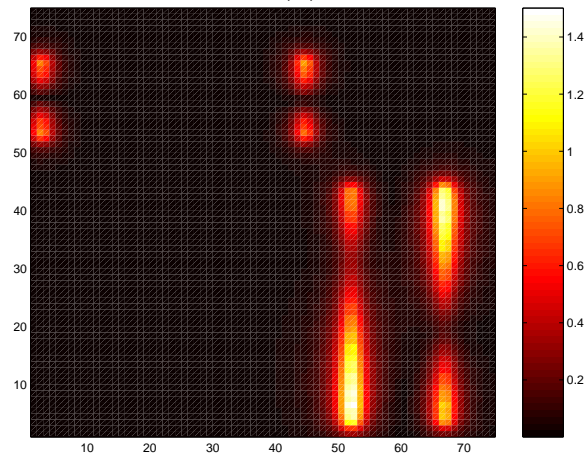
Figure 7.7:  $E_y$  near-field plots at 0.8 mm for a unit folded-slot cell with plane  $E_y$  of 1V/m at 2 GHz.



(a)

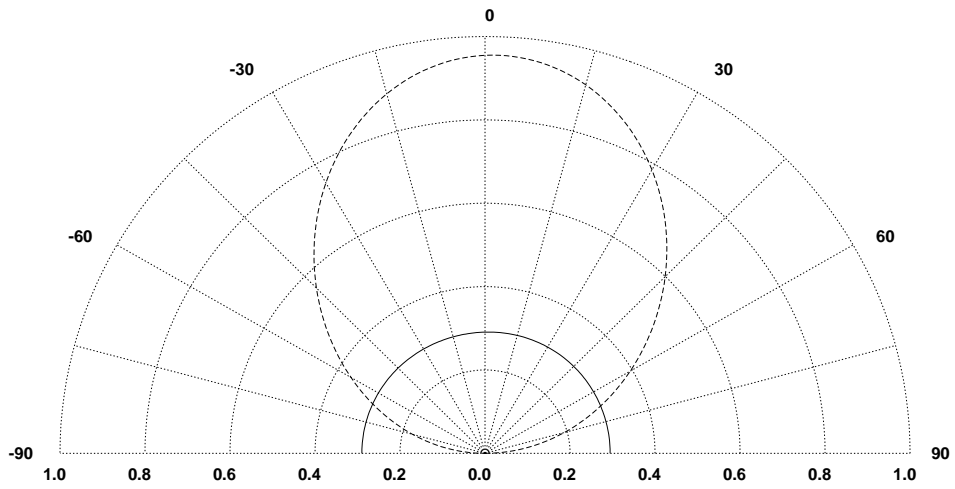


(b)

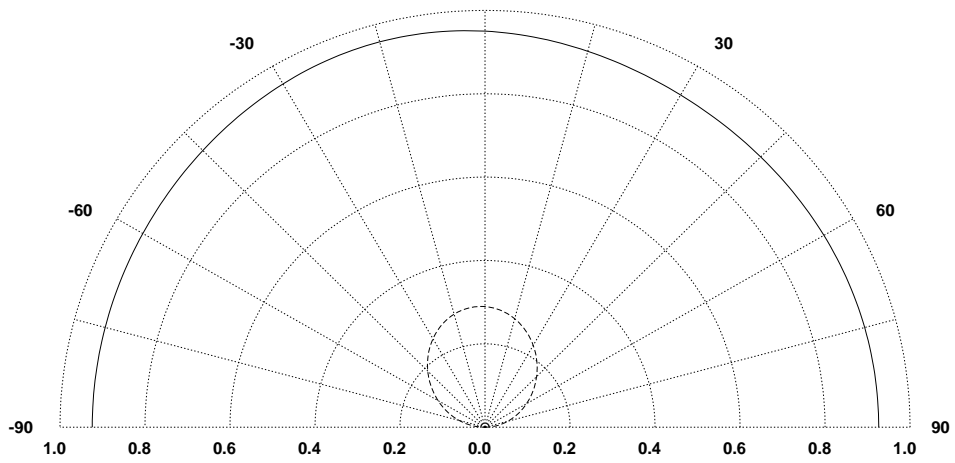


(c)

Figure 7.8:  $E_x$  near-field plots at 0.8 mm for a unit cpw cell with incident plane  $E_y$  of 1V/m at 2 GHz.



(a)



(b)

Figure 7.9: Radiation pattern of the unit cell at 2 GHz: (a) in  $\phi = 0$  plane ; (b) in  $\phi = 90$  plane ( $E_\theta$  dotted line and  $E_\phi$  solid line).

### 7.3.3 $1 \times 2$ Array

Following the study of the amplifier unit cell, as a simple array configuration, a  $1 \times 2$  array, is considered. Fig. 7.10 (b) shows the calculated S parameters for  $1 \times 2$  array shown in Fig. 7.10 (a) with  $a_x = 84$  mm. From this calculation we can say that, at the first resonance at 2 GHz, the coupling between the unit cell slots,  $S_{12}$ , is about -12 dB, however, the coupling between other ports,  $S_{13}$  and  $S_{14}$ , are -17 dB and -30 dB respectively.

### 7.3.4 $2 \times 2$ Array

A  $2 \times 2$  CPW array was simulated using *ArraySim*. Network parameters are extracted and analyzed. Fig. 7.11 shows a  $2 \times 2$  array. In this Fig.,  $D_x = D_y = 84$  mm are the unit cell pitch in the horizontal and vertical dimensions. Other dimensions include,  $L = 78$  mm,  $W = 6$  mm,  $W_{slot} = 2$  mm,  $\epsilon_r = 2.2$  and  $h = 0.813$  mm. Fig. 7.12 (a) and (b) show the S parameters for this  $2 \times 2$  array. Fig. 7.12 (a) compares  $S_{11}$  for a horizontal folded-slot, shown in Fig. 7.3, with  $S_{11}$  obtained for the  $2 \times 2$  array and  $S_{11}$  for the unit cell. Fig. 7.12 (b) shows  $S_{11}$ ,  $S_{12}$ ,  $S_{13}$ ,  $S_{14}$ ,  $S_{15}$ ,  $S_{16}$ ,  $S_{17}$ , and  $S_{18}$  for the  $2 \times 2$  array. Coupling effects due to unit cells next to one another is responsible for changes in impedance and S-parameters. Note, for this simulation, unit cells were separated by 6 mm from one another. This distance is fairly small, however, the  $2 \times 2$  array behavior is similar to that of the unit cell.

Fig. 7.13 shows near field plots in mesh view for a plane incident E field in the y-direction. Since, folded-slots are not connected, we expect horizontal slots in the x-direction to show higher field intensity than field intensities on vertical y-direction folded slots. Near field plots show results as expected. These plots are created at a distance of 0.8 mm from the array, in the z-direction.

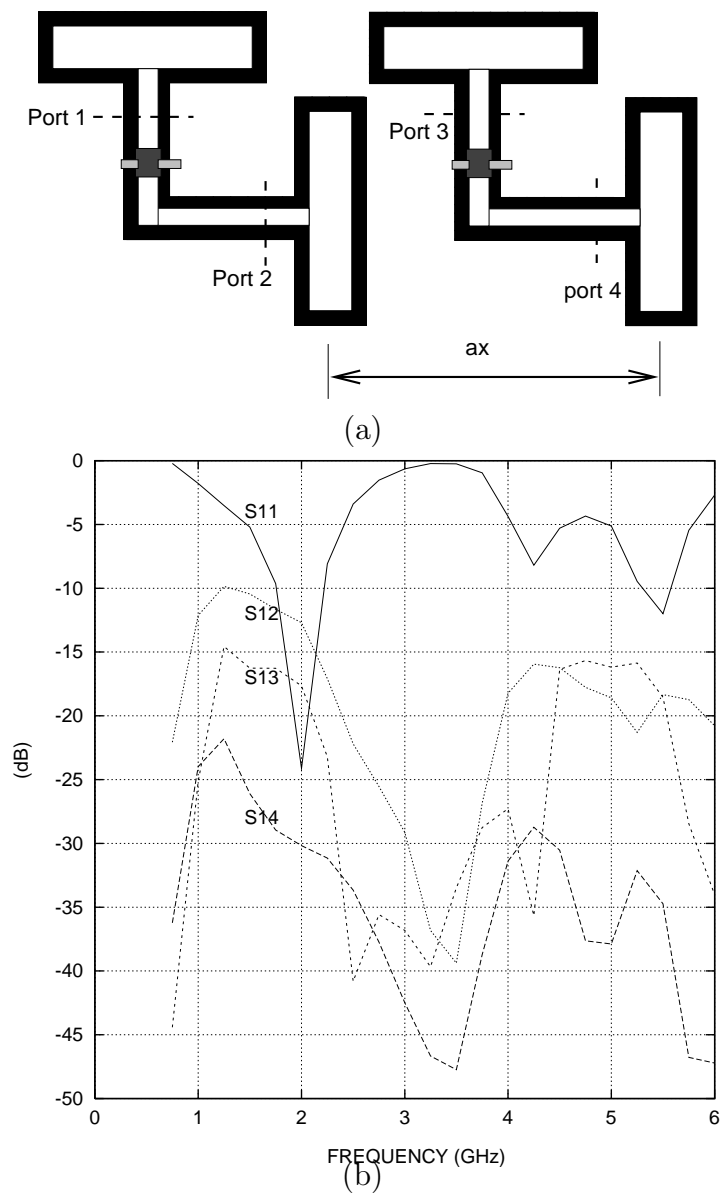


Figure 7.10:  $1 \times 2$  array: (a) layout ; (b) S-parameters.

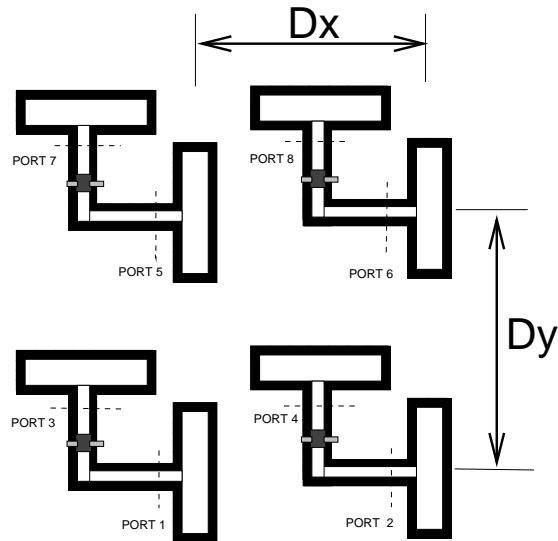


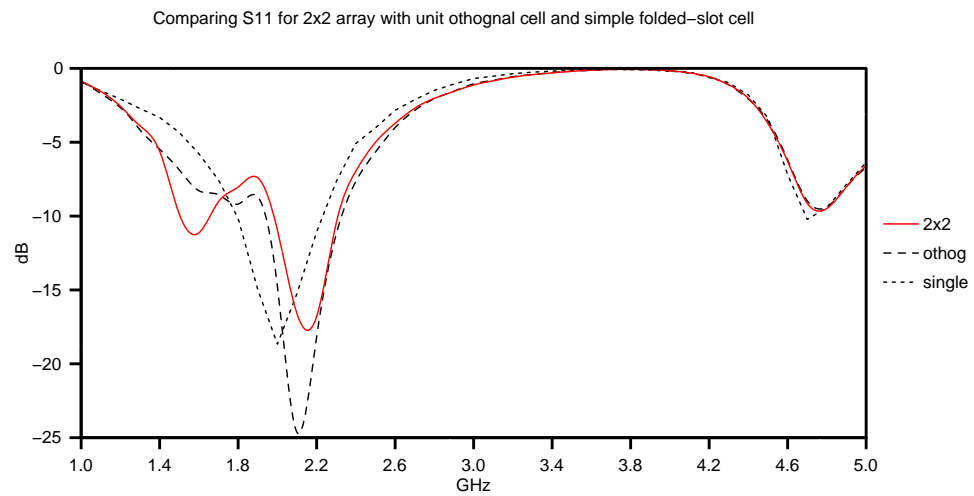
Figure 7.11: CPW 2x2 Array

### 7.3.5 4×4 Array

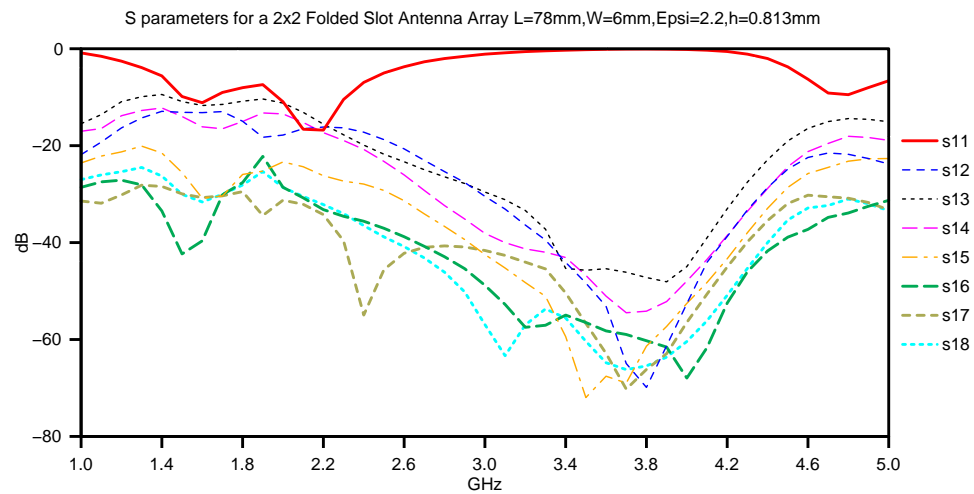
A 4×4 folded-slot array is simulated using *ArraySim*. Fig. 7.14 shows a 4×4 array of orthogonal folded-slots. Input impedance parameters for this array are plotted in Fig. 7.15 (a) and (b) with real and imaginary parts compared with unit cell  $Z_{11}$  to analyze coupling effects.

Active analysis involves interfacing *ArraySim* passive analysis with a circuit simulator. In order to perform active analysis for folded-slot based CPW structure, we first perform passive analysis and find the input impedance of the antenna. A CPW transmission line is then designed to match between the antenna and the active device impedances. Fig. 7.16 shows a CPW line whose characteristic impedance depends upon  $W$  and  $S$ , where  $W$  is the width of the CPW slot and  $S$  is the width of the CPW line (metal).  $Z_0$  of the CPW line is calculated using the equations from [211] which are

$$k_1 = \frac{S}{S + 2W} \quad (7.4)$$

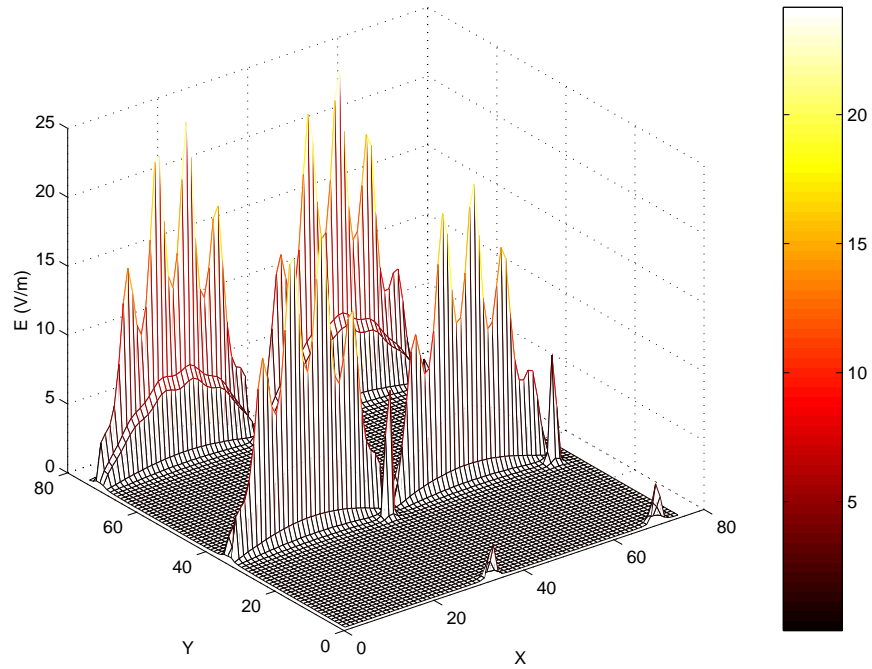


(a)

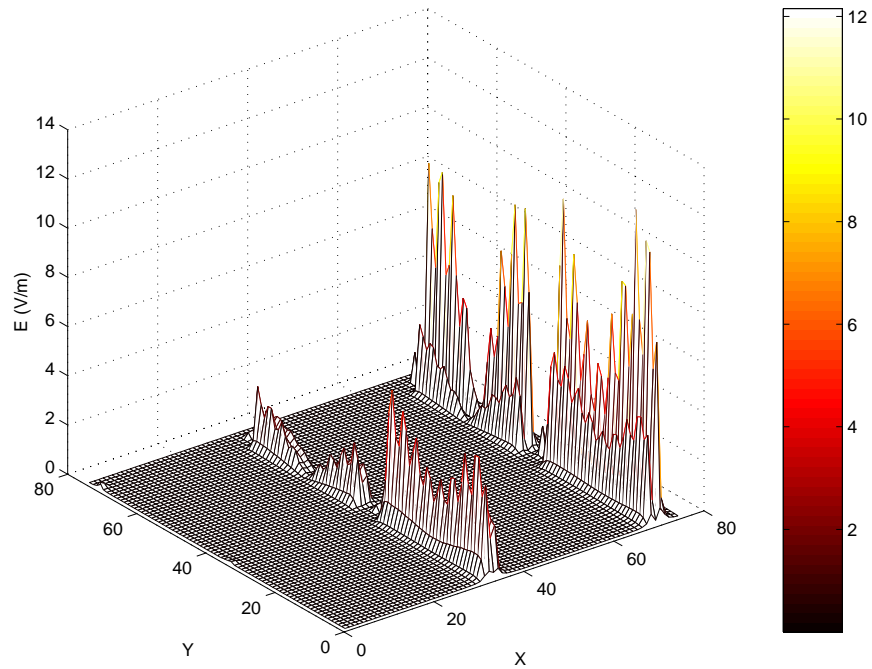


(b)

Figure 7.12: Passive simulation of folded-slot  $2 \times 2$  array (unit cells separated by 6mm): (a)  $S_{11}$  of single antenna, unit cell, and  $2 \times 2$  array (b) S parameters of  $2 \times 2$  array



(a)



(b)

Figure 7.13: Near field plots of folded-slot  $2 \times 2$  array at 0.8mm: (a)  $E_y$  (b)  $E_x$

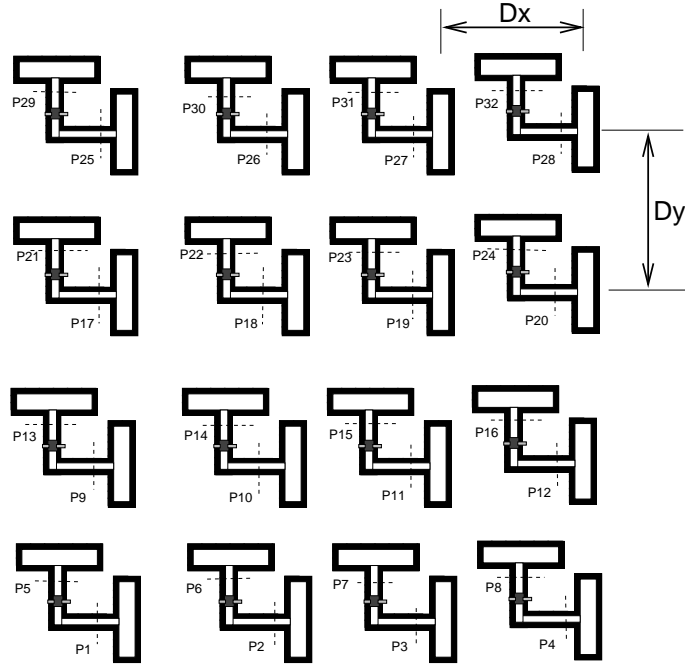


Figure 7.14: CPW 4x4 Array

$$\epsilon_{re} = \frac{\epsilon_r + 1}{2} \quad (7.5)$$

$$Z_0 = \frac{30\pi}{\sqrt{\epsilon_r}} \frac{K'(k_1)}{K(k_1)} \quad (7.6)$$

where  $K'(k_1)/K(k_1)$  depends on the value of  $k_1$  (see [211] for the  $K'(k_1)/K(k_1)$  expression).

After designing the CPW line for a certain impedance, the EIPG is computed and indirectly gives the gain of the passive antenna system. For the folded-slot based CPW unit cell discussed in [210] with dimensions;  $L = 18$  mm and  $W = 7$  mm, the CPW line is designed for  $Z_0 = 80 \Omega$ . Form (7.4)  $S = 0.37W$ . For this CPW characteristic impedance the cell size is  $0.33$  mm  $\times$   $0.33$  mm. To simulate the array with this cell size, a very large number of cells are needed to draw the layout. Greater number of cells implies higher simulation time and possibly memory problems for very large structure such as a  $4 \times 4$  array. So, as a compromise, in the

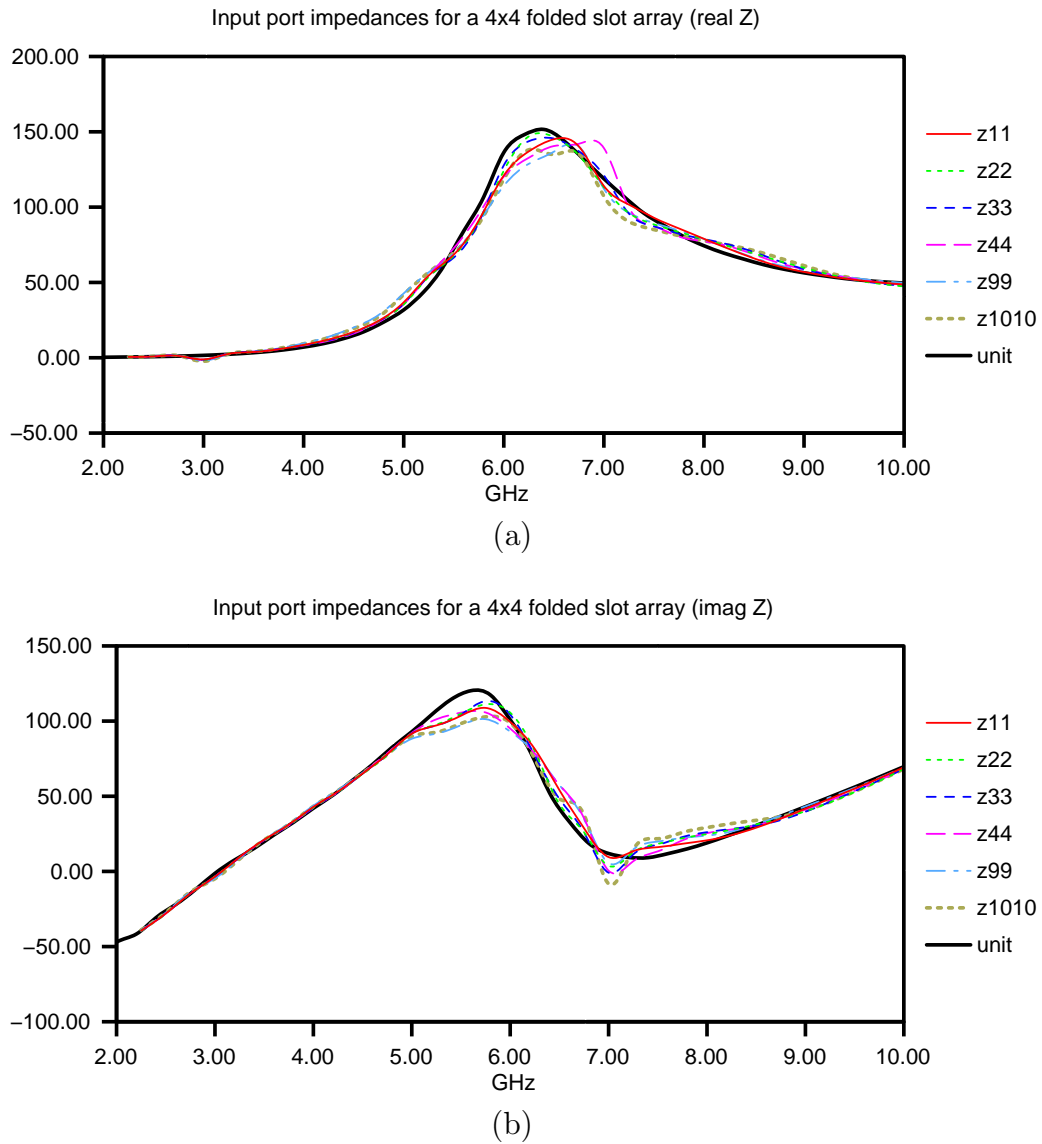


Figure 7.15: Input impedance of folded-slot array compared with unit cell. (a) real  
(b) imaginary

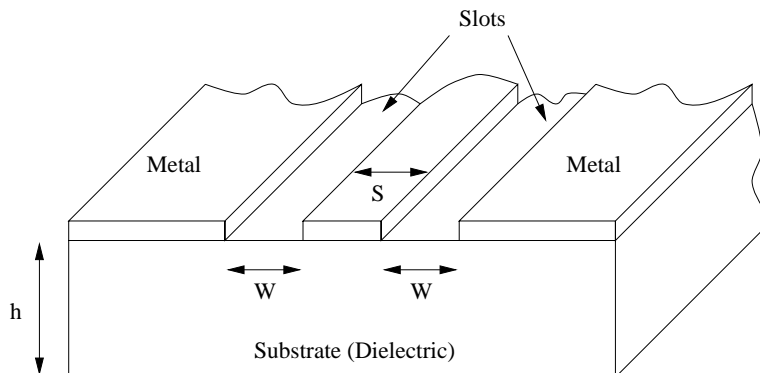


Figure 7.16: Coplanar waveguide (CPW) geometry

simulation we use layout cell size of  $0.5 \text{ mm} \times 0.5 \text{ mm}$  which gives a  $82 \Omega$  CPW characteristic impedance.

A passive analysis is done on the unit cell and the array to determine the passive network parameters and the open circuit voltages results from the incident wave. Fig. 7.17 (a) shows the equivalent setup for calculation of the open circuit voltages,  $V_r$  and  $V_t$ , at the receiving and transmitting terminals respectively (see Fig. 7.17 (b)).

An active device (MESFET) is then connected on the transmission line and currents and voltages for this amplifier are computed using circuit simulator. A simple small signal MESFET model (see Fig. 7.18 (b)) is used for AC analysis with  $Z_{in}$ ,  $Z_{out}$  and  $g_m$ . the exact device currents and voltages are then calculated. The currents are used to form a new excitation vector and overall gain (EIPG) is computed.

Fig. 7.18 (a) shows a connection of a MESFET with a two port based impedance matrix. The sign of the voltage sources should be resemble the actual excitation mechanism.

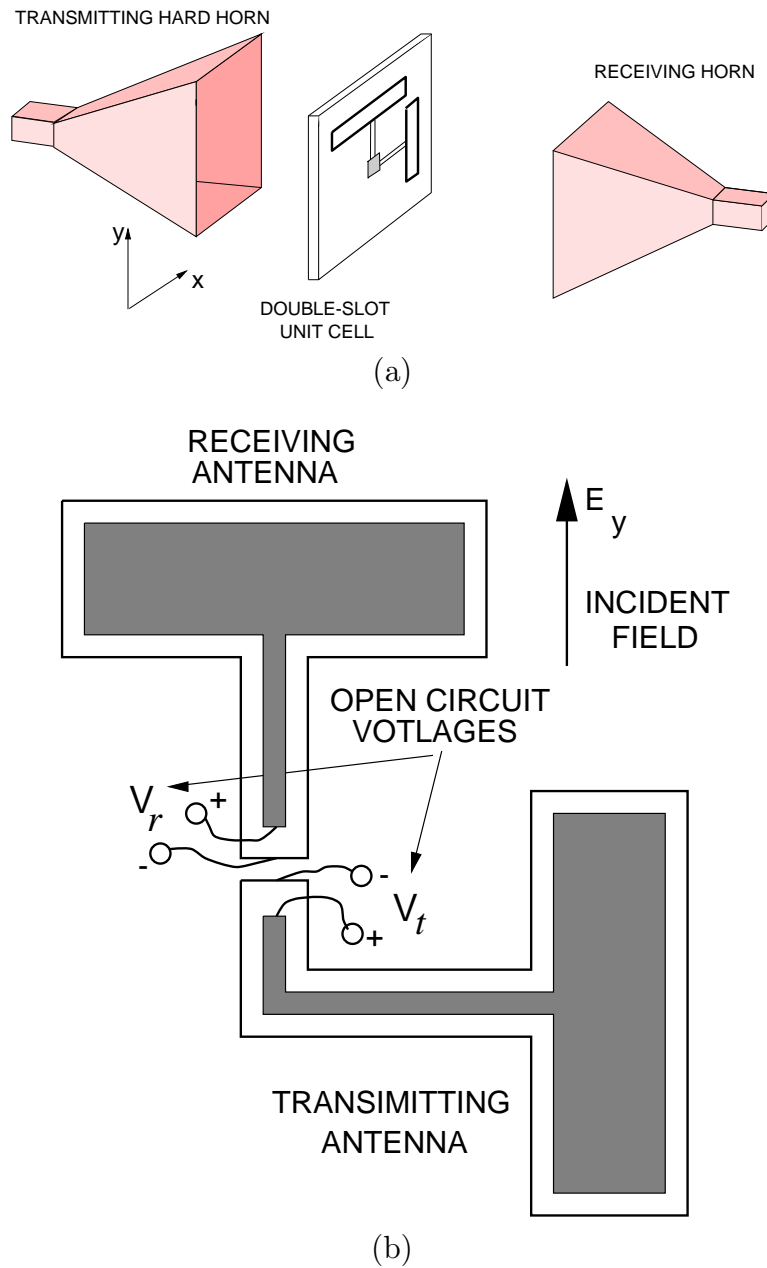


Figure 7.17: Simulation of the EIPG of a unit cell: (a) setup and; (b) open circuit voltages.

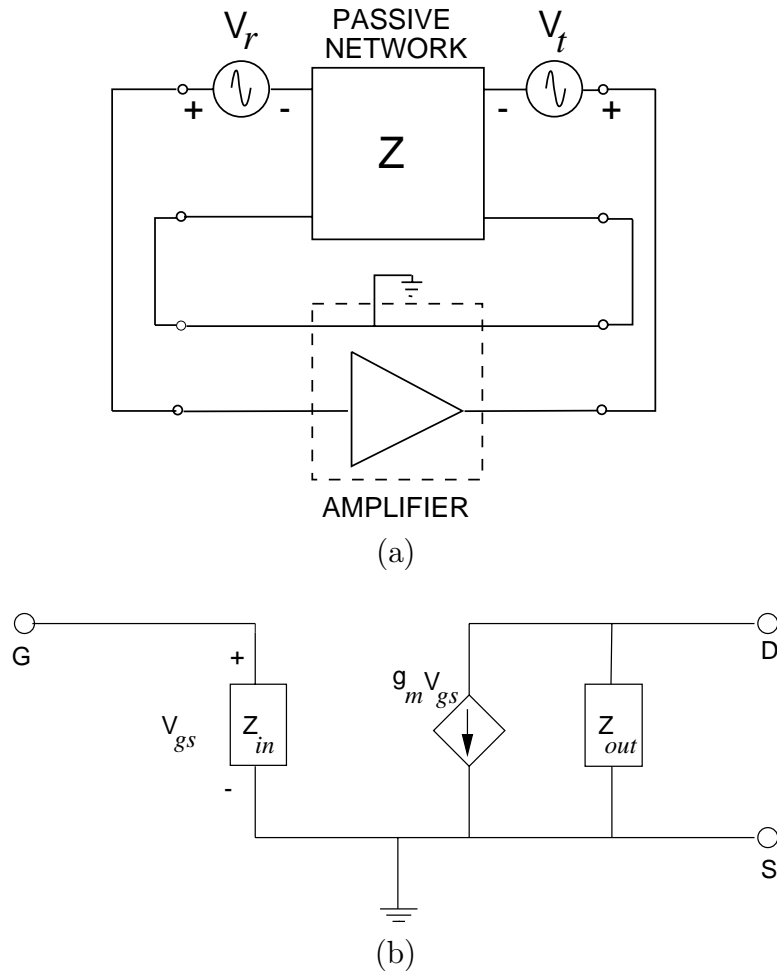


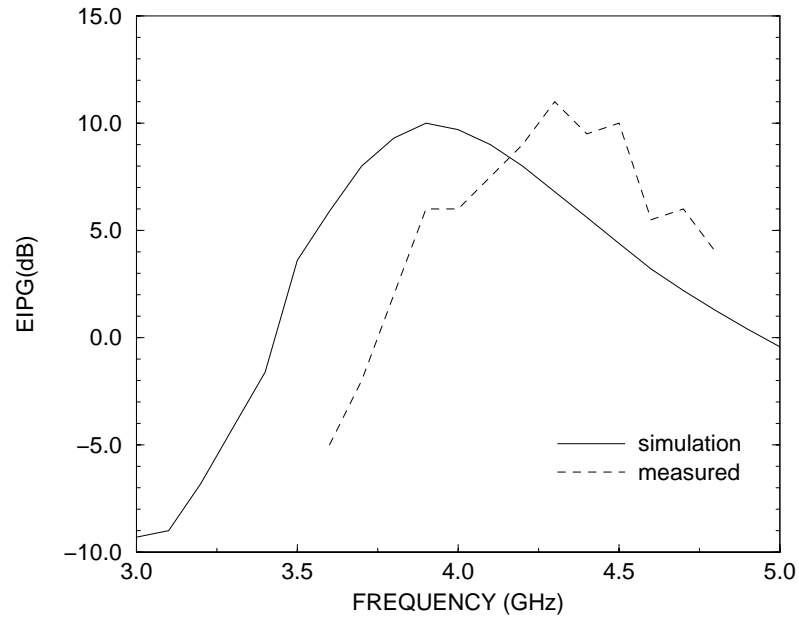
Figure 7.18: Circuit analysis of the spatial amplifier given a Z port based matrix: (a) circuit model; and (b) MESFET model.

### Amplifier and Antenna Parameters

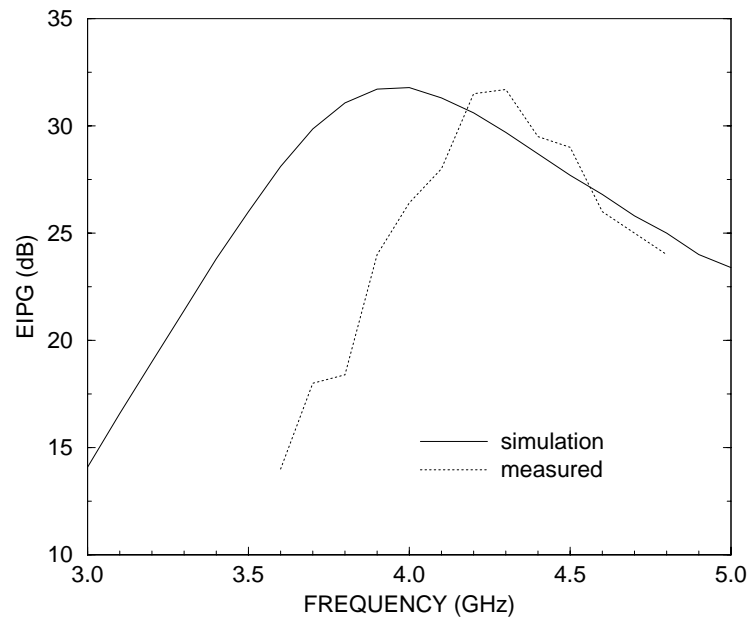
For a CPW-based folded slot active array the transverse view of which is shown in Fig. 7.14. Each dimension of this system is around two wavelengths. Each amplifying unit cell is an amplifier connected to the receiving and transmitting folded-slot antennas by CPW lines. The array consists of  $4 \times 4$  unit cells configured as shown in Fig. 7.5 (b). The  $x$ -spacing is 38.5 mm and the  $y$ -spacing is 27.5 mm. The amplifiers are GaAs MESFET's (NE32184A). From the manufacturer's data sheet, the transconductance of this MESFET,  $g_m$ , is typically 33 mS. Using the same parameters as in [210], leads to  $Z_{in} = Z_{out} = Z_{out} = 125 \Omega$ . The overall gain of the array can be expressed in term of the effective isotropic power gain (EIPG) which is defined as  $G_{FSd} G_{FSa} G_A$ , where  $G_A$  is the gain of the amplifier and  $G_{FSd}$  and  $G_{FSa}$  are the directional gains of the folded-slot antenna on the air and dielectric sides, respectively. The EIPG was simulated using far-field calculation of the radiated field result with plane wave excitation of the active array.

### Simulation Results

The EIPG of a single amplifier cell and the array are shown and compared with measurements in Fig. 7.19 (a) and (b) respectively. The simulated values have the same frequency dependence and the same maximum value as the measured values. The EIPG is around 11 dB for the unit amplifier and 32 dB for the array. Plots show a difference in the maximum gain frequency from simulated and measurement results. The simulated maximum EIPG occurred at 3.9 GHz which is less than that measured by 0.4 GHz. We believe that this shift in frequency is due to differences between the fabricated and simulated dimensions [212] and also to the limitations in the use of manufactures typical data in constructing the model of the MMIC.



(a)



(b)

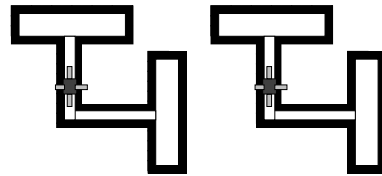
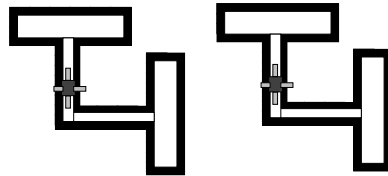
Figure 7.19: The calculated and measured EIPG. MoM simulation (solid line), and measurement (dashed line): (a) unit cell; and (b) array.

## 7.4 Designing Slot Arrays

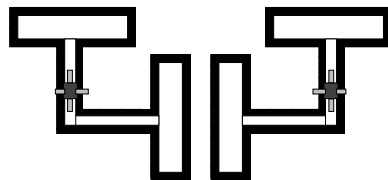
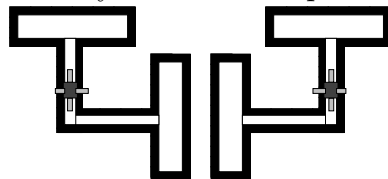
Coupling effects among unit cells in an array may degrade the performance of the overall system. In this section we look at three configurations of  $2 \times 2$  folded-slot arrays as shown in Fig. 7.20 and plot their near field plots at 0.8 mm and 10 mm away from the array to show which one of the three configuration may be a designer's choice. For all designs the length of the slots is 18 mm while the width is 7 mm (the same dimensions as described for the  $4 \times 4$  array). From near field plots shown in Fig. 7.21 we observe that design 3 is the most symmetric design and probability is a better choice than design 2 and design 1 because of its symmetric coupling cancelation.

## 7.5 Five-Slot Array

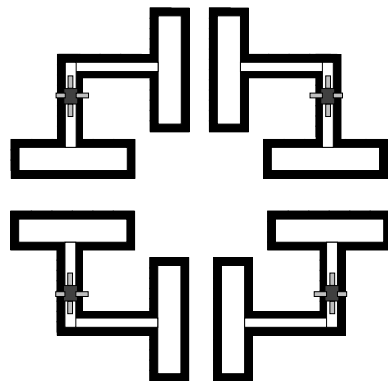
In spatial power combining systems components, such as oscillators, mixers, and amplifiers, matching network are used between the active devices and output antennas since impedances are not matched in general. There are some disadvantages to this process. First of all, the matching networks tend to limit the bandwidth of the circuits as well as complicating the design. Furthermore, the size of the unit cell would become larger, which is undesirable for most cases, if multiple stages matching network are required. All this can be eliminated if antennas with  $50 \Omega$  input impedance are used. The  $50 \Omega$  antenna structure allows us to integrate directly commercial MMIC chips that are designed for  $50 \Omega$  input/output impedance without any matching networks. By eliminating the matching networks, the circuit are greatly simplified and compact unit cells can be obtained. In this section, a  $4 \times 4$   $50 \Omega$  slot array is presented. In the beginning, the concept of antenna input impedance control with multiple slots is shown. First, a  $50 \Omega$  five-slot antenna performance



(a) Design 1: Array made from replicating unit cells



(b) Design 2: Array with its 2nd column a mirror image of its 1st column



(c) Design 3: Symmetric array

Figure 7.20: Three designs for  $2 \times 2$  folded-slot arrays with vertical slots as transmitting slots and horizontal slots as receiving slots

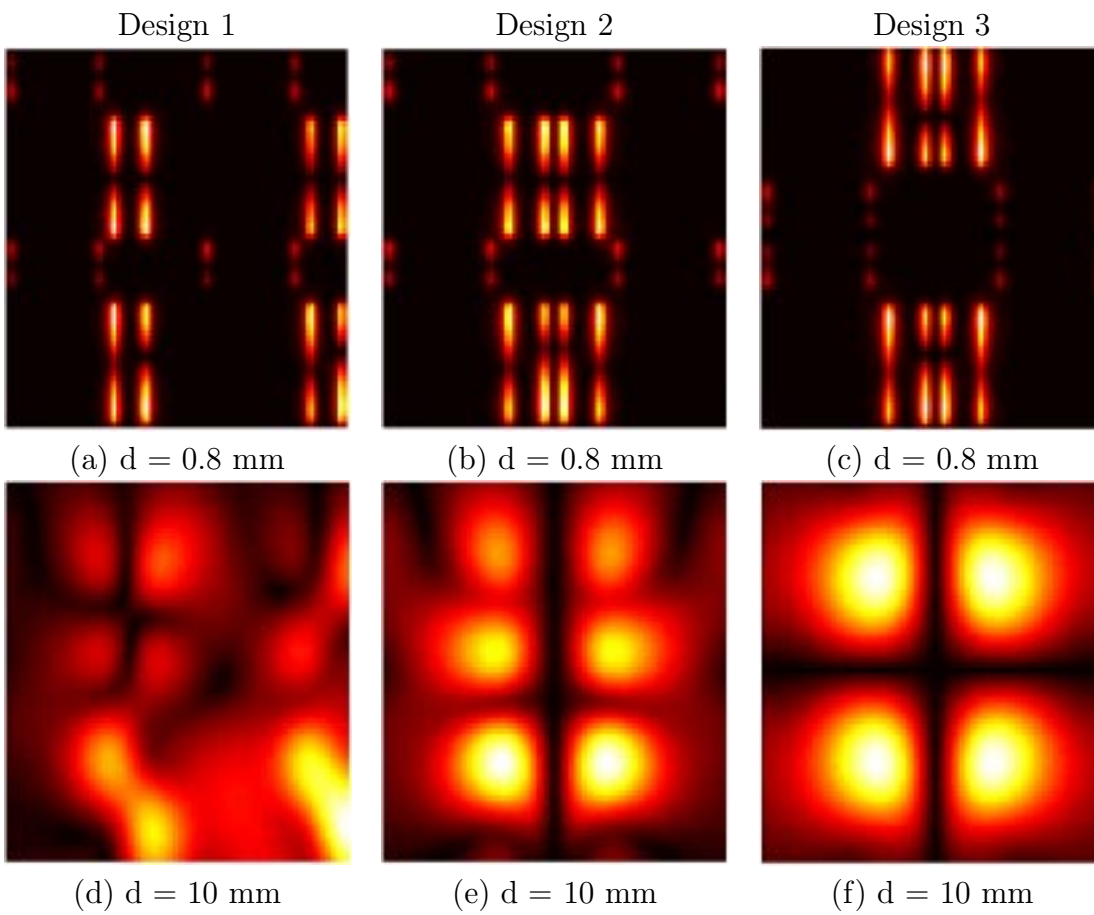


Figure 7.21: Near field plots for  $2 \times 2$  array at 9 GHz

and the discontinuities of transmission line effect are studied. At the end of this section, a full-wave system simulation of a finite  $4 \times 4$  five-slot array is presented and compared with measurements.

### 7.5.1 Impedance Control with Multiple Slots

*ArraySim* enables the behavior of a given structure to be studied in detail. One of the characteristics of slot antennas is the relation of the input port impedance to the number of slots. In this section we describe a rule of thumb that can be used to scale input port impedance by varying the number of slots. The input impedance of a dipole in free space at first resonance is around  $75 \Omega$  [192]. If this wire is folded, a folded dipole is created as two equal parallel currents with the same direction current flow on the wires. The input impedance of this folded dipole is on the order of  $300\Omega$ . The input impedance of a folded dipole is around 4 times that of the input impedance of a single dipole. This results in a simple rule of thumb given by

$$Z_{in} = N^2 Z_{dipole} \quad (7.7)$$

where  $Z_{dipole}$  is the input impedance of a single dipole (approximately  $75 \Omega$ ).

A similar relation holds for slot antennas. As described in [192] and [210] the input impedance of a half-wave slot is given as

$$Z_{single\_slot} = \frac{Z_0^2}{4Z_{dipole}} \quad (7.8)$$

where  $Z_0$  is the free space characteristic impedance and equals  $377 \Omega$ .

So, the input impedance of  $N$  slots is given as

$$Z_{slot} = \frac{Z_{single\_slot}}{N^2} \quad (7.9)$$

which shows that as the number of slots is increased, the input impedance lowers

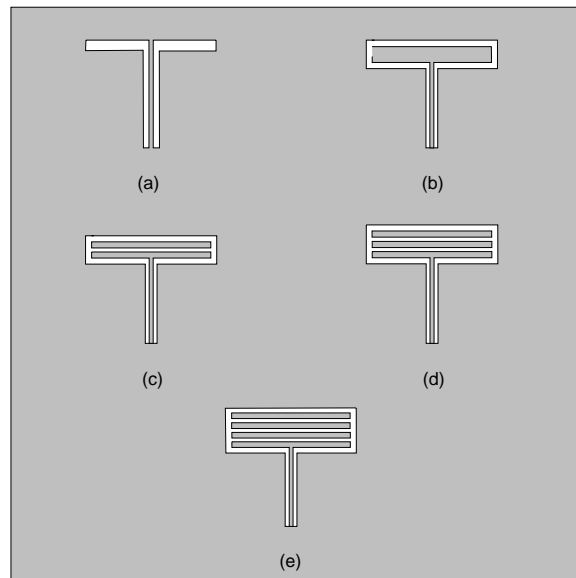


Figure 7.22: Layout of slot antenna element with CPW feeding line for antennas with varying number of slots: (a) a single slot; (b) a double slot; (c) a triple slot; (d) a four-slot; and (e) a five-slot CPW antenna.

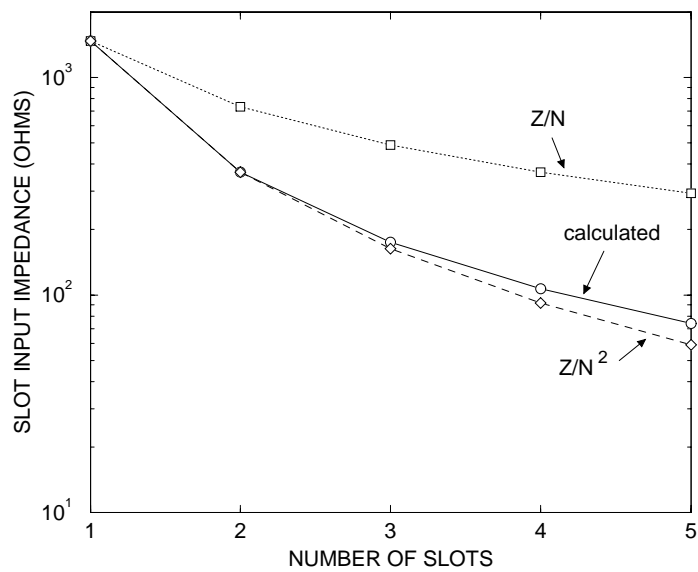


Figure 7.23: Variation of multi-slots antenna input impedance with number of slots.

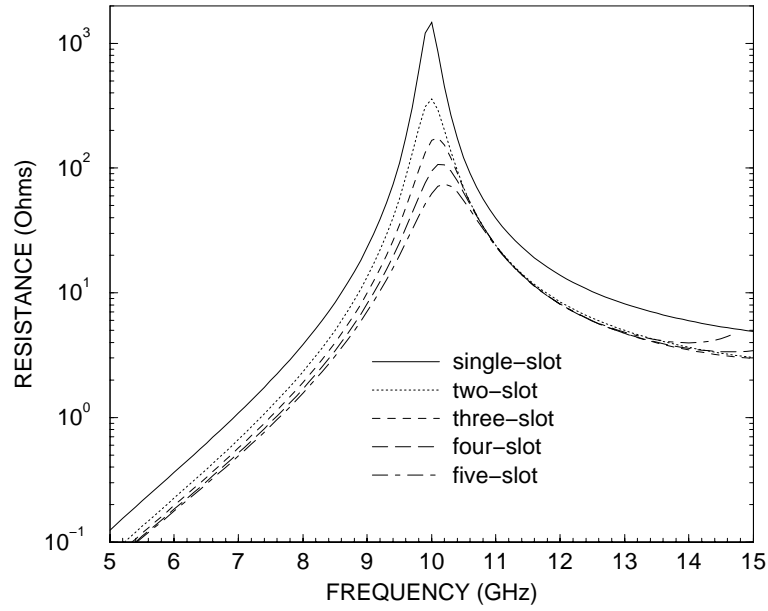
by a factor equal to the number of slots squared. So, adding additional slots allows the designer to vary the slot input impedance over a wide range. This simple design rule is useful for circuit designs that require impedance matching with slots.

Fig. 7.22 shows several types of slot antenna structures for various  $N = 1 \cdots 5$ . *ArraySim* was used to simulate these antennas with the same dimensions and other than the number of slots. Fig. 7.24 shows the simulated input impedances for one, two, three, four, and five-slot antennas. From simulations we see that the input impedance reduces with increasing number of slots by  $N^\alpha$  where  $\alpha$  is between 1 and 2 (see Fig. 7.23). Fig. 7.25 shows the driving point reflection coefficient for these antennas. We can clearly see the effect of the number of slots on the return loss. For five-slot antenna, it almost matched to  $50 \Omega$  at 10.5 GHz. The return loss is about 20 dB. The dimensions for Fig. 7.22 were;  $L = 7.2$  mm, slot gap = 0.3 mm, metal width = 0.3 mm, side width = 0.3 mm,  $\epsilon_r = 9.8$ , substrate thickness = 0.635 mm. Fig. 7.26 compares between the simulated and measured return loss of a five-slot antenna. The input impedance of this antenna at the resonance (10.5 GHz) is about  $50 \Omega$ . The simulation is in a good agreement with the measurements. The simulated resonance frequency is the same as measured. The simulation return loss is 20 dB where the measurement is 27 dB.

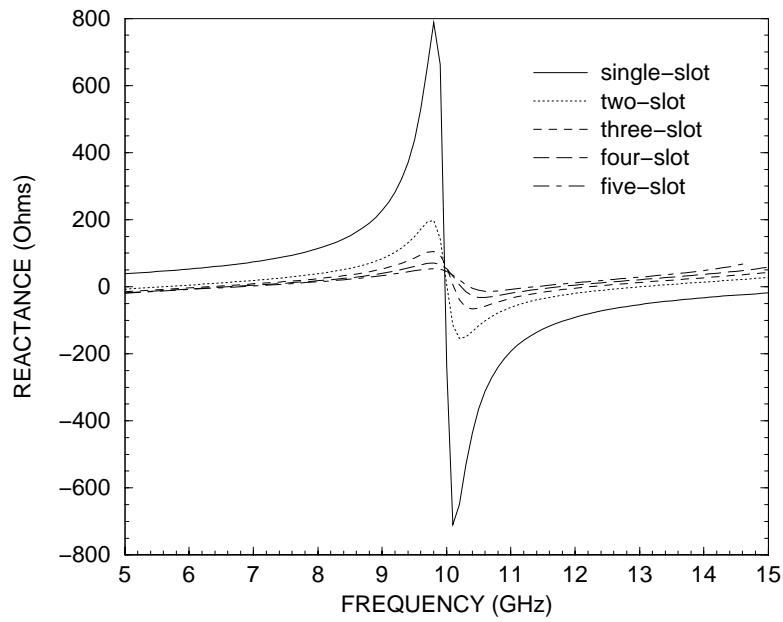
## 7.5.2 Transmission Line Discontinuity

Since a CPW transmission line is used to connect the antenna and the amplifier terminals, the effect of the discontinuities of the line with the amplifier terminal and the antenna should be taken into consideration. The effect of these discontinuities is very important and may degrade the total insertion loss within 10 dB.

Fig. 7.28 shows the driving point input reflection coefficient of the five-slot

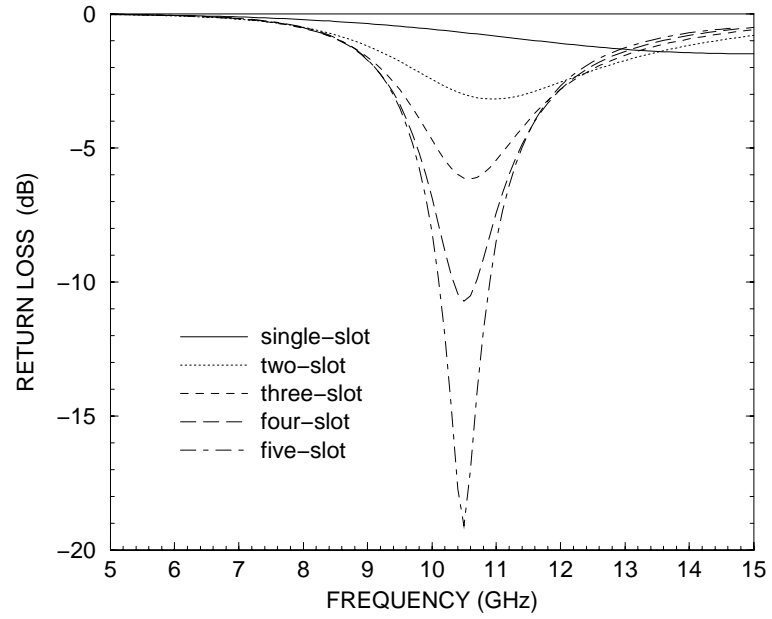


(a)

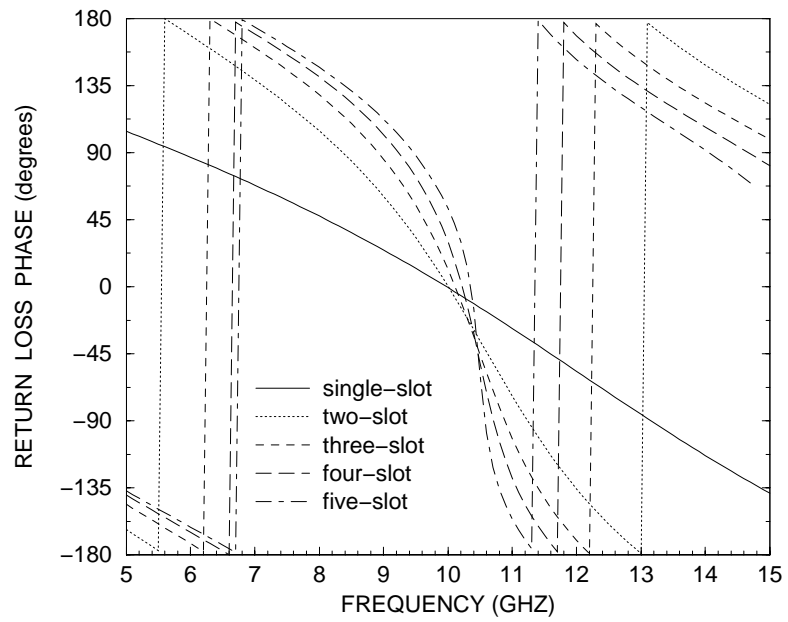


(b)

Figure 7.24: Input impedance with number of slots: (a) resistance; (b) reactance



(a)



(b)

Figure 7.25: S11 for the slot antenna

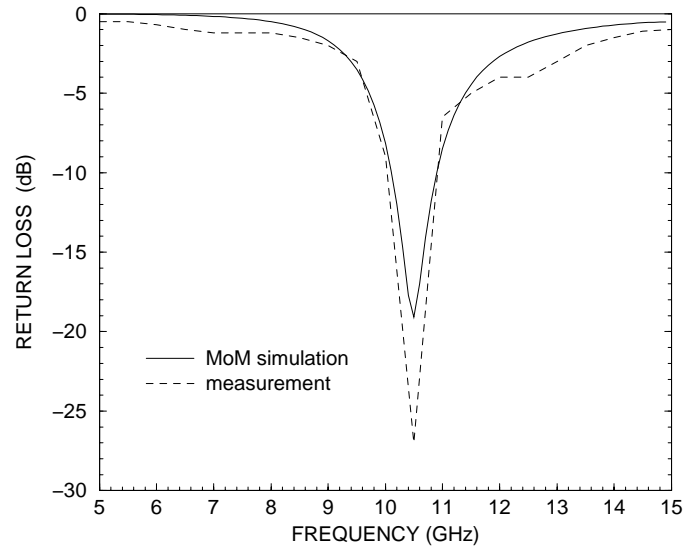


Figure 7.26: Return loss of the five-slot antenna.

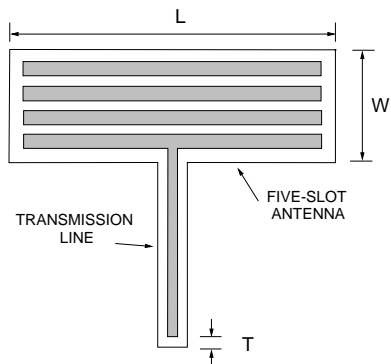


Figure 7.27: The layout of the five-slot antenna.

antenna shown in Fig.7.27. The reflection coefficient has been calculated without and with the CPW line. Also we see the effect of the gap length,  $T$ , on the magnitude of return loss. Wider gap is better than small one because the discontinuity effect tends to vanish when wider gap is used.

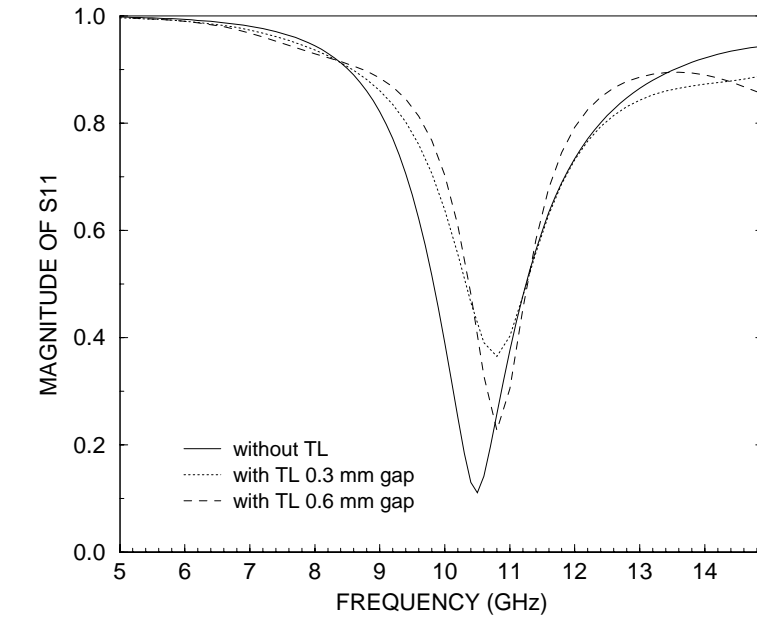
### 7.5.3 Radiation Pattern

The far field radiation pattern of the five-slot antenna has been calculated. Fig. 7.29 shows the calculated radiation pattern in both the  $E$  and  $H$  planes. The beam width in the  $H$  plane is about  $85^\circ$ .

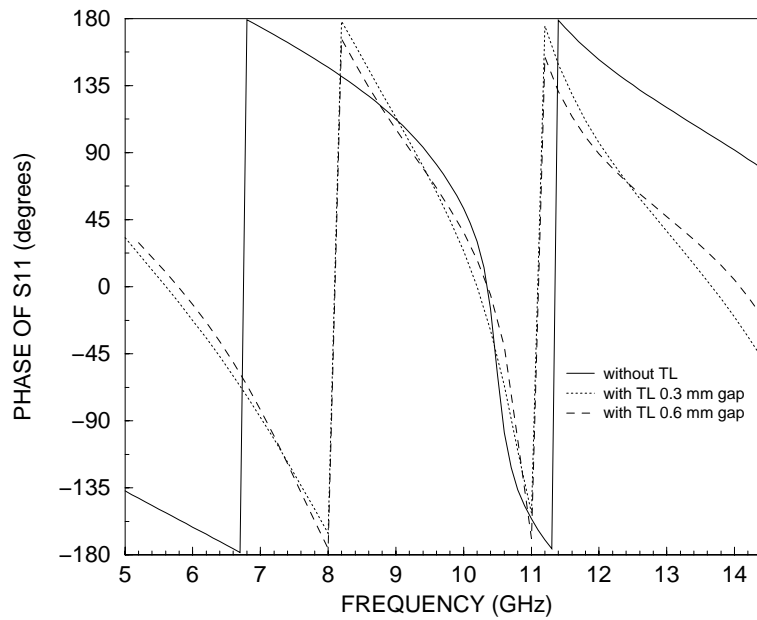
### 7.5.4 $4 \times 4$ five-Slot Array

The  $4 \times 4$  five-slot array shown in Fig. 7.30 (a) is consists of 16 unit cells configured as shown in Fig. 7.30 (b). The unit cell is the same as that considered in Section 7.3.2, the two antennas are polarized orthogonally to isolate the input and output signals as well as to avoid oscillation due to mutual coupling between antennas. A typical MMIC amplifier block is connected without any external matching network between the two five-slot antennas. A 10 dB Rockwell gain block is used [210]. This gain block is internally matched with  $50\Omega$  input and output impedances.

In Fig. 7.31, the EIPG of this array was compared with the measurement obtained from [210]. The maximum EIPG for the array is 35 dB. The array directivity is about 13.5 dB. This gives a peak gain of 8 dB, which is close to what is expected from the gain block (10 dB). The simulated bandwidth is wider than the measured due to lack of amplifier circuit model information. In the simulation, we assume that these amplifiers are perfectly matched to  $50\Omega$  in all the frequency range. Also, Fig. 7.32 shows the radiation pattern of the array and the beam-width is about  $22^\circ$ .

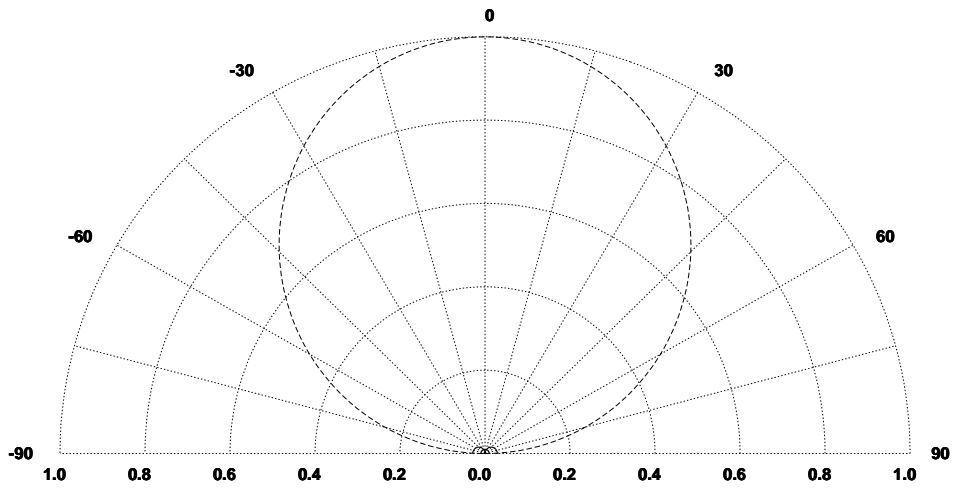


(a)

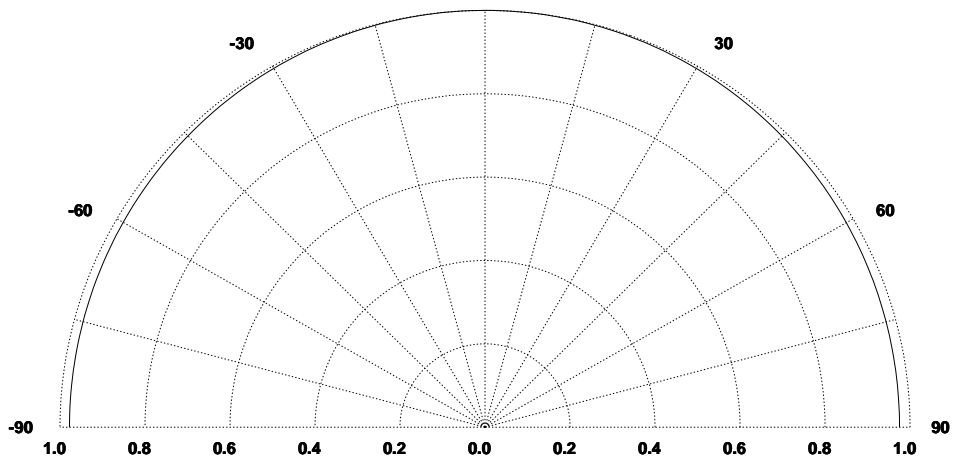


(b)

Figure 7.28: Effect of transmission line gap on  $S$  parameters of the five folded slot antenna: (a) magnitude; and (b) phase.

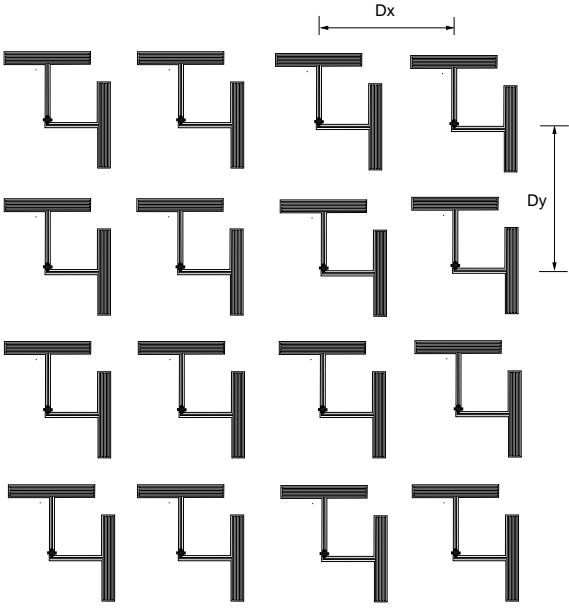


(a)

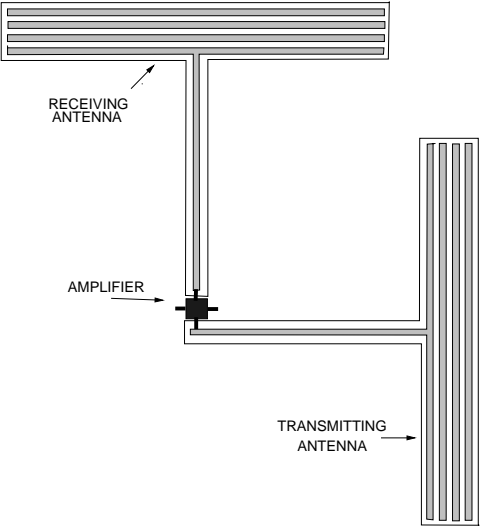


(b)

Figure 7.29: The calculated far field of the five-slot antenna:(a)H-plane; and (b) E-plane ( $E_\theta$  dotted line and  $E_\phi$  solid line).



(a)



(b)

Figure 7.30: The layout of five-slot spatial amplifier: (a) 4x4 array; (b) unit cell.

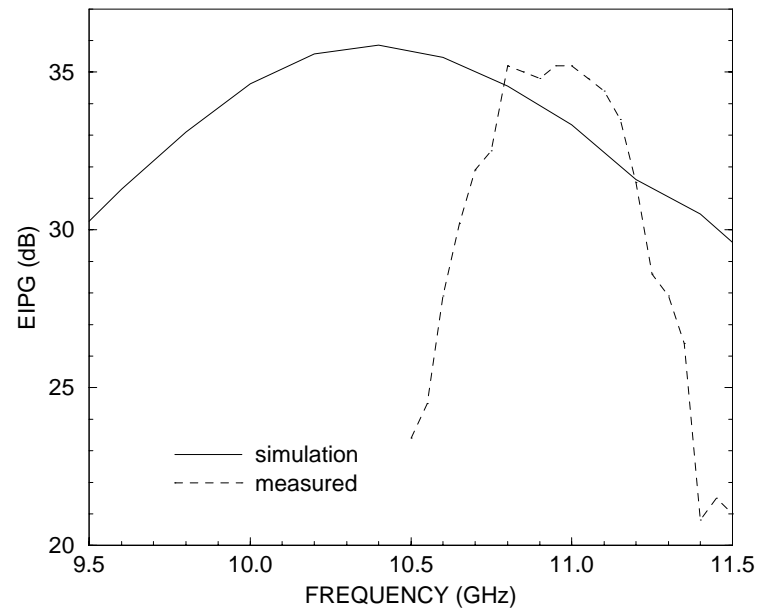


Figure 7.31: The EIPG of the 4x4 five-slot array.

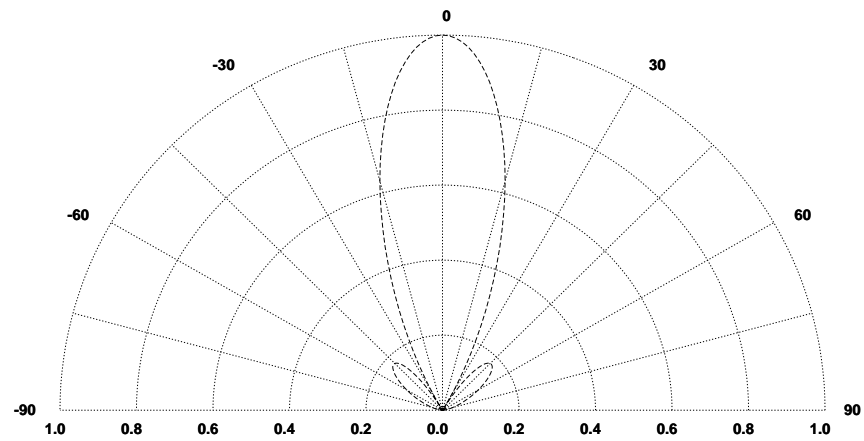


Figure 7.32: The calculated E-plane far field of the five-slot array.

## 7.6 Summary

In this chapter we depict *ArraySim* as a CAE tool to study the behavior of single layer structures. Folded-slot and five-slot antenna structures are used as a single layer structure and simulations are performed using *ArraySim* to study basic characteristics of active arrays. Simulation results are compared with published measurements that show close agreement. This very notion verifies *ArraySim* and shows how this tool can be used to study large structures like those used in quasi-optical systems. Coupling effect among slot unit cells was studied using near field plots. Generally, replicating unit cells one after the other to form arrays may not give an optimum performance. So, rearranging unit cells to get more symmetric arrays may give a better performance as seen from near field plots in Fig. 7.21.

## Chapter 8

# Slot-Stripline-Slot Antennas For Spatial Power Combining Applications

### 8.1 Introduction

This Chapter deals with the design and analysis of unit cells and arrays of SSS structure. This three layer antenna has a complicated behavior due to coupling between layers. The analysis and simulation presented in this chapter are oriented towards spatial power combining applications and based on MPIE-MoM model introduced in Chapters 5 and 6. *ArraySim* was used to simulate different configurations starting from a simple unit cell to more complicated structure such as  $3 \times 3$  array. Simulation results show close agreement with published results. Coupling between unit cells, faulty amplifier, and random variation in the phase and amplitude of the amplifiers are investigated. Also array beam forming, power combining mechanism, and far field radiation pattern are presented and discussed.

### 8.2 SSS Structure

SSS structure consists of three layers. The upper layer and the lower layers have slots cut into the metal while the middle layer is a stripline sandwiched between the upper and lower slots. Fig. 8.1 shows a unit cell description of a SSS antenna. Active device is connected in the middle layer. The basic idea is that incident electric field on the upper slot induces current on the stripline. This current is then

amplified by the active device and radiated out through the lower layer slot. For symmetry purpose, upper and lower layer are made identical with respect to the stripline, the middle layer. Replicating unit cells side by side results into an array of unit cells. Fig. 8.5 shows a  $3 \times 3$  array of SSS type. In spatial power combiners, arrays are made with active devices that are used to gain high output power. Before simulating an array structure, it is worth analyzing the behavior of a unit cell as an array usually behaves in a similar to that of a unit cell.

### 8.2.1 Unit Cell

A two layer unit cell is shown in Fig. 8.2. It is similar to unit cell in Fig. 8.1, but with one slot only. The dimensions of this unit cell are;  $W = 2.6$  mm,  $L = 30$  mm,  $H_1 = H_2 = 1.57$  mm,  $W_s = 2$  mm,  $L_s = 30$  mm,  $x_{\text{offset}} = 10$  mm,  $y_{\text{offset}} = 0$  mm, and  $\epsilon_r = 2.2$ . From [211] the characteristic impedance,  $Z_c$ , of the stripline is given by:

$$Z_c = \begin{cases} \frac{\pi Z_0}{8\sqrt{\epsilon_r}(\ln 2 + \pi W/(4H))}, & W \geq 2H \\ \frac{Z_0}{2\pi\sqrt{\epsilon_r}} \ln \frac{16H}{\pi W}, & W \leq 0.4H \end{cases} \quad (8.1)$$

The stripline width is selected as 2.6 mm as this width gives an impedance of  $50\Omega$  to the stripline.

*ArraySim* was used to simulate this simple two layer structure with the given dimensions. S-parameters were extracted for this structure and compared with published results [213]. A close agreement is seen in simulated and published results which shows the correct working of *ArraySim*. The simulated  $S_{11}$  plot is slightly shifted to the right of the published  $S_{11}$  plot. This shift is due to the stripline basis cells since we assumed that the current is only following in the  $x$  direction.

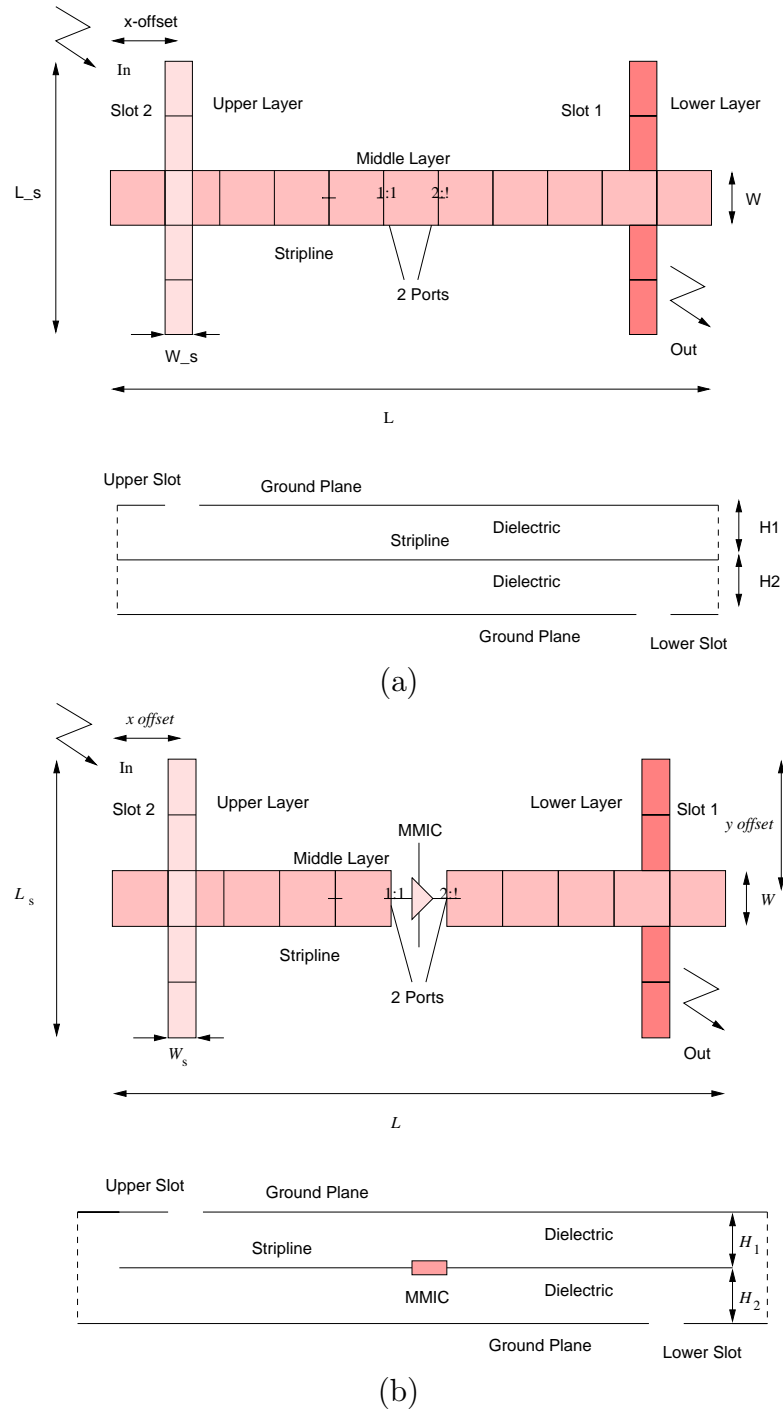
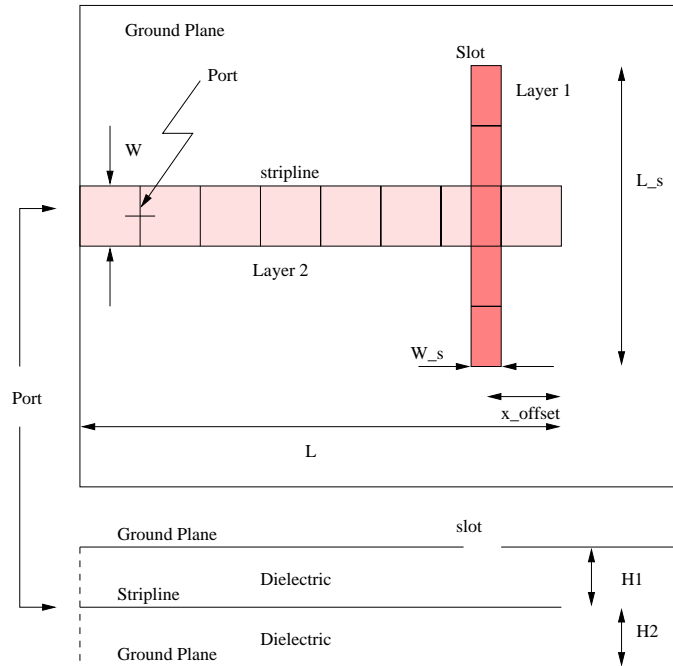
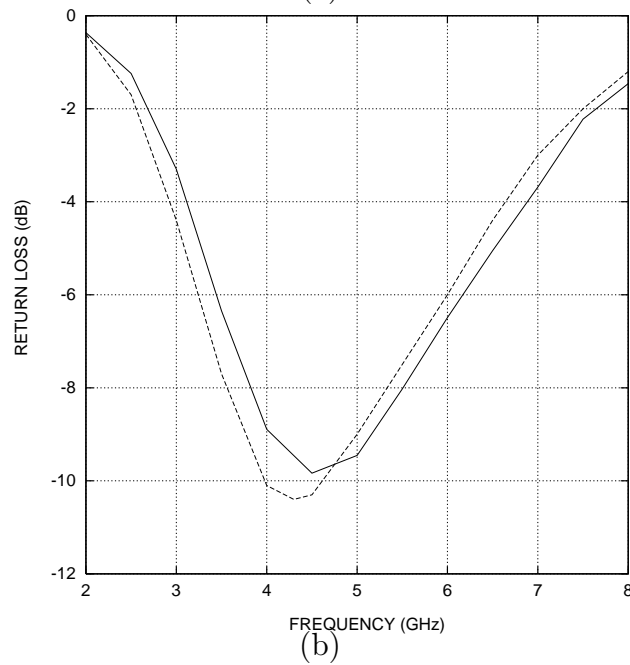


Figure 8.1: Three Layer SSS Unit Cell: (a) passive (b) active



(a)



(b)

Figure 8.2: Slot-Stripline antenna: (a) Structure layout; and (b) return loss (*ArraySim*; solid line, [213]; dotted line).

Since, SSS is a lossy structure (radiation losses), we observe that around 10 GHz, most of the input power is absorbed i.e. minimum reflection. This structure was fabricated and some measurements were made. Measurements show a maximum passive transmission of  $-10$  dB near 10.3 GHz (see Fig. 8.3) which agrees with simulated behavior as seen in Fig. 8.6. An HP8563E Spectrum analyzer was used to measure the array transmission loss. Port scattering parameters were not measured because it was not possible to drill into the stripline. The dimensions for this unit cell were;  $W = 4.5$  mm,  $L = 38.75$  mm,  $W_s = 1.5$  mm,  $L_s = 16$  mm,  $x_{\text{offset}} = 7.5$  mm,  $\epsilon_r = 2.2$ ,  $H_1=H_2=1.57$  mm,  $x$  offset of unit cell = 20 mm,  $y$  offset of unit cell = 20 mm,  $x_{\text{dist}} = 156.25$  mm, and  $y_{\text{dist}} = 88$  mm.

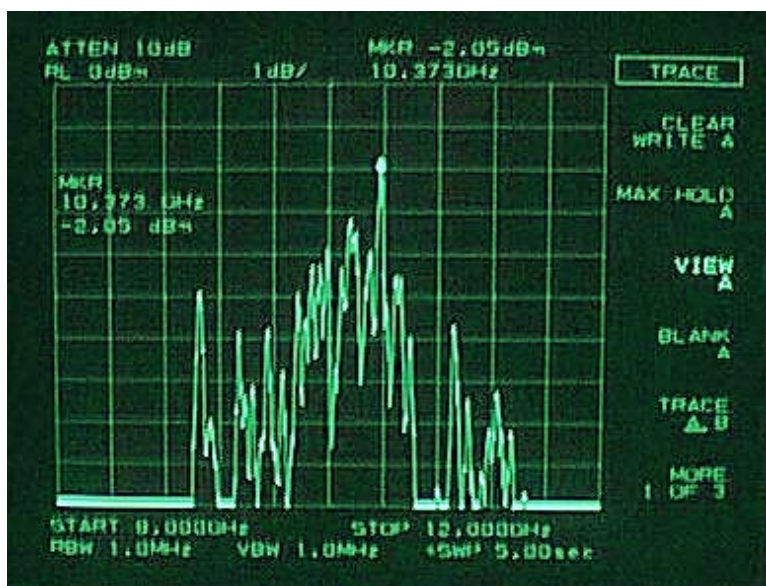


Figure 8.3: Measurement showing minimum insertion loss around 10.3 GHz as expected by simulation results.

### 8.3 $3 \times 3$ SSS Array

A  $3 \times 3$  SSS structure with dimensions shown below is simulated using *ArraySim*. Fig. 8.4 shows the physical sense of the simulation setup. The array is centered

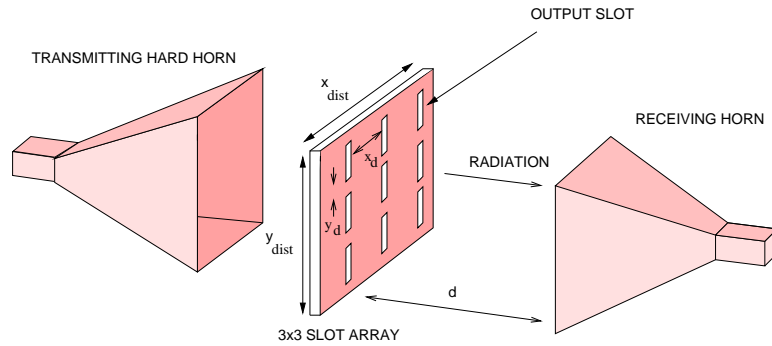


Figure 8.4: A  $3 \times 3$  SSS array is excited with a hard horn and near field plots are made at various distances,  $d$ , from array

between two hard horns (transmitting and receiving horns). A curve showing output radiation for a certain frequency range is plotted. This curve can be interpreted as S-parameters as it shows the frequency points at which the array resonates. The curves are formed by plotting the following equations.

$$S'_{11} = \sum_{i=1}^9 S_{1i}^2 \quad (8.2)$$

Similarly,

$$S'_{99} = \sum_{i=1}^9 S_{9i}^2 \quad (8.3)$$

The dimensions of this array are;  $W = 4.5$  mm,  $L = 38.75$  mm,  $W_s = 1.5$  mm,  $L_s = 16$  mm,  $x_{\text{offset}} = 7.5$  mm,  $\epsilon_r = 2.2$ ,  $H_1=H_2=1.57$  mm, x offset of unit cell = 20 mm, y offset of unit cell = 20 mm,  $x_{\text{dist}} = 156.25$  mm, and  $y_{\text{dist}} = 88$  mm. As expected, the array behaves similar to a unit cell. The array shows maximum transmission around 10 GHz.

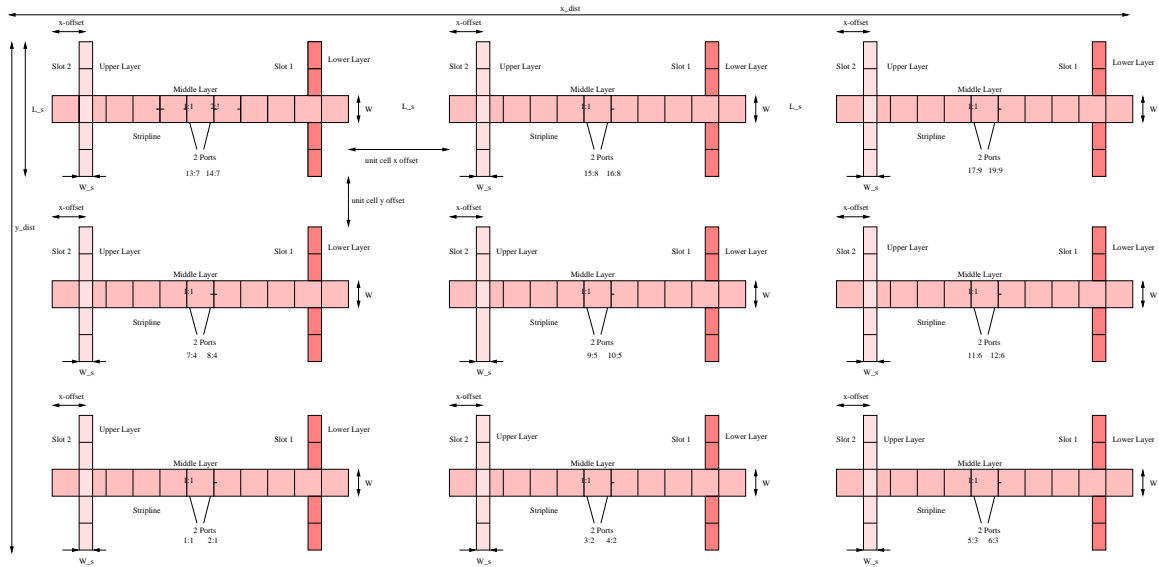


Figure 8.5: 3x3 SSS Array

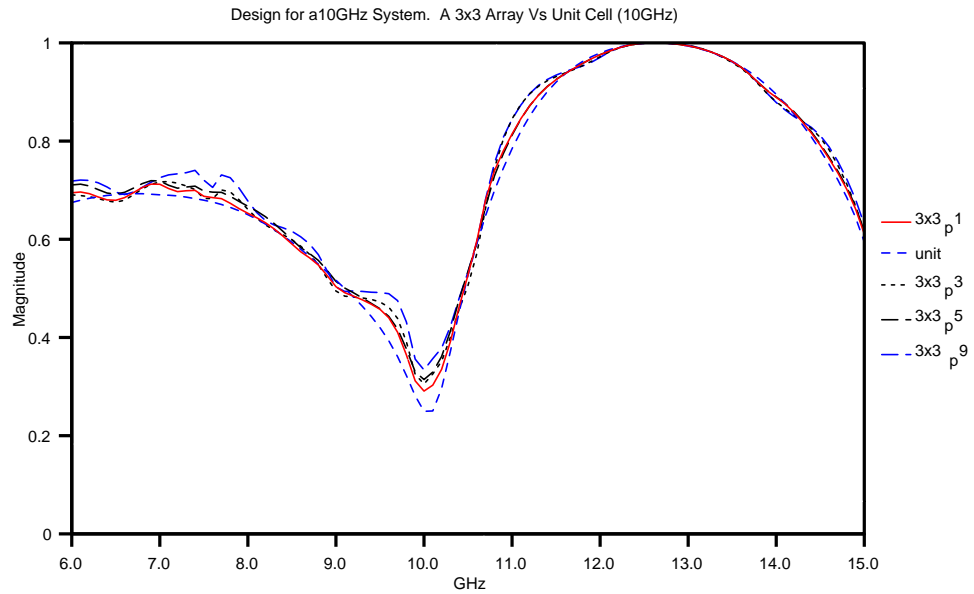


Figure 8.6: Simulation of a 3x3 SSS array shows minimum reflection of input power around 10 GHz

### 8.3.1 Coupling Effect

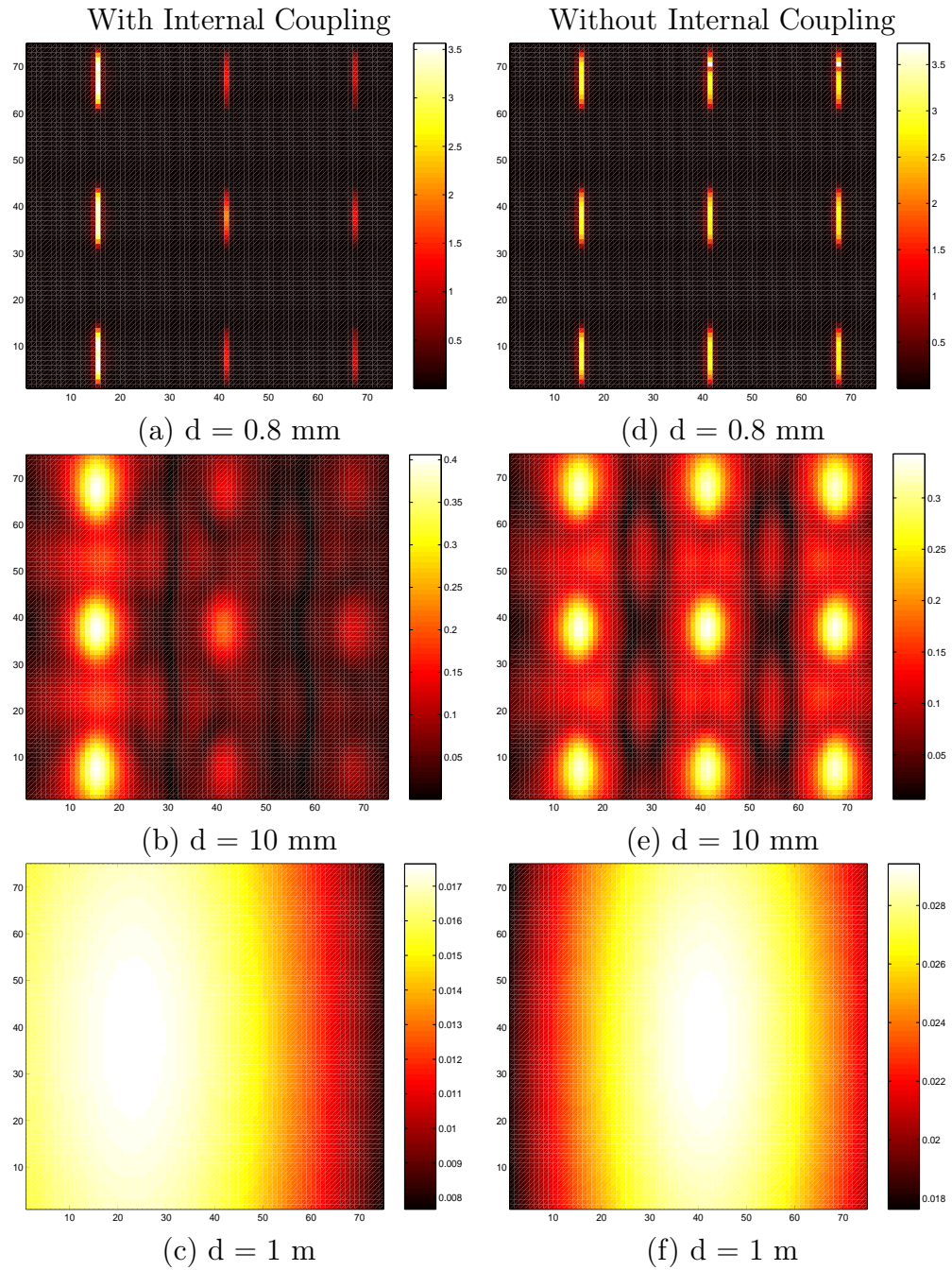
Near and far field plots were made for the  $3 \times 3$  array at 10 GHz. Fig. 8.7 shows near field plots at a distance of 0.8 mm, 10 mm, and 1 m. Note, at large distances, we see a beam as an output. Far field plot in  $y$  direction is shown in Fig. 8.8.

Near field plots in Fig. 8.7 describe coupling effects in great detail. If all unit cells are isolated, then near field plots of lower slots (transmitting slots) show almost equal output field intensity as shown in Fig. 8.7(d), (e) and (f) which is an ideal case. However, if coupling effects are taken into account, as shown in Fig. 8.7(a), (b) and (c), then the left lower layer slots show more output field intensity than the remaining lower layer slots. This behavior is attributed to the cancelation of input  $E$  fields in the middle and the right lower layer slots. However, the left lower slots are more isolated than the middle and the right lower slots and thus show more output  $E$  field intensity.

## 8.4 Power Combining Mechanism

Using *ArraySim* near-field simulation, we can study the mechanism of spatial power combining and main beam forming. This simulation can be used to study the power combining efficiency of the array and leads to optimized design and better performance.

In this section, as an example of this simulation capability, a near field study has been done over a  $3 \times 3$  array. Fig. 8.9 is field profiles at the output of the array at various distances from the surface of the transmitting antennas. The formation of the main beam and the side-lobes can be seen clearly. In this simulation the amplifiers were unit gain linear amplifiers. Fig. 8.10 are the same field profiles as above but now one of the amplifiers turned off. From this simulation, we can

Figure 8.7: Near field plots for  $3 \times 3$  array at 10GHz

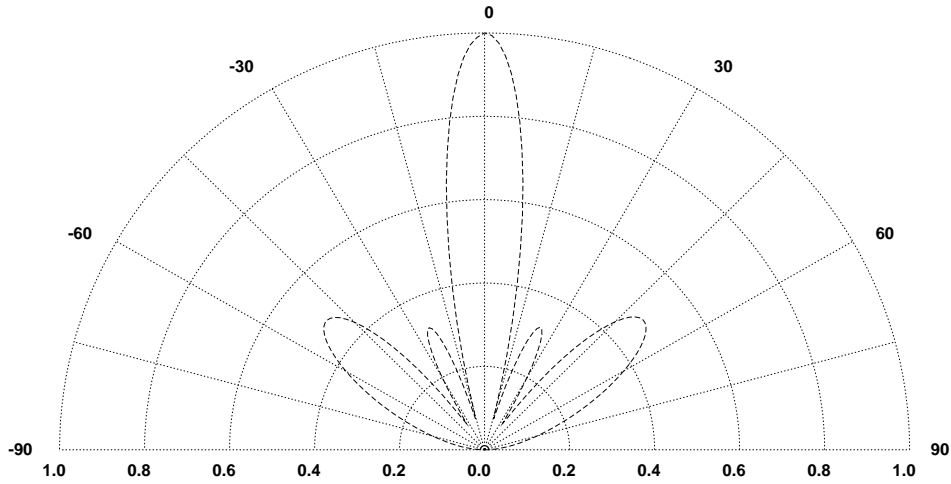


Figure 8.8:  $3 \times 3$  array radiation pattern of the H-plane at 10 GHz.

estimate the array performance and the effect of a unit cell failure on the overall power combining.

## 8.5 Tolerance of The Amplifiers

Another interesting problem faces array designers is to determine the effect of changing of phases and magnitudes of unit cell amplifiers on the main lobe and array beam performance. Fig. 8.11 shows the near field of the array when all the amplifiers are identical and the other case when there is a random variation in the amplifier phase and magnitude of  $\pm 10^\circ$  and  $\pm 1$  dB respectively. Fig. 8.11 shows that the main lobe is shifted from the center of the array.

The far-field radiation pattern for the identical case is shown in Fig. 8.12. The main lobe is centered and the  $H$  and  $E$  plane beamwidths are  $40^\circ$  and  $24^\circ$  respectively. In case of random variations, (see Fig.8.12), the main lobe of the  $H$  plane has been shifted  $3^\circ$  to the left while the  $E$  plane shifted  $1^\circ$ .

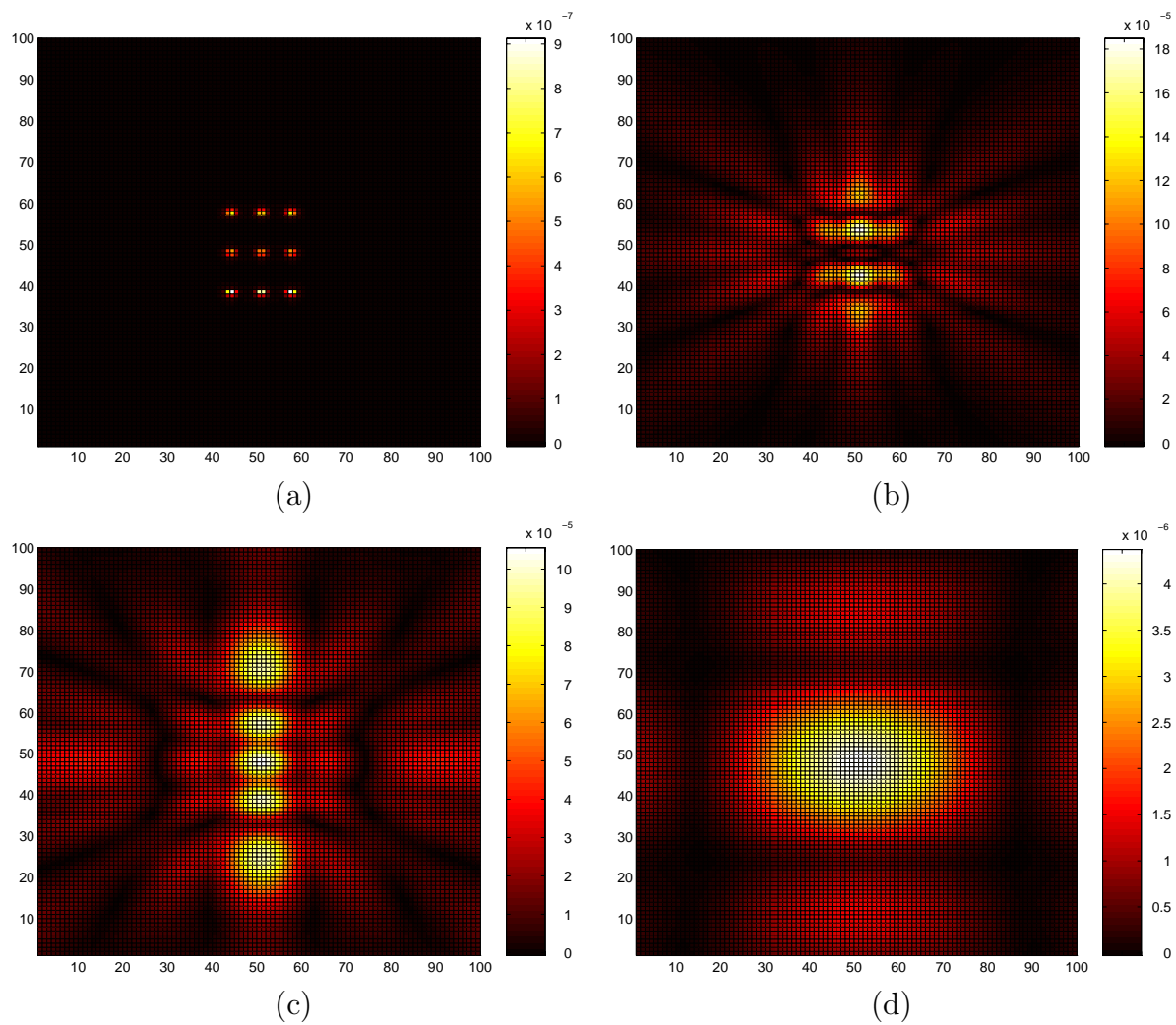


Figure 8.9: The magnitude of the horizontally polarized electric field at a distance  $z$  from the slot array surface: (b)  $z = \lambda/4$ . (c)  $z = \lambda/2$ . (d)  $z = 3\lambda$ .

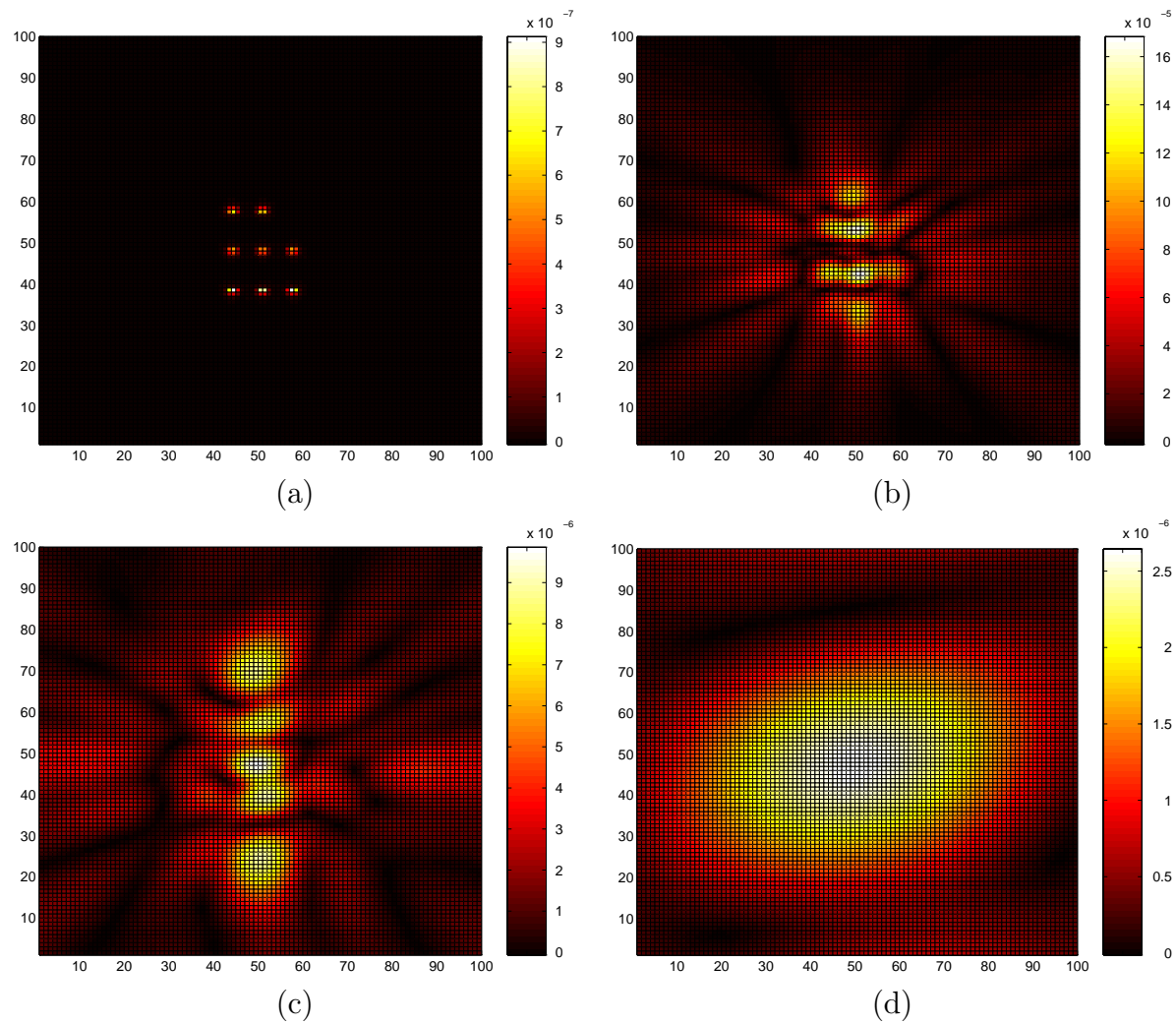


Figure 8.10: The magnitude of the horizontally polarized electric field at a distance  $z$  from the slot array surface with one of the amplifier off: (b)  $z = \lambda/4$ . (c)  $z = \lambda/2$ . (d)  $z = 3\lambda$ .

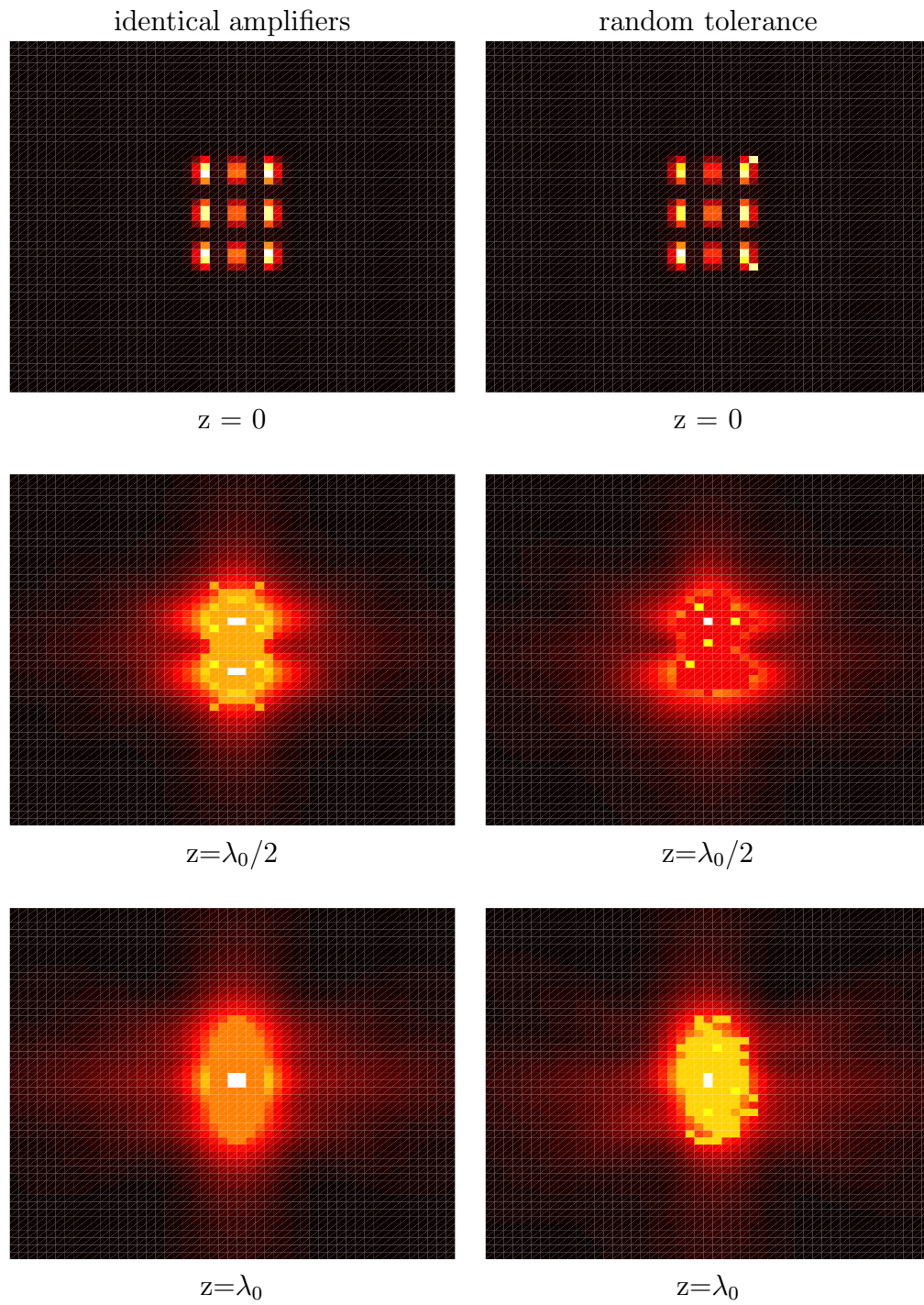


Figure 8.11: Near field plots for  $3 \times 3$  array at 38 GHz: left side; identical amplifiers, right side; random tolerance

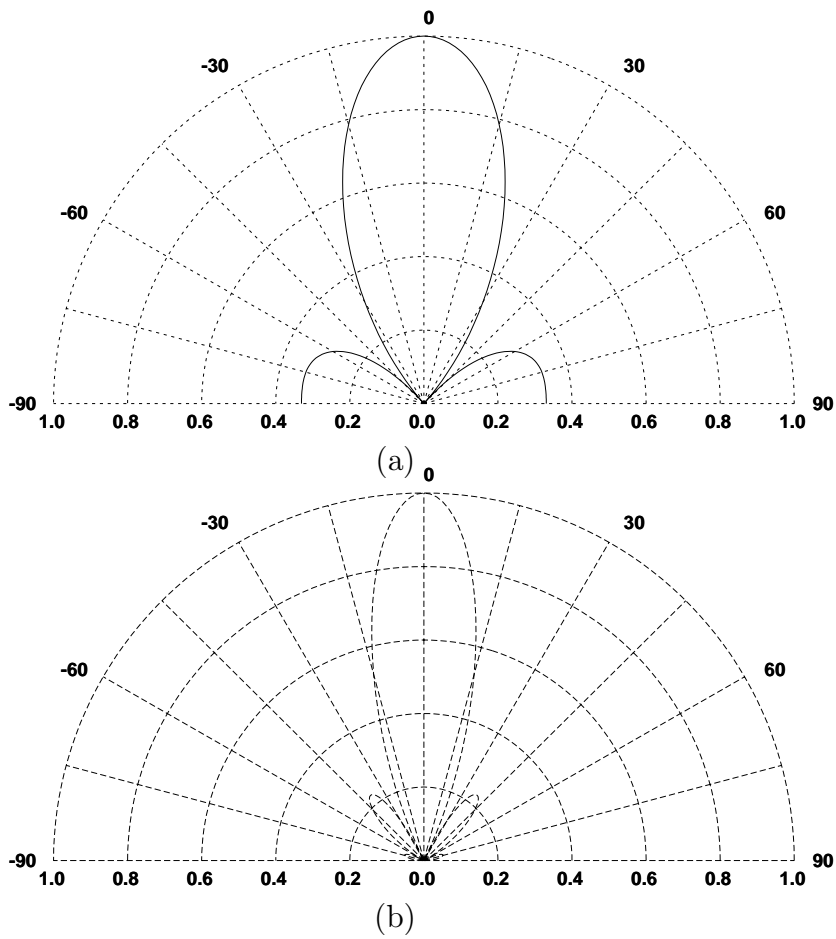


Figure 8.12:  $3 \times 3$  array radiation pattern for identical amplifier case at 38 GHz ( $E_\theta$ ; solid line;  $E_\phi$ ; dotted line) (a) H-plane ( $\phi = 0$ ); (b) E-plane ( $\phi = 90$ ).

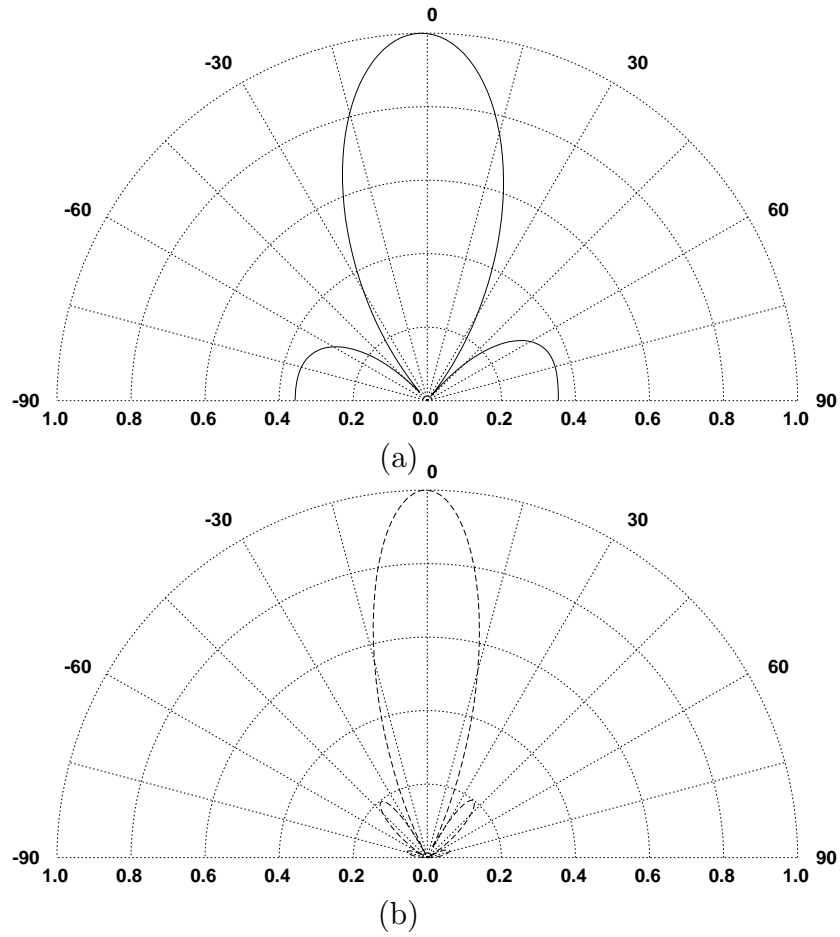


Figure 8.13:  $3 \times 3$  array radiation pattern for random variation in amplifier parameters at 38 GHz ( $E_\theta$ ; solid line;  $E_\phi$ ; dotted line) (a) H-plane ( $\phi = 0$ ); (b) E-plane ( $\phi = 90$ ).

## 8.6 Summary

In this chapter a three layer SSS structure was studied using *ArraySim*. A two layer slot-stripline structure is simulated and compared with published results and a close agreement has been seen between results. A unit SSS structure is simulated. By simulating this unit cell the maximum power transmission was around 10 GHz. This simulation is verified by observing a maximum transmission (of -10 dB) around 10.3 GHz for a fabricated SSS structure.

A  $3 \times 3$  SSS array is also designed and simulated. We studied the coupling effects as observed from near field analysis of the  $3 \times 3$  SSS array. Two cases are simulated and their near field plots are shown. In the first case, all unit cells are simulated as if they are isolated from one another while in the second case, unit cells are allowed to couple with other unit cells within the array. A shift in the output beam is seen for the later case while a centered output beam is observed for the isolated case. The shift in the beam is due to cancelation of input  $E_y$  field that falls on the upper slots.

Coupling effects among unit cells may result in low efficiency of the system where they are used and so unit cells should be isolated by some technique during fabrication of such arrays to produce uniform output field patterns. Coupling effects may be also reduced by rearranging unit cells in a fashion that gives minimum cancelation of input  $E_y$  thus enhancing overall system performance.

Also to show the capability of *ArraySim* as a CAE tool we simulated two different real situations. First, when one of the unit cell amplifier is off and the other when there are a random phase and magnitude difference between unit cell amplifiers.

## Chapter 9

### Conclusions and Future Research

#### 9.1 Conclusions

A full-wave method of moment (MoM) electromagnetic simulator was developed to study the behavior of two different structures, the CPW-slot and slot-stripline-slot structures (SSS), with applications oriented to spatial power combining systems. This simulator is based on mixed potential integral equation (MPIE) formulation and MoM technique. A computer aided engineering tool (CAE), *ArraySim*, was developed for simulating electrically large structures used in spatial power combiners. This CAE tool allows users to draw their structure on a commercial graphical layout editor that produces a layout CIF description.

The spatial and spectral domain Green's functions were derived for both structures. A numerically efficient MoM matrix filling was presented. The interaction MoM matrix elements of the self and overlapped cells are evaluated using the spectral domain while the interaction MoM matrix elements of the separated cells are evaluated using the spatial domain. In this way, an accurate and efficient numerical MoM matrix elements are guaranteed.

The port definitions in the MoM technique are presented. These port parameters are directly calculated from the MoM inverted matrix without computing the structure surface current. Also new methods, stub extraction and quarter wave length transformer, are developed to overcome the computational efforts needed in the vertical current method. Comparison of all these techniques and agreements

with published results have been shown in Chapter 6.

The MoM matrix is then solved and reduced to get a port based immittance matrix. An interface with a circuit simulator is defined that uses these port based immittance matrices along with excitation currents/voltages at the ports to compute currents and voltages of an active device. These new currents and voltages are used to form an updated excitation vector to find near and far fields due to inclusion of active device.

Sample simulations are done on a three layer SSS structure, two layer slot-stripline structure and a single layer CPW-slot structure. Unit cells as well as arrays are simulated and discussed. Simulation results are compared with measurements for specific dimensions. A close agreement is seen in simulated and measured results that verify the correct working of *ArraySim*.

*ArraySim* allows the user to model structures like active antennas and arrays provided their correct MoM routines are used. From near field analysis of various array configurations of single layer slot structures and triple layer SSS structure, we observe coupling effects at various distances from the arrays (on the output side). From these coupling effects we conclude that arrays should be designed carefully so as to reduce coupling effects among unit cells.

Convergence issues of the electromagnetic simulator were also investigated. The moment method showed convergence when the structures were divided into 10 to 20 cells per wavelength. In most cases 10 cells per wavelength was sufficient. In addition to convergence, the condition number of the moment matrix was computed indicating that the matrix was well-conditioned for the simulations presented in this dissertation.

The electromagnetic simulator developed in this dissertation has several significant developments and limitations. First the significant developments of the

modeling work are as follows:

- Finite sized arrays are considered. There is no need to make the simplifying assumption of an infinite periodic grid of identical unit cells as is required in all other quasi-optical system modeling approaches. By considering finite arrays, the coupling from every unit cell in the array is considered.
- The simulator is capable of computing results from DC to any frequency. This is an important requirement in computer aided design. All results presented here converge at DC.
- Losses in the dielectric substrate are considered. The losses in the dielectric layer is incorporated by considering the loss tangent. This results in a complex dielectric constant which is added to the formulation.
- The end result of the simulator is the computation of the multiport parameters of the array. The coupling coefficients are directly found from these port parameters. For integration of the multiport parameters in transient and harmonic balance analysis, the port parameters are converted to nodal admittance parameters.

Listed next are the limitations of the electromagnetic simulator:

- In this formulation the gridding of the antenna element must consist of equal sized cells.
- Losses in the antenna conductors are not considered. The conductor losses are difficult to include. As it stands the conductors of the antenna elements are assumed to have zero thickness. Conductor losses will be significant at millimeter wave frequencies.

The techniques presented in this dissertation will aid in the design and analysis of spatial power combining systems by accurately predicting the driving point impedances and port admittance of the passive elements in the spatial system. From a system development point of view the design of each element in the array can be individually optimized to achieve an optimum global solution in terms of stability, output power and efficiency.

## 9.2 Future Research

Simulating components of quasi-optical systems has become unavoidable. As this new research area is being explored, new and better techniques of simulating array structures are evolving. Basic problems of simulating these electrically large structures include; formulation of MoM Green's functions, computation time, matrix solution and memory. These problems are listed below with suggestions for improvement;

- One of the main issues that needs to be addressed is device field interactions. Currently the passive and active elements in the circuit are modeled individually and then cascaded together using port networks or circuit nodal parameters. When dealing at millimeter-wave frequencies the fields produced from the solid state devices are going to have some serious effects with fields from the passive structure. Other considerations that have not been considered are the thermal issues.
- *ArraySim* reduces computation time by using smart search routines that look for symmetries in the given structure and thus avoids re-computing symmetric reactions. Currently, sequential search routines are being used for searching purposes. These routines can be replaced by more efficient binary search

routines to further speed up simulation time by several folds.

- Simulating large structures like a  $10 \times 10$  CPW array, fixed size cells to mesh the layout generates an extremely large MoM matrix and thus increasing simulating time by thousands of folds. A practical approach to this problem is to use adaptive cell size.
- The size of MoM matrix is directly proportional to number of cells used in the layout as well as number of layers. For large arrays, like,  $5 \times 5$  arrays, matrix size could be easily as large as 6 million elements. It is not efficient to store such matrices in data structures at all times. Each sub-matrix should be computed and stored in a file and should only be read into data structures just before solving.
- Presently, matrix solving, that includes inversion and multiplication, takes up a chunk of total simulation time. This is because we use LU decomposition based matrix inversion. Since a new matrix is computed for every frequency point, other matrix inversion algorithms can be used that avoid the initial expensive step of LU decomposition.

*ArraySim* can be made more effective by introducing more MoM based routines describing variety of structures. This is analogous to adding more circuit models in Spice. Currently, SSS and folded-slot structure based MoM routines are interfaced as shown in Figure 9.1. By expanding the ability of *ArraySim*, we can model and study behaviors of various spatial power combiners.

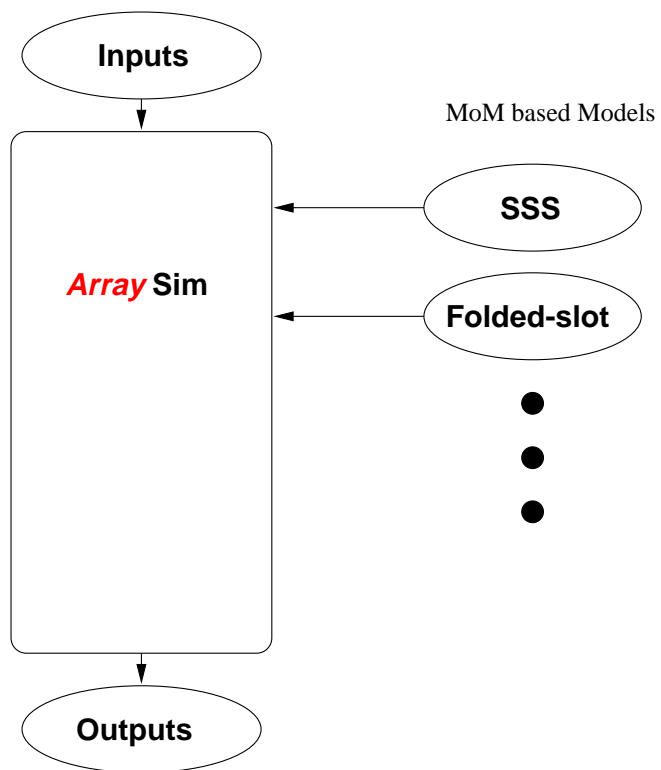


Figure 9.1: More MoM based routines can be interfaced to handle more structures

## References

- [1] K. J. Slegler, R. H. Abrams, Jr., and R. K. Parker, "Trends in solid-state microwave and millimeter-wave technology," *IEEE MTT-S Newsletter*, pp. 11-15, Fall 1990.
- [2] J. Hubert, J. Schoenberg, and Z. B. Popović, "High-power hybrid quasi-optical Ka-band amplifier design," *IEEE MTT-S Inte. Microwave Symp. Digest*, vol. 2, June 1995, pp. 585-588.
- [3] A. Sommerfeld, *Parthar Differential Equations*, Academic Press Inc., New York, 1949.
- [4] P. S. Simon, K. McInturff, D. L. Johnson, and J. A. Troychak, "Moment method analysis of a strip-fed finite slot using subdomain basis function," *1989 Antenna Application Symposium*, Monticello, Illinois, Sept. 1989, pp. 477-505.
- [5] T. Itoh, "Spectral domain immittance approach for dispersion characteristics of generalized printed transmission lines," *IEEE Trans. Microwave Theory Tech.*, vol. 28, pp. 733-736, July 1980.
- [6] U. A. Mughal, *Hierarchical Approach to Global Modeling of Active Antenna Arrays*, M.S.Thesis, North Carolina State University, 1999
- [7] R. Hertz, *Electric Waves*, Macmillian, 1983.
- [8] A. D. Frost, "Parametric amplifier antennas," *Proc. IRE*, vol. 48, pp. 1163, June 1960.
- [9] M. E. Pedinoff, "The negative conductance slot amplifier," *IRE Trans. Microwave Theory Tech.*, vol.9, pp. 557-566, November 1961.
- [10] H. Meinke and F. M. Landstorfer, "Noise and bandwidth limitations with transistorized antennas," *IEEE Antennas and Propagation Symp.*, September 1968.
- [11] F. M. Landstorfer, "Application and limitation of active aeriels at microwave frequencies." *European Microwave Conference*, pp. 122-123, September 1969.
- [12] P. A. Ramsdale and T. S. Maclean, "Active-loop-dipolee aeriels," *Proceeding of IEE*, Vol.23, pp. 1698-1710, December 1971
- [13] T. S. Maclean and P. A. Ramsdale, "Short range active transmission," *International Journal of electronics*, Vol. 36, pp. 261-269, Feb. 1974
- [14] T. S. Maclean and G. Morris, "Short Range active transmitting antenna with very large height reduction," *IEEE Trans. Antennas and Propagation*, Vol. 23, pp. 286-287, March 1975.
- [15] A. H. Al-Ani, A. L. Cullen, and J. R. Forrest, "A phase-looking method for beam steering in active array antennas," *IEEE Trans. Microwave Theory Tech.*, Vol. 22, pp. 698-703, June 1974.

- [16] B. M. Armstrong, R. Brown, F. Rix, and J. A. C. Stewart, "Use of Microstrip Impedance-measurement technique in the design of BARITT diplex Doppler sensor," *IEEE Trans. Microwave Theory Tech.*, Vol. 28, pp. 1437–1442, December 1980.
- [17] P. Bhartia and I. J. Bahl, "Frequency agile microstrip antenna," *Microwave Journal*, Vol. 25, pp. 67–70, October 1982.
- [18] H. J. Thomas, D. L. Fudge, and G. Morris, "Gun source integrated with microstrip patch," *Microwave and RF*, Vol. 24, pp. 87–91, Feb. 1985.
- [19] T. O. Perkins III, "Active microstrip circular patch antenna," *Microwave Journal*, Vol. 30, pp. 109–117, March 1987.
- [20] N. Carmirell and B. Bayraktaroughlu, "Monolithic millimeter wave IMPATT oscillator and active antenna," *IEEE Trans. Microwave Theory Tech.*, vol. 36, pp. 1670–1676, Dec. 1988.
- [21] W. P. Shillue, S. C. Wong, and K. D. Stephan, "Monolithic IMPATT millimeter-wave Oscillator Stabilized by open cavity Resonator," *IEEE MTT-S International Microwave Symposium Digest*, pp.739–740, 1989.
- [22] J. A. Navarro, K. A. Hummer, and K. Chang, "Active Integrated Antenna Elements," *Microwave Journal*, Vol.35, No.1, pp. 115–126, January 1991.
- [23] K. A. Hummer, K. Chang, "Spatial Power Combining Using Active Microstrip Antennas," *Microwave and Optical Technology Letters*, Vol. 1, No. 1, pp. 8–9, March 1988.
- [24] D. B. Rutledge, Z. B. Popovic, R. M. Weikle, M. Kim, K. A. Potter, R. Compton and R. A. York, "Quasi-optical power combining arrays," *IEEE MTT-S International Symposium Digest*, pp. 1201–1204, May 1990.
- [25] R. A. York and R. C. Compton, "Quasi-optical power combining using mutual synchronized oscillator arrays," *IEEE Trans. Microwave Theory Tech.*, vol. MTT-39, pp. 1000–1009, June 1991.
- [26] R. A. York and R. C. Compton, "Dual-device active patch antenna with improved radiation characteristics," *Electronics Letters*, vol 28, pp. 1019–1021, May 1992.
- [27] X. Gao and K. Chang, "Network modeling of an aperture coupling between microstrip line and patch antenna for active array applications," *IEEE Trans. Microwave Theory Tech.*, vol. 36, pp. 505–513, March 1988.
- [28] J. Lin and T. Itoh, "Two-dimensional quasi optical power combining arrays using strongly coupled oscillators," *IEEE Trans. Microwave Theory Tech.*, vol. 42, pp. 734–741, April 1994.
- [29] A. C. Davidson, F. W. Wise, and R. C. Compton, "A 60 GHz IMPATT oscillator array with pulsed operation," *IEEE Trans. Microwave Theory Tech.*, vol. 41, pp. 1845–1850, October 1993.

- [30] D. S. Hernandez and I. Roberston, "60 GHz-band active microstrip patch antenna for future mobile systems applications," *Electronic Letters*, vol. 30, pp. 677–678, May 1992.
- [31] X. D. Wu and K. Chang, "Novel active FET Circular patch antenna arrays for quasi optical power combining," *IEEE Transactions on Microwave Theory and Techniques*, Vol.42, No.5, pp. 766–771, May 1994.
- [32] N. J. Rohrer, M. A. Richard, G. J. Valco and K. B. Bhasin, "A 10 GHz Y-Ba-Cu-O/GaAs hybrid oscillator proximity coupled to circular microstrip patch antenna," *IEEE Transactions on Applied Superconductivity*, Vol.3, No.1, pp. 23–27, March 1993.
- [33] K. Chang, K. A. Hummer, and G. Gopalakrishnan, "Active radiating element using FET source integrated with microstrip patch antenna," *Electronic Letters*, Vol.24, No. 21, pp.1347–1348, October 1988.
- [34] V. F. Fusco and H. O. Burns, "Synthesis procedure for active integrated radiating elements," *Electronic Letters*, Vol. 26, No.4, pp. 263–264, February 1990.
- [35] J. Birkeland and T. Itoh, "Quasi-optical planar FET transceiver modules," *IEEE MTT-S International Microwave Symposium*, pp.119–122, 1989.
- [36] J. Birkeland and T. Itoh, "FET-based planar circuits for quasi-optical sources and transceivers," *IEEE Microwave Theory and Techniques*, Vol.37, No.9, pp. 1452–1459, September 1989.
- [37] J. Birkeland and T. Itoh, "Spatial power combining using push-pull FET oscillators with microstrip patch resonators," *IEEE MTT-S International Microwave Symposium*, pp. 1217–1220, 1990.
- [38] V.F. Fusco, "Series feedback integrated active microstrip antenna synthesis and characterization," *Electronics Letters*, Vol.28,No.14,pp.1362–1363, July 1992.
- [39] P. S. Hall and P. M. Haskins, "Microstrip active patch array with beam scanning," *Electronics Letters*, Vol.28, No.22, pp.2056–2057, October 1992.
- [40] P. S. Hall, I. L. Morrow, P. M. Haskins, and J. S. Dahele, "Phase control in injection locked microstrip antennas," *IEEE MTT-S International Microwave Symposium Digest*, pp. 11227–1230, 1994.
- [41] J. Birkeland and T. Itoh, "Two port FET oscillator with application to active arrays," *IEEE Microwave and Guided Wave Letters*, Vol.1, No.5, pp. 112–113, May 1991.
- [42] J. Birkel and T. Itoh, "16-element quasi-optical FET oscillator power combining array with external injection locking," *IEEE Transactiond on Microwave Theory and Techniques*, Vol.40, No.3, pp. 475–481, March 1992.
- [43] T. Mader, J. Schoenberg, L. Harmon, and Z. B. Popovic, "Planar MESFET transmission wave amplifier," *Electronics Letters*, Vol. 29, No.19, pp. 1699–1701, September 1993.

- [44] H. S. Tsai and R. A. York, "Polarization rotation quasioptical reflection amplifier cell," *Electronics Letters*, Vol. 29, No.24, pp.2125–2127, November 1993.
- [45] N. Shetch, T. Ivanov, A. Balasubramaniyan, and A. Mortazawi, "A nine HEMT spatial amplifier," *IEEE MTT-S International Microwave Symposium*, pp. 1239–1242, 1994.
- [46] R. A. York, R. D. Martinez, and R. C. Compton, "Active patch antenna element for array applications," *Electronics Letters*, pp. 494–495, Vol.26, No.7, March 1990.
- [47] X. D. Wu, K. Leverich and K. Chang, "Novel FET active patch antenna," *Electronics Letters*, Vol.28, No.20, pp.1853–1854, September 1992.
- [48] R. D. Martinez and R. C. Compton, "High efficiency FET/microstrip-patch oscillators," *IEEE Antennas and Propagation Magazine*, Vol.36, No.1, pp16–19, February 1994.
- [49] R. D. Martinez and R. C. Compton, "A quasi optical oscillator/modulator for wireless transmission," *IEEE MTT-S International Microwave Symposium Digest*, pp. 839–842, 1994.
- [50] P. M. Haskins, P. S. Hall, and J. S. Dahele, "Active patch antenna element with diode tuning," *Electronics Letters*, Vol.27, No.20, pp.1846–1847, September 1991.
- [51] P. S. Hall, "Analysis of radiation from active microstrip antennas," *Electronics Letters*, Vol.29, No.1, pp. 127–129, January 1993.
- [52] P. Liao and R. A. York, "A varactor-tuned patch oscillator for active arrays," *IEEE Microwave and Guided Wave Letters*, Vol.4, No.10, pp. 335–337, October 1994.
- [53] A. Balasubramaniyan and A. Mortazawi, "Two-dimensional mesfet-based spatial power combiners," *IEEE Microwave and Guided Wave Letters*, Vol.3, No.10, pp. 366–368, October 1993.
- [54] B. Robert, T. Razban, and A. Papiernik, "Compact active patch antenna," *IEEE 8th int. conf. on antennas and propagation, Edinburgh, UK*, pp. 307–310, April 1993.
- [55] D. V. Plant, D. C. Scott, D. C. Ni, and H. R. Fetterman, "Generation of millimeter-wave radiation by optical mixing in FET's integrated with printed circuit antennas," *IEEE Microwave and Guided Wave Letters*, Vol.1, No.6, pp. 132–134, June 1991.
- [56] D. V. Plant, D. C. Scott, D. C. Ni, and H. R. Fetterman, "Optically-generated 60 GHz mm-waves using AlGa/InGaAs HEMTs, integrated with both quasioptical antenna circuits and MMICs," *IEEE Photon. Tech. Letters*, Vol.4, pp. 102–105, 1992.
- [57] D. C. Scott, D. V. Plant, and H. R. Fetterman, "60 GHz sources using optically derived heterojunction bipolar transistors," *Applied Physics Letters*, Vol.61, pp.1–3, 1992.

- [58] T. Razban, M. Nannini, and A. Papiernik, "Integration of oscillators with patch antennas," *Microwave Journal*, Vol.36, No.1, pp. 104–110, January 1993.
- [59] G. F. Avitabile, S. Maci, G. Biffi Gentili, F. Ceccuti, and G. F. Manes, "A basic module for active antenna applications" *IEEE 8th int. conf. on antennas and propagation, Edinburgh, UK*, pp. 303–306, April 1993.
- [60] H. An, J. C. Nauwelaers, G. A. E. Vandenbosh, and A. Van de Capelle "Active antenna uses semi-balanced amplifier structure," *Microwaves and Rf*, Vol.33, No.13, pp. 153–156, December 1994.
- [61] R. Gillard, H. Legay, J. M. Floch, and J. Citerne, "Rigorous modeling of receiving active microstrip antennas," *Electronics Letters*, Vol.27, No.25, pp. 2357–2359, December 1991.
- [62] H. An, B. Nauwelaers, and A. Van de Capelle " Noise figure measurement of receiving active microstrip antennas," *Electronics Letters*, Vol.29, No.18, pp. 1594–1596, September 1993.
- [63] J. J. Lee, "G/T and noise figure of active array antennas," *IEEE Transactions on Antennas and propagation*, Vol. AP-41, No.2, pp. 241–244, February 1993.
- [64] U. Dahlgren, J. Svedin, H. Johanson, O. J. Hagel, H. Zirath, C. Karlsson, and N. Rorsman, "An integrated millimeterwave bcb patch antenna HEMT receiver," *IEEE MTT-S International Microwave Symposium Digest*, pp. 661–664, 1994.
- [65] K. Cha, S. Kawasaki, and T. Itoh, "Transponder using self-oscillating mixer and active antenna," *IEEE MTT Symposium Digest*, pp. 425–428, 1994.
- [66] V. A. Thomas, K. M. Ling, M. E. Jones, B. Toland, J. Lin, and T. Itoh, "FDTD analysis of an active antenna," *IEEE Microwave and Guided Wave Letters*, Vol.4, No.9, pp. 296–298, September 1994.
- [67] B. Toland, J. Lin, B. Houshmand, and T. Itoh, "Electromagnetic simulation of mode control of a two element active antenna," *IEEE MTT-S International Microwave Symposium Digest*, pp. 883–886 , 1994.
- [68] J. W. Mink, "Quasi-optical power combining of solid-state millimeter-wave sources," *IEEE Trans. Microwave Theory Tech.*, vol. MTT-34, pp. 273–279, Feb. 1986.
- [69] Z. B. Popović, M. Kim, and D. B. Rutledge, "Grid oscillators," *Int. Journal Infrared and Millimeter Waves*, vol. 9, pp. 1003–1010, Nov. 1988.
- [70] M. Kim, J. J. Rosenberg, R. P. Smith, R. M. Weikle II, J. B. Hacker, M. P. De Lizio, and D. B. Rutledge, "A grid amplifier," *IEEE Microwave Guided Wave Lett.*, vol. 1, pp. 322–324, Nov. 1991.
- [71] P. F. Goldsmith, "Quasi-optical techniques at millimeter and sub-millimeter wavelengths," in *Infrared and Millimeter Waves*, K. J. Button (Ed.), New York: Academic Press, vol. 6, pp. 277–343, 1982.

- [72] Special Issue on Quasi-Optical Techniques, J. W. Mink and D. B. Rutledge (eds.), *IEEE Trans. Microwave Theory Tech.*, vol. MTT-41, Oct. 1993.
- [73] R. A. York, "Quasi-optical power combining techniques," *SPIE Critical Reviews of Emerging Technologies*, 1994.
- [74] M. Gouker, "Toward standard figures-of-merit for spatial and quasi-optical power-combined arrays," *IEEE Trans. Microwave Theory Tech.*, vol. MTT-43, pp. 1614–1617, July 1995.
- [75] S. L. Young and K. D. Stephan, "Stabilization and power combining of planar microwave oscillators with an open resonator," *IEEE MTT-S Int. Microwave Symp. Dig.*, pp. 185–188, June 1987.
- [76] M. Nakayama, M. Hieda, T. Tanaka, and K. Mizuno, "Millimeter and submillimeter wave quasi-optical oscillator with multi-elements," *IEEE MTT-S Int. Microwave Symp. Dig.*, pp. 1209–1212, June 1990.
- [77] H. Kondo, M. Hieda, M. Nakayama, T. Tanaka, K. Osakabe, and K. Mizuno, "Millimeter and submillimeter wave quasi-optical oscillator with multi-elements," *IEEE Trans. Microwave Theory Tech.*, vol. MTT-40, pp. 857–863, May 1992.
- [78] M. Kiyokawa and T. Matsui, "A new quasi-optical oscillator with Gaussian output beam," *IEEE Microwave Guided Wave Lett.*, vol. 4, pp. 129–131, May 1994.
- [79] M. Kiyokawa, T. Matsui, and N. Hirose, "Dielectric loaded Gaussian beam oscillator in the 40 GHz band," *IEEE MTT-S Int. Microwave Symp. Dig.*, pp. 75–78, May 1995.
- [80] G. P. Monahan, *Experimental Investigation of an Open Resonator Quasi-Optical Power Combiner Using IMPATT Diodes*, Ph.D. Dissertation, North Carolina State University, 1995.
- [81] T. Fujii, H. Mazaki, F. Takei, J. Bae, M. Narihiro, T. Noda, H. Sakaki, and K. Mizuno, "Coherent power combining of millimeter wave resonant tunneling diodes in a quasi-optical resonator," *IEEE MTT-S Int. Microwave Symp. Dig.*, pp. 919–922, June 1996.
- [82] M. Sanagi, E. Yamamoto, and S. Nogi, "Axially symmetric Fabry-Perot power combiners with active devices mounted on both the mirrors," *IEEE MTT-S Int. Microwave Symp. Dig.*, pp. 1259–1262, June 1996.
- [83] Z. B. Popović, R. M. Weikle II, M. Kim, K. A. Potter, and D. B. Rutledge, "Bar-grid oscillators," *IEEE Trans. Microwave Theory Tech.*, vol. MTT-38, pp. 225–230, Mar. 1990.
- [84] Z. B. Popović, R. M. Weikle II, M. Kim, and D. B. Rutledge, "A 100-MESFET planar grid oscillator," *IEEE Trans. Microwave Theory Tech.*, vol. MTT-39, pp. 193–200, Feb. 1991.

- [85] R. M. Weikle II, M. Kim, J. B. Hacker, M. P. De Lisio, and D. B. Rutledge, "Planar MESFET grid oscillators using gate feedback," *IEEE Trans. Microwave Theory Tech.*, vol. MTT-40, pp. 1997–2003, Nov. 1992.
- [86] T. B. Mader, S. C. Bundy, and Z. B. Popović, "Quasi-optical array VCOs," *IEEE Trans. Microwave Theory Tech.*, vol. MTT-41, pp. 1775–1781, Oct. 1993.
- [87] J. B. Hacker, M. P. De Lisio, M. Kim, C.-M. Liu, S.-J. Li, S. W. Wedge, and D. B. Rutledge, "A 10-watt X-band grid oscillator," *IEEE MTT-S Int. Microwave Symp. Dig.*, pp. 823-826, May 1994.
- [88] W. A. Shiroma, B. L. Shaw, and Z. B. Popović, "A 100-transistor quadruple grid oscillator," *IEEE Microwave Guided Wave Lett.*, vol. 4, pp. 350–351, Oct. 1994.
- [89] J. Birkeland and T. Itoh, "A 16 element quasi-optical FET oscillator power combining array with external injection locking," *IEEE Trans. Microwave Theory Tech.*, vol. MTT-40, pp. 475–481, Mar. 1992.
- [90] A. Mortazawi, H. D. Folt, and T. Itoh, "A periodic second harmonic spatial power combining oscillator," *IEEE Trans. Microwave Theory Tech.*, vol. MTT-40, pp. 851–856, May 1992.
- [91] P. Liao and R. A. York, "A high power two-dimensional coupled-oscillator array at X-band," *IEEE MTT-S Int. Microwave Symp. Dig.*, pp. 909–912, May 1995.
- [92] M. Rahman, T. Ivanov, and A. Mortazawi, "An extended resonance spatial power combining oscillator," *IEEE MTT-S Int. Microwave Symp. Dig.*, pp. 1263–1266, June 1996.
- [93] C. Y. Chi and G. M. Rebeiz, "A quasi-optical amplifier," *IEEE Microwave Guided Wave Lett.*, vol. 3, pp. 164–166, June 1993.
- [94] M. Kim, E. A. Sovero, J. B. Hacker, M. P. De Lisio, J. C. Chiao, S. J. Li, D. R. Gagnon, J. J. Rosenberg, and D. B. Rutledge, "A 100-element HBT grid amplifier," *IEEE Trans. Microwave Theory Tech.*, vol. MTT-41, pp. 1762–1771, Oct. 1993.
- [95] M. Kim, E. A. Sovero, J. B. Hacker, M. P. De Lisio, J. J. Rosenberg, and D. B. Rutledge, "A 6.5 GHz source using a grid amplifier with a twist reflector," *IEEE Trans. Microwave Theory Tech.*, vol. MTT-41, pp. 1772–1774, Oct. 1993.
- [96] C. Liu, E. A. Sovero, W. J. Ho, J. A. Higgins, M. P. De Lisio, and D. B. Rutledge, "Monolithic 40-GHz 670-mW HBT grid amplifiers," *IEEE MTT-S Int. Microwave Symp. Dig.*, pp. 1123-1126, June 1996.
- [97] M. P. De Lisio, S. W. Duncan, D. Tu, S. Weinreb, C. Liu, and D. B. Rutledge, "A 44-60 GHz monolithic pHEMT grid amplifier," *IEEE MTT-S Int. Microwave Symp. Dig.*, pp. 1127–1130, May 1995.

- [98] A. Mortazawi and B. C. De Loach, "A nine-MESFET two-dimensional power-combining array employing an extended resonance technique," *IEEE Microwave Guided Wave Lett.*, vol. 3, pp. 214–216, July 1993.
- [99] T. Ivanov and A. Mortazawi, "Two stage double layer microstrip spatial amplifiers," *IEEE MTT-S Int. Microwave Symp. Dig.*, pp. 589–592, May 1995.
- [100] J. Schoenberg, T. Mader, B. Shaw, and Z. B. Popović, "Quasi-optical antenna array amplifiers," *IEEE MTT-S Int. Microwave Symp. Dig.*, pp. 605–608, May 1995.
- [101] J. Hubert, J. Schoenberg, and Z. B. Popović, "High-power hybrid quasi-optical Ka-band amplifier design," *IEEE MTT-S Int. Microwave Symp. Dig.*, pp. 585–588, May 1995.
- [102] H. S. Tsai and R. A. York, "Quasi-optical amplifier array using direct integration of MMICs and 50  $\Omega$  multi-slot antennas," *IEEE MTT-S Int. Microwave Symp. Dig.*, pp. 593–596, May 1995.
- [103] H. S. Tsai and R. A. York, "Multi-slot 50  $\Omega$  antennas for quasi-optical circuits," *IEEE Microwave Guided Wave Lett.*, vol. 5, pp. 180–182, June 1995.
- [104] E. A. Sovero, Y. Kwon, D. S. Deakin, A. L. Sailer, and J. A. Higgins, "A PHEMT based monolithic plane wave amplifier for 42 GHz," *IEEE MTT-S Int. Microwave Symp. Dig.*, pp. 1111–1114 May 1995.
- [105] A. Alexanian, H. Tsai, and R. A. York, "Quasi-optical traveling wave amplifiers," *IEEE MTT-S Int. Microwave Symp. Dig.*, pp. 1115–1118, May 1995.
- [106] C. H. Tsao and R. Mittra, "Spectral-domain analysis of frequency selective surfaces comprised of periodic arrays of crossed dipoles and Jerusalem crosses," *IEEE Trans. Antennas Propagat.*, vol. AP-32, pp. 478–486, May 1984.
- [107] T. A. Cwik and R. Mittra, "Scattering for a periodic array of free-standing arbitrary shaped perfectly conducting or resistive patches," *IEEE Trans. Antennas Propagat.*, vol. AP-35, pp. 1226–1234, Nov. 1987.
- [108] C. H. Chan and R. Mittra, "On the analysis of frequency-selective surfaces using subdomain basis functions," *IEEE Trans. Antennas Propagat.*, vol. AP-38, pp. 40–50, Jan. 1990.
- [109] L. B. Sjögren and N. C. Luhmann Jr., "An impedance model for the diode grid," *IEEE Microwave Guided Wave Lett.*, vol. 1, pp. 297–299, Oct. 1991.
- [110] A. Pance and M. J. Wengler, "Microwave modeling of 2-D active grid arrays," *IEEE Trans. Microwave Theory Tech.*, vol. MTT-41, pp. 20–28, Jan. 1993.
- [111] T. Wu, "Quasi-optical grids with thin rectangular patch/aperture elements," *Int. Journal Infrared and Millimeter Waves*, vol. 14, pp. 1017–1033, May 1993.
- [112] S. C. Bundy, W. A. Shiroma, and Z. B. Popović, "Design-oriented analysis of grid power combiners," *Proc. Workshop on Millimeter-Wave Power Generation and Beam Control*, pp. 197–208, Sept. 1993.

- [113] S. C. Bundy and Z. B. Popović, "Analysis of planar grid oscillators," *IEEE MTT-S Int. Microwave Symp. Dig.*, pp. 827–830, June 1994.
- [114] S. C. Bundy and Z. B. Popović, "A generalized analysis for grid oscillator design," *IEEE Trans. Microwave Theory Tech.*, vol. MTT-42, pp. 2486–2491, Dec. 1994.
- [115] S. C. Bundy, *Analysis and Design of Grid Oscillators*, Ph.D. Dissertation, University of Colorado at Boulder, 1994.
- [116] S. C. Bundy, W. A. Shiroma, and Z. B. Popović, "Analysis of cascaded quasi-optical grids," *IEEE MTT-S Int. Microwave Symp. Dig.*, pp. 601–604, May 1995.
- [117] W. A. Shiroma, S. C. Bundy, S. Hollung, B. D. Bauernfeind, and Z. B. Popović, "Cascaded active and passive quasi-optical grids," *IEEE Trans. Microwave Theory Tech.*, vol. MTT-43, pp. 2904–2909, Dec. 1995.
- [118] R. M. Weikle II, *Quasi-Optical Planar Grids for Microwave and Millimeter-Wave Power Combining*, Ph.D. Dissertation, California Institute of Technology, 1992.
- [119] P. L. Heron, F. K. Schwing, G. P. Monahan, J. W. Mink, and M. B. Steer, "A dyadic Green's function for the plano-concave quasi-optical resonator," *IEEE Microwave Guided Wave Lett.*, vol. 3, pp. 256–258, Aug. 1993.
- [120] P. L. Heron, G. P. Monahan, J. W. Mink, F. K. Schwing, and M. B. Steer, "Impedance matrix of an antenna array in a quasi-optical resonator," *IEEE Trans. Microwave Theory Tech.*, vol. MTT-41, pp. 1816–1826, Oct. 1993.
- [121] P. L. Heron, *Modeling and Simulation of Coupling Structures for Quasi-Optical Systems*, Ph.D. Dissertation, North Carolina State University, 1993.
- [122] P. L. Heron, G. P. Monahan, J. E. Bird, M. B. Steer, F. K. Schwing, and J. W. Mink, "Circuit level modeling of quasioptical power combining open cavities," *IEEE MTT-S Int. Microwave Symp. Dig.*, pp. 433–436, June 1993.
- [123] P. L. Heron, G. P. Monahan, F. K. Schwing, J. W. Mink, and M. B. Steer, "Multiport circuit model of an antenna array in an open quasi-optical resonator," *Proc. URSI*, p. 84, June 1993.
- [124] M. B. Steer, "Simulation of microwave and millimeter-wave oscillators, present capability and future directions," *Proc. Workshop on Integrated Nonlinear Microwave and Millimeter-wave Circuits*, Oct. 1992.
- [125] M. B. Steer and S. G. Skaggs, "CAD of GaAs microwave circuits: historical perspective and future trends," *Korea-United States Design and Manufacturing Workshop*, pp. 109–118, Nov. 1993.
- [126] G. P. Monahan, P. L. Heron, M. B. Steer, J. W. Mink, and F. K. Schwing, "Mode degeneracy in quasi-optical resonators," *Microwave and Optical Technology Letters*, vol 8, pp. 230–232, Apr. 1995.

- [127] T. W. Nuteson, G. P. Monahan, M. B. Steer, K. Naishadham, J. W. Mink, and F. K. Schwering, "Use of the moment method and dyadic Green's functions in the analysis of quasi-optical structures," *IEEE MTT-S Int. Microwave Symp. Dig.*, pp. 913–916, May 1995.
- [128] T. W. Nuteson, G. P. Monahan, M. B. Steer, K. Naishadham, J. W. Mink, K. Kojucharow, and J. Harvey, "Full-wave analysis of quasi-optical structures," *IEEE Trans. Microwave Theory Tech.* vol. 44, pp. 701–710, May 1996.
- [129] T. W. Nuteson, M. B. Steer, K. Naishadham, J. W. Mink, and J. Harvey, "Electromagnetic modeling of finite grid structures in quasi-optical systems," *IEEE MTT-S Int. Microwave Symp. Dig.*, pp. 1251–1254, June 1996.
- [130] T. W. Nuteson, *Electromagnetic modeling of quasi-optical power combiner*, Ph.D. Dissertation, North Carolina State University, 1996.
- [131] A. Alexanian, N. J. Koliass, R. C. Compton, and R. A. York, "Three-dimensional FDTD analysis of quasi-optical arrays using Floquet boundary conditions and Berenger's PML," *IEEE Microwave Guided Wave Lett.*, vol. 6, pp. 138–140, Mar. 1996.
- [132] L. W. Epp, R. P. Smith, "A generalized scattering matrix approach for analysis of quasi-optical grids and de-embedding of device parameters," *IEEE Trans. Microwave Theory Tech.* vol. 44, pp. 760–769, May 1996.
- [133] A. R. Adams, R. D. Pollard, and C. M. Snowden, "Method of moments and time domain analyses of waveguide-based hybrid multiple device oscillators," *IEEE MTT-S Int. Microwave Symp. Dig.*, pp. 1255–1258, June 1996.
- [134] R. F. Harrington, *Field Computation by Moment Methods*, Macmillan, New York, 1968.
- [135] G. A. Thiele, "Wire antennas," in *Computer Techniques for Electromagnetics*, R. Mittra (ed.), Oxford: Pergamon Press Ltd., pp. 7-95, 1973.
- [136] W. A. Imbriale, "Applications of the method of moments to thin-wire elements and arrays," in *Numerical and Asymptotic Techniques in Electromagnetics*, R. Mittra (ed.), New York: Springer-Verlag, pp. 5–50, 1975.
- [137] P. A. Ramsdale, "Wire antennas," in *Advances in Electronics and Electron Physics*, vol. 47, New York: Academic Press, pp. 123–196, 1978.
- [138] E. K. Miller and F. J. Deadrick, "Some computational aspects of thin-wire modeling," in *Numerical and Asymptotic Techniques in Electromagnetics*, R. Mittra (ed.), New York: Springer-Verlag, pp. 89–127, 1975.
- [139] R. Mittra and C. A. Klein, "Stability and convergence of moment method solutions," in *Numerical and Asymptotic Techniques in Electromagnetics*, R. Mittra (ed.), New York: Springer-Verlag, pp. 129–163, 1975.
- [140] Y. Rahmat-Samii and R. Mittra, "Integral equation solution and RCS computation of a thin rectangular plate," *IEEE Trans. Antennas Propagat.*, vol. AP-22, pp. 608–610, July 1974.

- [141] J. R. Mautz and R. F. Harrington, "H-field, E-field, and combined field solutions for conducting bodies of revolution," *AEÜ*, vol. 32, pp. 157–164, Apr. 1978.
- [142] E. H. Newman and D. M. Pozar, "Electromagnetic modeling of composite wire and surface geometries," *IEEE Trans. Antennas Propagat.*, vol. AP-26, pp. 784–789, Nov. 1978.
- [143] A. W. Glisson and D. R. Wilton, "Simple and efficient numerical methods for problems of electromagnetic radiation and scattering from surfaces," *IEEE Trans. Antennas Propagat.*, vol. AP-28, pp. 593–603, Sept. 1980.
- [144] S. M. Rao, D. R. Wilton, and A. W. Glisson, "Electromagnetic scattering by surfaces of arbitrary shape," *IEEE Trans. Antennas Propagat.*, vol. AP-30, pp. 409–418, May 1982.
- [145] T. Itoh and R. Mittra, "Spectral domain approach for calculating the dispersion characteristics of microstrip line," *IEEE Trans. Microwave Theory Tech.*, vol. MTT-21, pp. 496–499, July 1973.
- [146] D. M. Pozar, "Input impedance and mutual coupling of rectangular microstrip antennas," *IEEE Trans. Antennas Propagat.*, vol. AP-30, pp. 1191–1196, Nov. 1982.
- [147] R. W. Jackson and D. M. Pozar, "Full-wave analysis of microstrip open-end and gap discontinuities," *IEEE Trans. Microwave Theory Tech.*, vol. MTT-33, pp. 1036–1042, Oct. 1985.
- [148] D. M. Pozar, "Finite phased arrays of rectangular microstrip patches," *IEEE Trans. Antennas Propagat.*, vol. AP-34, pp. 658–665, Jan. 1987.
- [149] N. K. Das and D. M. Pozar, "A generalized spectral-domain Green's function for multilayer dielectric substrates with application to multilayer transmission lines," *IEEE Trans. Microwave Theory Tech.*, vol. MTT-35, pp. 326–335, Mar. 1987.
- [150] R. W. Jackson, "Full-wave, finite element analysis of irregular microstrip discontinuities," *IEEE Trans. Microwave Theory Tech.*, vol. MTT-37, pp. 81–89, Jan. 1989.
- [151] D. M. Pozar, "Analysis and design considerations for printed phased-array antennas," in *Handbook of Microstrip Antennas*, J. R. James and P. S. Hall (eds.), London: Peter Peregrinus Ltd., pp. 693–753, 1989.
- [152] A. K. Skrivervik and J. R. Mosig, "Analysis of finite phase arrays of microstrip patches," *IEEE Trans. Antennas Propagat.*, vol. AP-41, pp. 1105–1114, Aug. 1993.
- [153] G. Pan, J. Tan, and J. D. Murphy, "Full-wave analysis of microstrip floating-line discontinuities," *IEEE Trans. Electromagnetic Compat.*, vol. EMC-36, pp. 49–59, Feb. 1994.

- [154] J. R. Mosig and F. E. Gardiol, "A dynamic radiation model for microstrip structures," in *Advances in Electronics and Electron Physics*, vol. 59, New York: Academic Press, pp. 139–237, 1982.
- [155] J. R. Mosig and F. E. Gardiol, "General integral equation formulation for microstrip antennas and scatterers," *Proc. IEE*, pt. H, vol. 132, pp. 424–432, Dec. 1985.
- [156] J. R. Mosig, "Arbitrarily shaped microstrip structures and their analysis with a mixed potential integral equation," *IEEE Trans. Microwave Theory Tech.*, vol. MTT-36, pp. 314–323, Feb. 1988.
- [157] J. R. Mosig, "Integral equation technique," in *Numerical Techniques for Microwave and Millimeter-Wave Passive Structures*, T. Itoh (ed.), New York: John Wiley & Sons, pp. 133–213, 1989.
- [158] K. A. Michalski and D. Zheng, "Analysis of microstrip resonators of arbitrary shape," *IEEE Trans. Microwave Theory Tech.*, vol. MTT-40, pp. 112–119, Jan. 1992.
- [159] R. Gillard, J. Corre, M. Drissi, and J. Citerne, "A general treatment of matched terminations using integral equations - modeling and applications," *IEEE Trans. Microwave Theory Tech.*, vol. MTT-42, pp. 2545–2553, Dec. 1994.
- [160] G. V. Eleftheriades and J. R. Mosig, "On the network characterization of planar passive circuits using the method of moments," *IEEE Trans. Microwave Theory Tech.*, vol. MTT-44, pp. 438–445, Mar. 1996.
- [161] P. B. Katehi and N. G. Alexopoulos, "Frequency-dependent characteristics of microstrip discontinuities in millimeter-wave integrated circuits," *IEEE Trans. Microwave Theory Tech.*, vol. MTT-33, pp. 1029–1035, Oct. 1985.
- [162] J. R. Mosig and F. E. Gardiol, "Analytical and numerical techniques in the Green's function treatment of microstrip antennas and scatterers," *Proc. IEE*, pt. H, vol. 130, pp. 175–182, Mar. 1983.
- [163] J. R. Mosig and T. K. Sarkar, "Comparison of quasi-static and exact electromagnetic fields from a horizontal electric dipole above a lossy dielectric backed by an imperfect ground plane," *IEEE Trans. Microwave Theory Tech.*, vol. MTT-34, pp. 379–387, Apr. 1986.
- [164] Y. L. Chow, J. J. Yang, D. G. Fang and G. E. Howard, "A closed-form spatial Green's function for the thick microstrip substrate," *IEEE Trans. Microwave Theory Tech.*, vol. MTT-39, pp. 588–592, Mar. 1991.
- [165] M. I. Aksun and R. Mittra, "Derivation of closed-form Green's functions for a general microstrip geometry," *IEEE Trans. Microwave Theory Tech.*, vol. MTT-40, pp. 2055–2062, Nov. 1992.
- [166] G. Dural and M. I. Aksun, "Closed-form Green's functions for general sources and stratified media," *IEEE Trans. Microwave Theory Tech.*, vol. MTT-43, pp. 1545–1552, July 1995.

- [167] D. M. Pozar, "Improved computational efficiency for the moment method solution of printed dipoles and patches," *Electromagnetics*, vol. 3, pp. 299–309, 1983.
- [168] H. Y. Yang, A. Nakatani, and J. A. Castañeda, "Efficient evaluation of spectral integrals in the moment method solution of microstrip antennas and circuits," *IEEE Trans. Antennas Propagat.*, vol. AP-38, pp. 1127–1130, July 1990.
- [169] U. V. Gothelf and A. Østergaard, "Full-wave analysis of a two-slot microstrip filter using a new algorithm for computation of the spectral integrals," *IEEE Trans. Microwave Theory Tech.*, vol. MTT-41, pp. 101–108, Jan. 1993.
- [170] E. H. Newman, "Generation of wide-band data from the method of moments by interpolating the impedance matrix," *IEEE Trans. Antennas Propagat.*, vol. AP-36, pp. 1820–1824, Dec. 1988.
- [171] T. W. Nuteson, K. Naishadham, and R. Mittra, "Spatial interpolation of the moment matrix for efficient analysis of microstrip circuits," *IEEE MTT-S International Symposium Digest*, pp. 971–974, June 1993.
- [172] B. Z. Steinberg and Y. Leviatan, "On the use of wavelet expansions in the method of moments," *IEEE Trans. Antennas Propagat.*, vol. AP-41, pp. 610–619, May 1993.
- [173] K. Sabetfakhri and L. B. Katehi, "Analysis of integrated millimeter-wave and submillimeter-wave waveguides using orthonormal wavelets expansions," *IEEE Trans. Microwave Theory Tech.*, vol. MTT-42, pp. 2412–2422, Dec. 1994.
- [174] G. Wang and G. Pan, "Full wave analysis of microstrip floating line structures by wavelet expansion method," *IEEE Trans. Microwave Theory Tech.*, vol. MTT-43, pp. 131–142, Jan. 1995.
- [175] K. Sabetfakhri and L. B. Katehi, "Fast wavelet analysis of 3-D dielectric structures using sparse matrix techniques," *IEEE MTT-S Int. Microwave Symp. Dig.*, pp. 829–832, May 1995.
- [176] T. Itoh, *Numerical Techniques for Microwave and Millimeter-Wave Passive Structures*, John Wiley & Sons, Inc., New York, 1989.
- [177] L. P. Dunleavy and P. B. Katehi, "A generalized method for analyzing shielded thin microstrip discontinuities," *IEEE Trans. Microwave Theory Tech.*, vol. 36, Dec. 1988, pp. 1758–1766.
- [178] P. B. Katehi and N. Alexopoulos, "On the modeling of electromagnetically coupled microstrip antennas-the printed dipole," *IEEE Trans. Antennas and Propagat.*, vol. 32, Dec. 1984, pp. 116–118.
- [179] J. C. Rautio, "A new definition of characteristic impedance," *1991 IEEE MTT-S Int. Microwave Symp. Digest*, June 1991, pp. 761–764.

- [180] S. B. Goldberg, M. B. Steer, P. D. Franzon and J. S. Kasten, "Experimental electrical characterization of interconnects and discontinuities in high speed digital systems," *IEEE Trans. on Components Hybrids and Manufacturing Technology*, vol. 14, December, 1991, pp. 761–765.
- [181] S. B. Goldberg, M. B. Steer, and P. D. Franzon, "Accurate experimental characterization of three-ports," 1991 *IEEE MTT-S Int. Microwave Symp. Digest*, June 1991, pp. 241–244.
- [182] R. Gillard, J. H. Corre, M. Drissi, and J. Citerne, "A general treatment of matched terminations using integral equations modeling and application," *IEEE Trans. Microwave Theory Tech.*, vol. 42, Dec. 1994, pp. 2545–2553.
- [183] E. K. L. Yeung, J. C. Beal, and Y. M. M Antar, "Matched load simulation for multiport microstrip structures," *Electronic Letters* ., vol.29, May 1993, pp.867–868.
- [184] C. A. Chisoffersen, M .A. Summeres, and M. B. Steer, "Harmonic balance analysis for systems with circuit-field interaction," 1998 *IEEE MTT-S Int. Microwave Symp. Digest*, June 1998, pp.1131–1134.
- [185] T. W. Nuteson, G. P. Monahan, M. B. Steer, K. Naishadham, J. W. Mink, K. Kojucharoff and J. Harvey, "Full-wave analysis of quasi-optical structures," *IEEE Trans. Microwave Theory Tech.*, vol.44, May 1996, pp. 701–710.
- [186] M. N. Abdulla, U. A. Mughal, and M. B. Steer, "Network characterization of a finite array of folded-slot antennas for spatial power combining application," *Proc. IEEE Antenna and Propagation Symp.*, July, 1999.
- [187] M. N. Abdulla, U. A. Mughal, H.-S. Tsai, M. B. Steer, and R. A. York, "A full-wave system simulation of a folded-slot spatial power combining amplifier array," 1999 *IEEE MTT-S Int. Microwave Symp. Digest*, June 1999.
- [188] M. B. Steer, J. F. Harvey , J. W. Mink, M. N. Abdulla, C. E. Christoffersen, H. M. Gutierrez, P. L. Heron, C. W. Hicks, A. I. Khalil, U. A. Mughal, S. Nakazawa, T. W. Nuteson, J. Patwardhan, S. G. Skaggs, M. A. Summers, S. Wang, and A. B. Yakovlev, "Global modeling of spatially distributed millimeter-wave systems," *IEEE Trans. Microwave Theory Tech.*, vol. 47, June 1999.
- [189] G. V. Eleftheriades, and J. R. Mosig, "On the network characterization of planar passive circuits using the method of moments," *IEEE Trans. Microwave Theory Tech*, Mar. 1996, pp. 438–445.
- [190] L. Zhu, and K. Wu, "Characterization of unbounded multiport microstrip passive circuit using an explicit network-based method of moments," *IEEE Trans. Microwave Theory Tech.*, vol.45, Dec. 1997, pp. 2114–2124.
- [191] R. F. Harrington, *Time-Harmonic Electromagnetic Fields*, New York: McGraw-Hill, 1961.
- [192] C. A. Balanis, *Antenna Theory: Analysis and Design*, New York: John Wiley, 1984.

- [193] R. E. Collin, *Field Theory of Guided Waves*, New York: IEEE Press, 1991.
- [194] J. A. Kong, *Electromagnetic wave Theory*, New York: Macmillan, 1968.
- [195] L. B. Felsen and N. Marcuvitz, *Radiation and Scattering of Electromagnetic Waves*, New York: IEEE Press, 1994.
- [196] M. Naguib, H. Ghali, and H. El-Hennawy, "Mixed analytical numerical calculation of microstrip antenna green s function using personal computer C-language," *IE Proc. of the 1995 IEEE AP-S Int. Symposium*, 1995
- [197] D. G. Dudley, *Mathematical Foundations for Electromagnetic Theory*, New York: IEEE Press, 1994.
- [198] R. F. Harrington, "Matrix methods for field problems," *Proc. IEEE*, vol. 55, pp. 136–149, Feb. 1967.
- [199] C. A. J. Fletcher, *Computational Galerkin Methods*, New York: Springer-Verlag, 1984.
- [200] C. Tai, *Dyadic Green's Functions in Electromagnetic Theory*, Second Edition, New York: IEEE Press, 1994.
- [201] W. L. Stutzman and G. A. Thiele, *Antenna Theory and Design*, New York: John Wiley, 1981.
- [202] R. A. York and Z. B. Popović, *Active and quasi-optical arrays for solid-state power combining*, John Wiley & Sons, Inc., 1997.
- [203] M. N. Abdulla, and M. B. Steer, "A partitioning approach to large scale electromagnetic problems applied to an array of microstrip coupled slot antennas," *IEEE MTT-S Inte. Microwave Symp. Digest*, June 1998, pp. 1783–1786.
- [204] A. I. Khalil and M. B. Steer, "Circuit theory for spatially distributed microwave circuits," *IEEE Trans. Microwave Theory Tech.*, Vol. 146, Oct. 1998, pp. 1500–1503.
- [205] R. Lampe, P. Klock, and P. Mayes, "Integral transformars useful for the accelerated summation of periodic, free-space Green's functions," *IEEE Trans. Microwave Theory Tech.*, vol. 33, pp. 734–736, Aug., 1985.
- [206] S. M. El-Ghazalyr and T. Itoh, "Electromagnetic interfacing of semiconductor devices and circuits," *Proc. of the 1997 IEEE MTT-S International Microwave Symposium*, Vol. 1, June 1997, pp. 151–154.
- [207] P. Ciampolini, P. Mezzanotte, L. Roselli and R. Sorrentino, "Accurate and efficient circuit simulation with lumped-element FDTD technique ," *IEEE Trans. Microwave Theory Tech.* Vol. 44, Dec. 1996, pp. 2207–2215.
- [208] M. N. Abdulla, and M. B. Steer, "A finite double-layer slot array structure for spatial power combining amplifier," *Pro. IEEE Antenna and propagation Symp.* , 1998, pp. 1206–1209.

- [209] C. Chen, W. E. McKinzie, and N. G. Alexopoulos, "Strip-fed arbitrarily shaped printed-aperture antennas," in *IEEE Trans. Antenna and Propagation*, Vol. 45, July 1997, pp. 1186–1198.
- [210] Huan-Shang Tsai, *Quasi-Optical Amplifier Arrays and FDTD Analysis of Planar Antennas*, Ph.D. Dissertation, UCSB, 1995
- [211] R. E. Collin, *Foundations for Microwave Engineering*, 2nd Edition, McGraw Hill, 1992, pp. 53–56.
- [212] H. S. Tsai, M. J. W. Rodwell, and R. A. York, "Planar Amplifier Array with Improved bandwidth Using Folded-slots," *IEEE Microwave and Guided wave letters*, Vol.4, No.4, April 1994, pp. 112-114.
- [213] C. Chen, and N. G. Alexopoulos, "Radiation by aperture antennas of arbitrary shape fed by a covered microstrip line," *Pro. IEEE Antenna and propagation Symp.*, pp. 438-445, 1993.

## Appendix A

### Evaluation of The Radiation Pattern

The radiation pattern of the antenna can be obtained with MoM techniques using Huygen's principle, which states that the fields outside some closed surface are uniquely determined by the tangential components of the fields on the surface. Once the field distributions on the surface surrounding the antenna are known, the radiation pattern of this antenna can be evaluated. This is most easily accomplished using the artifice of equivalent sources on the surrounding surface (Love's theory) as shown in Fig. A.1.

#### A.1 Far Field

The far-fields can be computed from the equivalent sources using the following equations with the coordinate system shown in Fig. A.2:

$$E_r \approx 0 \quad (\text{A.1})$$

$$E_\theta \approx -\frac{jk e^{-jkr}}{4\pi r} L_\phi \quad (\text{A.2})$$

$$E_\phi \approx +\frac{jk e^{-jkr}}{4\pi r} L_\theta \quad (\text{A.3})$$

where

$$L_\theta = \int_S [M_x \cos \theta \cos \phi + M_y \cos \theta \sin \phi - M_z \sin \theta] e^{jkr' \cos \psi} dS' \quad (\text{A.4})$$

$$L_\phi = \int_S [-M_x \sin \phi + M_y \cos \phi] e^{jkr' \cos \psi} dS' \quad (\text{A.5})$$

and

$$r' \cos \psi = x' \sin \theta \cos \phi + y' \sin \theta \sin \phi + z' \cos \theta \quad (\text{A.6})$$

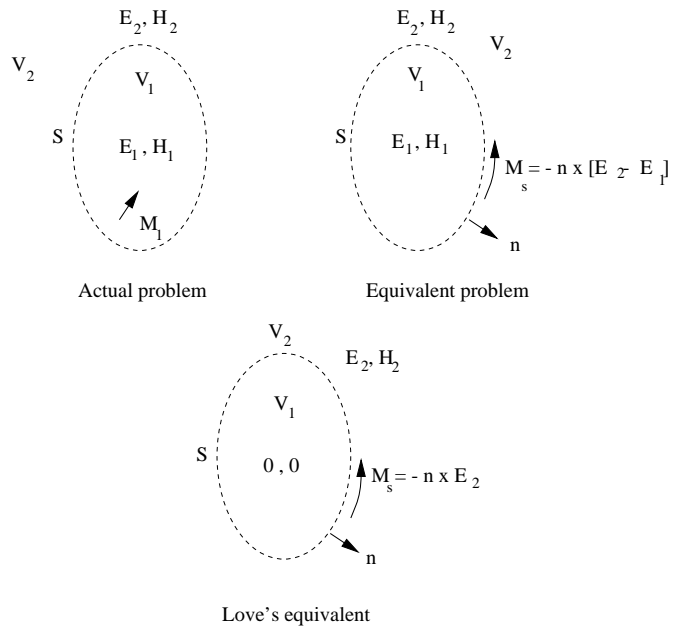


Figure A.1: Actual and equivalent problem models.

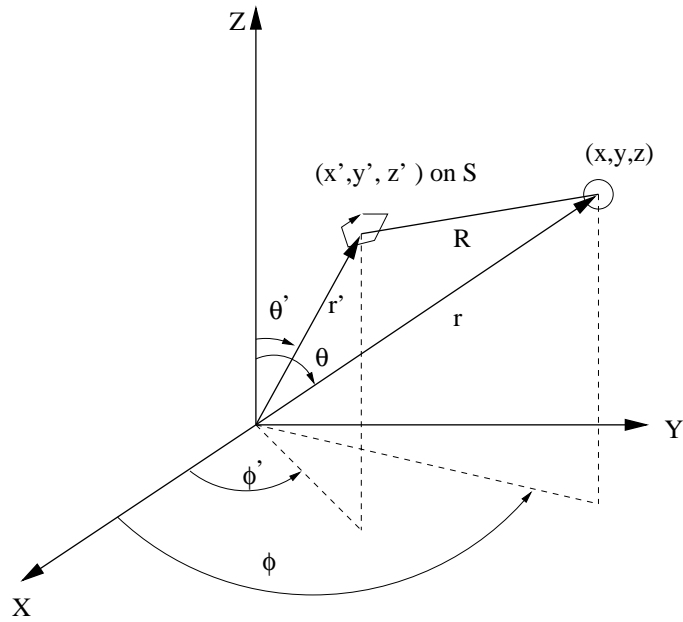


Figure A.2: The coordinate system.

### A.1.1 Input Format

The input files for the far field program contains the current distribution on the slot. the current distribution file format is

| x        | y        | Real           | Imag            |
|----------|----------|----------------|-----------------|
| -.065000 | 0.027700 | 0.000000271008 | 149.9575243634  |
| -.065000 | 0.028400 | 0.000000414812 | 153.7015607189  |
| -.065000 | 0.029100 | 0.000000539462 | 157.6550458958  |
| -.065000 | 0.029800 | 0.000000641049 | 162.2385823992  |
| -.065000 | 0.030500 | 0.000000724803 | 167.6615358527  |
| -.065000 | 0.031200 | 0.000000795231 | 174.2221070673  |
| -.065000 | 0.031900 | 0.000000859991 | -177.7868866032 |
| -.065000 | 0.032600 | 0.000000927145 | -169.3710837835 |
| -.065000 | 0.033300 | 0.000000980150 | -164.2265570293 |

### A.1.2 Output Format

The output file from the farfield program is “gnurad” which is gnuplot file. When you load “gnurad”, farfield postscript files are generated.

### A.1.3 Source Code of Farfield.f

```

c-----
c   farfield.f
c   program farfield pattern
c   Created by Mostafa Abdulla
c-----
c
c   program farfield
c
c   implicit none
c   integer nx,ny,n,i,j,k
c   real*8 pi,eps0,mu0,k0,k1,r,ri,theta,phi,temp
c   real*8 freq,epsr,d,xloc,yloc,xir,xii,yir,yii
c   real*8 etp0(0:180),epp0(0:180),etp90(0:180),epp90(0:180)
c   real*8 etp0max,epp0max,etp90max,epp90max
c   complex*16 cj,cxi,cyi,cxsum,cysum,ftheta,fphi
c   character*64 name
c
c   common /const/ freq,mu0,epsr,k0,k1,d,r,pi
c
c--input & output files
c
c   write(*,*) 'Enter file name containing current distributions:'
c   read(*,'(a)') name
c   open(10,file=name,status='unknown')
c   open(11,file='etp0.dat',status='unknown')
c   open(12,file='etp90.dat',status='unknown')
c   open(13,file='epp0.dat',status='unknown')

```

```

        open(14,file='epp90.dat',status='unknown')
        read(10,*) freq,epsr,d,nx,ny,n
c
c--define constants
c
    r=3.d0 ! m
    pi=dasin(1.d0)*2.d0
    cj=dcmplx(0.d0,1.d0)
    eps0=8.854185d-12 ! f/m
    mu0=pi*4.d-7 ! h/m
    k0=2.d0*pi*freq*dsqrt(mu0*eps0) ! 1/m
    k1=dsqrt(epsr)*k0 ! 1/m
c
c--initialize etmax and epmax
c
    etp0max=0.d0
    epp0max=0.d0
    etp90max=0.d0
    epp90max=0.d0
c
c--compute for phi=0 and phi=90 degrees
c
    do 20 k=1,2
    if (k.eq.1) then
    phi=0.d0
    else
    phi=pi/2.d0
    end if
c
c--compute far-field radiation
c
    do 50 j=0,180
    theta=dfloat(j)*pi/180.d0-pi/2.d0
c
c--array factor (due to x currents)
c
    cxsum=dcmplx(0.d0,0.d0)
    do 100 i=1,nx
    read(10,*) xloc,yloc,xir,xii
    cxi=dcmplx(xir,xii)
    ri=xloc*dsin(theta)*dcos(phi)+yloc*dsin(theta)*dsin(phi)
    cxsum=cxsum+cxi*cdexp(cj*k0*ri)
c 100 continue
c
c--array factor (due to y currents)
c
    cysum=dcmplx(0.d0,0.d0)
    do 200 i=1,ny
    read(10,*) xloc,yloc,yir,yii
    cyi=dcmplx(yir,yii)
    ri=xloc*dsin(theta)*dcos(phi)+yloc*dsin(theta)*dsin(phi)

```

```

        cysum=cysum+cyi*cdexp(cj*k0*ri)
    200 continue
c
c--reset input data file
c
        rewind(10)
        read(10,*) freq,epsr,d,nx,ny,n
c
c--compute e fields
c
        if (k.eq.1) then
* e theta for phi = 0 degrees
        etp0(j)=cdabs(cdexp(-cj*k0*r)/(4.d0*pi*r)*
&          (ftheta(theta,phi)*cxsum +
&          ftheta(theta,phi-pi/2.d0)*cysum))
* find e theta max
        temp=etp0(j)
        if (temp.gt.etp0max) etp0max=temp
* e phi for phi = 0 degrees
        epp0(j)=cdabs(cdexp(-cj*k0*r)/(4.d0*pi*r)*
&          (fphi(theta,phi)*cxsum +
&          fphi(theta,phi-pi/2.d0)*cysum))
* find e phi max
        temp=epp0(j)
        if (temp.gt.epp0max) epp0max=temp
        else
* e theta for phi = 90 degrees
        etp90(j)=cdabs(cdexp(-cj*k0*r)/(4.d0*pi*r)*
&          (ftheta(theta,phi)*cxsum +
&          ftheta(theta,phi-pi/2.d0)*cysum))
* find e theta max
        temp=etp90(j)
        if (temp.gt.etp90max) etp90max=temp
* e phi for phi = 90 degrees
        epp90(j)=cdabs(cdexp(-cj*k0*r)/(4.d0*pi*r)*
&          (fphi(theta,phi)*cxsum +
&          fphi(theta,phi-pi/2.d0)*cysum))
* find e phi max
        temp=epp90(j)
        if (temp.gt.epp90max) epp90max=temp
        end if
        50 continue
        20 continue
c
c--output file
c
        do 60 j=0,180
        theta=dfloat(j)*pi/180.d0-pi/2.d0
        write(11,7) theta*180.d0/pi,etp0(j)/etp0max
        write(13,7) theta*180.d0/pi,epp0(j)/epp0max
        write(12,7) theta*180.d0/pi,etp90(j)/etp90max

```

```

        write(14,7) theta*180.d0/pi,epp90(j)/epp90max
    60 continue
c
c--screen output
c
    write(*,*) 'phi = 0 degrees'
    write(*,*) ' |e| theta maximum: ',etp0max,' v/m'
    write(*,*) ' |e| phi maximum: ',epp0max,' v/m'
    write(*,*) 'phi = 90 degrees'
    write(*,*) ' |e| theta maximum: ',etp90max,' v/m'
    write(*,*) ' |e| phi maximum: ',epp90max,' v/m'
c
c--gnuplot output
c
    call gnuplot(etp0,epp0,etp90,epp90,etp0max,epp0max,etp90max,
&                epp90max)

    7 format(2(g15.7,2x))
    stop
    end
c-----
c
c      ----- pattern factors -----
c
c-----
c
    complex*16 function ftheta(theta,phi)

    implicit none
    real*8 theta,phi,freq,mu0,epsr,k0,k1,r,pi,d,num,a1
    complex*16 cj,carg,den
    common /const/ freq,mu0,epsr,k0,k1,d,r,pi
    cj=dcmplx(0.d0,1.d0)
    carg=-cj*2.d0*pi*freq*mu0*dcos(phi)*dcos(theta)
    a1=dsqrt(epsr-dsin(theta)**2)
    num=a1
    den=a1-cj*epsr*dcos(theta)*dcos(k1*d*a1)/dsin(k1*d*a1)
    ftheta=carg*num/den*cdexp(-cj*k0*r)/r
    return
    end
c-----
c
    complex*16 function fphi(theta,phi)

    implicit none
    real*8 theta,phi,freq,mu0,epsr,k0,k1,r,pi,d,num,a1
    complex*16 cj,carg,den
    common /const/ freq,mu0,epsr,k0,k1,d,r,pi
    cj=dcmplx(0.d0,1.d0)
    carg=cj*2.d0*pi*freq*mu0*dsin(phi)*dcos(theta)
    a1=dsqrt(epsr-dsin(theta)**2)
    num=1.d0
    den=dcos(theta)-cj*a1*dcos(k1*d*a1)/dsin(k1*d*a1)

```

```

    fphi=carg*num/den*cdexp(-cj*k0*r)/r
    return
    end
c-----
    subroutine gnuplot(etp0,epp0,etp90,epp90,etp0max,epp0max,
&                    etp90max,epp90max)

    implicit none
    real*8 etp0(0:180),epp0(0:180),etp90(0:180),epp90(0:180)
    real*8 etp0max,epp0max,etp90max,epp90max,theta,r,x,y
    real*8 pi,xetp0,yetp0,xep90,yep90,xetp90,yetp90,xep90,yep90
    integer j,i
c--data files
    open(15,file='gnu_polar_data.dat',status='unknown')
    open(16,file='gnu_polar_grid.dat',status='unknown')
    open(17,file='gnurad',status='unknown')
c
c--compute circles for polar plot
c
    pi=dasin(1.d0)*2.d0
    r=0.d0
    do 30 i=1,5
    r=r+0.2d0
    do 20 j=0,180,2
    theta=dfloat(j)*pi/180.d0
    x=r*dcos(theta)
    y=r*dsin(theta)
    write(16,2) x,y
    20 continue
    write(16,3)
    30 continue
c
c--compute radius lines for polar plot
c
    do 40 i=0,180,15
    theta=dfloat(i)*pi/180.d0
    x=dcos(theta)
    y=dsin(theta)
    write(16,2) 0.d0,0.d0
    write(16,2) x,y
    write(16,3)
    40 continue
c
c--plot fields
c
    do 10 j=0,180
* shifted by 90 degrees
    theta=dfloat(j)*pi/180.d0
    i=180-j
* fields in real and imaginary format
    xetp0=etp0(i)/etp0max*dcos(theta)

```

```

yetp0=etp0(i)/etp0max*dsin(theta)
xepp0=epp0(i)/epp0max*dcos(theta)
yepp0=epp0(i)/epp0max*dsin(theta)
xetp90=etp90(i)/etp90max*dcos(theta)
yetp90=etp90(i)/etp90max*dsin(theta)
xepp90=epp90(i)/epp90max*dcos(theta)
yepp90=epp90(i)/epp90max*dsin(theta)
write(15,1) xetp0,yetp0,xepp0,yepp0,xetp90,yetp90,xepp90,yepp90
10 continue
c
c--generate "gnurad" file
c
write(17,4)
write(17,5)
write(17,6)
write(17,7)
c
c--format statements
c
1 format(8(g15.8,1x))
2 format(2(g15.8,1x))
3 format(/)
4 format('set nokey',/, 'set nozeroaxis',/, 'set noyzeroaxis',/,
& 'set noborder',/, 'set noxtics',/, 'set noytics',/,
& 'set size 0.766, 0.514',/)
5 format('# polar plot labels',/,
& 'set label "-90" at -1.12,0.0',/,
& 'set label "90" at 1.05,0.0',/,
& 'set label "0" at 0.0,1.05',/,
& 'set label "-60" at -0.98,0.52',/,
& 'set label "-30" at -0.6,0.92',/,
& 'set label "30" at 0.54,0.92',/,
& 'set label "60" at 0.92,0.52',/,
& 'set label "1.0" at -1.04,-.05',/,
& 'set label "0.8" at -0.84,-.05',/,
& 'set label "0.6" at -0.64,-.05',/,
& 'set label "0.4" at -0.44,-.05',/,
& 'set label "0.2" at -0.24,-.05',/,
& 'set label "0.0" at -0.04,-.05',/,
& 'set label "0.2" at 0.16,-.05',/,
& 'set label "0.4" at 0.36,-.05',/,
& 'set label "0.6" at 0.56,-.05',/,
& 'set label "0.8" at 0.76,-.05',/,
& 'set label "1.0" at 0.96,-.05',/)
6 format('# ex components',/, 'set term x11',/,
&'plot "gnu_polar_data.dat" u 1:2 w l, "gnu_polar_data.dat" u 7:8 w
& l, "gnu_polar_grid.dat" w l 4',/,
&'pause -1',/, 'set term postscript eps "helvetica-bold" 12',/,
&'set output "far_ex.ps"',/, 'replot',/)
7 format('# ey components',/, 'set term x11',/,
&'plot "gnu_polar_data.dat" u 5:6 w l, "gnu_polar_data.dat" u 3:4 w

```

```

& 1, "gnu_polar_grid.dat" w l 4',/,
&'pause -1',/, 'set term postscript eps "helvetica-bold" 12',/,
&'set output "far_ey.ps"',/, 'replot',/)
return
end

```

## A.2 Near fields

Based on the near field equations presented in Section 4.9.1, a FORTRAN code was written to calculate the near fields.

### A.2.1 Input Format

The input file format is

```

38.          frequency(GHz)
.050         lx(meter)
.050         ly(meter)
0.0005       aslot(x cell size)
0.0006       bslot(y cell size)
50           nc (number of y pixels)
50           nr (number of x pixels)
90           ny (total number of current cells )
.008         z  (the distance from the array (meter))

```

### A.2.2 Output Files

The output files from the nearfield program are :

```

ex           (the magnitude of the electric field in x direction)
ex_phase     (the phase of the electric field in x direction)
ey           (the magnitude of the electric field in y direction)
ey_phase     (the phase of the electric field in y direction)

```

### A.2.3 Matlab File

The following matlab file is used to generate a 2D contour color plot for the near field using the output files from the near field program.

```

%*****
%
% File: nearplot.m
% This file plots the Ex and Ey fields
% obtained from near field analysis
%

```

```

% History:
%   Mostafa           Created
%   Usman Mughal     Edited
%*****
clear;
fid=fopen('ex');
%fid=fopen('ex_phase');
%fid=fopen('ey');
%fid=fopen('ey_phase');
a=fscanf(fid,'%g',[1 inf]);
a=a';
fclose(fid);
n=length(a);
for i=1:n;
    z(i)=a(i);
end
n=sqrt(n);
for i=1:n
    for j=1:n
        Z(i,j)=z((i*n-n)+j);
    end
end
Z=Z'; x=1:n; y=x;
figure
colormap(gray);
grid; contour(x,y,Z,10); colorbar;
figure
surf(x,y,Z) mesh(Z) hidden on
colormap(hsv); colorbar;
xlabel('E (V/m)') xlabel('X') ylabel('Y')
colormap(hot) colorbar
figure
contour(x,y,Z,10); colorbar
figure
pcolor(x,y,Z) axis([1 n 1 n]) shading flat
colormap(hot) colorbar

```

## A.2.4 Source Code of Nearfield.f

```

c-----
c   nearfield.f
c   program nearfield pattern
c   Created by Mostafa Abdulla
c-----
    program fieldpattern

    implicit none
    integer nymax,ny,nx
    parameter(nymax=500)

```

```

integer nc,nr,i,ic,ir,j,jj
real*8 dx,dy,xoff,yoff,lx,ly,ys(nymax),xs(nymax),mr,mi,zt
real*8 pi,k0,freq,xt,yt,mmag,mphas,aslot,bslot
complex*16 mc(nymax),ex(200,200),ez(200,200),intgemxy,intgemzy
character*64 name

common/const/k0,pi
common/const/aslot,bslot
common/test/xt,yt,zt
pi=4.d0*atan(1.)
c-----
c freq start operating frequency (GHz)
c lx      the x width (m)
c      ly      the y length (m)
c nc number of the x-current cells of the stripline
c nr number of the y-current cells of the slot
c      ny
c-----
C-----
C      THE INPUT DATA FILE "inp_field"
C-----
      open(unit=2, file='inp_field',status='old')
      rewind(2)
      read(2,*)freq
      read(2,*)lx
      read(2,*)ly
      read(2,*)aslot
      read(2,*)bslot
      read(2,*)nc
      read(2,*)nr
      read(2,*)ny
      read(2,*)zt
      close(2)
      dx=lx/dfloat(nc-1)
      dy=ly/dfloat(nr-1)
      xoff=lx/2.
      yoff=ly/2.

      k0=2.d0*pi*freq*10.d0/3.

      write(*,*)'Enterfile name containing slot current distributions'
      read(*,'(a)') name
      open(12,file=name,status='unknown')
      rewind(12)
      read(12,*) freq,aslot,bslot,nx,ny
      do 45 i=1,ny
      read(12,*)xs(i),ys(i),mr,mi
      mc(i)=dcmplx(mr,mi)/bslot
45      continue
      close(12)

```

```

open(unit=13, file='ex',status='unknown')
rewind(13)
open(unit=14, file='ez',status='unknown')
rewind(14)

do 150 i=1,nc
do 155 j=1,nr
  ex(i,j)=dcmplx(0.d0,0.d0)
  ez(i,j)=dcmplx(0.d0,0.d0)

155  continue
150  continue

do 100 ic=1,nc
xt=dfloat(ic-1)*dx-xoff
do 100 ir=1,nr
yt=-dfloat(ir-1)*dx+yoff
do 10 i=1,ny
ex(ic,ir)=ex(ic,ir)+mc(i)*intgemxy(xs(i),ys(i))
ez(ic,ir)=ez(ic,ir)+mc(i)*intgemzy(xs(i),ys(i))
10  continue
100  continue
do 16 i=1,nc
do 15 j=1,nr
write(13,1)cdabs(ex(i,j))
15  continue
write(14,1)cdabs(ez(i,j))
16  continue
close(14)
close(13)
1  format(2x,f16.8)
2  format(I3,2x,I3)
end

c-----
complex*16 function intgemxy(xs,ys)

implicit none
integer lx,ly
complex*16 cj,cval,gemxy
real*8 xs,ys,xt,yt,zt,k0,pi,aslot,bslot
real*8 xl,xu,yl,yu
external gemxy
common/const/k0,pi
common/const/aslot,bslot
common/test/xt,yt,zt

cj=dcmplx(0.d0,1.d0)
xl=xs-bslot/2.
xu=xs+bslot/2.
yl=ys-aslot/2.
yu=ys+aslot/2.

```

```

lx=2
ly=2

call dcgq2(gemxy,xl,xu,yl,yu,lx,ly,cval)
intgemxy=cval
return
end
c-----
complex*16 function gemxy(xs,ys)

implicit none
complex*16 cj
real*8 r,xs,ys,xt,yt,zt,k0,pi,aslot,bslot
common/const/k0,pi
common/const/aslot,bslot
common/test/xt,yt,zt

cj=dcmplx(0.d0,1.d0)
r=dsqrt((xt-xs)**2.+(yt-ys)**2.+zt*zt)
gemxy=(-1./2/pi)*((1.+cj*r*k0)/r/r)*zt*cdexp(-cj*k0*r)/r
return
end
c-----
complex*16 function intgemzy(xs,ys)

implicit none
integer lx,ly
complex*16 cj,gemzy,cval
real*8 xs,ys,xt,yt,zt,k0,pi,aslot,bslot
real*8 xl,xu,yl,yu
external gemzy
common/const/k0,pi
common/const/aslot,bslot
common/test/xt,yt,zt

cj=dcmplx(0.d0,1.d0)
xl=xs-bslot/2.
xu=xs+bslot/2.
yl=ys-aslot/2.
yu=ys+aslot/2.
lx=2
ly=2
call dcgq2(gemzy,xl,xu,yl,yu,lx,ly,cval)
intgemzy=cval
return
end
c-----
complex*16 function gemzy(xs,ys)

implicit none
complex*16 cj

```

```
real*8  r, xs, ys, xt, yt, zt, k0, pi, aslot, bslot
common/const/k0, pi
common/const/aslot, bslot
common/test/xt, yt, zt

cj=dcmplx(0.d0, 1.d0)
r=dsqrt((xt-xs)**2.+(yt-ys)**2.+zt*zt)
gemzy=(1./2/pi)*((1.+cj*r*k0)/r/r)*(xt-xs)*cdexp(-cj*k0*r)/r
return
end
```

## Appendix B

### ArraySim

#### B.1 Making ArraySim

The following FORTRAN programs are in

```
/ncsu/erl/mbs_group/work/mostafa/ArraySim_Must
```

```
mpie_inter.f      (FORTRAN main program)
nearfield.f      (nearfield calculation)
farfield.f      (farfield calculation)
param_S.f      (S-parameters calculation )
param_Z_to_S.f  (convert from Z to S parameters)
cpw_yel.f      (CPW MoM matrix element program)
scalargreen.f   (scalar Green's function)
spatial_integrand.f (spatial integrand of Green's functions)
spatial_mat_elem.f (Spatial MoM matrix element calculation)
ginterpolated.f (interpolation of the scalar Green's functions)
interpolation.f (Green's function interpolation)
spectral_integrand.f (spectral integrand of Green's functions)
math.f          (math subroutines)
zelement.f     (Spectral domain MoM matrix element calculation)
matrix_element.f (general MoM matrix element calculation)
zinput.f       (calculate the input impedance)
matrix_inversion.f (matrix inversion)
```

##### B.1.1 Makefile

The following is the make file that links between the FORTRAN and C files.

```
# Makefile for MOM
#
# Auther: Usman Mughal
#
# Date: 11/10/97
#
# Use: - the xlc compiler on IBM's RS6000,
#       - the g++ compiler on SUN workstations.
# Remove the comment flag '#' from the
# respective "CPP" definition.
```

```

# Compile your project with:
# "make"
#
# "make clean" will delete all extra files
# and executables (useful when switching systems).
#
CXX=g++
#CXX=xlC
#
FC=g77
#
#STL=-lstdc++
#
#CXXFLAGS=
CDFLAGS= -L/ncsu/gnu/lib -L/afs/eos.ncsu.edu/ \
        contrib/gcc272/lib -lf2c
#
XLIB=-lX11
#
# Set the DEBUG definition to be empty if you do not
# want debug.
#
#DEBUG=-DDEBUG -g
#
#use this for Active Analysis
#CXXSRC = PostTransim.C
#use this for Passive Analysis
CXXSRC = main_new.C
FSRCS = interpolation.f ginterpolated.f math.f \
        matrix_element.f \
        param_S.f scalargreen.f spatial_integrand.f \
        spatial_mat_elem.f \
        spectral_integrand.f zelement.f nearfield.f \
        zinput.f matrix_inversion.f cpw_farfield.f \
        cpw_interpolation.f cpw_yel.f param_Z_to_S.f
OBJS = $(FSRCS:.f=.o) $(CXXSRC:.C=.o)
#use this for Active Analysis
#all: PostTransim
#
#mom: $(OBJS)
# $(CXX) -o PostTransim $(DEBUG) $(OBJS) $(CDFLAGS)
#$
all: mom
#
mom: $(OBJS)
$(CXX) -o mom $(DEBUG) $(OBJS) $(CDFLAGS)clean:
-rm -f $(OBJS)
#use this for Avtive Analysis
#depend:
# g++ -M PostTransim.C >> Makefile
depend:

```

```
g++ -M main_new.C >> Makefile
```

## B.2 Running ArraySim

Two steps are involved in running *ArraySim*:

- Converting layout CIF into modified CIF file
- Running ArraySim with input parameter file and modified CIF file

For passive analysis the usage is:

```
cifParser filename.cif
mom input_param.txt filename.cif
```

*cifParser* converts *filename.cif* into modified CIF file keeping the same name, *filename.cif*. *ArraySim* executable is called *mom* that takes two arguments; *input\_param.txt* and *filename.cif*.

For active analysis, the usage is:

```
PostTransim input_param.txt filename.cif
```

where *input\_param.txt* and *filename.cif* are the same files used for passive analysis discussed earlier. An *Outputs* and *Inputs* directory has to be created to contain all output files.

## B.3 Input Files

Enter data in following format.

```
value Description
2 antenna type: 1:sss 2:cpw 0:not defined
2.0 frequency in GHz
0.635 substrate height in mm
10.8 epsilon_r
1 Search Table on/off. on == 1 off == 0
1e-6 Search Table Tolerance Level (Default: 1e-6)
0 Print Individual Matrices and Complete Matrix
0 Print Inverted Matrix (Default on)
2.0 START freq (GHz). Should be same as one in line 2
4.2 END frequency (GHz)
0.1 Step size for frequency range
180 Characteristic Imp of cpw in Ohms.
0 new port definition flag. If 1 use new method for Y_nn
1 stub length factor. if 1 then port is 1 cell away if 2.
***** INCIDENT WAVE INFO *****
1 E_o to generate input for antenna in V/m
0 Ein_x incident in V/m
1 Ein_y incident in V/m
```

```

***** FAR FIELD INFO *****
10      Far Field Distance in meters
***** NEAR FIELD INFO *****
0.030   near field window length (m) i.e l_x
0.030   near field window width (m)  i.e l_y
75      no. of columns (for resolution)
75      no. of rows (for resolution)
0.0008  distance away from array in meters
1       by pass field analysis

```

## B.4 Output Files

Output files include network parameter files containing network parameters (S,Z and Y) for each frequency point, set in *input\_param.txt*, matrix files that include MoM matrix as a whole, individual sub-matrices, and inverted MoM matrix, output magnetic currents in x and y direction on the slots, all currents i.e. on all layers, data for Transim (circuit analysis), data for active analysis, near and far field data.

## B.5 Sample Run

```

%
*****
*
*      ArraySim for Quasi Optical Systems      *
*
* Simulation Begins                            *
*
* Version 3.0      01/25/1999                  *
* ERL Group                                               *
* North Carolina State University                 *
*****
Parsing CIF FILE...
Num of Ports 1
ORDER OF PORTS IN PORTARRAY[]
9000, -12500 Port Group: 1
Num of Layers: 1
Layer 1 cells: 264
Layer 2 cells: 0
Layer 3 cells: 0
L1_BasisCell_x[ ] size is: 201
L2_BasisCell_x[ ] size is: 0
L3_BasisCell_x[ ] size is: 0
L1_BasisCell_y[ ] size is: 201
L2_BasisCell_y[ ] size is: 0
L3_BasisCell_y[ ] size is: 0
Reading INPUT FILE...

```

Table B.1: ArraySim Output Files

| Type          | File Name                            | Description  |  |
|---------------|--------------------------------------|--|--|
| Matrix files  | <i>out_IncidentVector.txt</i>        | contains all sub-matrices  |  |
|               | <i>out_Complete.txt</i>              | Full MoM $\mathbf{G}$ matrix   |  |
|               | <i>out_Inverse.txt</i>               | Inverted MoM $\mathbf{G}$ matrix   |  |
| Network Files | <i>out_Reduced_Mat.txt</i>           | contains port based reduce matrix  |  |
|               | <i>out_S_Port.txt</i>                | port S parameters  |  |
| Current Files | <i>out_AllCurrents.txt</i>           | current on all layers  |  |
|               | <i>out_Current_AllFreq_x.txt</i>     | magnetic current in x direction for all freq   |  |
|               | <i>out_Current_AllFreq_y.txt</i>     | magnetic current in y direction for all freq   |  |
|               | <i>out_Current_x.txt</i>             | magnetic current in x dir for last freq pt.  |  |
|               | <i>out_Current_y.txt</i>             | magnetic current in y dir for last freq pt.  |  |
|               |                                      |  |  |
| Transim Files | <i>out_TransimExcitationInfo.txt</i> | I or V sources at the ports used to excite the active device   |  |
|               | <i>out_TransimPortInfo.txt</i>       | contains port group num. and port num. with frequency info.  |  |
|               | <i>out_PostTransimInput.txt</i>      | contains row num. of $\mathbf{G}$ where ports are located. This info. is used to create a new excitation vector. |  |
|               |                                      |  |  |
|               |                                      |  |  |
|               |                                      |  |  |
| Near Field    | <i>ex</i>                            | E in the x direction   |  |
|               | <i>ey</i>                            | E field in the y direction   |  |
|               | <i>ex_phase</i>                      | Phase of E in the x dir  |  |
|               | <i>ey_phase</i>                      | Phase of E in the y dir  |  |
| Far Field     | <i>EIPG.dat</i>                      | Isotropic power gain in dB in the y-dir  |  |
|               | <i>epp0.dat</i>                      | radiation pattern phi=0  |  |
|               | <i>etp0.dat</i>                      | radiation pattern theta=0  |  |
|               | <i>epp90.dat</i>                     | radiation pattern phi=90   |  |
|               | <i>etp90.dat</i>                     | radiation pattern theta=90   |  |

```

Antenna Structure: CPW
Frequency (GHz):4   Substrate Height (mm): 0.635
Epsilon_r:         10.8 ST_on/off:         1   maxtol: 1e-06
Print Matrices: 0   Print Inverted Mat: 0
Start Freq:        4   End Freq:          5.2 Step Freq: 0.1
Charateristic Impedance of Stripline, Zc : 180
USE new port definition: 0
Incident Field Const: 1
Incident E-Field x: 0
Incident E-Field y: 1
Far Field Distance: 10
window_length_x 0.03
window_length_y 0.03
numOfCols        75
numOfRows        75
nearFieldDistance 0.0008
By Pass Field Analysis: 1
xmin :500 xmax: 26500
xMax_distance 27000
ymin :-19500 ymax: 6500
yMax_distance 27000
Frequency: 4
Done with Internal Parsing!
FREQUENCY : 4

```

```

Freq FILL 4
Creating Main Matrix...
Begin Filling...
Size of Sub Matrix is: 161604
Number of Quads in Y[s1,s1] 4

```

```

Total Number of SubMatrices are: 1
Calculate Data to Interpolate Array Region

```

```

Interpolation for CPW Structure:
&freq,&epsr,&d,&aline,&xmax, &ymax
4 10.8 0.000635 0.001 0.027 0.027
freq= 4.
polr= 1.00118569 poli= 0.
-----

```

```

Done with Interpolation
A ONE LAYER STRUCTURE ONLY
CALLING L1_XX
elm found: 39865 elm not found: 536**
CALLING L1_XY
elm found: 39749 elm not found: 652**
TRANSPOSING QUAD1 to get QUAD 2 for L1_YX
CALLING L1YY
elm found: 39865 elm not found: 536**
Merging all 4 Quads

```

Merging all submatrices to form one Matrix...  
End of Filling...  
LU Factorizing....  
Calling Matrix\_inverse  
Inverting Matrix....  
Reducing Matrix....  
Calculating Current Vector...  
Exiting Structure with incident Field....

CPW ANTENNA

Plane Perpendicular Incident Field with Hy zero  
Printing Incident Vector to file....  
Multiply Inverted Matrix with Incident Vector  
LHS VECTOR

Transim Port Parameters....

Converting Z port params to Y port parameters...

1.6816649013e-06 , 1.4958530703e-06

Calculating S Parameters...

Converting Z to S param

Printing Reduced Port Matrix...

CPW Array FAR FIELD ANALYSIS...

freq:= 4.

nx:= 201

ny:= 201

ax:= 0.001

ay:= 0.001

Phi = 0 degrees

|E| theta maximum: 0.000743245921 V/m

|E| phi maximum: 0.000417748433 V/m

Phi = 90 degrees

|E| theta maximum: 0.000419009956 V/m

|E| phi maximum: 0.000743258345 V/m

EIPG : 1.54894234

EIPG (dB): 1.9003525

EIRP (mW): 0.000290037328

EIRP (dBm): -35.375461

DONE CPW Array FAR FIELD ANALYSIS...

next freq....